Dark Matter and Variable Sources in M31

Jürgen Fliri

DARK MATTER AND VARIABLE SOURCES IN M31

Dissertation

an der

Fakultät für Physik

der

Ludwig-Maximilians-Universität München

vorgelegt von

Jürgen Fliri

München, den 08. März 2006

1. Gutachter: Prof. Dr. Ralf Bender
2. Gutachter: Priv. Doz. Dr. habil. Achim Weiss

Tag der mündlichen Prüfung: 12. Juni 2006

Für meine Großmutter

1904 — 2006

Zusammenfassung (Summary)

Diese Dissertation beschreibt die Ergebnisse des *Wendelstein Calar Alto Pixellensing Project (WeCAPP)*, welches in Richtung der Andromeda Galaxie (M31) nach Dunkler Materie in Form von "Massiven Kompakten Halo Objekten" (Machos) sucht. Die neuesten wissenschaftlichen Befunde legen ein Universum mit flacher Geometrie nahe, zu dessen Dichteinhalt Dunkle Materie ca. 23% beiträgt. Weitere 4.5% werden baryonischer Materie zugeschrieben, wobei von diesem Anteil bei kleiner Rotverschiebung bisher nur ca. 10% nachgewiesen werden konnten. Die Kandidaten für Machos in den Halos von Galaxien umfassen eine baryonische Komponente (vergangene Sterne wie z.B. Weiße Zwerge oder Neutronensterne), sowie eine nicht-baryonische Komponente, zum Beispiel in Form von primordialen Schwarzen Löchern. Da diese Objekte nur sehr schwach leuchten, sind sie dem direkten Nachweis entzogen. Sie können jedoch indirekt über den Gravitationslineneffekt nachgewiesen werden, den sie auf das Licht von Sternen im Hintergrund ausüben. Der beobachtbare Helligkeitsanstieg ist charakteristisch für solche sogenannten Mikrolinsenereignisse und läßt sich gut von der Helligkeitsänderung Veränderlicher Sterne unterscheiden. Die Seltenheit der Gravitationslinsenereignisse machte den Aufbau eines großen Datensatzes mit entsprechender zeitlicher Überdeckung notwendig, was durch simultane Beobachtungen an zwei Standorten (Wendelstein und Calar Alto) erreicht werden konnte. Nach einer kurzen Einführung gibt Kapitel 2 einen Überblick über das Experiment und die Beobachtungsstrategie und stellt die Teleskope und verwendeten Instrumente vor. Desweiteren behandelt Kapitel 2 die Eigenschaften des Datensatzes (1997 - 2005) und stellt die Algorithmen und Methoden vor, die zum Reduzieren der Daten angewandt wurden. Kapitel 3 präsentiert ein aktualisiertes Modell der Massen- und Lichtverteilung der Andromeda Galaxie, welches gut mit kinematischen Daten, als auch mit Vorhersagen von stellaren Populationsmodellen übereinstimmt. In Kapitel 4 wird dieses Modell genutzt, um die erwartete Rate von Gravitationslinsenereignissen und deren räumliche Verteilung für das WeCAPP Experiment zu berechnen. Kapitel 5 präsentiert die Kandidaten für Mikrolinsenereignisse, die im WeCAPP Datensatz identifiziert werden konnten. Sowohl die Anzahl der Ereignisse als auch ihre räumliche Verteilung deuten darauf hin, daß sie durch stellare Linsen in M31 selbst verursacht wurden (self-lensing). Der Machoanteil ist demgegenüber als eher gering einzuschätzen.

Der aufgebaute Datensatz ist aufgrund seiner langen zeitlichen Überdeckung hervorragend geeignet, intrinsisch Veränderliche Quellen in M31 zu studieren. In Kapitel 6 wird dieser Katalog von über 20 000 Veränderlichen Quellen präsentiert. Die gemessene Anzahldichte der Quellen weist eine starke Asymmetrie auf, die auf den Einfluß erhöhter Extinktion in den Spiralarmen zurückzuführen ist. Die Veränderlichen lassen sich in 3 Gruppen einteilen, wobei sich in Gruppe 1 die klassischen Cepheiden befinden. Gruppe 2 enthält unter anderem Klasse 2 Cepheiden und RV Tauri Veränderliche, wohingegen sich Gruppe 3 aus Langperiodischen Veränderlichen zusammensetzt. Die Parameter, die aus der Fourieranalyse der Lichtkurven klassischer Cepheiden extrahiert werden konnten, zeigen den bekannten Verlauf mit der Periode der stellaren Pulsation. Auch für die Klasse 2 Cepheiden und die RV Tauri Sterne konnte eine Korrelation bestimmter Phasenparameter gefunden werden, wobei die Relation der RV Tauri Sterne eine Fortführung der Relation der Klasse 2 Cepheiden ist. Dieses Ergebnis unterstützt die enge Verbindung zwischen beiden Arten von Veränderlichen. Neben pulsierenden Veränderlichen wurden auch über 60 klassische Novae identifiziert, deren Helligkeitsverlauf einen eruptiven Charakter aufweist. Der daraus resultierende Novakatalog, der in Kapitel 7 präsentiert wird, ist einer der größten und homogensten seiner Art. Eine Korrelation mit historischen Novae erbrachte 5 Kandidaten für wiederkehrende Novae. Für einige Novae gelang es, den Zeitpunkt des Ausbruchs genau zu bestimmen und damit zu zeigen, daß die Konstanz der Helligkeit 15 Tage nach Maximum für schnelle und moderat schnelle Novae zu gelten scheint. Sehr schnelle Novae scheinen jedoch davon abzuweichen. Mit Hilfe dieser Relation und den exponentiellen Angleichungen an die Lichtkurven konnte gezeigt werden, daß für mittlere Abfallzeitskalen t_2 die maximale Helligkeit linear mit dem Logarithmus der Abfallzeit skaliert, für große t_2 jedoch eine Abflachung dieser linearen Relation festzustellen ist.

Contents

List of Figures

List of Tables

Chapter 1

Introduction

The Wendelstein Calar Alto Pixellensing Project (WeCAPP) aims to detect dark matter in form of Massive Compact Halo Objects (Machos) towards the Andromeda Galaxy (M31). These candidates for dark matter are too faint to be observed directly, but can be detected by gravitational lensing of background stars. Besides detecting microlensing events WeCAPP contributed mainly to the field of variable star research, identifying and classifying thousands of variable sources in the central part of M31. In this introductory chapter we give an overview on dark matter and its possible constituents. Furthermore we introduce gravitational microlensing and give an overview of some properties of the classes of the intrinsic variable sources we have detected in course of the survey.

1.1 The dark matter problem

In the last decades, more and more evidence had been found that besides ordinary matter another type of matter, so called dark matter, must exist. Today, the existence of dark matter has been inferred on very different scales, from the scales of galaxies, galaxy clusters up to the scale of the Universe. These discoveries have given rise to various associated problems. For example dark matter acting in galaxies or galaxy halos may be of different nature as dark matter responsible for a sizeable fraction of the density of the Universe (e.g., Bosma 1998, Carr & Sakellariadou 1999).

1.1.1 Cosmological dark matter

In the cosmological standard model the universe was created in a hot big bang and is expanding since then. Its isotropy and homogeneity on large scales implies that its geometry can be described by the Robertson-Walker metric which reads in spherical coordinates (r, θ, ϕ)

$$ds^2(t) = c^2 dt^2 - a(t)^2 R_0^2 \left(\frac{dr^2}{1 - kr^2} + r^2(d\theta^2 + \sin^2(\theta)d\phi^2) \right) \quad . \tag{1.1}$$

Here we have introduced a dimensionless scale factor $a(t) = \frac{R(t)}{R_0}$ with the expansion parameters $R(t)$ and R_0 at epochs t and t_0, respectively. Using the Robertson-Walker metric Einstein's field equations,

connecting the energy content and the geometry of the Universe, write as

$$\left(\frac{\dot{a}}{a}\right)^2 + \frac{kc^2}{a^2 R_0^2} = \frac{8\pi G}{3}\rho_{tot} \quad , \tag{1.2}$$

and

$$2\frac{\ddot{a}}{a} + \left(\frac{\dot{a}}{a}\right)^2 + \frac{kc^2}{a^2 R_0^2} = -8\pi G \frac{p}{c^2} \quad , \tag{1.3}$$

with the pressure p and the total density $\rho_{tot} = \rho_{rad} + \rho_M + \rho_\Lambda$ being the sum of the the radiation density (ρ_{rad}), the matter density (ρ_M), and the vacuum density connected to a cosmological constant ($\rho_\Lambda = \frac{\Lambda c^2}{8\pi G}$). Equations 1.2 and 1.3 are also called the Friedmann-Lemâitre equations. The curvature parameter k describes the geometry of the Universe: open for $k = -1$, flat for $k = 0$, and closed for $k = +1$. Furthermore, G is the Gravitational constant, c the vacuum speed of light, and $\dot{a}, \ddot{a}$ denote the first and second time derivatives of the scale factor. For a single composition fluid with equation of states $p_{rad} = \frac{1}{3}\rho_{rad}c^2$ and $p_M = 0$ the densities scale as $\rho_{rad} = \rho_{rad,0}a^{-4}$ and $\rho_M = \rho_{M,0}a^{-3}$, where the index '0' refers to the present value. With the Hubble parameter $H(t) = \frac{\dot{a}(t)}{a(t)}$ describing the expansion of the Universe we can rewrite Eq. 1.2 as

$$\frac{H^2(z)}{H_0^2} = \Omega_{rad}(1+z)^4 + \Omega_M(1+z)^3 - \frac{kc^2}{R_0^2 H_0^2}(1+z)^2 + \Omega_\Lambda \tag{1.4}$$

where we introduced $\Omega_{rad} = \frac{\rho_{rad,0}}{\rho_{crit,0}} = \frac{8\pi G}{3H_0^2}\rho_{rad,0}$, $\Omega_M = \frac{\rho_{M,0}}{\rho_{crit,0}} = \frac{8\pi G}{3H_0^2}\rho_{M,0}$, $\Omega_\Lambda = \frac{\rho_\Lambda}{\rho_{crit,0}} = \frac{\Lambda c^2}{3H_0^2}$, and $H_0 \equiv H(z=0)$. Moreover, in Eq. 1.4 we have introduced the redshift z defined as

$$z = \frac{\lambda_o - \lambda_e}{\lambda_e} \tag{1.5}$$

where λ_e is the emitted wavelength, which, due to the cosmic expansion, is Doppler shifted to the longer, i.e. redder observed wavelength λ_o. The redshift z and the scale parameter a are connected by

$$(1+z) = \frac{a_0}{a} = \frac{1}{a} \quad . \tag{1.6}$$

As can be seen in Eq. 1.4, it is convenient to express the different components of the total density today in units of the present day critical density

$$\rho_{crit} = \frac{3H_0^2}{8\pi G} = 1.88 \times 10^{-26} h^2 \, \text{kg} \, \text{m}^{-3} \tag{1.7}$$

with $H_0 = 100h \, \text{km} \, \text{s}^{-1} \, \text{Mpc}^{-1}$ being the present Hubble constant. The parameter h is introduced to scale the results for different values of the expansion constant H_0. Current measurements yield a value $h = 0.71^{+0.04}_{-0.03}$ (Bennett *et al.*, 2003). From Eq. 1.4 we finally obtain

$$1 = \frac{8\pi G(\rho_{rad,0} + \rho_{M,0})}{3H_0^2} + \frac{\Lambda c^2}{3H_0^2} - \frac{kc^2}{R_0^2 H_0^2} \quad . \tag{1.8}$$

Setting $\Omega_k = -\frac{kc^2}{R_0^2 H_0^2}$ this writes as

$$1 = \Omega_M + \Omega_{rad} + \Omega_\Lambda + \Omega_k = \Omega_0 + \Omega_k \tag{1.9}$$
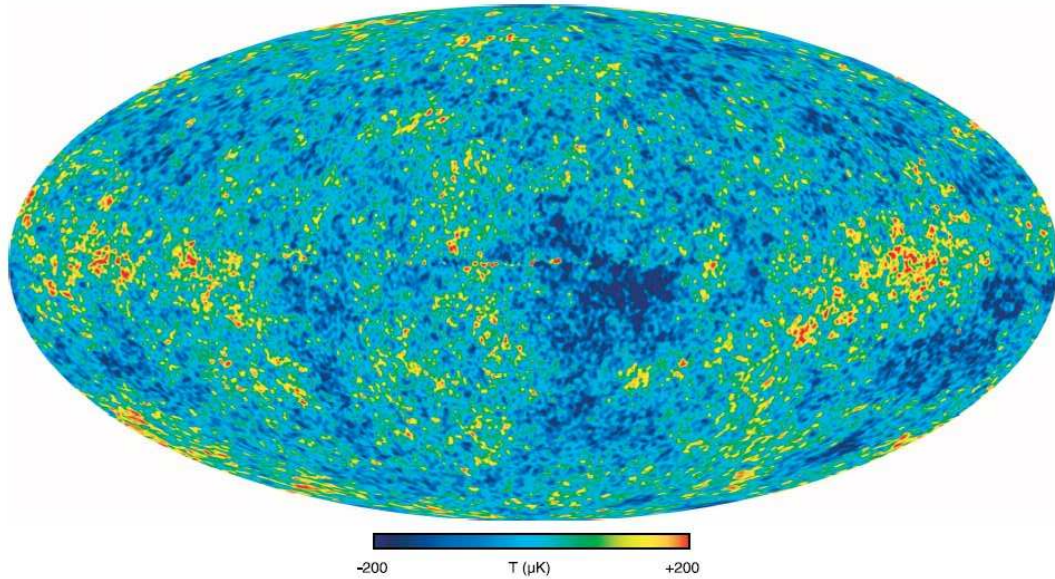
Figure 1.1: Image of the CMB background as seen by WMAP. The small fluctuations (shown as color differences) correspond to the seeds which eventually become the galaxies and structures we observe at present epoch (Bennett *et al.*, 2003).

with the cosmic density parameter Ω_0, defined as

$$\Omega_0 = \frac{\rho_0}{\rho_{crit}} = \frac{8\pi G \rho_0}{3 H_0^2} \quad . \tag{1.10}$$

In cases of $\Omega_0 < 1$ the Universe is open, as its density is too low to stop expansion. For $\Omega_0 > 1$ the Universe contains enough (matter and energy) density to close the Universe. For a density being being exactly the critical density, i.e. $\Omega_0 = 1$ the Universe is flat. The present value of the radiation density Ω_{rad} is orders of magnitudes smaller than the density of non-relativistic matter and therefore can be neglected at current epochs (e.g., Overduin & Wesson 2003). The most precise determinations of Ω_0 and its constituents rely on the measurements of anisotropies in the cosmic background radiation (CBR). This relic radiation from the big bang manifests itself in the cosmic microwave background (CMB). As the Universe expanded and cooled down, electrons and protons recombined and the Universe became transparent for photons. After decoupling from matter at a redshift $z_{dec} = 1089 \pm 1$ (Spergel *et al.*, 2003) the photons cooled down according to

$$T_{z=0} = \frac{T_{dec}}{(1 + z_{dec})} \tag{1.11}$$

and can be observed as a quasi isotropic radiation of $T = 2.725 \pm 0.002\,K$ (Spergel *et al.*, 2003) at microwave wavelengths. The detection of the CMB and its almost perfect blackbody spectrum over three decades of frequency (1-1000 GHz) still is one of the most powerful pieces of evidence in favor of the big bang. Although the CMB is largely isotropic, it shows small anisotropies at the $\Delta T / T \approx 10^{-5}$ level which were the seeds to form the large structures and galaxies we see today. Simple estimates show that in a completely baryonic Universe galaxies could not form in the time

available between BBN and now (for details see e.g., Padmanabhan 1995). As the baryons were coupled to the photons due to Thomson scattering for $z > z_{dec}$ they would not have had enough time to develop the structures. There must have been potential wells created by dark matter (which is not interacting with radiation) that could grow efficiently after the epoch of matter-radiation equality at $z_{eq} = 3233^{+194}_{-210}$ (Spergel *et al.*, 2003), in which the baryons then could settle after the Universe became transparent at z_{dec}.

Figure 1.1 shows an image of the CMB temperature fluctuations as detected by the WMAP satellite experiment, which improved the first detections of the CMB anisotropies by the COBE satellite (Efstathiou *et al.*, 1992) and balloon experiments (MAXIMA – Hanany *et al.* 2000 and BOOMERANG – Melchiorri *et al.* 2000) and yielded the most precise measurement of the CMB to date. It is useful to expand the CMB temperature fluctuations in spherical harmonics $Y_{lm}(\theta, \phi)$ according to

$$\frac{\Delta T}{T}(\theta, \phi) = \sum_{lm} a_{lm} Y_{lm}(\theta, \phi) \quad , \tag{1.12}$$

and to calculate the multipole amplitudes. The CMB anisotropy power spectrum (Fig. 1.2) can be split into three main regimes. For angular separations $\Theta > 2 \deg$ (or $l \lesssim 90$) the spectrum is dominated by the Sachs-Wolfe plateau (Sachs & Wolfe, 1967). In this part an almost primordial fluctuation spectrum can be observed, as larger separations were not in causal contact at the epoch of decoupling. This domain is followed by the acoustic peak region for angular separations $0.2 \deg < \Theta < 2 \deg$ which is described by the acoustic oscillations of an approximately $3000\,K$ hot plasma responding to perturbations of the gravitational potential. Diffusion of photons (Silk damping, Silk 1968) and the relatively large number of hot and cold regions along the line of sight inside the recombination shell damp the fluctuations for even smaller scales ($\Theta < 0.2 \deg$).

The CMB anisotropy power spectra can be used to discriminate between different cosmological models, as the location and the height of the different acoustic peaks depend on the values of several cosmological parameters like Ω_0, Ω_M, Ω_Λ, and the cosmic baryon density Ω_B. In Fig. 1.2 we show the anisotropy power spectrum as derived from the WMAP data (Spergel *et al.*, 2003).

For adiabatic density fluctuations the position of the first peak in the CMB power spectrum scales as $l \approx 220/\sqrt{\Omega_0}$, hence higher Ω_0 shifts the location of the first (and strongest) peak to smaller multipoles. The matter density Ω_M can be inferred from the overall amplitude of the peaks, whereas the baryon density is determined mainly by the peak ratios of odd and even peaks, corresponding to compressions and rarefactions, respectively (Page *et al.*, 2003). Moreover, both Ω_B and H_0 affect the height of the peaks.

The WMAP measurements favor a close to flat universe ($\Omega_0 = 1.02 \pm 0.02$) with a sizeable dark matter component (Spergel *et al.*, 2003; Bennett *et al.*, 2003)

$$\Omega_M = 0.27 \pm 0.04 \quad . \tag{1.13}$$

The density connected to 'dark energy' and a cosmological constant is derived to

$$\Omega_\Lambda = 0.73 \pm 0.04 \quad . \tag{1.14}$$

It is also interesting that not all of the matter can be baryonic as the baryon density is constrained to

$$\Omega_{B,CMB} = 0.044 \pm 0.004 \quad . \tag{1.15}$$
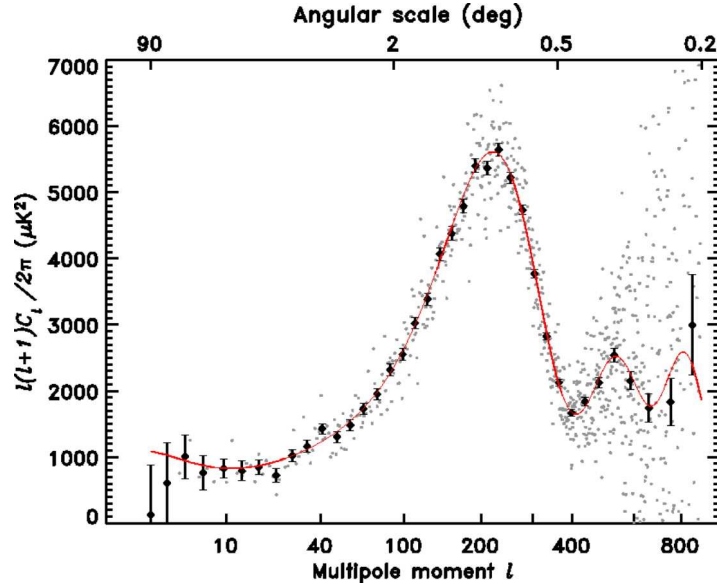
Figure 1.2: WMAP temperature angular power spectrum. Shown is the power $\Delta T^2 = \frac{l(l+1)}{2\pi}C_l$ (with $C_l = \langle |a_{lm}|^2 \rangle$) per logarithmic interval of the multipole moment l. The red line shows the best fitting ΛCDM model, the grey dots are the un-binned data (Spergel *et al.*, 2003).

This is confirmed by the cosmic baryon density derived from Big Bang Nucleosynthesis (BBN). The derivation of Ω_B from BBN is based on the measurements of primordial element ratios. During BBN a number of light elements are produced, namely ^{2}D, ^{3}He, ^{4}He, and ^{7}Li. The abundances and element ratios are determined by the nuclear cross sections σ_{nuc}, the neutron lifetime τ_n, the number of neutrino families N_ν, and the baryon-to-photon ratio $\eta = n_b/n_\gamma$ at the time of element production (Wagoner *et al.*, 1967). With σ_{nuc}, N_ν, and τ_n given by particle physics and n_γ being related to the temperature of the CBR, the baryon abundance can e.g. be inferred from the abundance of ^{2}D in primordial, i.e. high redshift, low metalicity hydrogen clouds. High precision measurements of the primordial abundance of ^{2}D can be achieved by observations of absorption line systems in the spectra of distant quasars, caused by intervening cold clouds. Based on the abundances of ^{2}D and ^{7}Li the baryon density was derived to (Cyburt, 2004)

$$\Omega_{B,BBN}h^2 = 0.0229 \pm 0.0013 \quad , \tag{1.16}$$

in close agreement with Ω_B inferred from the CMB. In Fig. 1.3 we show the current boundaries for Ω_M and Ω_Λ emerging from different kinds of experiments. Also included are the likelihood contours derived from the analysis of the power spectra derived from the distribution of galaxies. These power spectra trace the Large Scale Structure (LSS), as seen by large galaxy surveys like 2dFGRS (Percival *et al.*, 2001). Finally, Fig. 1.3 includes the results from supernovae experiments using supernovae of type SNIa as standard candles. Also the luminosity decrease of SNIa as a function of redshift points to an accelerating Universe, i.e. a non-zero cosmological constant (e.g., Riess *et al.* 2001).
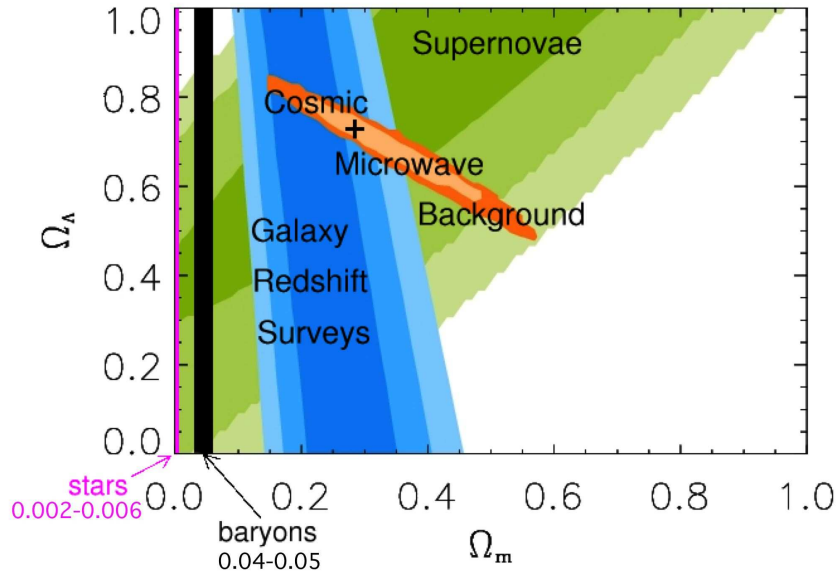
Figure 1.3: Boundaries for Ω_M and Ω_Λ derived from different experiments. The differently colored regions give the 1σ, 2σ, and 3σ intervals, respectively. The value of the concordance cosmological model with $\Omega_M \approx 0.27$ and $\Omega_\Lambda \approx 0.73$ is marked with a cross. Also shown are the regions of the baryonic density and the density associated with stars. Figure adapted from Gondolo (2004), based on Verde *et al.* (2002).

1.1.2 Dark matter in galaxy clusters

First evidence for the existence of dark matter came from the observations of galaxy clusters. The estimate of the amount of dark matter depends on the determination of the dynamical mass inside the virial radius of the object and the comparison with the mass associated with known visible populations. The dynamical mass can be derived for example from the velocity dispersion of the galaxies in the cluster (see Zwicky 1933 for a first estimate of the mass to light ratio $\left(\frac{M}{L}\right)$ of the Coma cluster), from the observations of hot X-ray cluster gas, or using gravitational lensing of background galaxies. The measurement of the velocity dispersion of the cluster members can be inferred from optical or radio data. The X-ray emission basically measures the temperature, its radial gradient, and the radial gradient of the density of the hot ionized gas inside the cluster. This can then be related to the potential well assuming hydrostatic equilibrium (e.g., Reiprich & Böhringer 2002; Castillo-Morales & Schindler 2003). Gravitational lensing uses the positions of the strongly lensed images and arcs of galaxies in the background of the cluster to infer the surface mass density in the plane of the cluster (e.g., Broadhurst *et al.* 2005). Also weak lensing studies, using the tangential alignment of background galaxies due to masses in the foreground, are used to infer the cluster masses. All these determinations point to large $\left(\frac{M}{L}\right)$ ratios in the range 100 to 500 for clusters. Comparing the different methods, Smail *et al.* (1997) find good agreement between the X-ray and lensing methods, the dynamical method yielding more deviant results. The difference is probably due to the enhanced influence of substructures on the determination of the cluster velocity dispersion.

1.1.3 Dark matter in spiral galaxies

Further evidence for the existence of dark matter came from the observations of rotation curves of spiral galaxies. Observations of the blue and redshifted spectral lines of cold neutral hydrogen (HI, using the 21cm emission line) or hot ionized hydrogen (HII, using the H_α emission line) in the disks of nearby galaxies showed that the rotation velocity v_{rot} stays approximately constant up to large radial distances from the center of the galaxy. In contrast to that, one would expect the rotation velocity to decline Keplerian with radius, i.e. $v_{rot} \sim r^{-0.5}$ for a model which assumes that all the mass is located in the galaxy center. For a more realistic model with an exponentially declining disk with scale radius r_d, and a radially constant $\left(\frac{M}{L}\right)$ ratio, v_{rot} should peak at approximately 2.2 r_d and should then decline towards Keplerian behavior (Freeman, 1970). As previously mentioned, the observations revealed that v_{rot} stays roughly constant for most of the surveyed galaxies, with some low mass spirals showing even rising v_{rot} at the outermost observed data point (e.g., van der Kruit & Bosma 1978, Bosma 1981a,b). Rubin et al. (1978, 1980, 1982) found a systematic trend of the rotation velocity curves with type and luminosity of the spiral galaxies in their H_α data. The flatness of the rotation curves in the outer parts points to a mass distribution $M(r)$ which is linearly rising with radius, i.e. $M(r) \sim r$. A density distribution $\rho(r)$ which matches the observations is that of an isothermal sphere with $\rho(r) \sim r^{-2}$.

The amount of dark matter necessary to reproduce the dynamics in spiral galaxies can be obtained by decomposing the light profile into a (probably flattened) bulge component and an exponential disk component. Having fixed the scale height of the disk and the $\left(\frac{M}{L}\right)$ ratios of bulge and disk, one is able to calculate the radial dependence of the circular velocity for each component. The total v_{rot} for the luminous matter is obtained by quadratically summing the rotation velocities of bulge and disk. From the difference of this 'luminous' contribution to the observed v_{rot} the 'dark halo' component can be deduced. Figure 1.4 shows one of the first examples of this method (van Albada et al., 1985). The decomposition technique has been applied to many galaxies, which showed that only a dark halo component brings the calculated and measured v_{rot} values in agreement. The discrepancy, however, can also be solved without a dark halo component by models assuming a maximum disk, but the agreement is only possible on expense of a moderate, i.e. not to high, $\left(\frac{M}{L}\right)$ ratio for the disk.

The question for local or disk dark matter was a controversial issue during the last decades. The matter content in the solar neighborhood can be obtained from star counts perpendicular to the Galactic disk and the mean-square of the stellar vertical velocities as a function of height over the Galactic plane. Creze et al. (1998) argue that their best solution for the local disk matter density (0.076 $\pm$ 0.015 $M_\odot$ pc^{-3}, derived from HIPPARCOS data) is in agreement with the sum of known populations and therefore leaves no space for disk dark matter. Also Kuijken & Gilmore (1991) and Holmberg & Flynn (2000) argue against disk dark matter. On the other hand, Bahcall (1984) and Bahcall et al. (1992) claim evidence for local disk dark matter. Moreover, Pfenniger et al. (1994) propose a fractal component of cold gas distributed over the whole disk as disk dark matter component.

1.2 Candidates for dark matter

Different dark matter candidates are distinguished according to their velocity at the time of recombination. Whereas kinematically Cold Dark Matter (CDM, non-relativistic at the onset of the matter-dominated epoch) can cluster on small scales, hot dark matter (HDM, i.e. relativistic at the onset of the matter-dominated epoch) escapes small substructures, but can cluster on larger scales. The
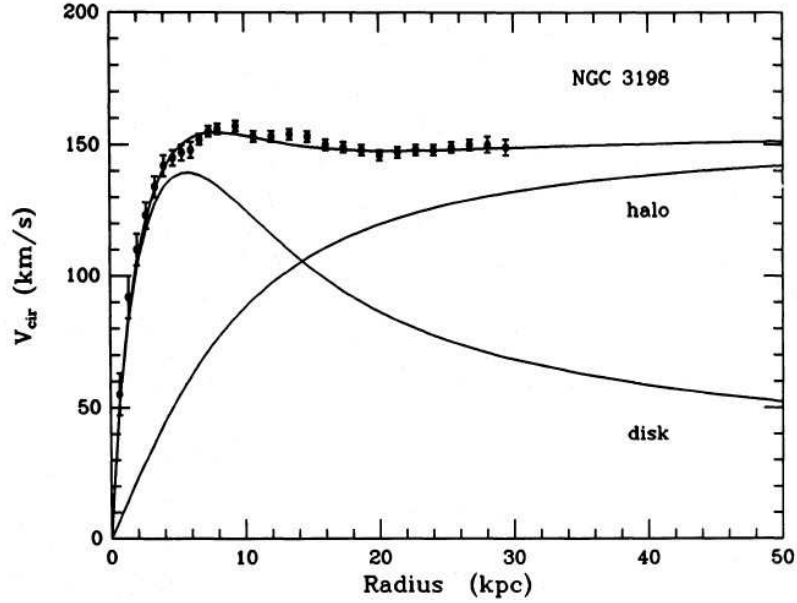
Figure 1.4: Decomposition of the rotation curve of the spiral galaxy NGC3198 into disk and dark halo components. Only with matter residing in a dark halo the measured rotation velocities can be reconciled with the models. Figure taken from van Albada *et al.* (1985).

most prominent candidates for HDM are neutrinos, whereas the most popular candidates for CDM are weakly interacting massive particles (WIMPS) as predicted by the supersymmetry theory. Furthermore, only a small fraction of the predicted baryonic matter could be detected up to now, which makes the study of baryonic dark matter to an important issue as well.

1.2.1   Non-baryonic dark matter

Hot dark matter

Neutrinos are the only non-baryonic dark matter particles detected until present time. As they are relativistic at the epoch of decoupling, they belong to the class of hot dark matter. Their mass can be constrained by measurements of oscillations between neutrino flavors which yield the differences between the squared masses of the neutrinos. From the small mass differences measured (e.g., Fukuda *et al.* 1998 and Ahmad *et al.* 2002) it seems that the mass of all three neutrinos is limited by (Gondolo, 2004)

$$m_i < 2.8\,\mathrm{eV} \quad (i = 1, 2, 3), \tag{1.17}$$

and the mass of the heaviest neutrino can be constrained to $\gtrsim 0.05\,\mathrm{eV}$. With these values the cosmic neutrino density can be calculated by

$$\Omega_\nu h^2 = \sum_{i=1}^{3} \frac{g_i m_i}{90\,\mathrm{eV}} \quad, \tag{1.18}$$

with $g_i = 1$ for the neutrino being a Majorana particle (i.e. its own antiparticle) and $g_i = 2$ for the neutrino being a Dirac particle (i.e not being its own antiparticle). As the WMAP results combined with measurements of the Large Scale Structure (LSS) put a limit on the density in hot neutrinos (Spergel *et al.*, 2003)

$$\Omega_\nu h^2 < 0.0076 \quad (95\% C.L.) \quad , \tag{1.19}$$

the masses of neutrinos can be constrained even further

$$(g_1 m_1 + g_2 m_2 + g_3 m_3) < 0.7 \, \text{eV} \quad . \tag{1.20}$$

Choosing $g_i = 1$, Ω_ν can be restricted to the range

$$0.0006 < \Omega_\nu h^2 < 0.0076 \quad . \tag{1.21}$$

Cold dark matter

The most often quoted candidates for CDM are weakly interacting massive particles. WIMPS are natural CDM candidates as they are dynamically cold. The most promising candidate in this respect is the the lightest particle (LSP) emerging from supersymmetric (SUSY) models which often is the lightest neutralino. WIMPs can be detected directly in bolometer experiments by measuring the energy release of elastic nucleus-WIMP scattering. Experiments like CDMS (Akerib *et al.*, 2003), EDELWEISS (Nollez & The EDELWEISS Collaboration, 2002), CRESST (Cozzini *et al.*, 2002), and DAMA (Bernabei *et al.*, 2003) usually are carried out in underground laboratories, which shield the experiment from high energetic cosmic rays. Cryogenic detectors measure the small temperature rise due to the recoil energy and in this way are able to constrain the WIMP energy. In Fig. 1.5 (taken from Gondolo 2004) we show the current and future experimental limits for the spin independent WIMP-proton cross-section along with some theoretical predictions for the expected values.

The indirect measurement of a possible WIMP population is based on the annihilation signal of WIMPs e.g in the Galactic center. As WIMPs are Majorana particles they can annihilate and produce high energy neutrinos, positrons, antiprotons, and γ-rays (Bergstroem, 2000). Calculations of the expected event rates (e.g., Prada *et al.* 2004) show that a strong γ-ray signal should be detected with high signal-to-noise in the direction of the Galactic center. The γ-rays can be detected using a new generation of Imaging Atmospheric Cerenkov Telescope (IACTs) currently being built or already in operation (e.g., MAGIC – Lorenz & Martinez 2005; HESS – Chadwick 2005; GAW – Cusumano *et al.* 2002).

The CDM distribution in dark halos not necessarily has to be smooth. CDM simulations of the evolution of the Universe show lots of halo-substructure at present time rather than halos with a smooth density distribution. Assuming WIMP dark matter, Diemand *et al.* (2005) predicted over 10^{15} Earth-mass halos to survive in the halo of the Milky Way until present time (as a result from a high resolution simulation). This halos should be stable against disruption (Moore *et al.*, 2005), but also different claims appeared in the literature (Zhao *et al.*, 2005).

Another candidate for weak interacting dark matter are ultra heavy particles, called WIMPZILLAs (Chung *et al.*, 1998). Ziaeepour (2001) constrained the mass and lifetime of these potential non-thermal relics of the big bang. They should be stable and have masses in a range 10^{12} GeV to 10^{16} GeV, and therefore should be much more massive than WIMPS.

Finally, a possible population of Massive Compact Halo Objects (Machos) could also have a non-baryonic component, namely primordial black holes (PBH). For the creation of PBHs a variety of
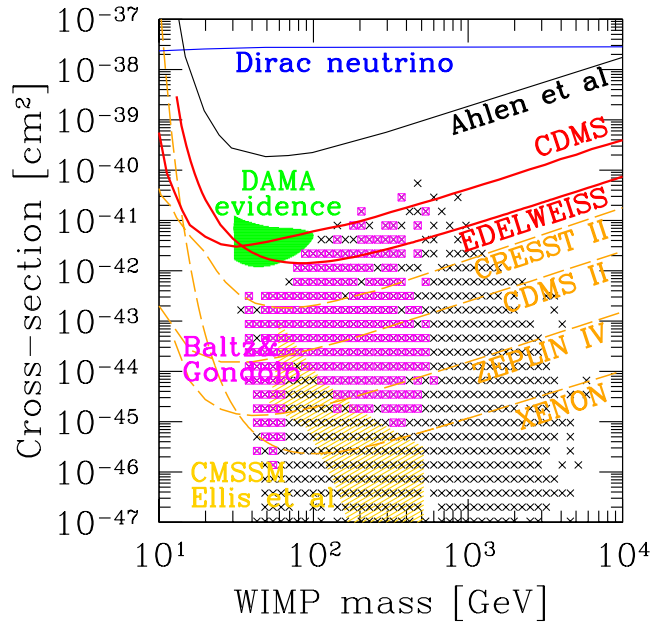
Figure 1.5: Current boundaries for the spin independent WIMP-proton cross-section as function of the WIMP mass. The upper limits of current experiments are labeled with CDMS (Akerib *et al.*, 2003) and EDELWEISS (Nollez & The EDELWEISS Collaboration, 2002). The claimed DAMA evidence (Bernabei *et al.*, 2003) is shown as a green region. The expected sensitivity regions of some selected forthcoming experiments are shown as dashed lines. The colored regions show some theoretical expectations for different WIMP models: the Constrained Minimal Supersymmetric Standard Model CMSSM (Ellis *et al.*, 2000) is shown as yellow region, the weak MSSM models of Baltz & Gondolo (2001, 2003) are shown as black crosses and magenta squares, respectively. Also shown are the theoretical predictions for a heavy Dirac neutrino which can be excluded as main constituent of Galactic dark matter in the mass range 3 GeV to 3 PeV. Finally the black line shows the first limit on WIMP dark matter by Ahlen *et al.* (1987). Figure taken from Gondolo (2004).

mechanism were proposed: creation during inflationary re-heating (García-Bellido & Linde, 1998), from a blue spectrum (i.e. spectral index $n > 1$) of primordial density fluctuations (Carr & Lidsey, 1993), or during a phase transition in the early universe (Khlopov *et al.*, 2000). The mass of these objects can span a wide range, from Jupiter masses of the order of 10^{-3} M$_\odot$ or even below to masses above 10^6 M$_\odot$. At the upper limit the mass of possible PBHs in galaxy halos is constrained by the velocity dispersion of the disks of spiral galaxies, as PBHs with masses above $10^3 M_\odot$ would heat the disk to much (e.g., Afshordi *et al.* 2003). Note, that the same dynamical arguments apply to massive associations of clumped baryonic Machos, as proposed by Metcalf & Silk (1996).

1.2.2 Baryonic dark matter

The baryonic matter density Ω_B is strongly confined both by BBN and measurements of the CMB (see above), both giving the same values inside the error bars. To estimate the amount of baryonic dark matter (BDM) one has to compare Ω_B with the density of luminous matter Ω_{lum}. Fukugita &

Peebles (2004) (FP04 in the following) estimate Ω_{lum} at the present epoch to

$$\Omega_{lum} = 0.005 \pm 0.004 \quad , \tag{1.22}$$

where they accounted for stars and stellar remnants in galaxies of different morphological type, and for gas in different media and of different temperatures. Here and in the following a value of $h = 0.7$ is assumed, unless otherwise stated.

Density in stars and remnants   The estimate is based on the the luminosity function (LF) and the mean mass-to-light ratio $\left(\frac{M}{L}\right)$ of galaxies. From the extensive local ($< z > \approx 0.1$) database of the Sloan Digital Sky Survey (SDSS, Abazajian *et al.* 2003) covering 220 square degrees, the LFs yield a luminosity density in the z-band of $L_z = (3.9 \pm 0.6) \times 10^8 h L_\odot$ (Mpc)$^{-3}$. Using 10^5 galaxies from the SDSS Kauffmann *et al.* (2003) derived the stellar $\left(\frac{M}{L}\right)_z \approx 1.85$ for bright galaxies and a smaller value (0.65) for fainter galaxies. FP04 took the LF-weighted mean of these two values ($\langle \left(\frac{M}{L}\right)_z \rangle \approx 1.5$) to calculate Ω_{star} from the luminosity density. Averaging the result with the value given in Cole *et al.* (2001), FP04 estimated the cosmic density in stars and its remnants to

$$\Omega_{star} = 0.0027 \pm 0.0005 \quad , \tag{1.23}$$

where the errors account for the uncertainty in the luminosity density ($\pm 15\%$), $\left(\frac{M}{L}\right)$ ($\pm 20\%$), and the errors due to the uncertainty in the adopted initial mass function (IMF, $\pm 20\%$).

Density in cool gas   The data of the large blind HIPASS HI survey (Zwaan *et al.*, 2003) with roughly 1000 galaxies constrained the density of neutral hydrogen and helium Ω_{HI+HeI} to

$$\Omega_{HI+HeI} = (6.2 \pm 1.0) \times 10^{-4} \quad . \tag{1.24}$$

Furthermore, the global density of molecular hydrogen Ω_{H_2} is estimated from the CO survey of Keres *et al.* (2003) to

$$\Omega_{H_2} = (1.6 \pm 0.6) \times 10^{-4} \quad . \tag{1.25}$$

Density in hot gas in the cluster environment   Under the assumption, that the baryonic-to-dark matter ratio in clusters agrees with the cosmic value, the hot gas density $\Omega_{cl,gas}$ can be derived by subtracting the stellar mass (see Eq. 1.23) from the total baryonic matter, and scaling the result with the cluster mass density parameter $\Omega_{cl} = 0.012^{+0.003}_{-0.004}$ (Reiprich & Böhringer, 2002), i.e. $\Omega_{cl,gas} = \Omega_{cl}(\Omega_{B,BBN} - \Omega_{star})/\Omega_M$. FP04 adopt $\Omega_{B,BBN} = 0.045 \pm 0.003$, which yields

$$\Omega_{cl,gas} = 0.0018 \pm 0.0007 \quad . \tag{1.26}$$

This is a larger result when compared with the density of hot cluster gas derived from the mean value of the cluster $\left(\frac{M}{L}\right)_B$ inside r_{200}, where r_{200} is the radius at which the mean cluster density $\langle \rho \rangle = 200 \rho_{crit}$. With $\langle \left(\frac{M}{L}\right)_B \rangle = (450 + 100)h$ and the stellar $(M_s/L)_B = 4.51 \pm 0.02$, the ratio of stellar mass to total mass gets $M_S/M_{tot} = 0.0143 \pm 0.003$, compared with $\Omega_{star}/\Omega_M = 0.01 \pm 0.002$.

Density in warm and cool plasma around galaxies   The estimate of the density of baryons associated with galaxies can again be inferred from the mean $\left(\frac{M}{L}\right)$ ratio and the mean the LF of galaxies. Prada *et al.* (2003) derived a mean $\langle (M/L)_B \rangle = 120h$ at the virial radius from the motion of 3000 satellites around host galaxies in the SDSS data. A less model dependent value can be obtained using the gravitational lensing shear around galaxies with known distance (see below). Using the SDSS data Sheldon *et al.* (2001) derived $\langle \left(\frac{M}{L}\right)_r \rangle = (170 \pm 21)h$ for radii smaller than 260 kpc. With this value and the SDSS *r*-band luminosity density $L_r = (2.32 \pm 0.25) \times 10^8 h L_\odot (Mpc)^{-3}$ (Blanton *et al.*, 2003), Fukugita (2003, in agreement with FP04) estimate $\Omega_{M,gal}$ within the virial radius of matter associated with galaxies $\Omega_{M,gal} = \langle \left(\frac{M}{L}\right)_r \rangle \frac{L_\odot}{M_\odot} L_r / \rho_{crit,0} = 0.14 \pm 0.02$. The density associated with a potential warm gas component can now be estimated by subtracting the known populations (Ω_{star}, Ω_{Hi+HeI}, Ω_{H_2}) from $\Omega_{B,gal} = \Omega_{M,gal} \frac{\Omega_{B,BBN}}{\Omega_M}$:

$$\Omega_{wc,gas} = 0.022 \pm 0.005 \quad . \tag{1.27}$$

Alternatively, one can obtain the density in warm baryons by subtracting the densities of stars and stellar remnants, neutral and hot ionized gas from the global baryon density as derived by CMB measurements or BBN,

$$\begin{aligned}
\Omega_{wc,gas} &= 0.045(\pm 0.003) - 0.0027(\pm 0.0005) - 0.0018(\pm 0.0007) - 0.0008(\pm 0.0001) \\
&= 0.040 \pm 0.003 \quad . \tag{1.28}
\end{aligned}$$

Therefore Eqs. 1.27 and 1.28 point to missing baryons not yet accounted for. FP04 have not counted the density of baryons in Lyman α clouds, but their contribution is by far not enough to explain the difference. Dark substructures, which have not formed stars and which appear in large numbers in CDM simulations (Ostriker *et al.*, 2003) could fill this gap. On the other hand, the missing baryons could also be at greater distances to the galaxies ($>$ a few hundreds kpc). Actually FP04 estimate a mean mass fraction $\rho(< r_{vir})/\rho_M$ of 0.6 within the virial radii of large galaxies, thus estimating that 60 % of the dark matter is gathered within the virialized parts of normal galaxies. If the baryons behave in the same way, the missing baryons could be in form of warm intergalactic plasma.

Dark fraction   Counting the detected entries in FP04 only, the density of known luminous matter Ω_{lum} (see Eq. 1.22) implies that a fraction

$$f_{BDM} = \frac{\Omega_{BDM}}{\Omega_B} = 1 - \frac{\Omega_{lum}}{\Omega_B} = (89 \pm 7)\% \tag{1.29}$$

of the total baryon density is invisible, or has not been detected until now. The candidates for BDM encompass compact stellar-like objects and diffuse mass distributions, i.e. diffuse intragalactic warm gas (see above). The first class are the typical Macho candidates that can be detected by the ongoing microlensing surveys (see below), and that include stellar remnants like white dwarfs, neutron stars, and stellar black holes (e.g. created in the collapse of massive stars), as well as anticipated stars like brown dwarfs or planets. This group of objects, optically faint or very faint ordinary matter, traditionally is thought to be the main contributors to a possible Macho population in halos of spiral galaxies. A potential diffuse component of warm gas ($\Omega_{wc,gas}$, see Eqs. 1.27 and 1.28) around galaxies should be difficult to detect. However, the intervening OVI absorption lines around galaxies and groups of galaxies in UV spectra of quasars could be the first observation of some of the claimed

warm intragroup gas (e.g., Tripp *et al.* 2000). Although the overall cosmic density of baryons is known quite accurately, the assumption that the baryons are similarly placed, in the hot cluster gas and in the warm and hot plasma in and around groups of galaxies, has not yet been convincingly observationally demonstrated, as pointed out by Fukugita & Peebles (2004). Therefore it is possible, that the abundance of baryonic dark matter changes with environment. Moreover, one can well expect that, if galaxies trace mass, about half of Ω_M should be localized in and near the virialized parts of galaxies.

To conclude this section, it appears likely that both baryonic and non-baryonic dark matter is needed. The relative contributions of both classes to the solutions of the various dark matter problems, however, may change from case to case (Carr, 2001).

1.3 Gravitational lensing

The best way to detect compact dark halo objects is to use gravitational lensing. Although these baryonic or non-baryonic objects may be too faint to be detected even with the largest telescopes, they are massive and therefore distort the spacetime in their surroundings. This distortion leads to a bending of light rays of background sources, which pass close by. The measurement of the exact deflection angle of light passing close to the sun during a solar eclipse (Eddington, 1919) was one of the first confirmations of Einstein's theory of general relativity. As the effects are very similar to light deflection by lenses in classical optics, these massive objects are also called 'gravitational lenses'. The first detected gravitational lens was a distant quasar, QSO 0957+561 A+B (Chang & Refsdal, 1979). Spectroscopical observations revealed that both objects (which are separated by 6 arcsec) are images of the same source, which is gravitationally lensed by a foreground structure. With the advent of high resolution space observatories like the Hubble Space Telescope (HST) it was possible to observe multiple images and spectacular arcs of background galaxies being lensed by rich clusters in the foreground. Using the position and shape of the multiple images it is possible to constrain the mass and mass profile of the lensing structure. Whereas strong lensing produces multiple images, arcs, and arclets, weak lensing can be used to measure the light bending in a statistical way, as massive foreground structures align the axes of elliptical galaxies tangentially to the center of mass.

The area of influence of a strong lens is typically characterized by its Einstein radius R_E, which depends on the geometry of the lens-source system and the lensing mass. Assume a source, that moves with constant projected relative velocity behind a static lens. At some time, the projected trajectory will enter the area of influence of the lens, which will alter the image of the source (see Fig. 1.6). For small lensing masses the separation of the multiple images will be of the order of microarcsec and therefore below the resolution limits of current instruments. However, since the surface brightness of the images stays constant, the changing shape and area of the images leads to a change of the integrated luminosity with time. For point sources, the maximum amplification depends only on the relative projected separation (in units of R_E) of lens and source. The temporal change of amplification (observed as light curve of the event) shows a characteristic shape, being symmetric around the epoch of highest magnification, and being achromatic when observed in different wavebands. Furthermore, microlensing events are unique, as the probability per star for lensing to occur is very low. In Fig. 1.7 we show light curves for different minimal normalized separations (called impact parameters) of lens and source.

The use of gravitational lensing to look for compact dark matter was first proposed by Paczynski
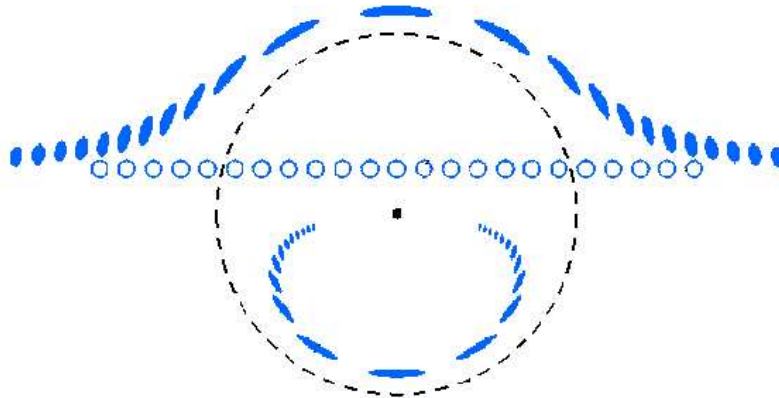
Figure 1.6: Gravitational lensing of a source which passes in the background of the lens. The dashed circle shows the Einstein radius R_E of the lens which is located in its center. The blue open circles mark the trajectory of the source and represent the images of the source in absence of the lens. The lensed images are shown as blue areas. At each position along the trajectory the source is lensed in two images, one of them inside R_E, the other one outside R_E. Since in the case of microlensing the separation of the two images is to small to be resolved the lensing event results in a temporal brightening of the source.

(1986). At the beginning of the following decade first experiments were initiated (MACHO – Alcock *et al.* 1993, EROS – Aubourg *et al.* 1993, and OGLE – Udalski *et al.* 2000), which observed millions of stars in the Large and Small Magellanic Clouds (LMC and SMC, respectively) and in the Galactic bulge to look for signatures of microlensing events. This large observational effort was necessary, as the probability per source star for lensing to occur is of the order of 10^{-6}. Hence, millions of sources have to be observed to detect an acceptable amount of events. First microlensing candidate events were already reported in 1993 (MACHO – Alcock *et al.* 1993, EROS – Aubourg *et al.* 1993) with the number of detected events rising fast since then. Especially the experiments towards the Galactic bulge delivered a large number of events which gave valuable insight in the distribution of stellar populations. Although the number of events reported from the halo probes towards the LMC was lower (13-17 for the MACHO collaboration depending on the detection thresholds, 3-4 for the EROS collaboration), it was sufficient to place upper limits for the halo fraction residing in Machos. Whereas EROS excluded a Macho fraction of more than approximately 20% (Lasserre *et al.*, 2000; Afonso *et al.*, 2003) for most lensing masses, the MACHO project reported a best fitting fraction of 20% for a typical halo model (with a 95% confidence interval of 8%-50%), and a best fitting Macho mass around $0.5M_\odot$ (Alcock *et al.*, 2000a). In Fig. 1.8 we show the EROS exclusion limits as function of lens mass taken from Lasserre *et al.* (2000).

The MACHO result and the supposed connection of the lenses with white dwarfs posed severe problems for theories of the chemical evolution of the Milky Way and the observations of metal enrichment (e.g., Fields *et al.* 2000). However, as the position of the lenses can be recovered in special cases only (e.g. in binary lensing events), discussions about the location of the lenses emerged very quickly. Some authors claimed that all of the events can be attributed to known stellar populations (stars lensing other stars as in the control experiment towards the Galactic bulge). This was based on
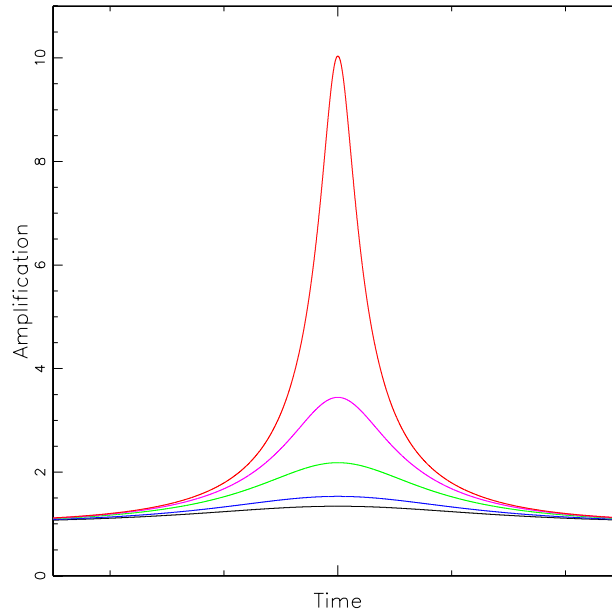
Figure 1.7: Theoretical light curves of microlensing events for different minimal separations u_0 (impact parameters given in units of R_E) of source and lens: u_0=1, 0.8, 0.5, 0.3, and 0.1 (black, blue, green, magenta, and red lines, respectively). As the approaches of lens and source get closer, the amplification of the source flux gets larger.

the result that the lenses, for which the position could be determined, reside in the LMC (e.g., Sahu 1994, 2003). The results of the Galactic microlensing experiments therefore remained inconclusive, which is reinforced by recent claims that more than 50% of the MACHO events towards the LMC are in reality variable stars and not caused by microlensing at all (Belokurov *et al.*, 2004). Although Griest & Thomas (2005) argue against this interpretation, and although the discrepancy could be due to differences in the used data sets (Evans & Belokurov, 2005), the nature of the events still is an open question.

To overcome the problem of unknown lens positions, Crotts (1992) and Baillon *et al.* (1992) proposed a new kind of experiment towards the Andromeda galaxy (M31), the nearest spiral galaxy. M31 possesses a dark halo of its own, and, as it has a high inclination, one expects an asymmetry of the event rates between lines of sight towards the near and the far side of the M31 disk (Crotts, 1992). Due to the different column densities of dark halo matter in these two directions, it should be possible to distinguish between halo lensing (showing an asymmetry) and star-star self-lensing (which does not show a big asymmetric signal) in a statistical way. The much higher distance of M31 relative to the Magellanic Clouds made it necessary to develop new methods to survey the, now unresolved, stars for brightness changes induced by lensing events. Two new techniques were proposed and subsequently implemented in experiments. The superpixel method was used by the AGAPE collaboration (Ansari *et al.*, 1997), whereas the Columbia/VATT experiment (Tomaney & Crotts, 1996) used the difference imaging technique. Since these experiments aim to extract the variations of a single source from the much smaller variations of the surface brightness of a galaxy, Gould (1996) invented the name 'pixellensing' for such surveys. The first lensing event towards M31 was detected by Agape (Ansari *et al.*, 1999), followed by a number of events until now. Based on 4 events, the Columbia/VATT
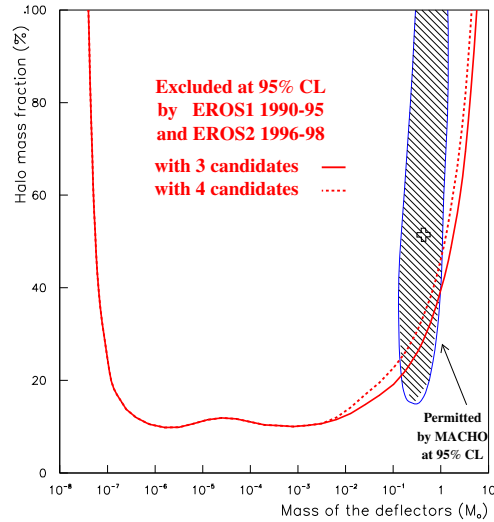
Figure 1.8: EROS exclusion limits (Lasserre *et al.*, 2000) for the halo fraction in compact objects as function of the lens masses (red lines). The limits are based on 3 and 4 events, respectively. Three of the events were detected towards the LMC (solid line exclusion limit), and one towards the SMC (included in the dashed line exclusion limit). Also shown are the limits and best fitting values (cross) of the MACHO project (Alcock *et al.*, 2000a), based on the analysis of 13-17 events (shaded region).

project claimed evidence of halo microlensing in M31, finding a microlensing halo mass fraction $f_b = 0.29^{+0.30}_{-0.13}$ for a nearly singular isothermal sphere model (Uglesich *et al.*, 2004).

At present six collaborations survey M31 for microlensing events: POINT-AGAPE (Paulin-Henriksson *et al.*, 2003), MEGA (de Jong *et al.*, 2004), SLOTT-AGAPE (Bozza *et al.*, 2000), NMS (Joshi *et al.*, 2005), Angstrom (Kerins *et al.*, 2005), and WeCAPP, the Munich-based Wendelstein Calar Alto Pixellensing Project (Riffeser *et al.*, 2001), which is subject of this thesis. POINT-AGAPE and MEGA shared the same data base (covering approximately 0.5 square degrees with a 2.5 m telescope) of the bulge and disk of M31, but used different methods to extract the microlensing events. Recently both groups published their results, whereas POINT-AGAPE finds evidence for a Macho contribution to the dark halo (based on 6 events, Calchi Novati *et al.* 2005), the MEGA results (based on 14 events, de Jong *et al.* 2005) are consistent with the expectations of pure self-lensing and a no-Macho halo, although a small Macho contribution is not ruled out. The discrepancies in the results are probably due to different M31 models involved.

1.4   Variable sources

Microlensing experiments naturally accumulate huge datasets of images, which cover the same area of sky for years. At the same time, the temporal coverage of the observations should be very good, since the probability of microlensing events to occur is very low and the events are comparably short. This is especially true for pixellensing experiments. The data sets of microlensing experiments therefore are perfectly suited for the study of all types of variable phenomena.

Variable sources are interesting objects in their own right. They trace stellar evolution, as almost

class	periods	detected
pulsating variables		
δ Scuti stars	≤ 0.3	-
RR Lyrae stars	$0.2 - 1.0$	-
type I Cepheids	$1 - 200$	X
type II Cepheids	$1 - 30$	X
RV Tauri stars	$30 - 150$	X
Long Period Variables	$30 - 1000$	X
erupting variables		
novae		X
supernovae		-
eclipsing binaries		X

Table 1.1: Overview of some major classes of variable stars. The second column gives the approximated range of their periods in days. In the last column we mark if the particular type of variable was detected in the WeCAPP survey (X).

all stars evolving from the main sequence enter a stage of variablity at one time or the other. As their frequency and period distribution depends on metalicity (abundance of elements more massive than helium) and age, they can be used to study stellar populations. In Table 1.1 we give an overview of some major classes of variable stars and mark if they were detected in the WeCAPP survey.

In Fig.1.9 (taken from Gautschy & Saio 1995) we show the position of the evolutionary sequences in the Hertzsprung-Russell-Diagram (HRD), where the luminosity L of stars is plotted against their effective temperature (T_{eff}). In the HRD, the stars are found in distinct regions and sequences, depending on their mass, metalicity, and evolutionary stage. The main sequence (MS), the core hydrogen burning phase, is the stadium where most of the observed stars can be found, as all stars spend most of their lifetime there. The position in the HRD at which stars originally enter the MS mainly depends on their initial mass (the more massive ones being brighter and having shorter MS lifetimes) and their metal content. After having ended central hydrogen burning the stars leave the MS and move to the red giant branch. During this stage the energy is produced by shell hydrogen burning on top of an inert contracting helium core. With the onset of helium burning in an electron degenerate core at the tip of the RGB, the low mass stars decline in luminosity and form the horizontal branch (for metal poor stars) or the red clump (for metal rich stars). After this stage the stars climb the Asymptotic Giant Branch (AGB) with He and H burning shells, and finally end as white dwarfs. For more massive stars with masses $\gtrsim 2.3 M_\odot$ the helium core burning sets in in a non-degenerate state. After an initial decline in luminosity they perform 'blue loops' in the HRD. Finally, they also climb the AGB and, like the lower mass stars, end up as white dwarfs. Massive stars with initial masses $\gtrsim 8 M_\odot$ explode in a supernova SNII and will end as neutron stars or stellar black holes.

Along their evolutionary sequence ('track') stars can enter a region of enhanced instability, the so called 'instability strip'. In this region, an almost vertical region in the HRD (see Fig. 1.9), stars are unstable against small perturbations of the equilibrium configuration. After a small perturbation the outer envelopes of the stars begin to oscillate, the mean density $\bar{\rho}$ and the oscillation period P being
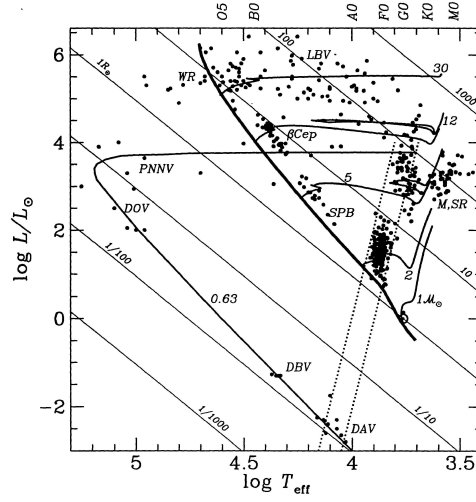
Figure 1.9: Hertzsprung-Russell diagram (HRD) showing the distribution of different types of variable stars. The zero-age MS is shown as thick solid line, thin lines show the evolutionary tracks for stars of solar metalicity and different masses (labels given in solar units). From the MS the lower mass stars move to the red giant branch, located at higher luminosity and smaller $\log(T_{\text{eff}})$. Due to the lower effective temperature the stars shift the maximum of their emission to longer wavelength, i.e. they become redder. The post-AGB track towards the white dwarf cooling sequence is shown just for one star. The instability strip is indicated by dashed lines. Thin diagonal lines mark positions with constant radius (labels given in solar units). Among other variable stars like β-Cepheids and Luminous Blue Variables (LBVs) the diagram also shows the position of the Mira and semi-regular variables (M, SR).

correlated as

$$\sqrt{\frac{\bar{\rho}}{\bar{\rho}_{\odot}}}P = Q \quad , \tag{1.30}$$

with the mean solar density $\bar{\rho}_{\odot}$ and the pulsation constant Q. The radial pulsation to be continuous and not damped requires some energy input at the time of compression and the release in a subsequent rarefaction. Eddington (1926) proposed a valve mechanism which feeds energy at the time of maximum compression. As the oscillating layers are not penetrating deep enough in the stellar body, the nuclear energy generated in the stellar core cannot be the source for the continuous energy input driving the pulsation. Rather, the oscillations are supported by several mechanisms acting simultaneously, the most important ones being the κ and γ mechanisms. The κ mechanism (Baker & Kippenhahn, 1962) is related to zones of high opacity in the outer layers of the star. After an initial compression these enhanced opacities prevent energy to be released immediately. The energy is stored below the ionization zone and is released later to drive the stellar pulsation.

The opacity of a region of the star is given by the Rosseland mean opacity κ with a temperature dependence according to

$$\kappa = \kappa_0 \rho^n T^{-s} \quad , \tag{1.31}$$

with a constant κ_0, the density ρ, and the temperature T. For the gas in the stellar envelope, where
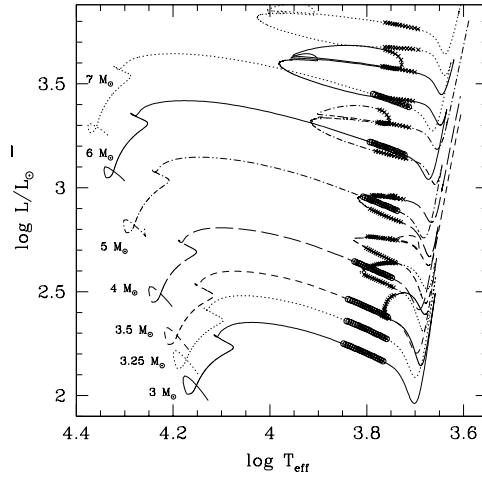
Figure 1.10: Theoretical HRD for stars with metalicity $Z = 0.2Z_\odot$ (metalicity of the SMC) and a helium abundance $Y = 0.25$. The evolutionary tracks for stars of different masses are shown as lines (labels given in solar units). Open circles and crosses (for the first and later crossings of the instability strip, respectively) mark the position of fundamental unstable modes (Baraffe *et al.*, 1998).

no abundant element (i.e. hydrogen or helium) is undergoing ionization, the slope of the energy dependence $s \approx 3.5$ and the slope of the density dependence $n \approx 1$. Thus, the opacity declines as the temperature rises and the energy can be radiated away more easily. However, in ionization zones of an abundant element, s gets small or even negative and energy can be stored. In fact, the second helium ionization zone is very efficient to drive pulsations with the κ mechanism. Also the first helium and the hydrogen ionization zones can drive pulsations, their strength depends however on the stellar type, in which pulsation is occurring.

Simultaneously to hindering the energy transport by the κ mechanism, the driving zones also absorb energy during compression to ionize the abundant element. The radiation flow is locally reduced and absorbed by the matter in the ionization region, which leads to a pressure maximum right after the epoch of minimum volume. This driving is called the γ mechanism (Cox *et al.*, 1966).

The driving mechanisms get more inefficient the more convection contributes to the energy transport. As convection in the envelopes gets more important as the stars get cooler (e.g., Baraffe *et al.* 1998), it is believed that this process limits the instability strip at the red edge. As stars get hotter and bluer the position of the ionization zone moves outward to less dense regions of the envelope. With the density being too low for an efficient driving, the stars again get stable against small perturbations of their equilibrium configuration (e.g., Christy 1966).

Model calculations of the stability of stellar envelopes have been widely used to determine the position of the instability strip in the HRD. In Fig. 1.10 we show the result of a self-consistent model of Baraffe *et al.* (1998), showing some evolutionary tracks for stars of different mass. At positions marked with crosses and circles stars are unstable against radial pulsation in the fundamental mode. As can be seen, the circles and crosses (marking the first and later crossings during an evolutionary track, respectively) are restricted to a small area, the instability strip.

The probably best known radially pulsating variable stars are the Cepheids. The classical Cepheids

are high mass, young and metal-rich (population I) red giants, whereas the type II Cepheids belong to an older population (also known as population II). Variables residing in the intersection of horizontal branch and instability strip are known as RR Lyrae stars. Due to the nature of the pulsation, period and luminosity are tightly correlated which can be observed in the period-luminosity (PL) relations for the different classes of stars. The logarithm of the pulsation period P is proportional to the (intensity- or magnitude-weighted) mean magnitude M ($\propto -\log(L)$) of the star

$$M = a\log(P) + b \quad , \tag{1.32}$$

where a denotes the slope and b denotes the zero-point. This type of relations makes variable stars excellent distance indicators. Once the extinction on the line of sight is known, the absolute (intrinsic luminosity at a standard distance) and apparent (i.e. observed) magnitudes can be linked to determine the distance of the star. Since their discovery (Leavitt & Pickering, 1912) the PL-relations for Cepheids were continuously improved. However, the studies regarding a possible metalicity and environmental dependence of the PL-relation are not finished yet.

Many of the stars on the upper red giant branch and AGB are variable. Long Period Variables with periods from about 30 days to over 1000 days can be found there. In these stars with predominantly convective envelopes the mechanisms driving the pulsation are not yet fully understood, although progress is made in the modeling. For example, Xiong *et al.* (1998) proposed that the dynamical and thermodynamical coupling between convection and oscillation could be the dominant factor for pulsation instability. Using this scheme they succeeded in showing the presence of an instability strip for red variables.

Apart from pulsation, stellar variability can also be due to eruptive processes, novae and supernovae being the best known examples of this class. Novae are caused by a thermonuclear runaway in a hydrogen-rich accretion disk around a white dwarf in a close binary system. In contrast, supernovae explosions of type II mark the final stage of stellar evolution of massive stars. As their type Ia counterparts they are of fundamental importance for the creation of heavy elements as well as for the metal-enrichment of the intergalactic medium.

Finally, variability can also be induced by environmental and geometrical effects. Eclipsing binary systems and ellipsoidal variables belong to this group, the first ones being important systems for the determination of distances.

1.5   Outline of the thesis

This thesis is organized as follows. In chapter 2 we give an overview of the WeCAPP survey. We present the basic properties of the data set, the telescopes and filters used, and present the data reduction techniques applied.

In chapter 3 we show our modeling of the Andromeda Galaxy. We use kinematical and photometric data to refine previous models from the literature. We show that with the adopted mass and luminosity distributions for the different components of the galaxy the mass-to-light ratios agree with theoretical predictions.

Chapter 4 introduces the basic properties of microlensing and pixellensing. We derive expressions for the expected distribution of microlensing events depending on the observables excess flux and full-

width-half maximum timescale of the events. Using the model presented in chapter 3 we calculate the number and spatial distribution of microlensing events for the WeCAPP survey without taking into account the efficiency of the experiment.

In chapter 5 we present the Macho candidates detected during the survey. A first search focused on short timescale and high signal-to-noise candidates in one years data and yielded two candidates. Assuming a full Macho halo the mass probability functions point to brown dwarfs as probable lenses. The whole data set allowed an unbiased search for microlensing events. We show the light curves of further five candidate events and give their basic properties.

Chapter 6 presents the variable star catalogue. In the data covering the years 2000-2003 we detected over 20000 intrinsic variable sources. We derived periods for the sources and classified the stars according to their position in the period-amplitude plane. For the Cepheid-like stars the classification is supported by Fourier decomposition of the light curves. We find a correlation between the phase terms for the classical Cepheids as well for the type II Cepheids and the RV Tauri stars.

Chapter 7 deals with the nova population of M31. We present the detection algorithms used and present the basic properties of the nova sample. We correlate our sample of over 60 novae with published and historical novae and find 5 candidates for recurrent novae. We show that the constancy of the luminosity 15 days past maximum seems to hold for fast and moderately fast novae. With this relation we derive the maximum luminosity-rate of decline diagram using a subsample of the detected novae.

We finally summarize this thesis in chapter 8.

Chapter 2

WeCAPP -
Tracing dark and bright matter in M31[1]

Abstract. We present WeCAPP, a long term monitoring project searching for microlensing events towards M31. Since 1997 the bulge of M31 was monitored in two different wavebands with the Wendelstein 0.8 m telescope. From 1999-2002 we extended our observations to the Calar Alto 1.23 m telescope. Observing simultaneously at these two sites we obtained a high time coverage during the observability of M31. We used the optimal image subtraction method by Alard & Lupton (1998) to check the thousands of frames for variability of unresolved sources. This enabled us to minimize the residuals in the difference image analysis (DIA) and to detect variable sources with amplitudes at the photon noise level. Thus we can detect microlensing events with corresponding amplifications $A > 10$ of red clump giants with $M_\mathrm{I} = 0$.

---

[1]This chapter is an updated version of the article Riffeser, Fliri, Gössl et al. (2001). Modified sections are highlighted by footnotes.

2.1 Introduction

In the last decade microlensing studies proved to be a powerful tool for searching dark matter in the Galactic halo. Several groups like the MACHO collaboration (Alcock *et al.*, 1993), OGLE (Udalski *et al.*, 1993), EROS (Aubourg *et al.*, 1993) and DUO (Alard *et al.*, 1995) followed the suggestion of Paczynski (1986) and surveyed millions of stars in the Large and Small Magellanic Clouds (LMC, SMC) and in the Galactic bulge for variability induced by gravitational microlensing. Although all of them discovered events compatible with gravitational lensing by Machos (Massive Astrophysical Compact Halo Objects) (Paczynski *et al.*, 1994; Ansari *et al.*, 1996; Alcock *et al.*, 1997; Alard & Guibert, 1997; Palanque-Delabrouille *et al.*, 1998; Alard, 1999; Afonso *et al.*, 1999; Alcock *et al.*, 2000a,b; Udalski *et al.*, 2000) they were not able to derive unambiguous constraints on the amount of baryonic dark matter and its distribution in the Galactic halo (see e.g., Evans & Kerins, 2000, and references therein).

Crotts (1992) and Baillon *et al.* (1993a) suggested to include M31 in future lensing surveys and pointed out that it should be an ideal target for these kind of experiments. In contrast to microlensing studies towards the LMC and the SMC, which are restricted to similar lines of sight through the Galactic halo, one can study many different lines of sight to M31, which allow to separate between self-lensing and true Macho events.

Since the optical depth for Galactic Machos is much greater towards M31 than towards the LMC, SMC or the Galactic bulge, one expects event rates greater than in previous lensing studies. Furthermore, M31 contributes an additional Macho population due to its own halo. Thus, three populations may contribute to the optical depth along the line of sight: Machos in the Galactic halo, Machos in the halo of M31 and finally stars in the bulge and the disk of M31 itself, a contribution called self-lensing.

The high inclination of M31 (77°) (Walterbos & Kennicutt, 1987) produces a near-far asymmetry of the event rates. The near side of the M31 disk will show less events than the more distant one (Crotts, 1992). Since Galactic halo-lensing as well as self-lensing events will not show this feature, a detected asymmetry will be evidence for the existence of M31 Machos.

As most of the sources for possible lensing events are not resolved at M31's distance of 770 kpc (Freedman & Madore, 1990) the name 'pixellensing' (Gould, 1996) was adopted for these kind of microlensing studies. In the mid nineties two projects started pixellensing surveys towards M31, AGAPE (Ansari *et al.*, 1997) and Columbia/VATT (Tomaney & Crotts, 1996). First candidate events were reported (Ansari *et al.*, 1999; Crotts & Tomaney, 1996), but could not yet be confirmed as Machos. This was partly due to an insufficient time coverage which did not rule out variable stars as possible sources.

In 1999, two new pixellensing projects, POINT-AGAPE (Kerins & the Point-Agape Collaboration, 2000), which reported 2001 a first candidate microlensing event (Auriere *et al.*, 2001), and MEGA (Crotts *et al.*, 1999), the successor of Columbia/VATT, began their systematical observations of M31. Another project, SLOTT-AGAPE (Slott-Agape Collaboration, 1999) will join them this year.

The Wendelstein Calar Alto Pixellensing Project started with a test and preparation phase on Wendelstein as WePP in autumn 1997 before it graduated after two campaigns to WeCAPP in summer 1999 by using two sites for the survey.

In this chapter we will give an introduction to the project, including information about the data obtained and our reduction pipeline. In Sect. 2 we briefly discuss the basic principles of pixellensing. In Sect. 3 we will give an overview of the project including information about the sites used and the data obtained. Section 4 refers to our data reduction pipeline and describes how light curves are extracted. In Sect. 5 we show first light curves and Sect. 6 summarizes this chapter.

2.2 Pixellensing

In microlensing surveys of isolated fields a resolved star is amplified by a function A which can be measured from the light curve and which yields direct information of the lensing parameters (Paczynski, 1986):

$$A(u) = \frac{u^2 + 2}{u\sqrt{u^2 + 4}}$$

and

$$u(t)^2 = \mu_E^2 (t - t_0)^2 + u_0^2 \quad , \qquad (2.1)$$

with $\mu_E = 1/t_E$, the inverse Einstein ring crossing time, u_0 the angular impact parameter in units of the angular Einstein ring radius θ_E, and t_0 the time of maximum amplification.

The angular Einstein ring radius θ_E is connected with the physical Einstein ring radius r_E and the properties of the gravitational lens by

$$\theta_E = \frac{r_E}{D_l}$$

and

$$r_E = \left(\frac{4GM}{c^2} \frac{D_l D_{ls}}{D_s} \right)^{\frac{1}{2}} \quad , \qquad (2.2)$$

with the mass of the lens M, and the distances between the observer and lens D_l, observer and source D_s, and lens and source D_{ls}. According to Eq. 2.1 a lensing event will produce a symmetric and, as lensing does not depend on the color of the source, achromatic light curve.

In more crowded fields it is not possible to determine the amplification $A(t)$ unambiguously because many unresolved sources may lie inside the solid angle of the point spread function Ω_{PSF} of a bright source. If one of these unresolved sources is amplified, the event could erroneously be attributed to the bright star, which results in a strong amplification bias (Han, 1997; Alard, 1997; Wozniak & Paczynski, 1997; Goldberg, 1998).

Similarly, in pixellensing studies the true amplification cannot be determined because many stars fall in one resolution element. Nevertheless one can still construct a light curve $\Delta F(t)$ by subtracting a reference frame from the image, in which a lensing event takes place:

$$\Delta F(t) = F(t) - B = F_i \cdot [A(t) - 1]$$

and

$$B = F_i + B_{res} \quad , \qquad (2.3)$$

with F_i the flux of the source after or before lensing and $B_{res} = \sum_{j \neq i} F_j$ being the residual flux from unlensed sources inside Ω_{PSF}. As there are many sources contributing to the flux inside Ω_{PSF}, pixellensing events will only be detected if the amplification A or the intrinsic flux F_i of the lensed source are high. However, this intrinsic problem in identifying events is balanced by the large number of possible sources for lensing events in the bulge of M31.

As pointed out by Gould (1996), the main difference between classical microlensing and pixellensing consists in the fact, that in the latter the noise within Ω_{PSF} is dominated by unlensed sources and therefore stays constant during an event. As only events with a high amplification can be detected, the Einstein timescale t_E is not a general observable in pixellensing. Therefore t_{FWHM} which describes the width of a lensing light curve at half of its maximum value is the only timescale one is able to measure with a certain accuracy.

Based on a previous work of Gondolo (1999), who pointed out that the optical depth towards M31 can be estimated without knowing t_E, Baltz & Silk (2000) showed how the measurement of a moment of the light curve $t_{\sigma n}$ permits to calculate the Einstein time t_E for a particular lensing event. Furthermore, principal component analysis of the light curves can yield a less biased information about the mass function of the lenses as shown by Alard (2001).

Site	Campaign	CCD	Size	[arcsec/px]	Field [arcmin^2]
We	1997-2005	TEK#1	$1K \times 1K$	0.49	8.3×8.3
CA	1999/2000	TEK7c_12	$1K \times 1K$	0.50	8.6×8.6
CA	1999/2000	TEK13c_15	$1K \times 1K$	0.50	8.6×8.6
CA	1999/2000	SITe2b_11	$2K \times 2K$	0.50	17.2×17.2
CA	1999/2000	SITe18b_11	$2K \times 2K$	0.50	17.2×17.2
CA	1999/2000	LOR11i_12	$2K \times 2K$	0.31	10.75×10.75
CA	1999-2002	SITe2b_17	$2K \times 2K$	0.50	17.2×17.2

Table 2.1: Properties of the CCD cameras used for WeCAPP at Wendelstein (We) and Calar Alto (CA) Observatories, respectively. All CCDs have a pixel size of $24\,\mu$m, except the Loral which has $15\,\mu$m pixels.

2.3 The WeCAPP project[2]

2.3.1 Telescopes and instruments

The Wendelstein 0.8 m telescope has a focal length f of 9.9 m, which results in an aperture ratio $f/D = 12.4$. Since the beginning of the project in September 1997 we used a TEK CCD with 1024×1024 pixels of $24\,\mu$m corresponding to 0.49 arcsec on the sky. With this CCD chip we were able to cover $8.3 \times 8.3\,\text{arcmin}^2$ of the bulge of M31. To increase the time sampling of our observations we started to use the Calar Alto 1.23 m telescope ($f = 9.8$ m, $f/D = 8.0$) in 1999. The observations were partly carried out in service mode. Six different CCD chips were used. Three of these CCDs cover a field of $17.2 \times 17.2\,\text{arcmin}^2$ and were used to survey the whole bulge for lensing events. A detailed overview of the properties of each CCD camera used for WeCAPP is given in Table 2.1.

Most of the sources for possible lensing events in the bulge of M31 are luminous red stars, i.e. giants and supergiants. Consequently, the filters used in our project should be sensitive especially to these kind of stars. We therefore chose R and I filters for our survey. At Wendelstein we used the $R2$ ($\lambda \simeq 650\,\text{nm}$, $\Delta\lambda \simeq 150\,\text{nm}$) and Johnson I ($\lambda \simeq 850\,\text{nm}$, $\Delta\lambda \simeq 150\,\text{nm}$) wavebands. The Calar Alto observations were carried

out with the equivalent filters, $R2$ ($\lambda \simeq 640\,\text{nm}$, $\Delta\lambda \simeq 150\,\text{nm}$) and Johnson I ($\lambda \simeq 850\,\text{nm}$, $\Delta\lambda \simeq 150\,\text{nm}$). Since June 2000 we are using the newly installed filters Johnson R ($\lambda \simeq 640\,\text{nm}$, $\Delta\lambda \simeq 160\,\text{nm}$) and Johnson I ($\lambda \simeq 850\,\text{nm}$, $\Delta\lambda \simeq 150\,\text{nm}$) at Calar Alto.

Despite of the combination of different telescopes, CCDs, and slightly different filter systems we observed no systematic effects in the light curves depending on these parameters. We could therefore combine the data points of Wendelstein and Calar Alto to one common and homogeneous data set.

2.3.2 Observing strategy

During the first two campaigns the survey was restricted to Wendelstein and therefore to a $8.3' \times 8.3'$ field of view (FOV). Following the suggestion of Tomaney & Crotts (1996) and Han & Gould (1996a) we selected a field (F1 in the following) along the minor axis of M31, which contains the area with the highest expected rate for pixellensing events. The main fraction of the field is covered by the bulge of M31 with the nucleus of M31 located at one corner of the field (see Fig. 2.1). From 1999 on, F1 was observed simultaneously from Wendelstein and Calar Alto. In 2000 we extended the Calar Alto observations to a field of $17.2' \times 17.2'$, which was centered on the nucleus of M31. A quadrant of the field coincided

---

[2]Modified section.
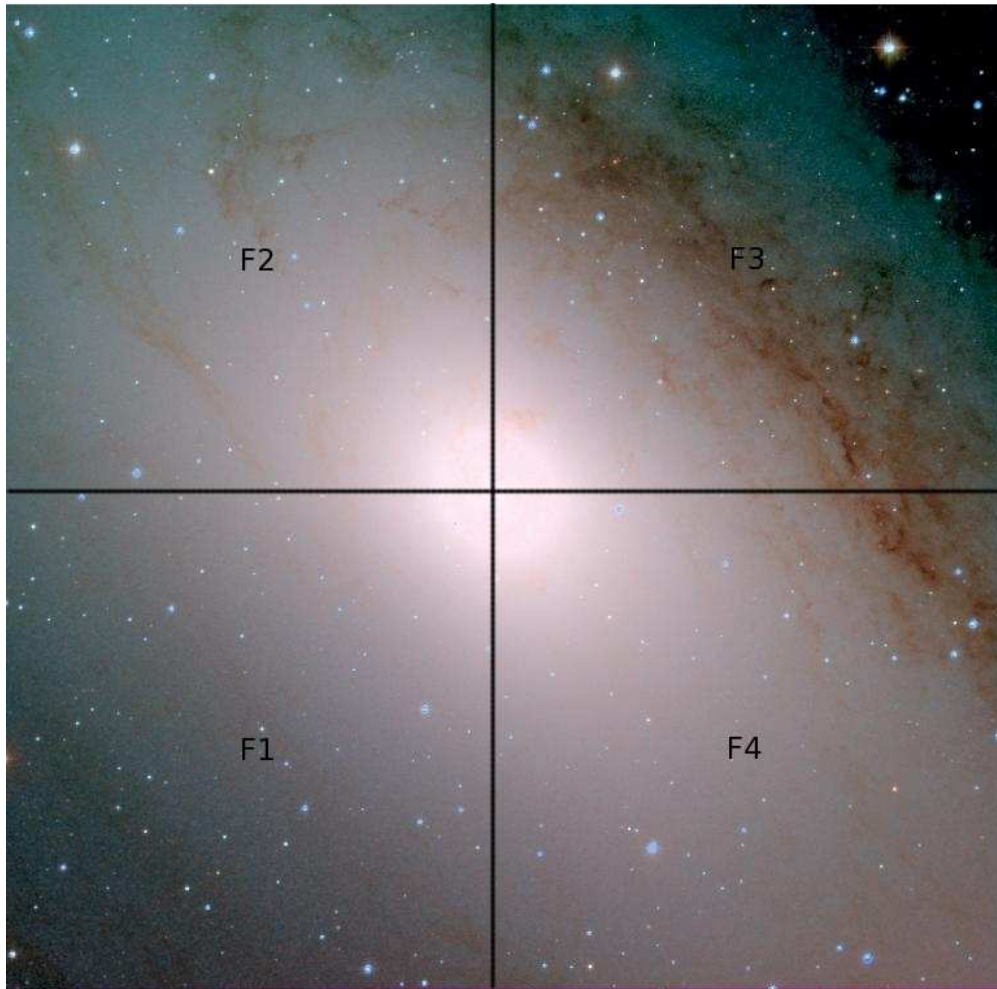
Figure 2.1: *V*-, *R*-, and *I*-band composite image of the observed fields F1 to F4, taken at Calar Alto Observatory during the campaign 2000/2001. The black lines mark the positions of fields F1 to F4.

with the maximal lensing field F1. At Wendelstein we continued with the observations of F1, accompanied by observations of F3, the opposite field along the NW minor axis. Due to the simultaneous observations we reached a very good time sampling during the observability of M31. Since summer 2002 we are mosaicing fields F1 to F4 with the Wendelstein telescope. An image of fields F1 to F4 taken at Calar Alto Observatory is shown in Fig. 2.1.

As gravitational lensing is achromatic, the amplification of the source is the same in different wavebands. However, as shown in several publications (e.g., Valls-Gabaud, 1994; Witt, 1995; Han *et al.*, 2000), blending and differential amplification of an extended source can lead to a chromatic, but still symmetric, lensing light curve. Under certain circumstances chromatic light curves permit to constrain the physical properties of the source-lens system (e.g., Gould & Welch, 1996; Han & Park, 2001), however, the light curves of intrinsic variable stars will generally change color in a different way. To be able to check the light curves for chromaticity, we therefore had to observe the M31 field in two wavebands.
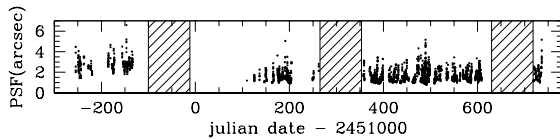
Figure 2.2: Illustration of PSF vs. time coverage during 1997-2000. Shaded regions mark the periods of time when M31 was not observable.

We split our observations in cycles, one of them comprising 5 images in the *R*-band and 3 images in the *I*- band, taking about 45 min including readout time. The cycles were repeated as often as possible during one night, usually at least twice. As we had to avoid saturation of stars in the observed field we made exposure times dependent of the actual seeing, whereas exposure times in the *I* bands where generally longer.

Stacking the images with an average exposure time of 150 sec in *R* and 200 sec in *I* results in a magnitude limit between (20.8 – 22.1) mag in *R* and (19.1 – 20.4) mag in *I* for a point source on the background of M31 and a signal-to-noise ratio $\left(\frac{S}{N}\right) = 10$ in over 95 % of the frame. The background of M31 typically has a surface brightness between (18.7 – 21.2) mag/arcsec^2 in *R* and (16.8 – 19.3) mag/arcsec^2 in *I*.

2.3.3   The data

We began our observations at Wendelstein with a test period in September 1997, observing on 35 nights until March 1998. The second observational period lasted from 1998 October 22nd until 1999 March 24th . During the first Calar Alto campaign we received two hours of service observations on 87 nights (1999 June 27th - 2000 March 3rd). From November 1st until November 14th we were able to observe during the whole night. In parallel we got data from 65 nights at Wendelstein. In this way we achieved during 1999/2000 an overall time coverage of 132 nights (52.6 %).

During the 1997/1998 test campaign conditions at the Wendelstein telescope were improved

significantly. A newly installed air conditioning system reduced dome seeing to a low level. Further improvements like fans just above the main mirror finally lead to a leap in the image quality obtained with the telescope. Figure 2.3 which presents the PSF statistics of Wendelstein images from the 1997/1998 and 1998/1999 campaigns respectively illustrates this fact. Comparing these values with the statistics of the Calar Alto data shows furthermore, that the Wendelstein data have a marginally better PSF distribution than Calar Alto (see Fig. 2.3).

Figure 2.2 shows the time sampling we reached with WeCAPP during 1997-2000. Because of time loss during the upgrades of the telescope, time coverage of the 1997/1998 campaign is only fragmentary. The same applies to the subsequent campaign due to a camera shutdown and a further time consuming project. The time coverage of the first joint campaign of Wendelstein and Calar Alto is very good due to the often opposite weather situation in Spain and Germany. In the following joint campaigns we enhanced the time sampling further, culminating in a coverage of 85% during the first two months of 2002.

In Figs. 2.4, 2.5, and 2.12 we give the basic properties of the complete data set being accumulated between autumn 1997 and spring 2005. Figure 2.4 shows the cumulative distribution of epochs with data taken at the two sites. One epoch corresponds to nightly stacks. Due to the earlier start of the observations and the continued high priority observations of field F1 at Wendelstein, F1 shows the best time coverage of all fields until spring of 2002. Since the summer of 2002, with only Wendelstein contributing to the observations, the time sampling is comparable for all four fields. In Fig. 2.5 we present the distribution of the full-width-half-maximum (FWHM) of the star PSFs in the co-added images. The *I*-band data shows a slightly better quality (i.e. smaller PSF values) than the *R*-band data. The median values for the *R*- and *I*-band data are shown in Table 2.2. Figure 2.12 finally shows the cumulative distribution of the weighting factors of the
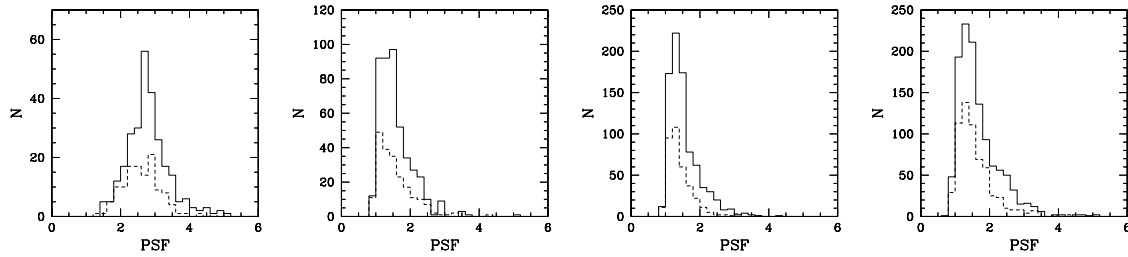
Figure 2.3: Histograms of the full-width-half-maximum (FWHM) of the point spread function (PSF) of the frames taken at Wendelstein Observatory during the 1997/1998 campaign (first panel), the 1998/1999 campaign (second panel), the 1999/2000 campaign (third panel), and at Calar Alto Observatory during the 1999/2000 campaign (fourth panel). Frames in the R-band are marked by a solid line, frames in the I-band by a dashed line. The lower limit of the PSF is restricted by a pixel size of 0.5 arcsec. Note, that the images used to construct this figure do not correspond to nightly stacks.

field	F1	F2	F3	F4
R	1.38	1.39	1.34	1.39
I	1.33	1.30	1.26	1.35

Table 2.2: Median values of the stellar PSFs, given in arcsec, for the R- and I- band data in the fields F1 to F4.

co-added images for fields F1 to F4. The weighting factors (see below) can be understood as quality flags and give the inverse of the noise present inside the area of the PSF in the photometrically aligned images. The weightings were normalized to unity in each field separately, giving maximal weight to the best quality frame in each field.

2.4 Data reduction[3]

Astronomical data nowadays are registered using CCDs (charge-coupled devices). A raw CCD frame, taken at optical wavelength, can be written as

$$
\begin{aligned}
raw(x,y) &= (obj + sky)\,\mathrm{eff}(x,y) \\
&\quad + dark + bias \quad , \qquad (2.4)
\end{aligned}
$$

with the object (*obj*) and sky (*sky*) fluxes, and the additive terms of the dark current and the

---

[3]Modified section.

bias level of the CCD. The factor $\mathrm{eff}(x,y)$ represents the optical transmission and the quantum efficiency of the CCD. To be able to extract scientific information from these frames, we first have to perform a couple of reduction steps.

The data were reduced using the WeCAPP reduction pipeline mupipe, which combines all reduction steps from de-biasing of the images until PSF photometry and the final measurements of the light curve. We implemented a difference imaging technique to overcome the severe crowding of sources in the observed fields. The reduction pipeline includes full error propagation from the first step to the last (Gössl & Riffeser, 2002) and, in brief, performs the following reduction steps, which are described in more detail below (see also Fig. 2.6):

1. standard CCD reduction including de-biasing, flatfielding and filtering of cosmic ray events

2. position alignment on a reference grid using a flux conserving interpolation routine

3. photometric alignment of the images

4. restoration of pixels damaged by CCD defects (cold and hot pixels, bad columns) or pixels hit by cosmic ray events
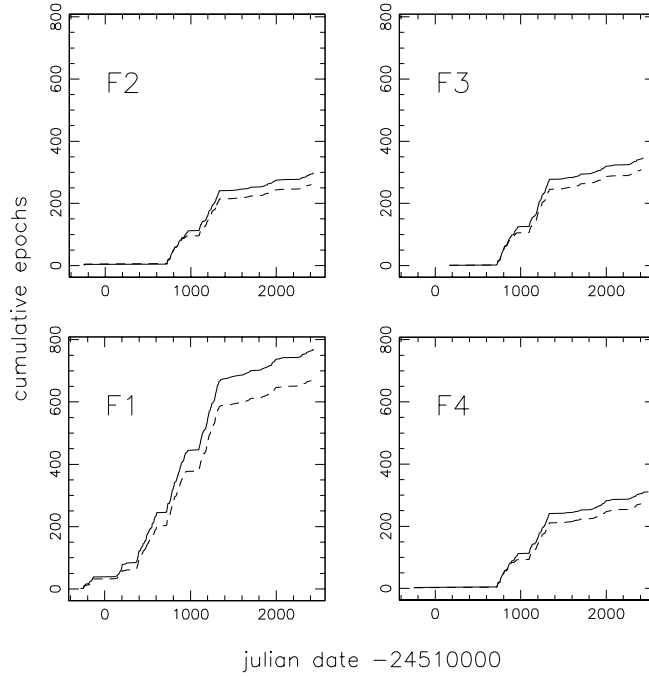
Figure 2.4: Cumulative number of observational epochs (1997-2005) for the WeCAPP fields F1 to F4. Solid line: *R*-band, dashed lines: *I*-band. The epochs refer to nightly stacks.
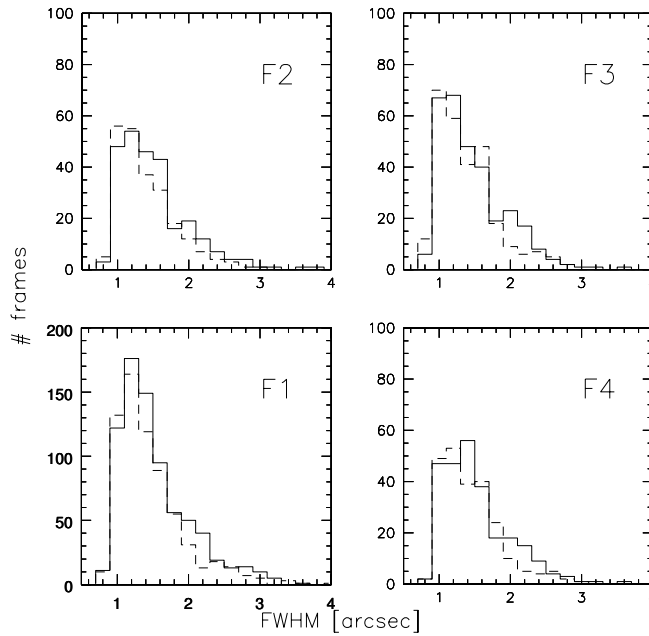
Figure 2.5: Histograms of the PSF of the stacked images of fields F1 to F4 for the full data set (1997-2005). *Solid line: R*-band, *dashed line: I*-band. The *I*-band images show a slightly better quality than the *R*-band images.

5. stacking of the frames of one epoch (i.e. night) using a weighting scheme to maximize the $\left(\frac{S}{N}\right)$ for point sources

6. matching of the PSF of a high $\left(\frac{S}{N}\right)$ reference frame to the PSF of each stacked frame using our implementation of the image subtraction method developed by Alard & Lupton (1998) and Alard (2000)

7. generation of difference images by subtracting the convolved reference frame from each stacked frame

8. PSF photometry of each pixel in the difference frames using the PSF extracted from the convolved high $\left(\frac{S}{N}\right)$ reference frame

9. extraction of the light curves .

2.4.1 Standard CCD reduction

Saturated pixels

Saturation can be induced either by the representation limit of the A/D (analogue to digital) converter or by the finite full-well capacity of the CCD pixels. Our CCDs have a A/D limit of 65535 counts (corresponding to a 16 bit representation), which, with our gain settings, is smaller than the full well limit ($> 350000 \, e^-$) of the CCD pixels. If the latter limit is reached during an exposure, the charges can overcome the boundary to neighboring pixels leading to 'blooming' of bright saturated stars.

Although our CCDs saturate only at count rates above 65535, we set all pixels with count rates above a somewhat lower threshold to zero. This second threshold was chosen differently for the CCD chips used, and was set rather conservatively to ensure that the CCD response is linear over the whole range. For pixel with count rates above the saturation threshold we additionally set adjacent pixels to zero, which eliminates regions affected by blooming. We flag saturated pixels in the error frame (see below) by setting them to
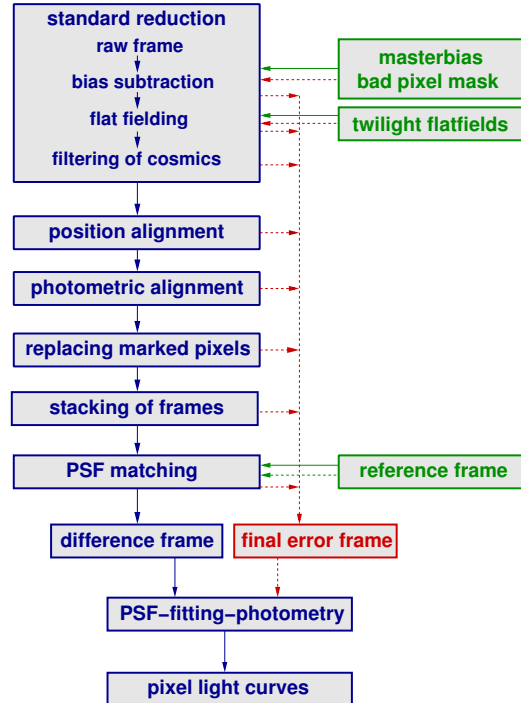
Figure 2.6: Floating chart of the WeCAPP reduction pipeline mupipe. The reduction package includes full error propagation for each pixel through all reduction steps.

(-1), which will kept dominant in any further reduction step.

After this reduction step we trim the frames to the exposed part and add a border of zero pixels to the frames. This enables us to shift the frames onto a larger reference grid without loosing parts of the image.

Bad pixel mask

Bad and defective areas (hot and cold pixels, dead rows) and pixels reacting nonlinear to exposures are masked in the reduction process. For the creation of the bad pixel mask, we used two series of dome flatfields (high $\left(\frac{S}{N}\right)$ calibration images used to compensate for pixel-to-pixel variations,

see below), one series with high count rates, the second one with low count rates. After averaging and normalizing both series, the resulting two flatfields were divided by one another. All pixels which deviated more than a threshold value from unity in the divided image were flagged as bad pixel in a mask containing '1' values for good pixels and '0' for bad pixels. All images were divided by this mask in the first reduction step, yielding zero values at the defective areas in the processed images.

Bias correction

The additive terms in Eq. 2.4 consist of the (usually temporal constant) bias and dark counts, which scale with the exposure time. Dark frames (i.e. exposures with the shutter kept closed) with different long ($t_{exp} > 10^3$ s) exposure times showed that the dark current is negligible for all our CCDs, so that we have not to apply a dark correction. We perform the bias correction by first subtracting the median of the overscan region. Furthermore we created a masterbias frame by 3σ clipping of the order of 100 (overscan subtracted) bias frames. The masterbias frame yields the deviation from the bias to the overscan for each pixel and is subtracted from the overscan corrected frames.

Error frames

Our error frames are similar to a data-quality mask as used in many pipelines, but differ in that their values are not representative flags but actually numerical errors, with the exception of saturated and bad pixels which are represented by simple flags (-1, 0). For each pixel (x,y) in an image I, the initial error $\delta_I(x,y) \equiv e.Ima(x,y)$ is calculated from the photon noise, the bias noise σ_{bias_I} (i.e. the readout noise), and the error in the determination of the bias level according to

$$\delta_I(x,y) = \sqrt{\frac{\text{counts}_I(x,y) - \text{bias}_I}{\text{gain}_I} + \sigma_{\text{bias}_I}^2 + \frac{\sigma_{\text{bias}_I}^2}{n_{\text{bias}_I}}}$$

(2.5)
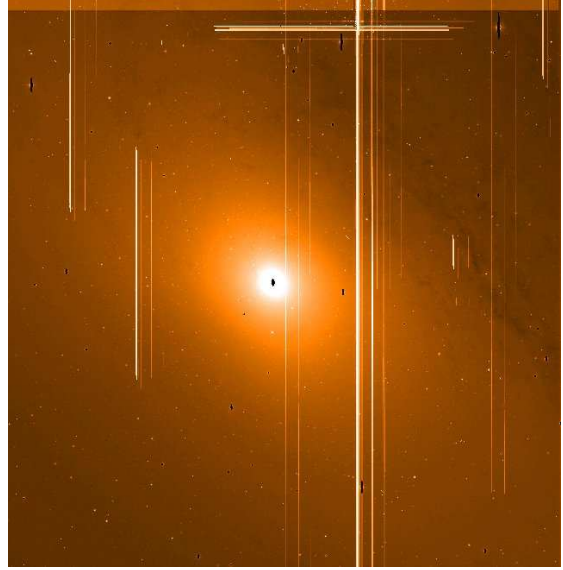
Figure 2.7: Typical error frame of a co-added image at the end of the reduction process. Brighter areas correspond to larger errors, see text for details.

where,

counts$_I$	=	flux of pixel (x,y) in image I in ADU,
bias$_I$	=	bias of the image,
gain$_I$	=	$\frac{\text{photons}_I}{\text{ADU}}$ = conversion factor,
n_{bias_I}	=	number of pixels actually used for the bias determination .

The errors in this initial error frame are propagated through all reduction steps using Gaussian error propagation

$$e.Ima = \sqrt{\sum_{i=1}^{N} \left(\frac{\partial f}{\partial \text{Ima}_i} e.\text{Ima}_i\right)^2} \quad , \qquad (2.6)$$

where $f(\text{Ima}_1, ..., \text{Ima}_N)$ describes the operation connecting the images. In Fig. 2.7 we show a typical error frame of a co-added image at the end of the reduction process.

Shutter correction

As the opening of the shutter takes time, the central parts of the images have a longer effective ex-

posure time than regions on the edges of the images. We correct for this effect by a shutter image T(x,y), constructed from two series of dome flatfields, one series with long exposures times t_l, the second one having short exposure times t_s. When illuminated with a constant source delivering $C(x,y)$ counts per second at the position (x,y) on the CCD chip, the images F_l and F_s are given by

$$F_l(x,y) = (t_l + T(x,y))C(x,y) \qquad (2.7)$$

and

$$F_s(x,y) = (t_s + T(x,y))C(x,y) \quad . \qquad (2.8)$$

Solving the equations for T(x,y) yields the shutter correction image

$$T(x,y) = \frac{F_l(x,y)t_s - F_s(x,y)t_l}{F_s(x,y) - F_l(x,y)} \quad , \qquad (2.9)$$

where $F_l(x,y)$ and $F_s(x,y)$ mark high $\left(\frac{S}{N}\right)$ averages of the two flatfield series. Figure 2.8 shows the shutter image for the Wendelstein camera. The values $T(x,y)$ in this image give the difference in effective exposure time due to the shutter mechanics. Using $T(x,y)$, the shutter corrected image $I(x,y)_{corr}$ (i.e. the image, in which all pixels were exposed for t_{exp}) is given by

$$I(x,y)_{corr} = \frac{I(x,y) \times t_{exp}}{t_{exp} + T(x,y)} \quad , \qquad (2.10)$$

where t_{exp} is the exposure time of $I(x,y)$.

Flatfield correction

In order to normalize the apparent photon sensitivity of all pixels in a single CCD frame, a calibration image (known as 'flatfield') has to be created. Ideally, this would be the image of an extended, homogeneous, flat, and white object at infinity. The optical transmission and quantum efficiency variations lead to an apparent photon sensitivity changing from pixel to pixel. The variations result from the geometric size, the coating, and the electronic properties of each single pixel.
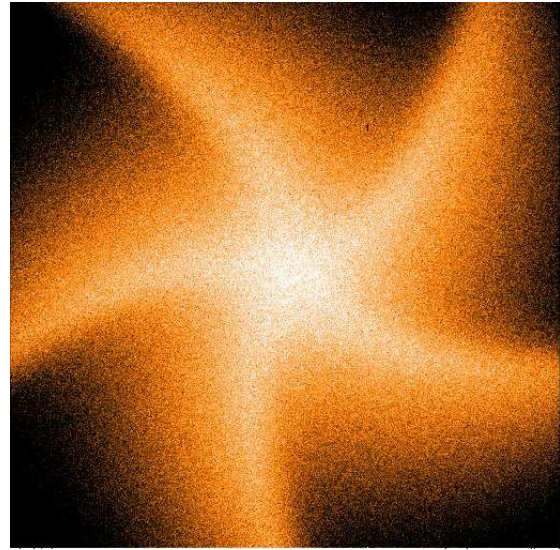
Figure 2.8: Shutter image $T(x,y)$ for the Wendelstein camera. The pattern results from the iris shutter of this camera.

But also the inherent properties of the optics (vignetting) and dust in the optics contribute to the variations in sensitivity.

The flatfields can be acquired by exposures of the illuminated dome ('dome-flatfields'), exposures of the twilight sky ('twilight-flatfields'), or from the science frames themselves ('sky-flatfields'). As the mapping of dust by the divergent light of lamps in the dome is different from the mapping by parallel light (as present in the science images), we only use twilight flatfields for the calibration of the images. To get rid of different illumination gradients and patterns in the twilight flatfields (e.g. due to different Zenith distances and different distances of the observed field to the rising or setting sun), we align all flatfields to the same reference illumination pattern. This pattern should reflect a rather uniformly illuminated CCD chip. We normalize the bias, shutter, and saturation corrected flatfields $F(x,y)$, and divide them by a normalized reference flatfield $F_{ref}(x,y)$ with a mostly homogenous illumination. The resulting hyperplane is fitted by a polynomial, yielding $C(x,y)$.

By multiplying the uncorrected flatfields with the illumination frame $C(x,y)$ we can correct for different illuminations present in the twilight flatfields

$$F(x,y)_{cor} = \frac{F(x,y)}{C(x,y)} \quad . \qquad (2.11)$$

The error frames are treated in the same way as the images, i.e.

$$e.F(x,y)_{cor} = \frac{e.F(x,y)}{C(x,y)} \quad . \qquad (2.12)$$

After the illumination correction the flatfields are combined to a master flatfield ('masterflat' in the following) with high $\left(\frac{S}{N}\right)$. Hereby, problems can arise from bright stars in the flatfields, even if the frames were well shifted ('dithered') between the exposures. If not taken care of, the stellar counts will corrupt the masterflat and subsequently the calibrated science images. To avoid such a contamination, we apply a two step procedure for the construction of the masterflat of a particular night. For every pixel in the ensemble of the illumination corrected flatfields we calculate the error weighted mean $ave(x,y)$ and use the propagated errors $err(x,y)$. In each flatfield we clip pixels with values $val(x,y) > \kappa_{max}\, err(x,y)$ and set them to zero. To be conservative, we also set all pixels in a box surrounding these pixels to zero. The masterflat finally is calculated by κ_{min}-clipping and subsequent averaging of the remaining, i.e. non-zero pixel values, using the error weighted mean and the propagated errors of the remaining pixels in the ensemble of flatfields. In our implementation we used $\kappa_{max} = 5$ and $\kappa_{min} = 3$.

In Fig. 2.9 we show an image representing the number of input flatfields entering the final master flatfield, which is used for the calibration of one nights data. In the brighter areas less images could be used to construct the masterflat. The apparent trajectories in Fig. 2.9 correspond to stars, which positions move from one frame to another, as the telescope was slightly shifted between the exposures.
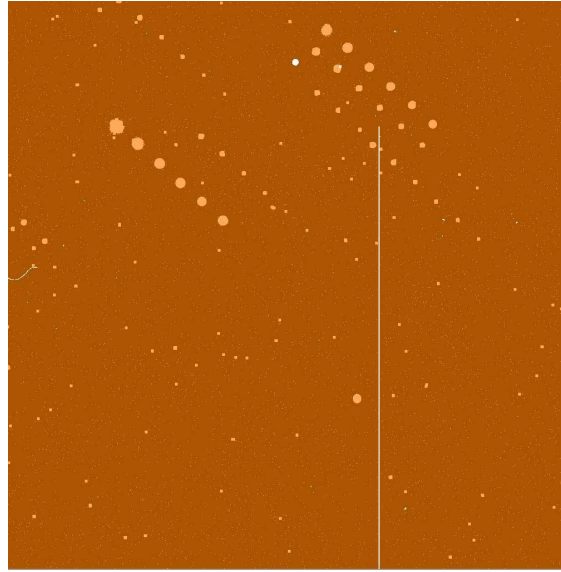
Figure 2.9: Image showing the number of input flatfields entering the final flatfield. In the brighter areas less images are used to construct the masterflat. Stars removed during the construction of the masterflat show up as brighter areas. The white areas in this image mark bad pixels and bad columns, which were set to zero using a bad pixel mask.

Filtering of cosmic ray hits

Cosmic ray hits are removed by applying a straightforward Gaussian filter to every single image (for further details see Gössl & Riffeser 2002). We fit five-parameter, two-dimensional Gaussians $f_{\mathrm{gauss}}(x,y)$ to all local maxima of an image. The Gaussians have the form

$$C + A \exp\left[-4\ln 2\left(\frac{x'^2}{x_{\mathrm{fwhm}}^2} + \frac{y'^2}{y_{\mathrm{fwhm}}^2}\right)\right] \quad , \qquad (2.13)$$

with

$$x'(x,y) = (x-x_0)\cos\alpha + (y-y_0)\sin\alpha \quad ,$$
$$y'(x,y) = (y-y_0)\cos\alpha - (x-x_0)\sin\alpha \quad ,$$

and the surface constant C, the amplitude A, and the rotation angle α. Furthermore, x_{fwhm} and

y_fwhm represent the major and a minor axis full-widths-half-maximum of the function.

All Gaussians with an amplitude of t_limit times the propagated error of the center pixel and a full-width-half-maximum in one axis smaller than a limiting $\text{FWHM}_\text{cosmic}$ are defined as *cosmic* and set to zero in the image and the corresponding error frame.

This filter has been proven to be very efficient in detecting cosmic rays. It successfully detects cosmic ray events even in the wings or the center of stellar PSFs. In Fig. 2.10 (left panel) we have marked the pixels hit by cosmic rays by blue circles. All of them are detected by the filtering algorithm and set to zero in the cleaned image (right panel).

2.4.2   Position alignment

To project the image to the same reference grid we first derive the solution of the coordinate transformation and subsequently build the shifted image by a flux preserving interpolation routine. After determining the coordinates of the reference objects in the image $I(x,y)$ and the positional reference frame $I_{ref}(x',y')$ (e.g. by PSF fitting using Eq. 2.13), we calculate a linear coordinate transformation to project the positions in an image I onto the reference grid I_{ref}. As the telescopes and cameras used in the project do not have significant optical field distortions, it was not necessary to use non linear relations for the transformation. We determine a 2×2 linear matrix and a two-dimensional translation vector

$$\begin{pmatrix} x \\ y \end{pmatrix} = \begin{pmatrix} a_{11} & a_{12} \\ a_{21} & a_{22} \end{pmatrix} \begin{pmatrix} x' \\ y' \end{pmatrix} + \begin{pmatrix} t_1 \\ t_2 \end{pmatrix}$$
(2.14)

with a least-squares fit. By solving Eq. 2.14 we match the positions of stars (x',y') in the reference system with the positions (x,y) in the un-shifted image.

The flux interpolation for non-integer coordinate shifts is calculated by a flux conserving procedure. We interpolate the un-shifted image in boxes of $(n+1)^2$ pixels size centered on each

pixel. The polynomial interpolates the values of the $(n+1)^2-1$ adjacent pixels and preserves the flux of the central pixel, using the boundary condition

$$\begin{aligned} p(x_i,y_i) &= \int_{x_i}^{x_i+\Delta x} \int_{y_i}^{y_i+\Delta y} \sum_{i=0}^{n} \sum_{j=0}^{n} a_{ij} x^i y^j dx dy \\ &= Ima(x_i,y_i) \quad, \end{aligned}$$
(2.15)

that the integral of the polynomial over the area of the pixel $(\Delta x \cdot \Delta y)$ equals the value of the image $Ima(x_i,y_i)$ at the particular pixel. By construction, this interpolating integral preserves the flux of the image in each pixel. In order to build the shifted frame, we divide the pixels in both images in $n' \times n'$ sub-pixels. The solution of Eq. 2.14 is used to relate the original and the shifted sub-pixel positions. The shifted frame is then built by re-distributing the sub-pixels of the original image to pixels on the shifted grid. During the re-distribution each sub-pixel contributes the count value of the interpolating integral to the pixel value in the shifted image.

2.4.3   Photometric alignment

As the properties of the sky background and the absorption of the source flux by the atmosphere differ from image to image, we have to align the frames photometrically before we continue with the matching the PSFs of the frames.

Two images, $I_1(x,y)$ and $I_2(x,y)$, taken at different times, are connected by

$$I_2(x,y) = p_{abs}(x,y)I_1(x,y) + p_{sky}(x,y) \quad, \quad (2.16)$$

where the polynomial $p_{abs}(x,y)$ describes the multiplicative 'absorption' component and the polynomial $p_{sky}(x,y)$ describes the additive 'sky' component. The exposure times influence the absorption factor in the most easiest way, yielding $p_{abs}(x,y) = const = t_{exp,2}/t_{exp,1}$ for all (x,y), if all other multiplicative factors stay constant during the exposures. Furthermore, $p_{abs}(x,y)$ is influenced by the atmosphere's transparency, the Zenith distance of the observed field, and possible clouds during the exposures. Finally, also an
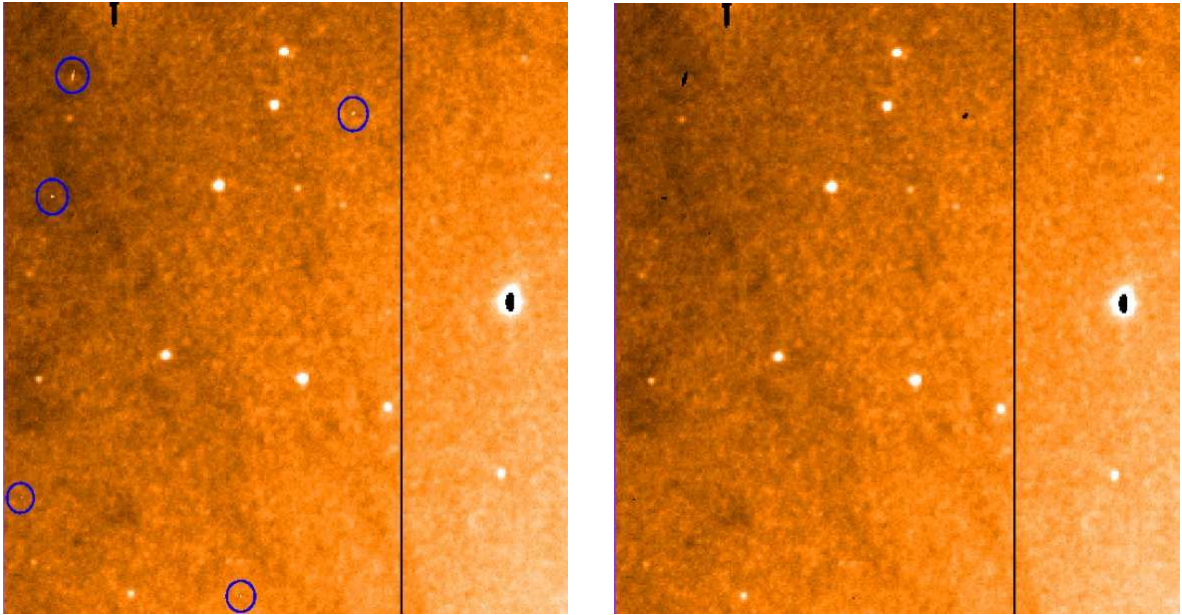
Figure 2.10: *Left panel:* Extract of the observed M31 field. Pixels hit by cosmic rays are marked by blue circles. *Right panel:* The same image after the cosmic ray cleaning process, in which affected pixels are set to zero (black areas).

inhomogeneous illumination of the CCD (e.g. by a color mismatch of the object and flatfield) can affect the measured count rates in a multiplicative way.

Various effects like for example emission and absorption lines caused in the Earth atmosphere make the night sky highly variable. Also moon phases, a changing angular distance between the positions of moon and observed field, and finally stray light inside the dome change the sky background and contribute to a positionally varying $p_{sky}(x,y)$. The brightness of the night sky and its variablity depend strongly on the wavelength regime of the observation, both being larger at infrared than at optical wavelengths. Fortunately, the temporal change of the additive background is only modest in the optical range, thus we do not to take sky calibration exposures after each science exposure.

In order to determine $p_{abs}(x,y)$ and $p_{sky}(x,y)$, we use the high $\left(\frac{S}{N}\right)$ information of the surface brightness profile of M31. We select a frame with a low sky contribution and a small PSF as photo-metric reference and align each other frame to this image by applying Eq. 2.16. The mean absorption p_0 is calculated using the difference imaging technique (see below) in the open kernel option with the normalization of the kernel as additional free parameter. The algorithm aligns both images, where the mean absorption is determined from the normalization of the convolution kernel. After we have aligned the absorption differences between the images, we determine $p_{sky}(x,y)$. We bin both images in areas centered on a grid of interpolation points, subtract the images from one another and interpolate the resulting hyperplane. The corresponding error image is scaled with $p_{abs}(x,y) = p_0 = constant$, as the subtraction $p_{sky}(x,y)$ does not change the noise properties of the image.

2.4.4 Replacing of marked pixels

At this stage we have zero-value pixels in the shifted and photometrically aligned images. These result from masking CCD defects and pixels hit by cosmic rays. Fortunately, the shifting of

the telescope between the exposures ensures that the affected regions lie on different positions in the shifted images. Therefore, we are able to use the information in the non affected images rather than loose the affected pixels in the stacked image. We use the information resulting from least-squares fits of a Gaussian to the PSFs of stars distributed over the field. We then compare the PSF of the image, in which we want to replace the zero-value pixels with the values from the other images of the particular night. We define a parameter $s_{i,i+1}$, describing the similarity between two frames as

$$s_{i,i+1} = \sum_{\Omega_{psf}} \frac{|C_{psf,i} - C_{psf,i+1}|}{n^2} \quad , \qquad (2.17)$$

where $C_{psf,i}$ and $C_{psf,i}$ represent the PSF values of images i and $i+1$, which were evaluated on a grid of $n \times n$ points inside the area of the PSF Ω_{psf}. The image, which difference parameter $s_{i,i+1}$ to the image to be replaced is below a threshold t, is chosen to replace the zero-pixels in the other image.

2.4.5 Weighted stacking

To decide, which images of one night should enter the stack, we developed an automatic weighting scheme, which we applied to all images before summing them up. The individual weightings ensure that the $\left(\frac{S}{N}\right)$ for point sources in the final co-added image is maximal.

For two images, the signal S_{tot} and the noise N_{tot} are calculated by

$$S_{tot} = S_1 + \alpha S_2 \quad , \qquad (2.18)$$

and

$$N_{tot} = \sqrt{N_1^2 + (\alpha N_2)^2} \quad , \qquad (2.19)$$

where the S_i, N_i, $i = 1, 2$ are the signal and noise values in both images. The parameter α describes the weighting of the second image relative to the first one, where the first image is given unit

weight. The noise in the images is given by

$$N_i = \sqrt{(S_i + B_i \times \Omega_{psf,i})} \ (i = 1, 2) \quad , \quad (2.20)$$

where $B_i \times \Omega_{psf,i}$ describes the background (i.e. sky) flux inside $\Omega_{psf,i} \sim \pi \text{FWHM}^2$. The weighting factor α is obtained by maximizing

$$\left(\frac{S}{N}\right)_{tot} = \frac{S_{tot}}{N_{tot}} \quad , \text{i.e.} \qquad (2.21)$$

$$\frac{d\left(\frac{S}{N}\right)_{tot}}{d\alpha} \overset{!}{=} 0 \quad . \qquad (2.22)$$

This yields

$$\alpha = \frac{S_2}{S_1} \frac{S_1 + B_1 \Omega_{psf,1}}{S_2 + B_2 \Omega_{psf,2}} \qquad (2.23)$$

The weighting reflects the interplay of the signal strength and the noise contribution inside the seeing area. For bright sources the background noise in the second term of Eq. 2.23 can be neglected yielding $\alpha = 1$. The opposite is true for faint sources, for which the weight is obtained by neglecting the fluxes S_i in the second term, yielding

$$\alpha = \frac{S_2}{S_1} \frac{B_1 \Omega_{psf,1}}{B_2 \Omega_{psf,2}} \quad . \qquad (2.24)$$

This weighting scheme maximizes the $\left(\frac{S}{N}\right)$ for faint point sources and was already applied to FORS Deep Field (FDF) data (Heidt *et al.*, 2003; Gabasch *et al.*, 2004). In the WeCAPP data the background noise can not be exclusively attributed to the sky background, but rather to the combination of sky background and the surface brightness of M31. To calculate the weight we therefore use the error images of the photometrical aligned images to estimate the weighting factors. We calculate the median error in a region without bright stars at the outer parts of the M31 field. The information on Ω_{psf} is extracted from Gaussian fits to bright stars in the field (see above). With these informations we calculate the

weights α_i for each frame. Images of one night are then summed up according to

$$I_{sum} = \frac{\sum\limits_{i=1}^{N} \alpha_i I_i}{\sum\limits_{i=1}^{N} \alpha_i} \quad , \qquad (2.25)$$

with weights α_i. The corresponding error image is derived as

$$e.I_{sum} = \frac{\sqrt{\sum\limits_{i=1}^{N} (\alpha_i e.I_i)^2}}{\sum\limits_{i=1}^{N} \alpha_i} \quad . \qquad (2.26)$$

In Fig. 2.11 we show two histograms of the error images of a stacked image. For the dashed histogram all images of one night entered the stack with unit weight. The solid histogram was calculated from a stack of the identical images, but this time the images were added according to Eq. 2.25. As the quality of the input images differed strongly, the weighted stack shows much smaller errors than the stack using unit weights. In Fig. 2.12 we show the cumulative distribution of the weighting factors for the co-added frames of fields F1 to F4.

2.4.6 PSF matching

In order to extract light curves of variable sources from the data we use a method called Difference Image Analysis (DIA), proposed by Ciardullo *et al.* (1990) and first implemented by Tomaney & Crotts (1996) in a lensing study.

The idea of DIA is to subtract two positionally and photometrically aligned frames which are identical except for variable sources. The resulting difference image should than be a flat noise frame, in which only the variable point sources are visible. The crucial point of this technique is the requirement of a perfect matching of the point spread functions between the two frames.
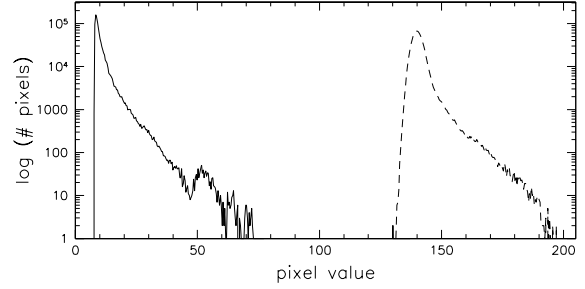
Figure 2.11: Two histograms of the error images of a stacked image representing the noise properties in the co-added images. Both stacks were produced with identical input images. *Dashed line:* unit weight for all images. *Solid line:* weighted stack according to Eq. 2.25. The weighted stack shows much smaller errors than the stack using unit weights due to the large differences between the noise properties of the images entering the stack.

The PSF of the reference frame r is convolved with a kernel k to match the broader PSF of an image i,

$$\begin{aligned} i(x,y) &\approx r(u,v) \otimes k(u,v) + bg(x,y) \\ &\equiv \tilde{r}(x,y) \end{aligned} \qquad (2.27)$$

where bg accounts for the background level and $\tilde{r}$ is the transformed reference frame. In order to obtain an optimal kernel k, we implemented a least-squares fitting method as proposed by Alard & Lupton (1998), which determines the kernel by decomposing it into a set of basis functions. We use a combination of three Gaussians with different widths σ_i (σ_1=1, σ_2=3, σ_3=9), which are multiplied with polynomials up to 6$^{\text{th}}$ order. This leads to the following 49 parameter decomposition of $k(u,v)$:

$$\begin{aligned} \sigma_1 : \quad & e^{-\frac{u^2+v^2}{2\sigma_1^2}} \ (a_1 + \cdots + a_{22}u^6 + \cdots + a_{28}v^6) \\ \sigma_2 : \quad & e^{-\frac{u^2+v^2}{2\sigma_2^2}} \ (a_{29} + \cdots + a_{39}u^4 + \cdots + a_{43}v^4) \\ \sigma_3 : \quad & e^{-\frac{u^2+v^2}{2\sigma_3^2}} \ (a_{44} + \cdots + a_{47}u^2 + \cdots + a_{49}v^2) \end{aligned}$$
$$\qquad (2.28)$$
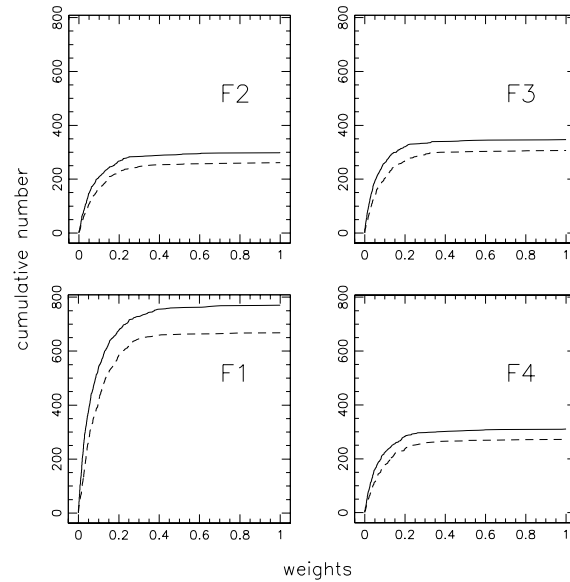
Figure 2.12: Cumulative distribution of the weighting factors of the stacked images of fields F1 to F4 (1997-2005). *Solid line: R*-band, *dashed line: I*-band. The weighting factors were normalized to unity in each field separately, giving maximal weight to the best quality frame in each field.
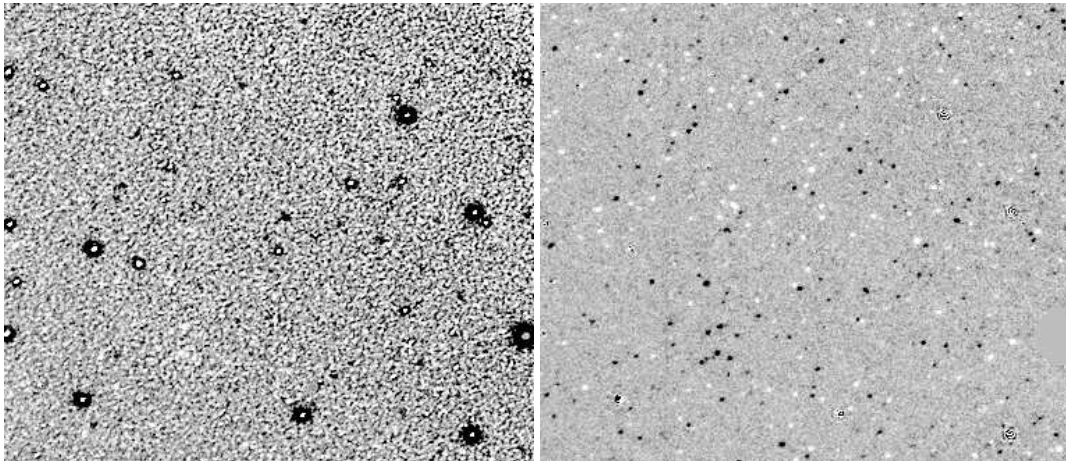
Figure 2.13: Difference images of a part of the M31 bulge ($3.25 \times 2.82\,\mathrm{arcmin}^2$), centered at 6.6 arcmin distance from the nucleus. *Left panel:* difference frame without matching of the PSFs. Because of the relatively large residuals from stars no identification of faint variable stars is possible. *Right panel:* difference frame after matching the PSFs of both images. Bright and dark spots are variable sources.

Additionally parameters are used to fit the background $bg(x,y)$, whereas the order of the background polynomial can be adjusted as required for the data set

$$bg(x,y) = a_{50} + a_{51}x + a_{52}y + ... \quad . \quad (2.29)$$

To solve the the problem of a PSF varying over the area of the CCD we divide the images in sub-areas of approximately 150 x 150 pixels each. In all sub-areas a locally valid convolution kernel is calculated. We chose a kernel size of 17×17 pixels and therefore effectively use over 160×160 pixels to derive $k(u,v)$. As we force the kernel to unity the PSF convolution preserves the flux of the reference frame.

Please note that differential refraction causes a star's PSF to depend on its color (Tomaney & Crotts, 1996). However these second order effects are negligible for our data set and do not lead to residuals in the difference images.

For the difference imaging analysis we have to choose a reference frame r which will be subtracted from all other co-added frames i and which determines the baseline of the light curve. The difference imaging analysis shows best results for a small PSF and a high $\left(\frac{S}{N}\right)$ reference frame. Combining the best images, the R-band reference frame comprises more than 50 images taken at Calar Alto during 5 different nights, having a FWHM of the PSF of $1.15''$ (slightly larger than 2 pixels for all CCDs except one at Wendelstein and Calar Alto). For the I-band we co-added more than 40 Calar Alto frames from 7 different nights, yielding an image with a FWHM of $1.22''$. Figure 2.13 shows a typical difference image obtained by using our implementation of the difference imaging technique. Dark and bright spots are variable sources, i.e. sources which changed their luminosity between the epochs of the image and the reference frame.

2.4.7 Photometry of the variable sources

We implemented a profile fitting technique to perform photometry of the detected sources. The in-

formation on the PSF in the difference images is obtained from bright and unsaturated stars in the convolved reference frame. After alignment, this frame has the same PSF as the corresponding difference image and, due to its high $\left(\frac{S}{N}\right)$, is perfectly suited for the extraction of the stellar PSF. The background subtracted pixel values of the standard star are saved as PSF matrix $PSF(x',y')$.

After the shape of the PSF has been determined in this way, linear fits of the PSF to each pixel in the difference image are used to derive the variation amplitude $A(x,y)$ in each pixel. To get an optimal $\left(\frac{S}{N}\right)$ and, at the same time, a minimal influence of crowding by other nearby variable sources, we chose a relatively small fitting area ω_{psf} centered on (x,y) for the flux determination of the variable sources. The amplitude $A(x,y)$ (normalized to the flux of the photometric standard star) is then calculated by

$$S_{xx} = \sum_{\omega_{psf}} PSF(x',y')PSF(x',y') \quad , \quad (2.30)$$

$$S_{xy} = \sum_{\omega_{psf}} PSF(x',y')Ima(x,y) \quad , \quad (2.31)$$

and

$$A(x,y) = \frac{S_{xy}}{S_{xx}} \quad , \quad (2.32)$$

where $Ima(x,y)$ are the pixel values in ω_{psf}, centered on (x,y).

2.4.8 Calibration of the light curves

As the co-added images are already normalized to the reference frame, we do not have to calibrate each image separately. Only the reference frame has to be calibrated once. To calculate magnitudes $m_{R'}$ in our R-band, which corresponds to Johnson R, we determined the instrumental zeropoint $ZP_{R'}$ and the extinction coefficient κ:

$$m_{R'} = -2.5\log[ADU/t] - \kappa \cdot AM + ZP_{R'} \quad (2.33)$$

where t is the exposure time and AM is the airmass.

Aperture photometry with 7 different Landolt standard stars (Landolt, 1992) observed at different airmasses was performed for a photometric night at Calar Alto Observatory. With these stars the extinction κ for the night was calculated to $\kappa_{R'} = 0.073 \pm 0.005$. To determine the zero-point for the R$'$ band we used an A0V-star, Feige 16, with the colors $(B-V) = -0.012$, $(U-B) = 0.009$, $(V-R) = -0.003$, $(R-I) = 0.002$, and a visual magnitude of $V = 12.406$ mag. The zero-point was determined according to Eq. 2.33 to $ZP_{R'} = 23.05 \pm 0.02$ mag and used to calculate the magnitudes for the reference frame.

In the following, we only give the values of the difference fluxes for the sources in our filter system, because the intrinsic magnitudes and colors of our unresolved sources cannot be determined with sufficient accuracy. We show the light curves in flux differences according to

$$\Delta f_{R'} = f_{R',\text{Vega}} \frac{\Delta ADU_{R'}}{t} 10^{0.4 \kappa \text{ AM}} 10^{-0.4 ZP_{R'}}$$

(2.34)

with $f_{R',\text{Vega}} = 3124$ Jy obtained from an integration over the CCD-filter system.

The same transformations were done for our I' band, corresponding to Johnson I (Calar Alto), with $\kappa_{I'} = 0.025 \pm 0.005$, $ZP_{I'} = 21.82 \pm 0.03$ mag and $f_{I',\text{Vega}} = 2299$ Jy. The color terms between all filter sets we used in our observation are negligible.

After applying these equations to the count rates of the standard stars for the PSF photometry, we can transfer the amplitudes $A(x,y)$ (Eq. 2.32) to physical units by

$$\Delta F(x,y) = A(x,y) F_{standard} \quad , \quad (2.35)$$

where $F_{standard}$ is the calibrated flux of the photometric standard star.

2.5 Results

To show the efficiency of the difference imaging method we present a some examples of light curves extracted from a subsample of the whole
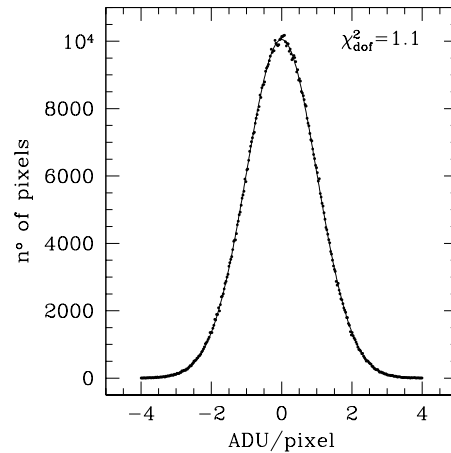
Figure 2.14: Histogram of the pixel values of a simulated difference image $d_{xy} = i_{xy} - r_{uv} \otimes k_{uv}$ (r is the reference frame, i is a second frame and k is the convolution kernel). The pixel values are divided by the expected rms errors, as derived from error propagation. The solid curve shows a Gaussian with $\sigma = 1$. We calculated the reduced chi-square χ^2_{dof} of 19 different simulated images in the range between -3 and 3. The median $\bar{\chi}^2_{\text{dof}}$ is 1.1, which means that expected and measured errors match almost perfectly and that the residuals of the difference imaging analysis are at the photon noise level.

dataset (covering the years 1997-2000). Time spans when M31 was not observable are marked by shaded regions. Because of bad dome seeing conditions and an inappropriate auto-guiding system, errors were largest during the first Wendelstein campaign 1997/98. During the second period 1998/99 we were able to decrease the FWHM of the PSF by a factor of two, thus the photometric scatter is also clearly smaller. During the third period 1999/2000 we observed simultaneously at Calar Alto and Wendelstein and got data points for 53 % of the visibility of M31.

The DIA method can be applied for very crowded fields like M31 and gives residual errors at the photon noise level (see Fig. 2.14). A good estimate for the average noise present in the area Ω_{PSF} of a PSF is $N = 0.1 \cdot 10^{-5}$ Jy. The light
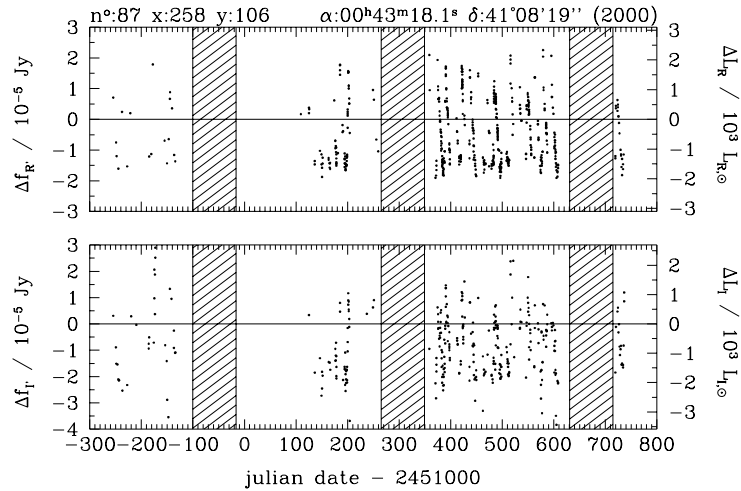
Figure 2.15: Light curve of a δ-Cepheid variable. *Upper panel:* R$'$ band, *lower panel:* I$'$ band.

curves of variable stars presented in the Figs. 2.15 through 2.23 indicate a typical scatter which is in good agreement with the above estimate. This means that a red clump giant with a brightness of $M_I = 0$ (Grillmair *et al.*, 1996, Fig. 7) and a color of $(R - I) = 0.5$ (Lejeune *et al.*, 1998) has to be amplified by a factor of 10 to be detected with a peak signal-to-noise ratio of $\left(\frac{S}{N}\right) = 3$ in our survey. The brightest RGB stars with a $M_I = -3.5$ and a color of $(R - I) = 1$ need an amplification of 1.6 only.

Already in the subsample covering the years 1997-2000 we detected over 5000 variable sources in a $8 \times 8\,\mathrm{arcmin}^2$ field. An analysis of the light curves shows that we detected various types of variable stars including novae and other types of eruptive variables. Among the pulsating variable stars we found Cepheids, semi-regular, Mira-type and other longperiodic variables. A more detailed analysis of the variable star population detected by WeCAPP can be found in chapters 6 and 7.

In Fig. 2.15 we present one example of the δ-Cepheid variable stars in the R$'$ and I$'$ bands. Figure 2.16 shows the R$'$ light curve of this star convolved with its period, which was determined to 15.76 ± 0.01 days. In Fig. 2.17 we present

the light curve of a nova, which is the brightest variable source detected in our M31 field. Figure 2.18 shows an example of an eruptive variable star, which could be misclassified as a microlensing event, if the time coverage is not appropriate. Figures 2.19 to 2.22 display light curves of variable stars, which were classified as longperiodic in a preliminary analysis. Finally we present the light curve of a RV Tauri star in Fig. 2.23.

2.6 Summary

We presented an overview of the Wendelstein Calar Alto Pixellensing Project (WeCAPP). We showed that, despite observing at different sites with different instruments, all data can be used for the difference imaging technique following Alard & Lupton (1998). This method can be applied for very crowded fields like the central part of M31 and gives residual errors at the photon noise level. A red clump giant of $M_I = 0$, which is amplified by a factor of 10 by a microlensing event, can be detected with our data. We described the data reduction procedure until the extraction of the light curves and the measurements of the excess fluxes of the variable sources.
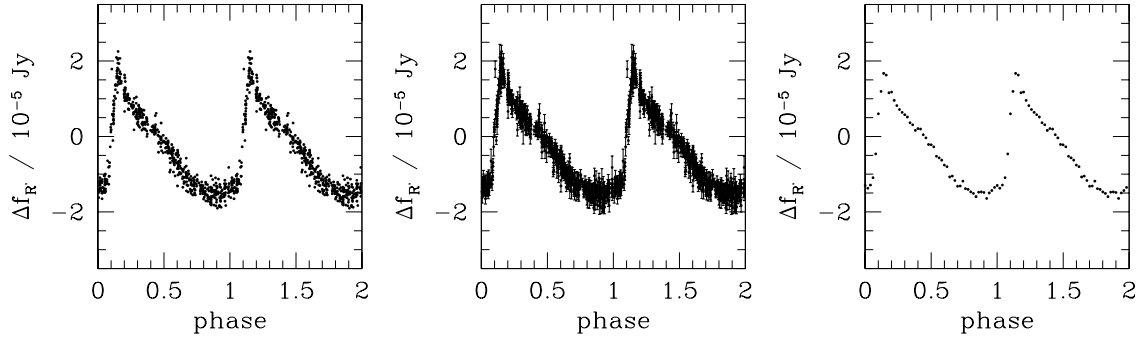
Figure 2.16: Light curve of the δ-Cepheid star of Fig. 2.15 in the R$'$ band, convolved with its period of $P = 15.76 \pm 0.01$ d. Plotted without (*left panel*) and with (central panel) 1σ error bars, which represent fully propagated errors through all reduction steps. *Right panel:* Binned R$'$ light curve of this star.
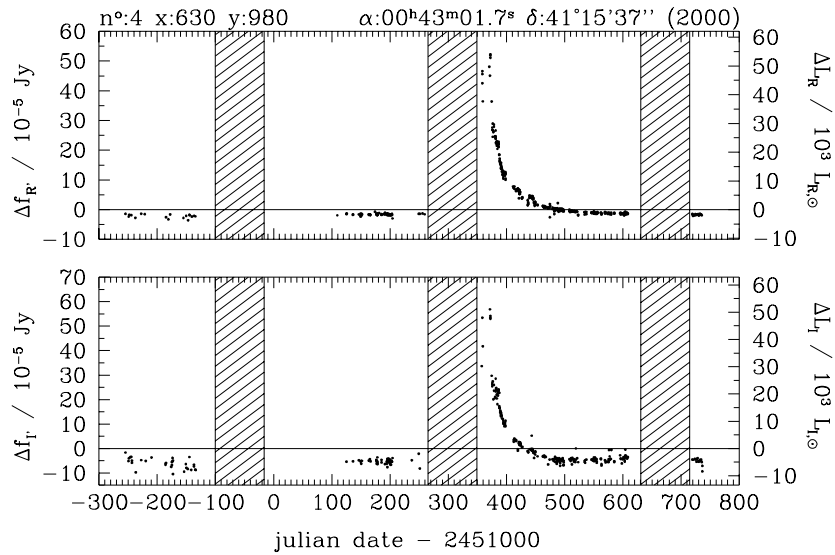
Figure 2.17: Light curve of a nova, representing the brightest variable source detected in our M31 field. *Upper panel:* R$'$-Band, *lower panel:* I$'$-Band.
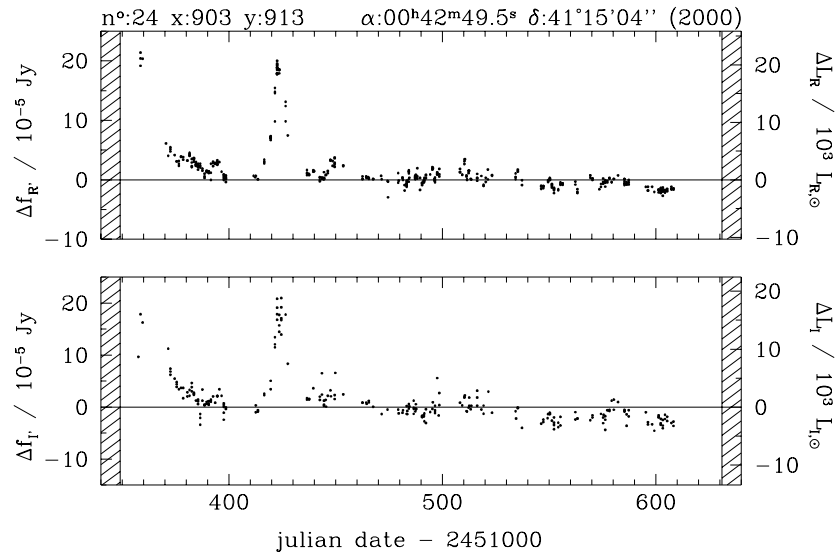
Figure 2.18: Light curve of an eruptive variable, which could be misclassified as a microlensing event, if the time coverage is not appropriate. *Upper panel:* R$'$ band, *lower panel:* I$'$ band.
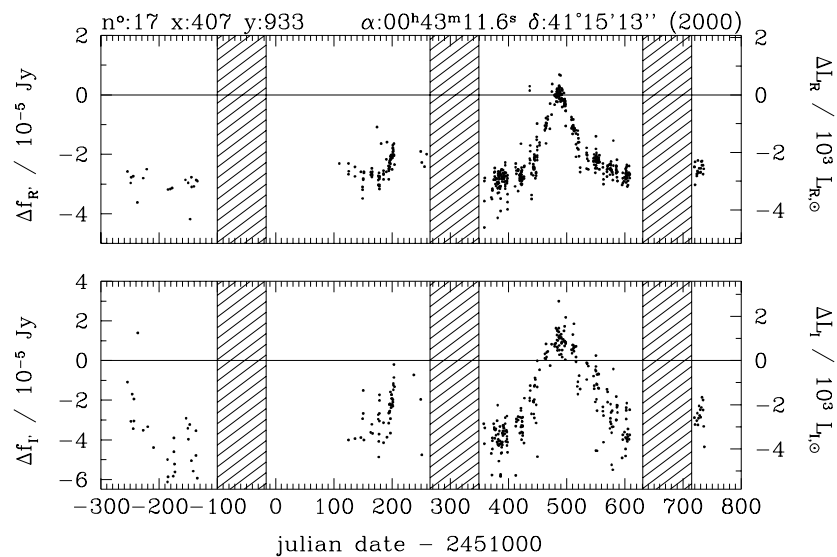
Figure 2.19: Light curve of a longperiodic variable. *Upper panel:* R$'$ band, *lower panel:* I$'$ band. Note, that a inappropriate time coverage could result in a false identification of this variable as a microlensing event.
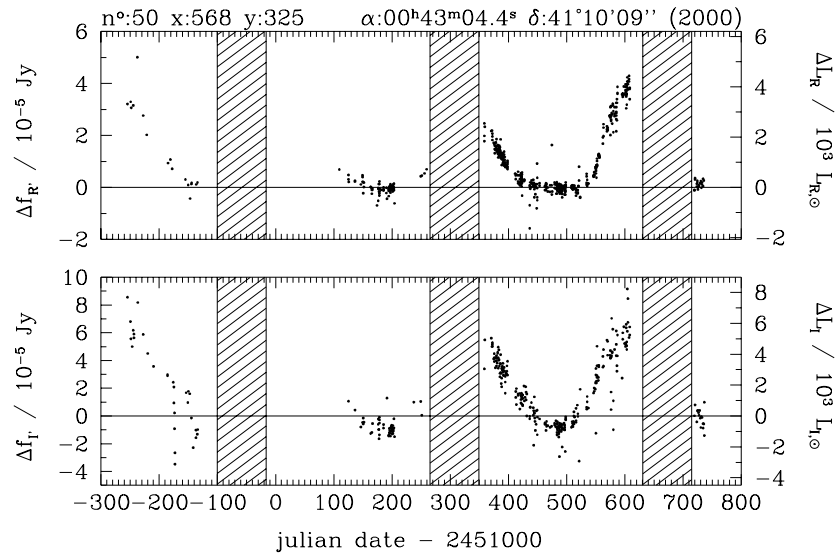
Figure 2.20: Light curve of a longperiodic variable. *Upper panel:* R$'$ band, *lower panel:* I$'$ band.
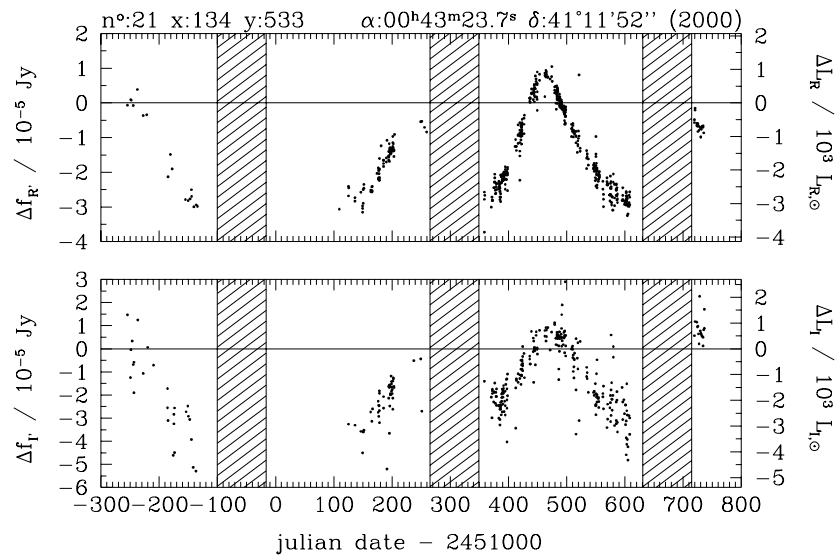
Figure 2.21: Light curve of a longperiodic variable. *Upper panel:* R$'$ band, *lower panel:* I$'$ band.
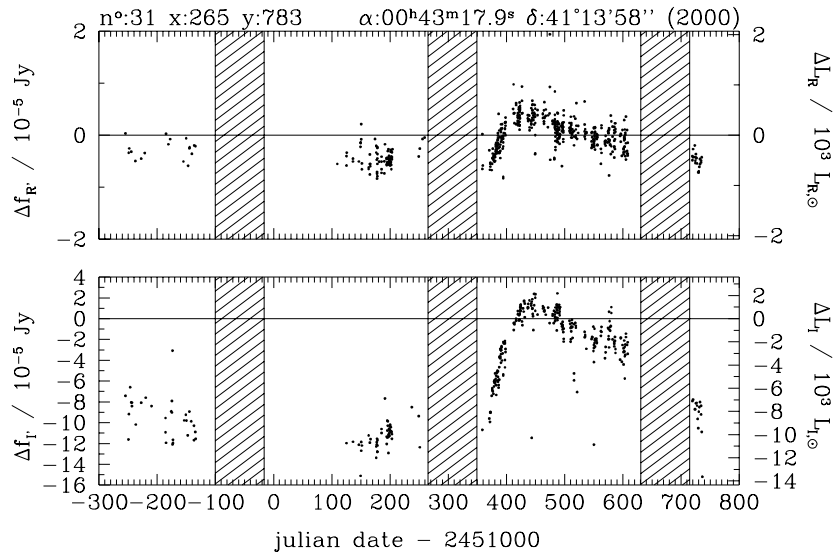
Figure 2.22: Light curve of a longperiodic variable star with a very large variation in the I′ band. *Upper panel:* R′ band, *lower panel:* I′ band.
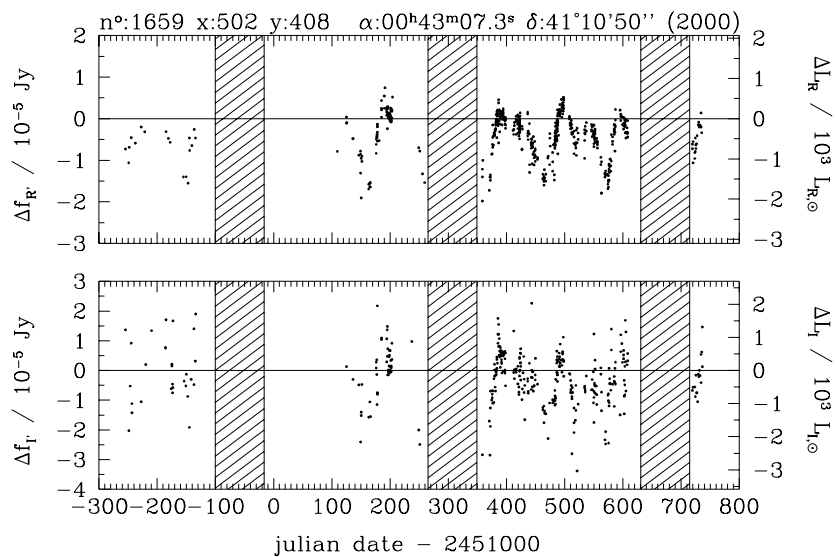
Figure 2.23: Light curve of a RV Tauri star in the R′ (*upper panel*) and I′ (*lower panel*) bands. Due to the good time coverage, the typical double-wave shape with alternating deep and shallow maxima of the light curves of this class of variable stars is uncovered.

We presented a small sample of light curves for illustration of the abilities of the survey. In future publications we will present a full catalogue of variable sources which we found in our M31 field, including potential Macho light curves (see chapters 5, 6, and 7).

Chapter 3

Modeling of M31[1]

Abstract. This chapter contains the models for the bulge-, disk- and halo-density of M31 and the comparison with observations. We show that taking a bulge with the same total mass as Kent (1989b) and a disk with the same total mass as Kerins *et al.* (2001) implies mass-to-light ratios for the stellar populations of bulge and disk in good agreement with expectations from population synthesis models. Our bulge model matches the observed surface brightness values of M31 better than previously published analytical models, which is important for the correct self-lensing prediction in the central part of M31. The contributions of the bulge and disk to the rotation curve are almost identical to that shown in Kerins *et al.* (2001), which allows us to assume the same density distribution for the dark halo as they did.

---

[1]This chapter is taken from the article Riffeser, Fliri, Seitz & Bender (2005).

3.1 The mass function

3.1.1 The mass function for the bulge and disk sources

For the M31-bulge we take the mass function (MF) $\xi(M) \sim M^{-1.33}$ of Zoccali *et al.* (2000) as derived for the Galactic bulge. At the lower the MF is cut off at $0.01\,M_\odot$. The main sequence turn-off at $1.01\,M_\odot$, obtained for a 12 Gyr old single stellar population (SSP) with a metalicity $Z = 2Z_\odot$, cuts the MF at the upper end.

We describe the disk sources with a Gould *et al.* (1997) MF, $\xi(M) \sim M^{-2.21}$, which flattens below $0.59\,M_\odot$ according to $\xi(M) \sim M^{-0.56}$. We cut the disk MF at $0.01\,M_\odot$ and $1.71\,M_\odot$, corresponding to the turn-off of a 2 Gyr old SSP with $Z = Z_\odot$, where $Z_\odot$ refers to the solar value. Of course, the number of stars with a given mass changes for different cut-off values or for alternative mass functions (e.g., Chabrier 2003). The investigation of halo-lensing and self-lensing rates for different MFs, however, is not subject of this thesis.

3.1.2 The mass function for the halo

The mass function $\xi(M)$ for the potential Macho population residing in the halo of M31 is of course unknown. We therefore simply assume that the halo consists of objects with the same mass M_0 only,

$$\xi(M) = \frac{\delta(M - M_0)}{M_0} \quad , \tag{3.1}$$

satisfying the normalization constraint

$$\int M \xi(M) \, dM = 1 \quad . \tag{3.2}$$

3.2 The luminosity function and and the color-magnitude diagram

We use a stellar luminosity function (LF) obtained from isochrones of the *Padova database of stellar evolutionary tracks and isochrones* given by Girardi *et al.* (2002, based on Marigo & Girardi 2001). The luminosity function can be extracted from the mass function $\xi(M)$ and the mass-magnitude relation provided by theoretical stellar isochrones. Each mass bin $[M_i, M_{i+1}]$ of stars is connected to a absolute brightness bin $[\mathcal{M}_i, \mathcal{M}_{i+1}]$[2]:

$$\int_{\mathcal{M}_i}^{\mathcal{M}_{i+1}} \Phi(\mathcal{M}) \, d\mathcal{M} \overset{!}{=} \int_{M_i}^{M_{i+1}} \xi(M) \, dM \tag{3.3}$$

and therefore

$$\Phi(\mathcal{M}) \approx \frac{\int_{M_i(\mathcal{M}_i)}^{M_{i+1}(\mathcal{M}_{i+1})} \xi(M) \, dM}{\mathcal{M}_{i+1} - \mathcal{M}_i} \quad , \qquad \mathcal{M}_i \leq \mathcal{M} \leq \mathcal{M}_{i+1} \quad . \tag{3.4}$$

---

[2]Here we use magnitudes $\mathcal{M}_i$, which are related to the fluxes $\mathscr{F}_i$ by $\mathcal{M}_i = -2.5 \log(\frac{\mathscr{F}_i}{\mathscr{F}_{\text{Vega}}})$, with $\mathscr{F}_{\text{Vega}}$ being the flux of Vega.

For the bulge we assume a 12 Gyr old SSP with $Z = 2Z_\odot$, which leads to good results for the stellar content of the bulge (C. Maraston, priv. comm.). For the disk we use a 2 Gyr old SSP with $Z = Z_\odot$ which leads to an acceptable agreement with the disk data given in Williams (2002). With the mass function $\xi(M)$ and the luminosity function $\Phi(\mathcal{M})$ we obtain the mass-to-light ratio

$$\left(\frac{M}{L}\right)_{\mathcal{M}} = \frac{\int_{M_{\min}}^{M_{\max}} M\,\xi(M)\,dM\,/M_\odot}{\int_{-\infty}^{+\infty} \mathcal{F}_{\text{Vega}} 10^{-0.4\mathcal{M}}\,\Phi(\mathcal{M})\,d\mathcal{M}\,/\mathcal{F}_\odot} = \frac{\int_{M_{\min}}^{M_{\max}} M\,\xi(M)\,dM\,/M_\odot}{<\mathcal{F}> \int_{-\infty}^{+\infty}\Phi(\mathcal{M})\,d\mathcal{M}\,/\mathcal{F}_\odot} \quad . \tag{3.5}$$

For a bulge MF as in 3.1.1 we get a characteristic flux $< \mathcal{F}_R >= 0.20\mathcal{F}_\odot$, yielding a $\left(\frac{M}{L}\right)_R$ in the R-band of $\left(\frac{M}{L}\right)_R = 2.67$ and a $(B-V) = 1.14\,\text{mag}$. For a disk MF as in 3.1.1 we get a characteristic flux $< \mathcal{F}_R >= 0.67\mathcal{F}_\odot$, yielding a $\left(\frac{M}{L}\right)_R$ in the R-band of $\left(\frac{M}{L}\right)_R = 0.61$ and a $(B-V) = 0.88\,\text{mag}$.

Note that other values of $M_{\min}$ and $M_{\max}$ give different mass-to-light ratios, as the decrease of $M_{\min}$ increases only the mass of the population, but not its luminosity. We show the LF for the bulge population, along with the stellar radii data (see Sect. 3.3), in Fig. 3.1.

3.3 Radius-brightness relations for stars

For the inclusion of finite source effects in the calculation of microlensing event rates (see chapter 4) one needs the radius-brightness relation of stars. The radius can easily be correlated to the brightness, the color $\mathcal{C}$ and the luminosity function using the logarithm of the luminosity L_i and the logarithm of the effective temperature $T_{\text{eff},i}$, as given by the theoretical stellar isochrones (see Sect. 3.2)

$$R_*(\mathcal{M}_i, \mathcal{C}_i) = \frac{10^{(\log(L_i)+\log(L_{i+1}))/4}}{\sqrt{4\pi\sigma_{\text{B}}}\,10^{\log(T_{\text{eff},i})+\log(T_{\text{eff},i+1})}} \quad , \qquad \mathcal{M}_i \leq \mathcal{M} \leq \mathcal{M}_{i+1}, \quad \mathcal{C}_i \leq \mathcal{C} \leq \mathcal{C}_{i+1} \quad . \tag{3.6}$$

To use the color information, $\mathcal{C} := \mathcal{M} - \mathcal{M}'$, we construct a normalized color-flux distribution $p_{\text{cmd}}(\mathcal{M}, \mathcal{C})$ from the color-magnitude diagram of stars,

$$\int\int p_{\text{cmd}}(\mathcal{M}, \mathcal{C})\,d\mathcal{M}\,d\mathcal{C} \stackrel{!}{=} 1 \quad , \tag{3.7}$$

which is related to the luminosity function as

$$\Phi(\mathcal{M}) = \int p_{\text{cmd}}(\mathcal{M}, \mathcal{C})\,d\mathcal{C} \quad . \tag{3.8}$$

The color averaged source radius $\overline{R}_*$ is then calculated as

$$\overline{R}_*(\mathcal{M}) = \int p_{\text{cmd}}(\mathcal{M}, \mathcal{C})\,R_*(\mathcal{M}, \mathcal{C})\,d\mathcal{C} \quad , \tag{3.9}$$

We show the minimal and maximal radii of stars of a certain luminosity as well as the color averaged value in Fig. 3.1.
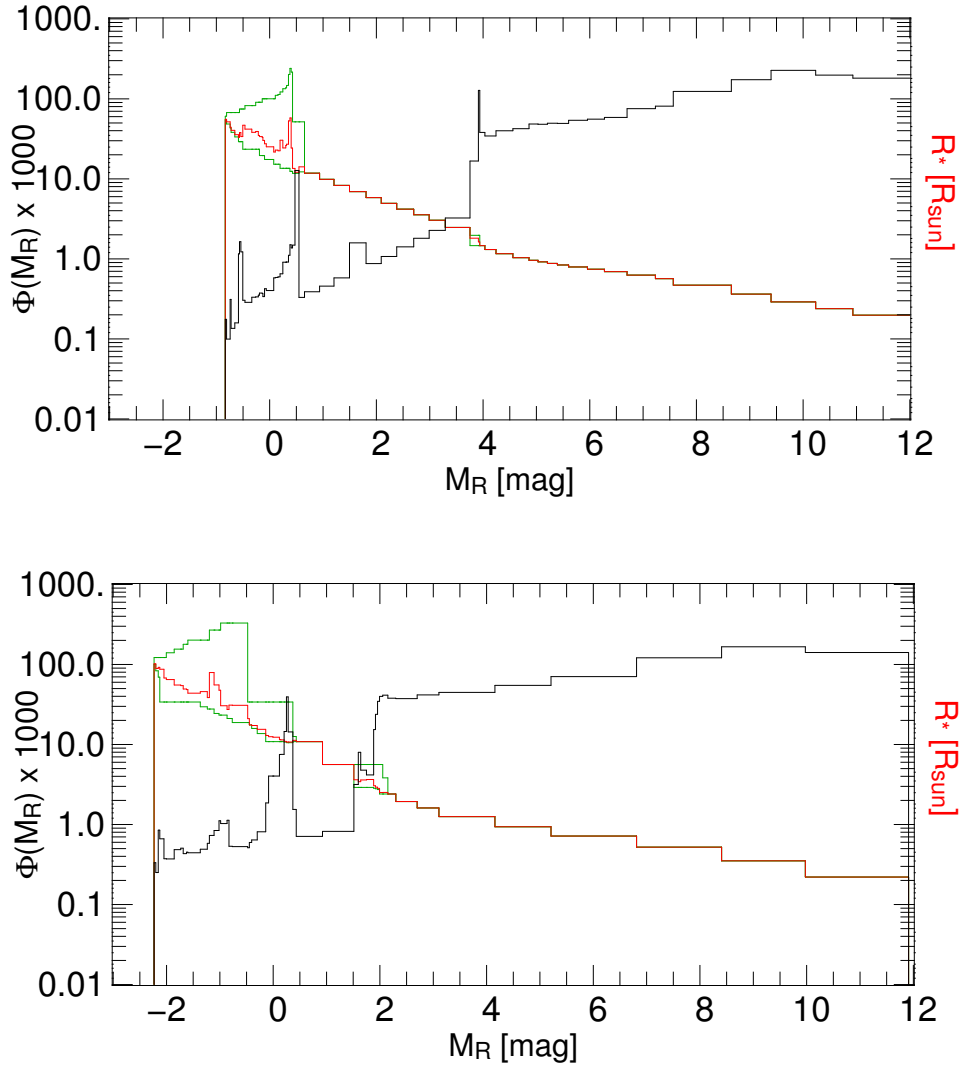
Figure 3.1: Theoretical LFs in the *R*-band $\Phi_R(\mathcal{M})$. *Top*: Bulge LF assuming a 12 Gyr old SSP of 2 $Z_\odot$ metalicity. *Bottom*: Disk LF assuming a 2 Gyr old SSP of 1 $Z_\odot$ metalicity. In red and green we show the values of the stellar radii obtained with Sect. 3.3 and the theoretical luminosities for the stars of the model SSP. The red line shows the average radius $\overline{R}_*$ according to Eq. 3.9. In green we give the minimal and maximal radii of stars (reflecting the different values in color space) in the particular magnitude range. The LFs were scaled by a factor of 1000 to show the two different histograms with the same scaling. The unit of the LFs is number of stars per magnitude, the radii distributions are given in solar radii.

3.4 The velocity distributions for the M31 components

The random velocity components of bulge, disk and halo are assumed to be of Gaussian shape with dispersions taken from Kerins *et al.* (2001):

$$
\begin{aligned}
\sigma_{\text{bulge}} &= 100\,\text{km/s} \quad , \\
\sigma_{\text{disk}} &= 30\,\text{km/s} \quad , \\
\sigma_{\text{halo}} &= 166\,\text{km/s} \quad , \\
\sigma_{\text{MW}-\text{halo}} &= 156\,\text{km/s} \quad .
\end{aligned}
\tag{3.10}
$$

In addition, we account for rotation in bulge and disk of $v_{\text{rot,bulge}} = 30\,\text{km/s}$ and $v_{\text{rot,disk}} = 235\,\text{km/s}$ (Kerins *et al.*, 2001).

In a previous work (Han & Gould, 1996a, based on Lawrie 1983) used $\sigma_{\text{halo}} = 170\,\text{km/s}$ for the halo, but a value of $\sigma_{\text{bulge}} = 156\,\text{km/s}$ for the bulge and disk. In the following two sections we derive the relative source-lens velocity v_0 taking into account rotation of the source and lens objects and the observers motion. The combination of all contributions results in one movement with

$$
v_0(D_{\text{S}}, D_{\text{L}}, v_{\text{rot,l}}, v_{\text{rot,s}}, v_{\odot-\text{M31}}) \quad .
\tag{3.11}
$$

3.4.1 Additional rotation for lenses and sources

The additional rotation of the lens system $v_{\text{rot,l}}$ (for bulge and disk lenses) and/or of the source system $v_{\text{rot,s}}$ changes the relative velocity v_0. For the calculation of the effect we first have to transform the positional components of a lens located at $(x, y, z := D_{\text{L}} - d_{\text{m31}})$ along the line of sight to the components (x_0, y_0, z_0) in the M31 system. In this thesis we use the disk major axis coordinate system (x_0, y_0, z_0), which is centered on the nucleus of M31. In this system the M31 disk major axis is oriented horizontally (at a position angle P.A. $= 38°$ as seen on the sky). In the internal system the position is given by

$$
\begin{aligned}
x_0 &= x \quad , \\
y_0 &= y\cos i - z\sin i \quad , \\
z_0 &= y\sin i + z\cos i \quad ,
\end{aligned}
\tag{3.12}
$$

with the inclination angle $i = 77°$ (Stanek & Garnavich, 1998) and the distance to M31 $d_{\text{m31}} = 770$ kpc. Projecting on the base $\rho = \sqrt{x_0^2 + y_0^2}$, the rotation angle can be expressed as $\omega = \arccos(x_0/\rho) = \arcsin(y_0/\rho)$. Re-projecting the components of the rotation velocity v_{x} and v_{yz} (calculated for a clockwise rotation)

$$
\begin{aligned}
v_{\text{x}} &= v_{\text{rot}}\sin\omega = -\frac{y_0}{\sqrt{x_0^2 + y_0^2}}\, v_{\text{rot}} \quad , \\
v_{\text{yz}} &= \sqrt{v_{\text{rot}}^2 - v_{\text{x}}^2} = \frac{x_0}{\sqrt{x_0^2 + y_0^2}}\, v_{\text{rot}} \quad ,
\end{aligned}
\tag{3.13}
$$

to the *y*- and *z*- plane yields[3]

$$
\begin{aligned}
v_{\text{y}} &= v_{\text{yz}}\cos i \quad , \\
v_{\text{z}} &= v_{\text{yz}}\sin i \quad ,
\end{aligned}
\tag{3.14}
$$

which is depending on the position along the line of sight (x,y,z). This velocity vector $(v_{\text{x}}, v_{\text{y}}, v_{\text{z}})$ has to be projected to the lens plane (see Sect. 3.4.2), before it can be combined with the other velocities.

---

[3]The relations are valid for the first quadrant, else the sign has to change.
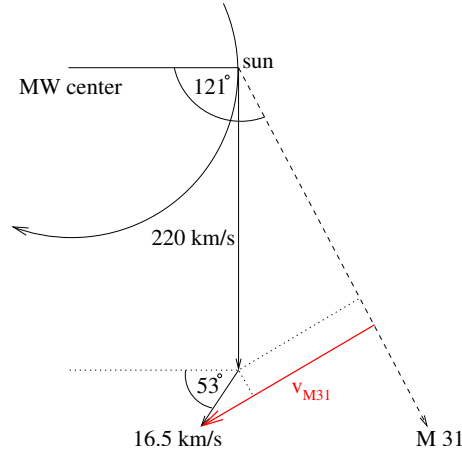
Figure 3.2: Geometry of the Galaxy-M31 system. A star at solar distance is assumed to move on a circular orbit with a rotational velocity of 220 km/s (local standard of rest, LSR). M31 is located at Galactic coordinates $l_{M31} = 121.2°$ and $b_{M31} = -21.6°$. The Sun has a velocity of 16.5 km/s relative to the LSR. The transversal velocity of M31 is shown as v_{M31}.

3.4.2 Observers motion

We finally have to account for the transversal velocity of M31 v_{M31}, arising from the observers motion against M31. A hypothetic star on a circular orbit at solar distance (local standard of rest, LSR) has the velocity $v_l(R_\odot) = 220 \pm 15$ km/s. The Sun is moving with $v_\odot = 16.5$ km/s relative to the LSR towards the directions $l = 53°$, $b = 25°$ (Binney & Tremaine, 1987). For simplicity we neglect the contributions to the galactic height and calculate the transversal velocity of M31 as (see also Fig. 3.2)

$$v_{\odot-M31} \approx 220\,\text{km/s}\,\sin(l_{M31} - 90°) + 16.5\,\text{km/s}\,\sin(121° - l_{LSR}) = 129\,\text{km/s} \quad , \tag{3.15}$$

with the galactic coordinates of M31 $l_{M31} = 121.2°$ and $b_{M31} = -21.6°$. The relative velocity between the velocity distribution of the lenses and the sources is calculated by projecting $v^p_{\odot-M31}$ to the lens plane

$$v^p_{\odot-M31} \approx \frac{D_S - D_L}{D_S} 129\,\text{km/s} \; . \tag{3.16}$$

For lenses residing in M31 this motion is negligible compared to the rotation described in Sect. 3.4.1.

3.5 Density distribution

3.5.1 Bulge of M31

The M31 bulge model is based on Table I of Kent (1989b), containing the Gunn-r surface brightness- and ellipticity-values $\rho_r^{\text{Kent}}(a)$ and $\varepsilon^{\text{Kent}}(a)$ as a function of major-axis distance a to the center of M31. We assumed 50° for the position angle of the bulge. Figure 3.3 shows that with

$$\left(\frac{1}{1 - \varepsilon(a)}\right)^2 := 0.254\frac{a}{\text{arcmin}} + 1.11 \tag{3.17}$$

the ellipticity $\varepsilon(a)$ (red curve) becomes an excellent approximation of $\varepsilon_r^{\text{Kent}}(a)$ (blue crosses) between 0.5 and 6 arcmin. With this relation we convert (x_0, y_0, z_0) to a by solving the quadratic equation $a^2 = x_0^2 + y_0^2 + (0.254a + 1.11) z_0^2$,

$$a(x_0, y_0, z_0) = \frac{0.254 z_0^2 + \sqrt{0.254^2 z_0^4 + 4\left(x_0^2 + y_0^2 + 1.11 z_0^2\right)}}{2} \qquad [\text{arcmin}] \quad, \tag{3.18}$$

with x_0, y_0, z_0 and a given in arcmin. The 3d-decomposed spatial brightness density profile of the M31 bulge derived by Kent is well approximated by an $a^{1/4}$-law (see Fig. 3.3b). With Eq. 3.18 the bulge mass density becomes

$$\rho_{\text{bulge}}(x_0, y_0, z_0) := \begin{cases} \rho_0 \, 10^{-0.4(0.97 a^{1/4})} & a \leq 0.014 \, \text{arcmin} \\ \rho_0 \, 10^{-0.4(20.4 a^{1/4} - 6.68)} & 0.014 < a \leq 0.09 \, \text{arcmin} \\ \rho_0 \, 10^{-0.4(7.1 a^{1/4} + 0.61)} & a > 0.09 \, \text{arcmin} \end{cases} \quad, \tag{3.19}$$

where

$$\rho_0 := \left(\frac{M}{L}\right)_X 10^{-0.4(\rho_{r,0}^{\text{Kent}} - (r-X) - \text{ext}_X - d_{\text{mod}} - X_\odot)} \frac{M_\odot}{\text{arcsec}^3} \tag{3.20}$$

is the central mass density derived from the central brightness density in the r-band, $\rho_{r,0}^{\text{Kent}} = 15.19 \, \text{mag arcsec}^{-3}$ (Kent 1989b, Table I). Furthermore, $\left(\frac{M}{L}\right)_X$ is the bulge mass-to-light ratio in a fiducial waveband X, $(r-X) := m_r - m_X$ is the color of the bulge population, $X_\odot := -2.5 \log \frac{\mathscr{F}_{\odot X}}{\mathscr{F}_{\text{Vega} X}}$ is the absolute brightness of the Sun in that filter, and d_{mod} is the distance modulus to M31.

Kent (1989b) fixes the bulge mass to $4 \cdot 10^{10} M_\odot$, which for $d_{\text{mod}} = 24.19 \, \text{mag}$ (690 kpc) and without correcting for dust extinction implies a $\left(\frac{M}{L}\right)_r$-ratio of 6.05 (using our analytic approximation for ρ_{bulge}) and $5.5 - 6.6$ (integrating the tabulated values of Kent and estimating the maximal uncertainties due to the coarseness of the table). In the latter case we derive the upper and lower limit for the total brightness of the bulge by summing over ellipses with an area $A_i := \pi a_i^2 (1 - \varepsilon_i)$ at semi-major distance a_i, where $A_1 = 0$. With a surface brightness

$$l_{r,i} := L_{r,\odot} 10^{-0.4(\mu(a_i) - d_{\text{mod}} - \mathscr{M}_{r,\odot})} \quad, \tag{3.21}$$

we get

$$L_{r,\text{tot}}^{\min}/L_{r,\odot} = \sum_{i=2}^{77} l_{r,i} \left(A_i - A_{i-1}\right) \tag{3.22}$$

and

$$L_{r,\text{tot}}^{\max}/L_{r,\odot} = \sum_{i=2}^{77} l_{r,i-1} \left(A_i - A_{i-1}\right) \quad. \tag{3.23}$$

These limits lead to a slightly higher $\left(\frac{M}{L}\right)_r$ between 5.5 and 6.6 than the value $\left(\frac{M}{L}\right)_r = 5 \pm 0.5$ as given in Kent (1989b).

Using the favored distance to M31 ($d_{\text{mod}} = 770 \, \text{kpc}$) and applying reasonable extinction values, the dust corrected mass-to-light-ratios for a constant bulge mass of $4 \cdot 10^{10} M_\odot$ reduce to lower values (see Table 3.1). The R-band values were obtained with the solar luminosity $R_\odot = 4.42 \, \text{mag}$, a bulge color $(B - V) \approx 1.05$ (Walterbos & Kennicutt, 1987) and the color transformation $(r - R) = 0.43 + 0.15(B - V) = 0.59$ (Moro & Munari, 2000).
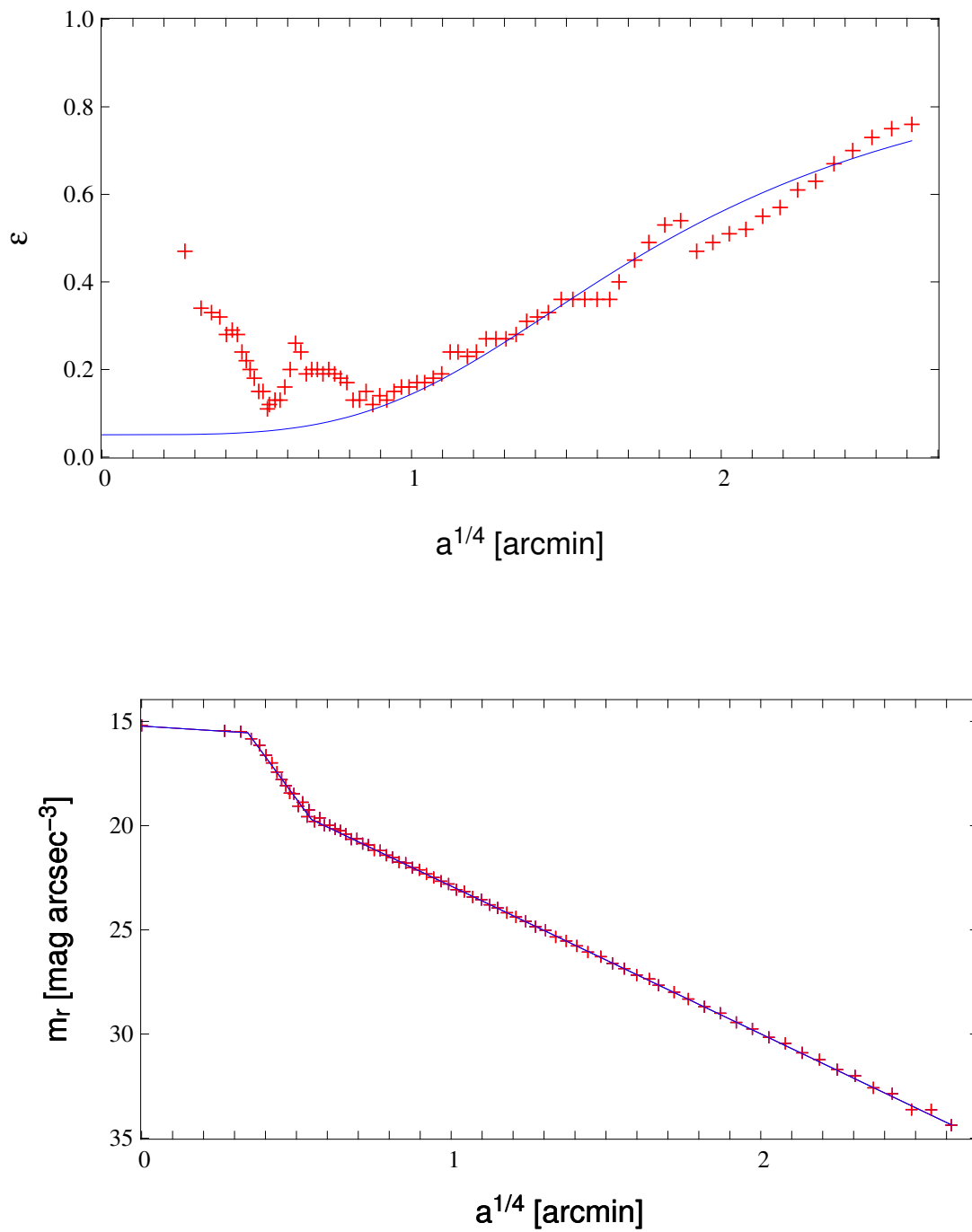
Figure 3.3: *Top panel, 3.3a:* The blue curves shows our approximation for $\varepsilon(a)$ as defined in equation (3.17), and the red crosses the tabulated values of Kent (1989b); within 0.5 and 6 arcmin the agreement is excellent. *Bottom panel, 3.3b:* This figure shows the bulge surface brightness by Kent (1989b) with red crosses, and our approximation from Eq. (3.19) as blue curve.

$M_{tot}/M_\odot$	dist [kpc]	band X	$(r-X)$	ext_X	$L_{X,tot}/L_{X,\odot}$	$\left(\frac{M}{L}\right)_X$	comment
$4 \cdot 10^{10}$	690	r	0	0	$6.61 \cdot 10^9$	6.05	Kent's model using Eq. 3.20
$4 \cdot 10^{10}$	770	R	0.59	0.36	$13.5 \cdot 10^9$	2.96	our model

Table 3.1: This table shows that a bulge mass of $M = 4 \cdot 10^{10} M_\odot$ as proposed by Kent is a good estimate, even for the more realistic value (770 kpc) for the M31 distance.

According to Han (1996) the effect of an asymmetric bulge light extinction caused by the highly inclined M31 disk is negligible. We therefore adopt his values for the mean internal extinctions towards the bulge in the V- and I-bands of $ext_V = 0.24$ mag and $ext_I = 0.14$ mag, and interpolate to the R-band which yields $ext_R = 0.19$. With the foreground extinction of $ext_R = 0.17$ (Schlegel et al., 1998) the total extinction becomes $ext_R = 0.36$. In this case, the mass-to-light ratio corresponding to Kents bulge mass becomes $\left(\frac{M}{L}\right)_R = 2.96$ (line two in Table 3.1).

For a 12 Gyr old SSP of $Z = 2Z_\odot$ metalicity, and assuming a Zoccali et al. (2000) mass function, one would obtain $(M/L)_{stellar} = 2.67$ (Girardi et al., 2002), close to the value of our model. We conclude therefore, that a normalization (Eq. 3.20) of

$$\rho_0 = 2.07 \cdot 10^6 \, M_\odot \, arcsec^{-3} = 3.97 \cdot 10^4 \, M_\odot \, pc^{-3} \quad , \tag{3.24}$$

which reproduces Kents bulge mass of $M = 4 \cdot 10^{10} M_\odot$, is a reasonable assumption and represents an upper limit for the luminous matter in the bulge.

3.5.2 Disk of M31

As in Kerins et al. (2001), we model the disk by a $sech^2$-law,

$$\rho_{disk}(x_0, y_0, z_0) = \rho_0 \exp\left(-\frac{\sigma(x_0, y_0)}{h_\sigma}\right) sech^2\left(\frac{z_0}{h_z}\right) \quad , \tag{3.25}$$

with $\sigma(x_0, y_0) = \sqrt{x_0^2 + y_0^2}$ being the radial distance in the disk plane inclined by $77°$. The radial scale length $h_\sigma = 28.57$ arcmin and the vertical scale lengths $h_z = 1.34$ arcmin are chosen equivalent to Kerins et al. (2001) ($h_\sigma = 6.4$ kpc and $h_z = 0.3$ kpc), assuming a M31-distance of 770 kpc.

Adopting a central brightness density of the disk in the r-band $\rho_{r,0}^{Kent} = 27.39$ mag arcsec^{-3} yields a surface brightness profile matching the data of Kent (1989b) on the major axis. It also agrees well with his central surface brightness of $\mu_0 = 20.4$ mag in the r-band. The discrepancies on the minor axis (see Fig. 3.4) can be explained by the imprints of the spiral arms and the extinction by dust.

As for the bulge, we transform the luminosity density to a matter density. With the disk color $(r-X)$, the disk extinction ext_X, and the disk mass-to-light ratio $\left(\frac{M}{L}\right)_X$ we get

$$\rho_0 = \left(\frac{M}{L}\right)_X 10^{-0.4(\rho_{r,0}^{Kent} - (r-X) - ext_X - d_{mod} - X_\odot)} \frac{M_\odot}{arcsec^3} \quad , \tag{3.26}$$

where we have also used the absolute brightness of the sun $X_\odot$ and the distance modulus to M31 d_{mod}. We normalize Eq. 3.26 with

$$\rho_0 = 10.4 \, M_\odot \, arcsec^{-3} = 0.2 \, M_\odot \, pc^{-3} \tag{3.27}$$
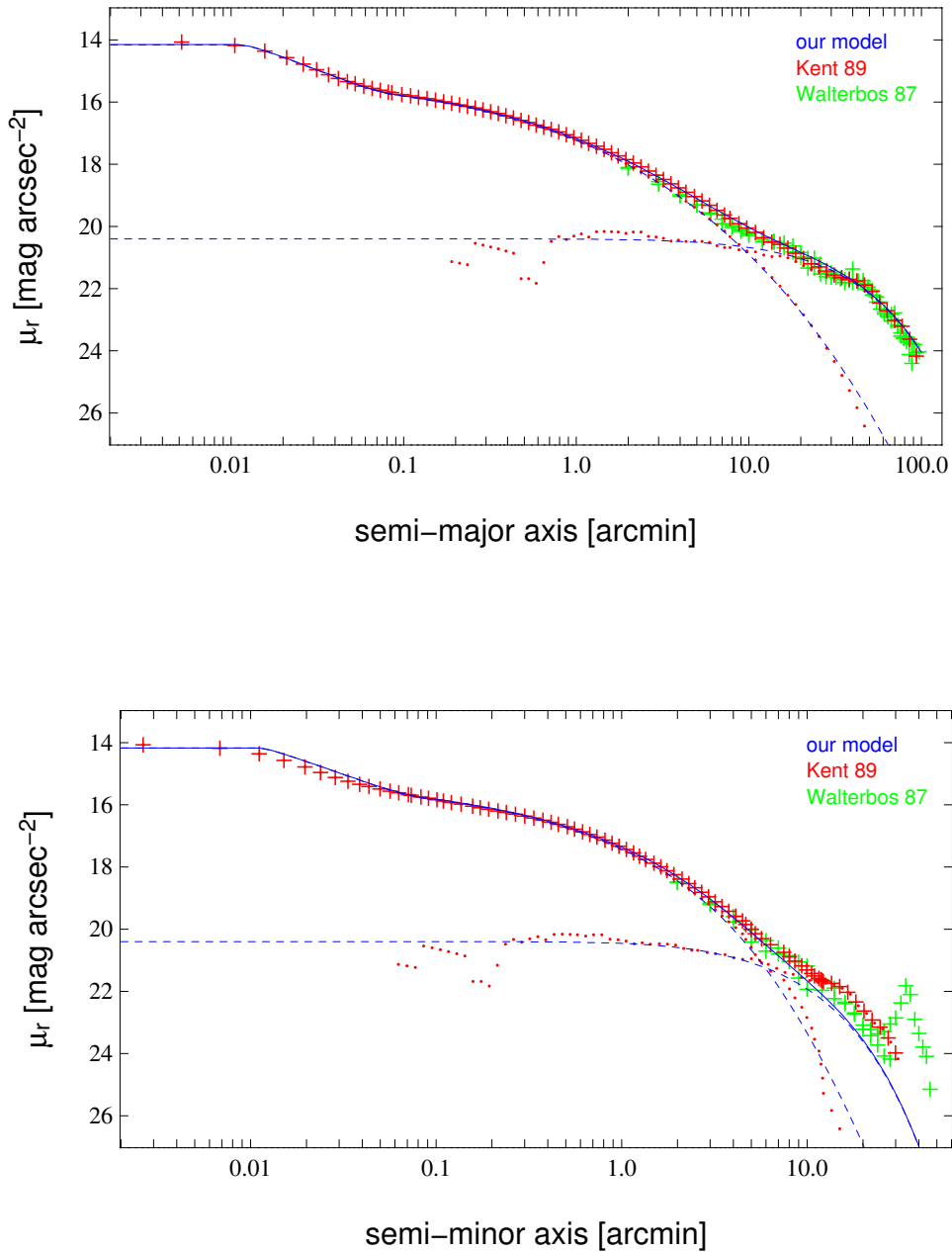
Figure 3.4: Surface-brightness profile of M31 in the Gunn *r*-band. Red crosses are the *r*-band data for the central region of M31 (Kent, 1989b), where the green crosses show the Walterbos & Kennicutt (1987) data transformed to the *r*-band. The upper and lower figures show the profiles along semi-major and semi-minor axis, respectively. Kent's decomposition of the surface brightness profile into the bulge and disk component is shown by red dots. For comparison we have superposed our bulge and disk surface brightness models from Eqs. 3.19 and 3.25. With the exception of spiral arm imprints, our models match the observations extremely well.

$M_{\text{tot}}/M_\odot$	dist [kpc]	band X	$(r-X)$	ext_X	$L_{X,\text{tot}}/L_{X,\odot}$	$\left(\frac{M}{L}\right)_X$	comment
$16 \cdot 10^{10}$	690	gunn r	0	0	$1.4 \ldots 1.7 \cdot 10^{10}$	$11.3 \ldots 9.6$	for Kent's max. disk mass
$3.09 \cdot 10^{10}$	690	gunn r	0	0	$1.34 \cdot 10^{10}$	2.31	for Kerins' disk mass
$3.09 \cdot 10^{10}$	770	R	0.54	0.68	$3.5 \cdot 10^{10}$	0.88	our model

Table 3.2: This table shows that the maximum disk – assumed by Kent (1989b) (first line) – would imply a much too large mass-to-light ratio. This problem is usually present in models invoking a maximum disk models. In its last two lines we give the mass-to-light ratios resulting from the disk mass of $3.09 \cdot 10^{10} M_\odot$ (Kerins *et al.*, 2001). The mass-to-light ratio for a more realistic extinction (last line), is close to a theoretical $(M/L)_{\text{stellar}} = 0.62$ for a 2 Gyr old, solar metallicity SSP disk population (based on Gould *et al.* 1997 and Girardi *et al.* 2002).

to obtain the same disk mass as Kerins *et al.* (2001)

$$M_{\text{disk}} = \int \int \rho \, dz \, d\sigma = 4\pi \rho_0 h_z h_\sigma^2 = 3.09 \cdot 10^{10} M_\odot \quad . \tag{3.28}$$

The extinction in the M31 disk is obtained from $E(B-V) = 0.22$ (Stephens *et al.*, 2003) which yields a V-band extinction $\text{ext}_V = 3.1E(B-V) = 0.682$. This translates to $\text{ext}_R = 0.748 \, \text{ext}_V = 0.51$ (Binney & Merrifield, 1998). Adding the foreground extinction $\text{ext}_R = 0.17$ (Schlegel *et al.*, 1998), we obtain $\text{ext}_R = 0.68$ for the total extinction for sources residing in the disk of M31.

The central luminosity density of the disk is obtained from the r-band value given in Kent (1989b) and the color transformation $(r-R) = 0.53$ as $\rho_{R,0}^{\text{Kent}} = 26.86 \, \text{mag} \, \text{arcsec}^{-3}$. For the transformation equation we assumed as disk color of $(B-V) \approx 0.7$ (Walterbos & Kennicutt, 1987). This normalization yields a extinction corrected disk luminosity of $L_{R,\text{tot}}/L_{R,\odot} = 3.5 \cdot 10^{10}$ using a M31 distance of 770 kpc. With the disk mass given in Kerins *et al.* (2001) our $\left(\frac{M}{L}\right)_R$-ratio becomes 0.88 (see also Table 3.2), which is well consistent with a theoretical $\left(\frac{M}{L}\right)_{\text{stellar}} = 0.62$ for a 2 Gyr old, solar metallicity SSP disk population (based on Gould *et al.* 1997 and Girardi *et al.* 2002).

For comparison, we also summarize the maximum disk model of Kent (1989b) in Table 3.2 (first line). This model implies a four times higher $\left(\frac{M}{L}\right)_r$-ratio, which is difficult to reconcile with population synthesis models. Note, that the results from Han & Gould (1996a) are not easy to compare with ours as they used a double exponential disk with $\rho_0 = 0.35 \, M_\odot \, \text{pc}^{-3}$, $h_z = 0.4$ kpc, and $h_\sigma = 6.4$ kpc corresponding to a disk mass of $7.2 \cdot 10^{10} M_\odot$ and a bulge that is more massive than ours ($4.9 \cdot 10^{10} M_\odot$).

3.5.3 Halo of M31

Our density models for the bulge and disk differ only slightly from that of Kerins *et al.* (2001). The largest differences appear in the central region. The contributions to the rotation velocity resulting from the different populations are therefore very much the same as in the Kerins *et al.* (2001) model. This implies, that we can use the halo density distribution from Kerins *et al.* (2001) to obtain a halo model consistent with the observed M31 rotation curve. This halo density distribution is that of an isothermal sphere with a core radius of $r_c = 2$ kpc, i.e.

$$\rho_{\text{halo}}(x_0, y_0, z_0) = \frac{\rho_0}{1 + \left(\frac{r}{r_c}\right)^2} \qquad r \leq 200 \, \text{kpc} \quad , \tag{3.29}$$

with $r = \sqrt{x_0^2 + y_0^2 + z_0^2}$, $r_c = 2$ kpc, and $\rho_0 = 0.23 \, M_\odot \, \text{pc}^{-3}$. Figure 3.5 shows the overall rotation curve of our model. In the model of Han & Gould (1996a) the core-radius of the halo is much larger
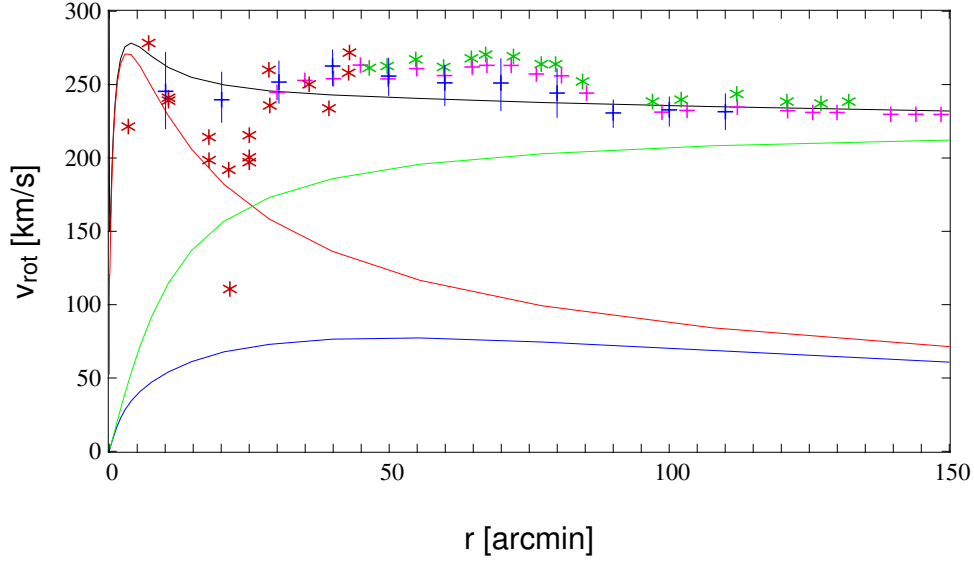
Figure 3.5: This figure shows the overall rotation curve of our model (black curve) and its contributions of the bulge (red), disk (blue), and halo (green). These rotation curves match with Fig. 3b in Kerins *et al.* (2001). In red crosses we show the data points derived from CO measurements of Loinard *et al.* (1995); in green HI measurements from Brinks & Burton (1984); in blue averaged data points from Widrow *et al.* (2003, based on Kent 1989a and Braun 1991); in magenta are the data points of Kerins *et al.* (2001, based on Kent 1989b).

($r_c = 6.5\,$kpc) to compensate for their higher disk and bulge mass in order to match the rotation curve of M31.

3.5.4 Halo of the Milky Way

The halo of the Milky Way (MW) is modeled as a cored isothermal sphere,

$$\rho_{\mathrm{MW}}(D_{\mathrm{L}}) = \frac{\rho_0}{1 + \left(\frac{r}{r_c}\right)^2} \qquad r \leq 200\,\mathrm{kpc} \quad , \tag{3.30}$$

with the line of sight distance D_{L}. We chose a core radius of $r_c = 2\,$kpc as used in Han & Gould (1996a) and Gyuk & Crotts (2000). The central density is taken from (Han & Gould, 1996a),

$$\rho_0 = 0.0079\,\mathrm{M_\odot\,pc^{-3}} \left(1 + \left(\frac{r_\odot}{r_c}\right)^2\right) = 0.1343\,\mathrm{M_\odot\,pc^{-3}} \quad . \tag{3.31}$$

We convert the galactocentric distance r to our line of sight coordinate system according to

$$r(D_{\mathrm{L}}) = \sqrt{r_\odot^2 - 2r_\odot D_{\mathrm{L}} \cos(l)\cos(b) + D_{\mathrm{L}}^2} \quad , \tag{3.32}$$

using the M31 galactic coordinates $l = 121.14988°$, $b = -21.61707°$ and the solar galactocentric distance $r_\odot = 8\,$kpc (Bahcall *et al.*, 1983).

Chapter 4

Microlensing towards crowded fields[1]

Abstract. We present a comprehensive treatment of the pixellensing theory and apply it to lensing experiments and their results towards M31. Using distribution functions for the distances, velocities, masses, and luminosities of stars and (potential) Machos, we derive lensing event rates as a function of the event observables. In the microlensing regime (resolved sources), the observables are the maximum magnification of the source and the Einstein time scale of the event. In the pixellensing regime (crowded or unresolved sources) only the maximum excess flux of the source above a background and the full-width-half-maximum time of the event can be measured. We use an updated model of M31, which reproduces consistently photometry, kinematics and stellar population to calculate the lensing event distribution functions for the specific case of M31. We predict the halo- and self-lensing event rates for bulge and disk stars in M31, and treat events with and without finite source signatures separately. We use the M31-photon-noise profile (related to the surface-brightness-profile) and obtain the expected event rates for the WeCAPP experiment as a function of position, field-of-view and $\left(\frac{S}{N}\right)$ full-threshold at maximum magnification. The detection of two events with a signal-to-noise ratio larger than 10 at peak flux and a time scale larger than 1 day in the WeCAPP 2000/2001 data is in good agreement with our theoretical calculations.

---

[1]This chapter is a considerably shortened version of the article Riffeser, Fliri, Seitz & Bender (2005).

4.1   Introduction

Searches for compact dark matter towards the Large and Small Magellanic Clouds (LMC and SMC) and the Galactic bulge identified numerous microlensing events in the past decade (MACHO (Alcock *et al.*, 1997), EROS (Aubourg *et al.*, 1993), OGLE (Udalski *et al.*, 2000), DUO (Alard & Guibert, 1997)). In parallel to these observations, a lot of effort has been spent on the prediction of number, spatial distribution, amplitude and duration of lensing events towards these targets. The underlying models require knowledge of the density and velocity-distribution, as well as of the luminosity and mass function of lensing and lensed stars. The halo Macho-mass fraction and lens mass are free parameters. From that, the contributions of self-lensing and halo-lensing is obtained. The self-lensing predictions (minimum lensing that has to occur due to star-star lensing) serve as a sanity check for observations and models. An excess of lensing relative to self-lensing can then be attributed to halo-lensing, from which finally the Macho-parameters are inferred.

Paczynski (1986) was the first to present such a lensing model for the Galaxy halo and to estimate the probability of lensing (i.e. a magnification larger than 1.34) taking place at any time. This probability is also called microlensing optical depth. Based on this work Griest (1991) evaluated the optical depth with more realistic assumptions on halo density and velocity structure. He also obtained the event rate and distributions for lensing time scales and amplifications. Alcock *et al.* (1995a) related the Einstein time scale distribution of the events to the microlensing rate and optical depth. They evaluated these distributions for several axisymmetric disk-halo models in the framework of the Macho project.

Any microlensing light curve can be characterized by the maximum magnification, the time to cross the Einstein radius (Einstein time) and the time of the event. The first two observables depend on the line of sight distance of the source and lens, the minimum projected transverse lens-source distance (impact parameter), the transverse lens-source velocity and the lens mass.

These quantities therefore can not be extracted separately from an individual lensing event; instead, one can only derive probability distributions for them (see de Rujula *et al.* (1991) and Dominik (1998)). Most interesting are of course the object masses responsible for the measured lensing light curves: Jetzer & Massó (1994) have derived the lens mass probability function for an event with given Einstein time and amplification. Han & Gould (1996b) have determined the Macho mass spectrum from 51 Macho candidates using their observed Einstein times.

Blending has proven to be a severe limitation in the analysis of microlensing events. It can be overcome partly by using low noise, high spatial resolution HST-images for measurements of the un-lensed source fluxes (see e.g., Alcock *et al.* 2001). For extragalactic objects however, this can provide a precise source flux for a fraction of lensed stars only. One can also use an advanced technique called difference imaging analysis which is insensitive to crowding and allows to measure pixel flux differences in highly crowded fields at the Poisson noise level. Therefore, lensing searches could be extended to more distant targets like M31 (AGAPE (Ansari *et al.*, 1999), Columbia-VATT (Crotts & Tomaney, 1996), WeCAPP (Riffeser *et al.*, 2001, 2003), POINT-AGAPE (Paulin-Henriksson *et al.*, 2003; Calchi Novati *et al.*, 2005), MEGA (de Jong *et al.*, 2004), SLOTT/AGAPE (Bozza *et al.*, 2000; Calchi Novati *et al.*, 2003), NMS (Joshi *et al.*, 2001)), or M87 (Baltz *et al.*, 2004).

Gould (1996) called microlensing of unresolved sources 'pixellensing'. This definition encompasses surveys at the crowding limit as well as extragalactic microlensing experiments (e. g. towards M31 or M87) where hundreds of stars contribute to the flux within one pixel. Gould (and also Ansari *et al.* 1997) showed that the comparison of pixel fluxes at different epochs can extend the search for

microlensing events up to distances of a few Megaparsecs. Applying his equations Gould (1996), Han (1996) and Han & Gould (1996a) obtained the optical depth and distributions of time scales and event rates for a pixellensing survey towards M31.

If one does not know the flux of the un-lensed source accurately (i.e. if one is not in the classical microlensing regime anymore), the information that can be extracted from light curves is reduced. Wozniak & Paczynski (1997) were the first to note that the light curve maximum does not provide the maximum magnification of the source anymore, and, second, one can not obtain the Einstein time from the full-width-half-maximum time of an event (since the latter is a product of the Einstein time and a function of the magnification at maximum).

This initiated efforts to deal with the lacking knowledge of the Einstein time scales in the pixel-lensing regime (see Gondolo 1999; Alard 2001) and the suggestion to extract the Einstein time using the width of the 'tails' of the lensing light curves by Baltz & Silk (2000) and Gould (1996). However, it is more straightforward to compare quantities that one can easily measure in an experiment with model predictions for the same quantity. The two independent and most precisely measurable observables are the flux excess of the light curve at its maximum and its full-width-half-maximum time scale. Baltz & Silk (2000) followed that strategy and derived the event rate as a function of the full-width-half-maximum time scale of the events. We proceed in that direction and calculate the contributions to the event rate as a function of the event's full-width-half-maximum time and maximum excess flux, because both the excess flux and time scale determine the event's detectability.

This chapter is organized as follows: we introduce our notation for the micro- and pixellensing regime in Sect. 4.2 and also describe the treatment of finite source effects. In Sect. 4.3 we combine the probability distributions for location, mass, source-lens velocity and impact parameter distribution to obtain the lensing event rate distribution as a function of these parameters. Section 4.4 summarizes the statistical properties of the source populations, i.e., their luminosity function and their number density. In Sect. 4.5 we calculate the optical depth and the observables in the microlensing regime: single star event rate and the distribution of the Einstein time scale. Section 4.6 deals with the pixellensing regime. We calculate the event rate as a function of the maximum excess flux and full-width-half-maximum time of the event in the point sources approximation. We also show how the event rate changes, if source sizes (shifting events to larger time scales and smaller flux excesses) are taken into account. In Sect. 4.7 we obtain the event rate for pixellensing surveys with spatially varying photon noise (related to the surface brightness contours of M31) but fixed signal-to-noise threshold for the excess flux at maximum magnification. We predict the number of halo- and self-lensing events in the WeCAPP survey (without taking into account the sampling efficiency of the survey) for the M31-model presented in chapter 3. We demonstrate that accounting for the minimum full-width-half-maximum of the events is extremely important to correctly predict the number of events. We also compare the characteristics of self-lensing events with halo-lensing events. The chapter is summarized in Sect. 4.8.

4.2 Basics of lensing by a point mass

In this section we summarize the basics of microlensing theory and introduce our notation. The change in flux $\Delta F(t)$ caused by a microlensing event depends on the un-lensed flux F_0 and the magnification $A(t)$:

$$\Delta F(t) := F_0 \left[A(t) - 1 \right] \quad . \tag{4.1}$$

For a point-like deflector and a point-like source moving with constant relative transversal velocity v_t the amplification is symmetric around its time of maximum t_0 and is connected to the Einstein radius R_E, and the impact parameter b as follows (Paczynski, 1986):

$$A(u(t)) = \frac{u^2 + 2}{u\sqrt{u^2 + 4}} \overset{u \ll 1}{\approx} \frac{1}{u} \quad , \tag{4.2}$$

$$u(r(t)) := \frac{r(t)}{R_E} := \sqrt{\frac{v_t^2(t - t_0)^2 + b^2}{R_E^2}} \quad , \tag{4.3}$$

$$R_E := \frac{\sqrt{4GM}}{c}\sqrt{\frac{D_L(D_S - D_L)}{D_S}} \quad , \tag{4.4}$$

with M being the mass of the lens, D_L and D_S being the distances to the lens, and $r(t)$ is the distance between source and lens in the lens plane. With the Einstein time scale $t_E := \frac{R_E}{v_t}$ and the normalized impact parameter $u_0 := \frac{b}{R_E}$ we obtain

$$u(t) = \sqrt{\frac{(t - t_0)^2}{t_E^2} + u_0^2} \quad . \tag{4.5}$$

The maximum amplification (at $t = t_0$) becomes

$$A_0 := \frac{u_0^2 + 2}{u_0\sqrt{u_0^2 + 4}} \overset{u_0 \ll 1}{\approx} \frac{1}{u_0} \quad . \tag{4.6}$$

Equation 4.2 can be inverted to

$$u(A) = \left(2A(A^2 - 1)^{-1/2} - 2\right)^{1/2} \overset{A \gg 1}{\approx} \frac{1}{A} \quad . \tag{4.7}$$

Inserting A_0 in Eq. 4.7 its derivative writes as

$$\begin{aligned}
\frac{du_0}{dA_0} &= -\frac{2\left((A_0^2 - 1)^{-1/2} - 1/2 A_0(A_0^2 - 1)^{-3/2} 2A_0\right)}{2\left(2A_0(A_0^2 - 1)^{-1/2} - 2\right)^{1/2}} = -\left[2\left(\frac{A_0}{(A_0^2 - 1)^{1/2}} - 1\right)(A_0^2 - 1)^3\right]^{-1/2} \\
&= \frac{-\sqrt{2}}{2}\frac{\left(A_0 + (A_0^2 - 1)^{1/2}\right)^{1/2}}{(A_0^2 - 1)^{5/4}} \quad .
\end{aligned} \tag{4.8}$$

The full-width-half-maximum time scale t_{fwhm} of a light curve is defined by $A\left(\frac{t_{fwhm}}{2}\right) - 1 := \frac{A_0 - 1}{2}$. It is related to the Einstein time scale t_E by

$$t_{fwhm} = t_E w(u_0) = t_E \Upsilon(A_0) \quad , \tag{4.9}$$

where $w(u_0)$ was first obtained by Gondolo (1999)[2]:

$$w(u_0) := 2\sqrt{u\left(\frac{A(u_0) + 1}{2}\right)^2 - u_0^2} = 2\sqrt{\frac{2[A(u_0) + 1]}{\sqrt{[A(u_0) - 1][A(u_0) + 3]}} - 2 - u_0^2} \overset{u_0 \ll 1}{\approx} \sqrt{12}\, u_0 \quad , \tag{4.10}$$

---

[2] with $\beta \equiv u_0$ and $\delta(\beta) \equiv A_0 - 1$.

and $\Upsilon(A_0) := w(u_0(A_0))$ can be approximated as

$$\Upsilon(A_0) \approx \frac{\sqrt{12}}{A_0} \tag{4.11}$$

in the high magnification case ($A_0 \gg 1$). Hence the easy measurable time scale t_{fwhm} is a product of the quantity t_{E}, which contains the physical information about the lens, and the magnification of the source at maximum light A_0.

4.2.1 Finite source effects

If the impact parameter of a source-lens system becomes comparable to the source radius projected on the lens plane $R_* \frac{D_{\text{L}}}{D_{\text{S}}}$, the point-source approximation is not valid anymore. The amplification then saturates at a level below the maximum magnification in Eq. 4.6. Gould (1994) parameterized the ratio of the source-lens separation $r(t)$ and source radius R_* projected onto the lens plane with

$$z(t) := \frac{r(t)}{R_*} \frac{D_{\text{S}}}{D_{\text{L}}} = \frac{u(t) R_{\text{E}}}{R_*} \frac{D_{\text{S}}}{D_{\text{L}}} \quad , \tag{4.12}$$

and calculated the value for the maximum magnification (in the high magnification regime) assuming a disk-like homogeneously radiating source (see Fig. 4.1). It turns out that for $z(t) < 0.5$ or equivalently $r(t) < r_{\text{fs}}$ with

$$r_{\text{fs}} := 0.5 R_* \frac{D_{\text{L}}}{D_{\text{S}}} \quad , \tag{4.13}$$

and

$$u_{\text{fs}} := u(A_0^{\text{fs}}) \overset{A_0^{\text{fs}} \gg 1}{\approx} \frac{R_* D_{\text{L}}}{2 R_{\text{E}} D_{\text{S}}} \quad , \tag{4.14}$$

the amplification is no longer directly connected to the impact parameter (Gould, 1995), but all impact parameters $b = r(t_0)$ below $b < r_{\text{fs}}$ have nearly the same maximum amplification. The maximum amplification in the finite source regime then becomes

$$A_0^{\text{fs}} \overset{A_0^{\text{fs}} \gg 1}{\approx} \frac{2 R_{\text{E}} D_{\text{S}}}{R_* D_{\text{L}}} \tag{4.15}$$

which equals the approximation of Baltz & Silk (2000) (Eq. 19). We therefore generalize Eq. 4.2 to approximately account for finite-source effects

$$A^{\text{fs}}(u) \approx \begin{cases} \frac{2 R_{\text{E}} D_{\text{S}}}{R_* D_{\text{L}}} & , \quad u < u_{\text{fs}} \\ \frac{u^2 + 2}{u \sqrt{u^2 + 4}} & , \quad u \geq u_{\text{fs}} \end{cases} \tag{4.16}$$

For light curves with finite source signatures ($u_0 < u_{\text{fs}}$) at a impact parameter

$$u \overset{A_0^{\text{fs}} \gg 1}{\approx} \frac{R_* D_{\text{L}}}{R_{\text{E}} D_{\text{S}}} \quad , \tag{4.17}$$

($z \approx 1$) the amplification of our approximation is half of the maximum and can be used to define the $t_{\text{fwhm}}^{\text{fs}}$

$$t_{\text{fwhm}}^{\text{fs}} := t_{\text{E}} \Upsilon^{\text{fs}} := \frac{2 R_{\text{E}}}{v_{\text{t}}} \sqrt{u \left(\frac{A_0^{\text{fs}} + 1}{2} \right)^2 - u_0^2} \approx t_{\text{fwhm}} \frac{1}{\sqrt{3}} \sqrt{\left(\frac{R_* D_{\text{L}}}{b D_{\text{S}}} \right)^2 - 1} \tag{4.18}$$
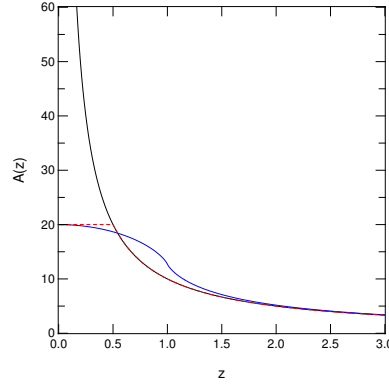
Figure 4.1: Amplification $A(z)$ versus $z(t) := \frac{r(t)}{R_*} \frac{D_S}{D_L}$ plotted for $\frac{R_*}{D_S} = 0.5 \frac{R_E}{D_L}$. Black curve: point source approximation, see Eq. 4.2. Blue curve: $A(z)$ with finite source effects (Gould (1994), Eq. 2.5). Red dashed curve: simple approximation $A^{fs}(z)$ for finite source effects according to Eq. 4.16.

with

$$\Upsilon^{fs}(u_0, R_*, D_L, D_S, M) := 2\sqrt{u\left(\frac{A_0^{fs}+1}{2}\right)^2 - u_0^2} = 2\sqrt{\frac{2(A_0^{fs}+1)}{\sqrt{(A_0^{fs}-1)(A_0^{fs}+3)}} - 2 - u_0^2} \quad . \qquad (4.19)$$

In Eq. 4.18 the full-width time scales for light curves that show finite source signatures are related to the values t_{fwhm} for the point source approximation using Eqs. 4.9 and 4.10. This demonstrates, that the source does affect the time scale of an event severely: a source with an impact parameter of a tenths the projected source radius, will have an event times scale almost 6-times as long as that in the point source approximation. The largest flux excess of a lensed, extended star becomes

$$\Delta F_{max} = F_0(A_0^{fs} - 1) \overset{A_0^{fs} \gg 1}{\approx} \frac{4\sqrt{G}}{c} \sqrt{\frac{D_S(D_S - D_L)}{D_L}} \sqrt{M} \frac{F_0}{R_*} \quad , \qquad (4.20)$$

irrespective of the fact weather the light curve shows finite source signatures or not.

4.3 Distribution function for lens parameters

For a source of fixed intrinsic flux F_0, position $\vec{r}_s = (x, y, D_S)$ and velocity vector $\vec{v}_s = (v_{s,x}, v_{s,y}, v_{s,z})$, the number and characteristics of lensing events are determined by the probability function $p(\vec{r}_l, \vec{v}_l, M)$ for a lens with mass M, velocity $\vec{v}_l$ being at position $\vec{r}_l$. For the change of magnification of the background source, only the transversal velocity components of source and lens are relevant (we assume velocities to be constant). Therefore, in addition to M and D_L only the projected relative transversal positions $r := r_{t,l} - \frac{D_L}{D_S} r_{t,s}$ and velocities $v_t := v_{t,l} - \frac{D_L}{D_S} v_{t,s}$ and the angle ϕ enclosed by relative position and velocity vector enter the lensing properties.

The distributions in r and ϕ can be reduced to the distribution of one parameter, the impact parameter b of the lens-source-trajectory. This is obvious, since in a symmetric potential the trajectory of a particle is fully described by its minimum distance.

Thus, the relevant lens parameters are D_L, v_t, M and b. We introduce the lens density and the distributions of D_L, v_t, M in the next two subsections. For those lenses which cause events, we will then derive the distribution of the impact parameters dN/db.

4.3.1 Distance and mass distribution

The probability distributions for a lens with mass M being at distance D_L are given by

$$p_{D_L} = \rho(D_L) \left(\int_0^{D_S} \rho(D_L) dD_L \right)^{-1} \quad , \tag{4.21}$$

$$p_M = \xi(M) \left(\int_0^{\infty} \xi(M) dM \right)^{-1} \quad , \tag{4.22}$$

with the lens mass density $\rho(D_L)$ and the lens mass function $\xi(M)$ (which itself can be normalized to $\int \xi(M) M dM = 1$, see Binney & Tremaine 1987). The number density per lens mass interval finally is defined by

$$n(D_L, M) := \rho(D_L)\xi(M) \quad , \tag{4.23}$$

where $n(D_L, M)$ has units of $\left[\text{length}^{-3}\text{mass}^{-1}\right]$.

4.3.2 Velocity distribution for lenses

We assume that the velocity distribution of the lenses around their mean streaming velocity is Gaussian:

$$p(v_{l,i}) = C_l e^{-\frac{v_{l,i}^2}{2\sigma_l^2}} \quad , i = x, y, z \quad , C_l = \frac{1}{\sqrt{2\pi}\,\sigma_l} \quad .$$

with σ_l being the dispersion. We furthermore assume that the combined transverse motion of observer and source relative to the mean transverse streaming velocity of the lenses is known and occurs in the x-direction with amplitude $v_0(x,y,z)$ as projected onto the lens plane. This means that the velocity v_s of the source turns into a projected velocity $v_p = D_L/D_S v_s$. The lensing time scales are determined by relative proper motions, not the absolute motions of lens and source.

We now define the relative projected velocity $v_{ls,x} := v_{l,x} + v_0$ (analogously $v_{ls,y} := v_{l,y} + 0$) and obtain the transverse lens-source velocity distribution as

$$
\begin{aligned}
p_{v_t}(v_t, v_0) = & \int \frac{1}{\pi\sigma_l^2} v_t \exp\left(-\frac{v_t^2 + v_0^2}{2\sigma_l^2}\right) \frac{\exp\left(-\frac{2v_0 v_{ls,x}}{2\sigma_l^2}\right)}{\sqrt{v_t^2 - v_{ls,x}^2}} dv_{ls,x} \\
= & \frac{1}{\sigma_l^2} v_t \exp\left(-\frac{v_t^2 + v_0^2}{2\sigma_l^2}\right) I_0\left(\frac{v_0 v_t}{\sigma_l^2}\right) \quad .
\end{aligned}
\tag{4.24}
$$

Here the Bessel function I_0 stretches the distribution depending on v_0.

4.3.3 Impact parameter distribution for events

In Paczynski (1986)'s definition for lensing events, lens-source configurations become lensing events, if the magnification of a source rises above a given threshold within the survey time interval Δt. This means that for each lens mass one can define a 'microlensing-tube' along the line of sight to the source which separates the high magnification region from the low magnification region, and a lens causes an event if it enters the tube.

We now calculate how lenses, which enter the magnification region of radius $b_T = u_T R_E$ during the time Δt, distribute over different impact parameters u_0. To derive this distribution, we calculate the flux of lenses of number density $n(D_L, M)$, which move with a transversal velocity v_t according to a distribution $p_{v_t}(v_t, D_L)$ through the radius b_T. With the angle θ between the normal onto this circle and the transversal velocity we get

$$
\frac{d^4 N}{dD_L\, dM\, dv_t\, db} = \int\limits_{-\pi/2}^{\pi/2} n(D_L, M)\, p_{v_t}(v_t, D_L)\, v_t \Delta t \cos\theta\, d\theta
$$
$$
= 2\rho(D_L)\, \xi(M)\, p_{v_t}(v_t, D_L)\, v_t \Delta t \quad . \tag{4.25}
$$

We now transfer the number N of the events per line of sight to the event rate (per line of sight), $\Gamma := \frac{N}{\Delta t}$, and write Eq. 4.25 as

$$
\frac{d^4 \Gamma}{dD_L\, dM\, dv_t\, db} = 2\rho(D_L)\, \xi(M)\, p_{v_t}(v_t, D_L)\, v_t \quad . \tag{4.26}
$$

With the relative impact parameter u_0 defined as $u_0 = \frac{b}{R_E(D_L, M)}$ this distribution can be rewritten as

$$
\frac{d^4 \Gamma}{dD_L\, dM\, dv_t\, du_0} = 2\rho(D_L)\, \xi(M)\, p_{v_t}(v_t, D_L)\, v_t R_E(D_L, M) \quad . \tag{4.27}
$$

As the result is not depending on u_0, the impact parameter distribution is constant.

4.4 The source distributions

In the case of pixellensing the parameters of the source cannot be determined. Therefore, we now introduce probability distributions for the source distance D_S, velocity $\vec{v}_s$, and unlensed flux F_0.

4.4.1 The transverse lens-source velocity distribution

We again assume that the velocity distributions of lenses l and sources s are approximately isotropic around their mean respective streaming velocities (see Eq. 4.24). Similar to Eq. 4.24, we obtain for the distribution of the transverse velocities

$$
p_{v_t}(v_t, v_0) = \frac{1}{\sigma_{ls}^2} v_t \exp\left(-\frac{v_t^2 + v_0^2}{2\sigma_{ls}^2}\right) I_0\left(\frac{v_0 v_t}{\sigma_{ls}^2}\right) \quad . \tag{4.28}
$$

with $v_0(x, y, D_L, D_S)$, $\sigma_l(x, y, D_L)$, and $\sigma_s(x, y, D_S)$. In the last step we have defined

$$
\sigma_{ls} := \sqrt{\sigma_l^2 + \left(\frac{D_L}{D_S}\right)^2 \sigma_s^2} \quad , \tag{4.29}
$$

which is the combined width of the velocity distribution of the lenses and that of the sources, projected onto the lens plane.

4.4.2 The luminosity function

The luminosity function (LF) $\phi\left[\text{flux}^{-1}\right]$ or $\Phi\left[\text{mag}^{-1}\right]$ is usually defined as the number of stars per luminosity bin. We instead use a normalization equal to one,

$$\int\limits_0^\infty \phi(\mathscr{F})\,d\mathscr{F} = \int\limits_{-\infty}^{+\infty} \Phi(\mathscr{M})\,d\mathscr{M} = 1 \quad, \tag{4.30}$$

as we obtain the amplitude of the LF from the matter density and the mass-to-light ratio of the matter components (i.e. bulge and disk). The mean, or so-called characteristic flux of a stellar population is obtained as

$$< \mathscr{F} >:= \frac{\int \mathscr{F}\,\phi(\mathscr{F})\,d\mathscr{F}}{\int \phi(\mathscr{F})\,d\mathscr{F}} \quad. \tag{4.31}$$

or, if one instead uses the luminosity function Φ in magnitudes [3]:

$$< \mathscr{F} >:= \frac{\int \mathscr{F}_{\text{Vega}}10^{-0.4\mathscr{M}}\,\Phi(\mathscr{M})\,d\mathscr{M}}{\int \Phi(\mathscr{M})\,d\mathscr{M}} \quad, \tag{4.32}$$

with $\mathscr{F}_{\text{Vega}}$ being in the flux of Vega. The luminosity functions in the literature are usually given for stars at a distance of 10 pc. The relations for the source flux F_0 at a distance D_S and its flux $\mathscr{F}$ at 10 pc, or its absolute magnitude are given by

$$F_0(\mathscr{F},x,y,D_S) := \mathscr{F} \cdot \left(\frac{10\,\text{pc}}{D_S}\right)^2 10^{-0.4\,\text{ext}(x,y,D_S)} \quad. \tag{4.33}$$

including the extinction $\text{ext}(x,y,D_S)$ along the line of sight.

4.4.3 The number density of sources

We characterize different source components (bulge and disk) by an index s with corresponding indices in the density, luminosity and mass-function of that component. With $(M/L)_s$ we describe the mass-to-light ratios of the components in solar units. The number density of sources is a function of the mass density, the mass-to-light ratio, and the characteristic flux of each component,

$$n_s(x,y,D_S) := \frac{d^3N_s}{dx\,dy\,dD_S} = \frac{\rho_s(x,y,D_S)}{\left(\frac{M}{L}\right)_s \frac{M_\odot}{\mathscr{F}_\odot} < \mathscr{F} >_s} \quad. \tag{4.34}$$

Note, that $\left(\frac{M}{L}\right)$ is the mass-to-light ratio of the total disk or bulge component, and has to include the mass in stellar remnants or in gas. Therefore, the value of $\left(\frac{M}{L}\right)$ is not necessarily equal to the stellar mass-to-light-ratio of the bulge and the disk. The normalized probability distribution for sources $p_s(D_S)$ at a distance D_S is

$$p_s(D_S) := \frac{\rho_s(D_S)}{\int\limits_0^\infty \rho_s(D_S)\,dD_S} \quad. \tag{4.35}$$

---

[3] With $d\mathscr{M} = -\frac{2.5}{\ln 10}d\mathscr{F}/\mathscr{F}$ the conversion of the luminosity function from flux to magnitudes becomes $\Phi(\mathscr{M}) = -0.4\ln 10\,\mathscr{F}_{\text{Vega}}10^{-0.4\mathscr{M}}\,\phi\left(\mathscr{F}_{\text{Vega}}10^{-0.4\mathscr{M}}\right)$.
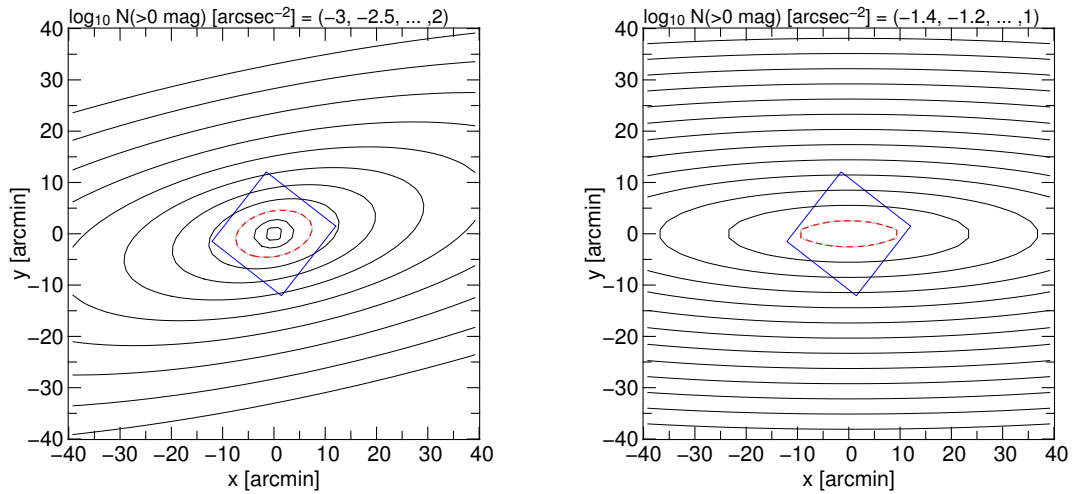
Figure 4.2: These figures illustrate the number density of bulge-stars (left) and disk-stars (right) brighter an R-band luminosity of $\mathscr{M}_R = 0\,\text{mag}$ in units of stars per arcsec^2. The axes x and y are given in the intrinsic M31 coordinate system, which is centered on the nucleus of M31 and where the M31 disk major axis is orientated horizontally (P.A. $= 38°$, see chapter 3). The contours were obtained from the number density and luminosity functions of the bulge and disk component of M31. The WeCAPP field, a square of 17.2 arcminutes, is shown as a blue box. The red dashed contours mark a density of $\mathscr{M}_R \leq 0$-stars of 10 stars/arcsec^2. This demonstrates that one can not resolve even giants in the central M31 field for the majority of ground-based data.

Using Eq. 4.34 and the model of M31 presented in chapter 3 we calculate the projected densities of bulge and disk stars brighter than $\mathscr{M}_R \leq 0\,\text{mag}$

$$\frac{d^2 N_{\mathscr{M} \leq 0}}{dx\,dy}(x,y) = \int\limits_{-\infty}^{\mathscr{M}=0} \int\limits_{0}^{\infty} \Phi_{\text{s}}(\mathscr{M}')\, n_{\text{s}}(x,y,D_{\text{S}})\, dD_{\text{S}}\, d\mathscr{M}' \quad . \tag{4.36}$$

and show the results in Fig. 4.2. Both populations contribute more than one bright star per square arcsec to basically any position monitored by WeCAPP. This demonstrates that crowding in the central bulge indeed is a major problem, even for the brightest stars with $\mathscr{M}_R \leq 0\,\text{mag}$, and even if the image PSFs are small.

4.5 Applications for the microlensing regime

In this section we derive the basic microlensing quantities and distributions using the 4-dimensional event rate differential derived in Sect. 4.3. We apply the equations to M31 using the M31-model presented in chapter 3.

4.5.1 Optical depth τ

The optical depth τ is defined as the number of lenses which are closer than their own Einstein radius R_{E} to a line of sight. τ is therefore the instantaneous probability of lensing taking place, given a line of

sight and a density distribution of the lenses. For a given source star at distance D_S, the optical depth equals the number of lenses within the microlensing tube defined by the Einstein radius $R_E(M, D_L, D_S)$ (Eq. 4.4) along the line of sight:

$$
\begin{aligned}
\tau(D_S) &= \int\limits_0^{D_S} \int\limits_0^\infty \int\limits_0^\infty \int\limits_0^{R_E} n(D_L, M, v_t) \cdot 2\pi r \, dr \, dv_t \, dM \, dD_L \\
&= \int\limits_0^{D_S} \int\limits_0^\infty \int\limits_0^\infty \rho(D_L) \, \xi(M) \, p_{v_t}(v_t, D_L) \int\limits_0^{R_E} 2\pi r \, dr \, dv_t \, dM \, dD_L \qquad (4.37) \\
&= \frac{4\pi G}{c^2} \int\limits_0^{D_S} \rho(D_L) D(D_L) \, dD_L \quad ,
\end{aligned}
$$

with $D(D_L) := D_L(D_S - D_L)/D_S$, equal to Paczynski (1986). This demonstrates that the optical depth depends on the mass density, but not on the mass-function $\xi(M)$ of the lenses. We use the source distance probability distribution (Eq. 4.35) to obtain the line of sight distance-averaged optical depth:

$$
<\tau>_s := \int p_s(D_S) \, \tau(D_S) \, dD_S \quad . \qquad (4.38)
$$

 Fig. 4.3 shows the average optical depth for the central part of M31 for lenses in the halo of M31 ('halo-lensing'), and for stellar lenses in the bulge and disk of M31 ('self-lensing'). The self-lensing optical depth is symmetric (with respect to the near and far side of M31) and dominates the optical depth in the central arcminute of M31. The halo-lensing optical depth is asymmetric and rises towards the far side of the M31 disk, since there are more halo lenses in front of the disk.

Fig. 4.3a shows the halo-disk optical depth. The results do not depend so much on the 3-dimensional structure of the disk but much more on the halo core radius assumed. We use $r_c = 2\,\mathrm{kpc}$ (see chapter 3). Gyuk & Crotts (2000) used core radii of $r_c = 1\,\mathrm{kpc}$ and $r_c = 5\,\mathrm{kpc}$ for their Figs. 1c and 1d, and our result lies in between of theirs, as expected. Baltz & Silk (2000) have obtained qualitatively similar results using $r_c = 5\,\mathrm{kpc}$, but assuming an M31 distance of 725 kpc and a slightly less massive halo than we do. The optical depth caused by all M31 components is shown in Fig. 4.3e. Comparison to Fig. 4.3e demonstrates that the total optical depth is dominated by bulge lenses in the central part of M31. The last panel of this figure shows the optical depth for bulge-lensing towards M31 sources. The bulge-lensing optical depth had been obtained by Gyuk & Crotts (2000) (see their Fig. 5), but the values that they obtained are up to a factor 5 larger than ours (which probably is due to their different M31-model).

4.5.2   Single star event rate

The optical depth is the probability of stars to be magnified above a threshold of 1.34 at any time. Observations, however, usually measure only a temporal change of the magnification. Therefore, the event rate, which is the number of events per time interval, is the relevant quantity for observations. The event rate is the integral of Eq. 4.26 over lens masses, lens distances, relative velocities and impact
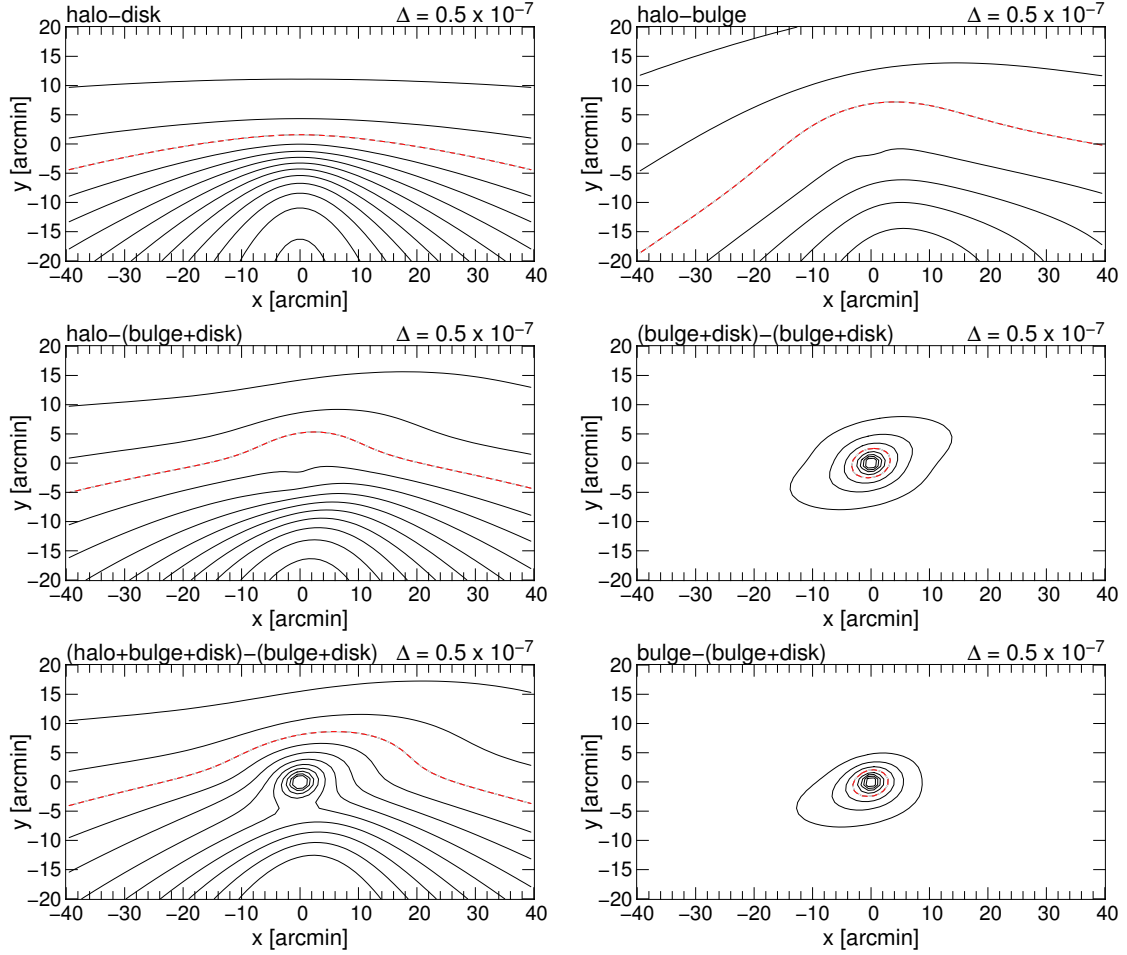
Figure 4.3: Contours of the line of sight averaged optical depth $\langle \tau \rangle_s$ (Eq. 4.38). x and y are given in the intrinsic M31 coordinate system. Halo-lensing of disk sources (first row left, a), halo-bulge lensing (first row right, b), halo-lensing of bulge & disk sources (second row left, c). The average optical depth for self-lensing of sources in M31 is shown in the second row (right, d). In the third row (left, e) we show the resulting total optical depth with the contributions of all lenses. The third row (right, f) displays the optical depth due to bulge lenses. The optical depth caused by the Milky Way (not shown) is nearly constant $\tau_{MW} = 0.78 \cdot 10^{-6}$. To obtain the values of $< \tau >_s$ we used the model of the luminous and dark matter of M31 presented in chapter 3. Here and in all following calculations a Macho fraction in the dark halo of M31 of unity was assumed. The spacing between adjacent contours are shown as inserts in each diagram. The contour lines $< \tau >_s = 2 \cdot 10^{-6}$ are shown as red dashed curves.

parameters b smaller than a threshold $u_T R_E$:

$$
\begin{aligned}
\Gamma_T(D_S) \quad &:= \int_0^\infty \int_0^{D_S} \int_0^\infty \int_0^{u_T R_E} \frac{d^4\Gamma}{dD_L\, dM\, dv_t\, db}\, db\, dv_t\, dM\, dD_L \\
&= 2u_T \int_0^\infty \xi(M) \int_0^{D_S} \rho(D_L) R_E(D_L, M) \int_0^\infty v_t\, p_{v_t}(v_t, D_L)\, dv_t\, dD_L\, dM \\
&= 2u_T \frac{\sqrt{4G}}{c} \int_0^{D_S} \rho(D_L) \sqrt{D(D_L)} \int_0^\infty \sqrt{M}\, \xi(M) \int_0^\infty v_t\, p_{v_t}(v_t, D_L)\, dv_t\, dD_L\, dM \\
&=: u_T \Gamma_1(D_S) \quad .
\end{aligned}
$$

(4.39)

This had been first evaluated (using a single mass instead of $\xi(M)$) by Griest (1991). The impact parameter threshold u_T is equivalent to a magnification threshold A_T. Therefore, the number of events with amplifications larger than $A_T(u_T)$ is proportional to the threshold parameter u_T. $\Gamma_1(D_S)$ is the event rate along a chosen line of sight to a distance of D_S. The relations above give the event rate per line of sight or per star. To compare this with measurements of the lensing rate for resolved stars, one has to account for the source-density.

4.5.3 Distribution for the Einstein time scale

Not only the number of lensing events per time and their spatial distribution but also their duration (given by their Einstein time t_E) is a key observable in microlensing surveys. Using the distribution function of the events (Eq. 4.27) with $|\frac{dv_t}{dt_E}| = \frac{R_E}{t_E^2}$ and integrating over the impact parameters up to a threshold u_T yields the the distribution of the Einstein time scales of the events as

$$
\frac{d\Gamma_T}{dt_E} := \frac{2u_T}{t_E^3} \int_0^\infty \int_0^{D_S} \rho(D_L)\, \xi(M)\, p_{v_t}\left(\frac{R_E}{t_E}\right) R_E^3\, dD_L\, dM \quad .
$$

(4.40)

This result corresponds to that of Roulet & Mollerach (1997)[4] and Baltz & Silk (2000)[5]. The (normalized) probability distribution for the Einstein time scales becomes

$$
p(t_E) := \frac{1}{\Gamma_T} \frac{d\Gamma_T}{dt_E} \quad .
$$

(4.41)

With this probability distribution the average time scale $\overline{t_E}$ of an event with line of sight distance D_S can be obtained,

$$
\begin{aligned}
\overline{t_E}(D_S) \quad &:= \int_0^\infty t_E\, p(t_E)\, dt_E \\
&= \frac{2u_T}{\Gamma_T} \int_0^\infty \int_0^\infty \int_0^{D_S} \rho(D_L)\, \xi(M)\, p_{v_t}\left(\frac{R_E}{t_E}\right) t_E\, \frac{R_E^3}{t_E^3}\, dD_L\, dM\, dt_E \\
&= \frac{2}{\pi \Gamma_1} \int_0^\infty \int_0^{D_S} \rho(D_L)\, \xi(M)\, \pi R_E^2\, dD_L\, dM \\
&= \frac{2}{\pi} \frac{\tau(D_S)}{\Gamma_1(D_S)} \quad ,
\end{aligned}
$$

(4.42)

---

[4]Their Eq. 31 corresponds to our formula converting their notation to ours $\Gamma \equiv \frac{\Gamma}{u_T}$, $\frac{dn}{dm} \equiv \rho(D_L)\xi(M)$, $T \equiv t_E$, $v^\perp \equiv v_t$, $\int_0^{2\pi} d\gamma v^\perp\, G(v_{dis}^l)\, G(v_{dis}^b) \equiv p_{v_t}(v_t)$.

[5]Their Eq. 9 corresponds to our formula converting their notation to ours $L \equiv D_S$, $t_E \equiv 2t_E$, $\beta_T \equiv u_T$, $v_c \equiv \sqrt{2}\sigma_l$, $x \equiv \frac{D_L}{D_S}$, $\eta \equiv \frac{v_0}{\sqrt{2}\sigma_l}$, $v \equiv \frac{v_t}{\sqrt{2}\sigma_l}$ and setting $\xi(M) = \frac{\delta(M - M_0)}{M}$, $\sigma_s = 0$.
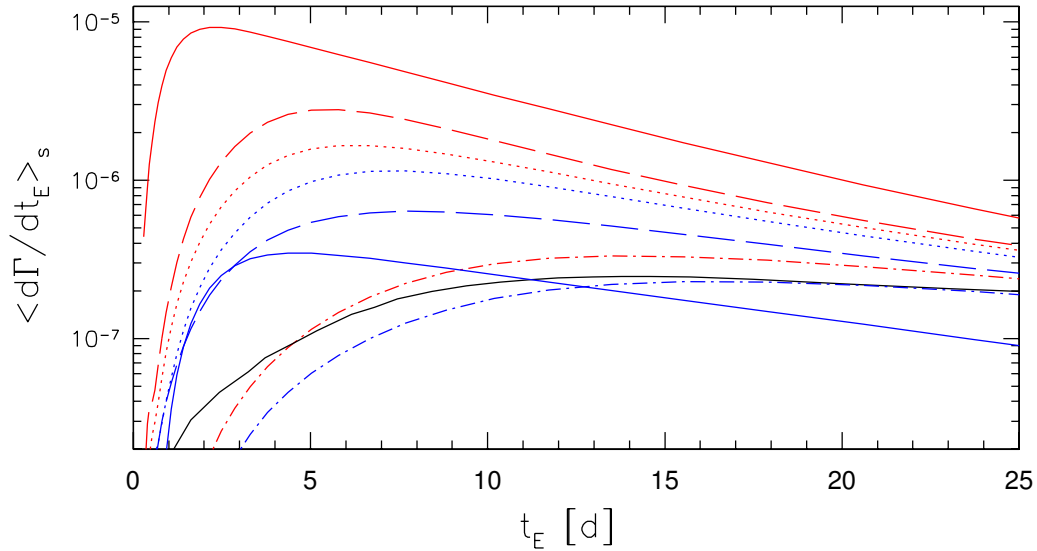
Figure 4.4: Line of sight distance-averaged distribution of the event rate with Einstein time scale $\left\langle \frac{d\Gamma}{dt_E} \right\rangle_s$ [y^{-1}] using the model of M31 presented in chapter 3 and assuming a 100% Macho halo. Results are shown for at $(x,y) = (1,0)$ arcmin (red lines), and at $(x,y) = (4.46, 4.46)$ arcmin (corresponding to $(x,y) = (1,1)$ kpc, blue lines) in the intrinsic M31 coordinate system The bulge-bulge Einstein time distribution is shown as solid line. The halo-bulge distributions have been evaluated for a Macho mass of $M_0 = 0.1 M_\odot$ (dotted line) and $M_0 = 0.5 M_\odot$ (dot-dashed line). The halo-disk lensing case is shown for a Macho mass of $M_0 = 0.1 M_\odot$ (dashed line). The Einstein-time distributions of the event rate differ considerably for halo-disk, halo-bulge and bulge-bulge lensing and also vary significantly with the line of sight position. For comparison we also plot the Einstein time scale distribution for M31 halo-lensing derived by Han & Gould (1996a) up to a pre-factor (that we chose equal to $3 \cdot 10^{-6}$) as a black solid curve. Han & Gould (1996a) considered the distributions for the halo-disk and halo-bulge lensing to be similar and not distinguish between them further. They used a Macho mass of $M_0 = 0.1 M_\odot$ for their curve. However, it looks more similar to our halo-bulge curve for $M_0 = 0.5 M_\odot$, and can not be moved on the halo-bulge or halo-disk for $M_0 = 0.1 M_\odot$ curve with another choice of the pre-factor.

which equals the result of Alcock *et al.* (1995a)[6]. The line of sight distance-averaged event rate per Einstein time t_E is given by

$$\left\langle \frac{d\Gamma_T}{dt_E} \right\rangle_s = \int p_s(D_S) \frac{d\Gamma_T}{dt_E} \, dD_S \quad . \tag{4.43}$$

 Figure 4.4 shows examples of this line of sight distance-averaged distribution $\left\langle \frac{d\Gamma_T}{dt_E} \right\rangle_s$ at $(x,y) = (1,0)$ arcmin and $(x,y) = (4.46, 4.46)$ arcmin $(= (1,1)$ kpc$)$ in the intrinsic M31 coordinate system. The distributions show a strong dependence on the line of sight position with the halo-bulge and halo-disk lensing time scales being longer than those of bulge-bulge lensing. An increase in Macho-mass decreases the event rate and the time scale of the events becomes longer (see the examples for $M_0 = 0.1 M_\odot$ and $M_0 = 0.5 M_\odot$ in Fig. 4.4).

---

[6]Their Eq. 2 with $\hat{t} \equiv 2t_E$.

4.6 Applications for the pixellensing regime

The microlensing parameters (F_0, t_E, and u_0) are not directly observable anymore in crowded or un-resolved stellar fields. In that case, the two measurable quantities are the full-width time scale t_{fwhm}, and the difference flux ΔF of an event. We now make use of the luminosity function $\Phi(\mathscr{M})$, and the source number density $n_s(x, y, D_S)$ of the source stars introduced in Sect. 4.4, and derive the event rate distribution function $\frac{d^2\Gamma}{dt_{fwhm}\,d\Delta F}$. This quantity can then be linked to the measured distributions most straightforwardly.

In the first subsection (Sect. 4.6.1) we derive the required distributions neglecting finite source effects. However, the high magnifications needed to boost main sequence stars to large flux excesses go in parallel with finite source effects which make these large flux excesses hardly possible. We show this in detail in Sect. 4.6.2 where we incorporate finite source effects in the calculations.

4.6.1 Changing variables of Γ to t_{fwhm} and ΔF

Event rate per star with absolute magnitude $\mathscr{M}$

We first obtain the event rate per full-width-half-maximum time $t_{fwhm}(t_E, u_0) = t_E\, w(u_0)$. Replacing t_E in Eq. 4.40 using the derivative $\left|\frac{dt_E}{dt_{fwhm}}\right| = w(u_0)^{-1}$ yields

$$\frac{d^2\Gamma}{dt_{fwhm}\,du_0} = \frac{2\,w^2(u_0)}{t_{fwhm}^3}\int_0^\infty \xi(M)\int_0^{D_S}\rho(D_L)\,p_{v_t}\left(\frac{R_E}{t_{fwhm}}w(u_0)\right)R_E^3\,dD_L\,dM \quad . \tag{4.44}$$

Note, that one can use $w(u_0) \approx \sqrt{12}\,u_0$ as high magnification approximation. Replacing the relative impact parameter u_0 by the maximum amplification A_0 (using Eqs. 4.7 and 4.8) yields an equivalent description of this result:

$$\frac{d^2\Gamma}{dt_{fwhm}\,dA_0} = \frac{2\Psi(A_0)}{t_{fwhm}^3}\int_0^\infty \xi(M)\int_0^{D_S}\rho(D_L)\,p_{v_t}\left(\frac{R_E}{t_{fwhm}}\Upsilon(A_0)\right)R_E^3\,dD_L\,dM \quad , \tag{4.45}$$

with $R_E(M, D_L, D_S)$, and $\Psi(A_0)$ being defined as

$$\Psi(A_0) := \left|\frac{du_0}{dA_0}\right|\Upsilon^2(A_0) \stackrel{A_0 \gg 1}{\approx} \frac{12}{A_0^4} \quad . \tag{4.46}$$

The derivative $\left|\frac{du_0}{dA_0}\right|$ was already defined in Eq. 4.8. We now insert $\Delta F(F_0, A_0) = F_0(A_0 - 1)$ by using $\left|\frac{dA_0}{d\Delta F}\right| = F_0^{-1}$ and obtain the event rate per full-width-half-maximum time, per flux excess, per lens mass and per source star with an absolute magnitude $\mathscr{M}$:

$$\frac{d^4\Gamma}{dt_{fwhm}\,d\Delta F\,dM\,d\mathscr{M}} = \frac{2}{t_{fwhm}^3}\Phi(\mathscr{M})\,\xi(M)\frac{\Psi}{F_0}\int_0^{D_S}\rho(D_L)\,R_E^3\,p_{v_t}\left(\frac{R_E}{t_{fwhm}}\Upsilon\right)dD_L \quad , \tag{4.47}$$

with the luminosity function in magnitudes $\Phi(\mathscr{M})$ and the conversion from absolute magnitudes to intrinsic source fluxes $F_0(\mathscr{M}, D_S)$. The dependences are given by $R_E(M, D_L, D_S)$, $A_0(F_0, \Delta F)$,

$t_{\text{fwhm}}(v_t, R_E, b)$, $\Psi[A_0(F_0, \Delta F)]$, and $\Upsilon[A_0(F_0, \Delta F)]$. Equation 4.47 is the transformation of Eq. 4.26 to the observables relevant in the pixellensing regime. It gives the event rate per star with absolute magnitude $\mathcal{M}$ and will be converted to the event rate per area using the density of stars below. For the special case of highly amplified events, $(A_0 \gg 1)$, the approximations $\Psi \approx 12 \frac{F_0{}^4}{\Delta F^4}$ and $\Upsilon \approx \sqrt{12} \frac{F_0}{\Delta F}$ can be inserted into Eq. 4.47.

Event rate per area

All previously derived event rates are per star, or per star with a given absolute magnitude $\mathcal{M}$. Observed, however, are event rates per area. These are obtained from the source density distribution along the line of sight $n_s(x, y, D_S)$ and Eq. 4.47:

$$\frac{d^6 \Gamma_{s,l}}{dx\,dy\,dt_{\text{fwhm}}\,d\Delta F\,d\text{M}\,d\mathcal{M}} = \frac{2\,\Phi_s(\mathcal{M})\,\xi_l(\text{M})}{t_{\text{fwhm}}{}^3} \int\limits_0^\infty n_s(x,y,D_S)\,\frac{\Psi}{F_0} \int\limits_0^{D_S} \rho_l(D_L)\,R_E{}^3\,p_{v_t}\!\left(\frac{R_E \Upsilon}{t_{\text{fwhm}}}, v_0\right) dD_L\,dD_S \quad, \quad (4.48)$$

where the quantities in the integral have the following functional dependences $F_0(\mathcal{M}, D_S)$, $\rho_l(x, y, D_L)$, $R_E(D_L, \text{M}, D_S)$, $\Psi(A_0(F_0, \Delta F))$, $\Upsilon(A_0(F_0, \Delta F))$, and $v_0(x, y, D_L, D_S)$. Equation 4.48 is the event rate per interval of lens plane area, full-width-half-maximum time, flux excess, lens mass and absolute magnitude of the lensed star. For highly amplified events one can replace Ψ and Υ in the integral by $12 \frac{F_0{}^4}{\Delta F^4}$ and $\sqrt{12} \frac{F_0}{\Delta F}$, respectively. Different lens (disk, bulge, or halo) and source (disk or bulge) populations are characterized by an index l and s in Eq. 4.48. For the total event rate Γ_{tot} one has to sum up the contributions of all lens-source configurations:

$$\frac{d^6 \Gamma_{\text{tot}}}{dx\,dy\,dt_{\text{fwhm}}\,d\Delta F\,d\text{M}\,d\mathcal{M}} := \sum_s \sum_l \frac{d^6 \Gamma_{s,l}}{dx\,dy\,dt_{\text{fwhm}}\,d\Delta F\,d\text{M}\,d\mathcal{M}} \quad . \quad (4.49)$$

The event rate per area is then obtained by multiplying Eq. 4.49 with the efficiency $\varepsilon(x, y, \Delta F, t_{\text{fwhm}})$ of the experiment and integrating over all lens masses, source magnitudes, time scales and flux excess values.

4.6.2   Event rate taking into account finite source effects

As described in Sect. 4.2.1 the point-source approximation is no longer valid, if the impact parameter u_0 is smaller than u_{fs}, i.e. half the source radius projected onto the lens plane (Eq. 4.14). In this case, the maximum amplification and thus the flux excess stays below the value for the point source approximation, and time scales of events are enlarged (see Eqs. 4.15 and 4.18). Baltz & Silk (2000) already accounted for the upper limit in magnification and obtained the correct value for the total number of events (i.e. events with and without finite source signatures) as a function of magnification threshold. Their approximation however is limited to high amplifications and ignores the change of magnification and event time scale[7]. Thus the flux excess and time scale distributions of the events are not predicted accurately. As finite source effects are likely already for small maximal magnifications and the change in time scale due to finite source effects can be large, we derive precise relations, and account for the finite source sizes as follows:

---

[7]Baltz & Silk (2000) Eq. 26 with Eq. 20 and Eq. 22 writes in our notation as

$$\frac{d\Gamma}{dt_{\text{fwhm}}} = \frac{D_S}{\text{M}_0} \int\limits_{-\infty}^\infty \Phi(\mathcal{M}) \int\limits_0^1 \theta\!\left(\left(1 + \frac{R_s^2 c^2}{16GMD_S u_T^2}\right)^{-1} - \frac{D_L}{D_S}\right) \rho(D_L) \int\limits_0^\infty \theta\!\left(2\frac{R_E}{t_{\text{fwhm}}}\sqrt{12}u_T - v_t\right) v_t{}^2 \, p_{v_t}(v_t)$$
$$\left\{w'\left[w^{-1}\!\left(\frac{t_{\text{fwhm}}v_t}{2R_E}\right)\right]\right\}^{-1} dv_t \, d\!\left(\frac{D_L}{D_S}\right) d\mathcal{M} \quad .$$

- Events with $u_0 > u_{fs}$, i.e. those for which the finite source sizes are irrelevant, are treated as before, i.e. we redo all calculations starting from Eq. 4.25. If the impact parameter b is involved in an integral we multiply the integrand with $\theta(b - R_E u_{fs})$. The step function allows only contributions in the integrand, if $b \geq R_E u_{fs}$ holds. To see how this transports into the dD_L-integration if the variables are changed from (b, v_t) to $(t_{fwhm}, \Delta F)$ in the Eqs. 4.47 and 4.48 we use

$$\theta(b - R_E u_{fs}) = \theta\left(A_0^{fs} - A_0\right) \approx \theta\left(\frac{D_S}{1 + \frac{c^2 R_*^2 \left(\frac{\Delta F}{F_0}\right)^2}{16 G M D_S}} - D_L\right) \quad . \tag{4.50}$$

Multiplying the integrand of Eqs. 4.47 and 4.48 with Eq. 4.50 extracts only those light curves, where finite-source effects can be neglected.

- For events where the finite source sizes are relevant, i.e. events with $u_0 < u_{fs}$, we use the approximations for the maximum amplification and the full-width-half-maximum time given in Eqs. 4.16 and 4.18. This means that we just replace the relation of the impact parameter and the maximum magnification, and the fwhm-time scale relation of events by Eq. 4.15 and Eq. 4.18 when switching from the point source to the finite source regime. We then can derive the equations for the event rates with finite source effects from Eq. 4.26 analogously to the point source approximation, but this time with a step function of $\theta(R_E u_{fs} - b)$ in the integrands allowing only small impact parameters.

With $A_0^{fs}(D_L, D_S, R_*, M)$, $u_{fs}(D_L, D_S, R_*, M)$, $v_t = \frac{R_E}{t_{fwhm}} \Upsilon^{fs}(A_0^{fs}, u_0)$, and $\left|\frac{dt_{fwhm}(v_t)}{dv_t}\right| = \frac{R_E}{v_t^2} \Upsilon^{fs}$ we obtain:

$$
\begin{aligned}
\frac{d^6 \Gamma_{s,l}}{dx\,dy\,dt_{fwhm}\,d\Delta F\,dM\,d\mathcal{M}} &= \\
&= \int_0^\infty n_s\, 2\,\Phi_s(\mathcal{M}) \int_0^{D_S} \rho(D_L)\,\xi(M)\,\delta\left(\Delta F - F_0(A_0^{fs} - 1)\right) \int_0^{R_E u_{fs}} p_{v_t}\left(\frac{R_E}{t_{fwhm}} \Upsilon^{fs}\right) \frac{R_E^2 \Upsilon^{fs\,2}}{t_{fwhm}^3}\, db\, dD_L\, dD_S \\
&= \int_0^\infty n_s(x,y,D_S) \frac{2}{t_{fwhm}^3}\, \Phi_s(\mathcal{M})\,\xi(M)\,\rho(D_L) \left|\frac{dD_L(\Delta F, D_S)}{d\Delta F}\right| R_E^3 \int_0^{u_{fs}} p_{v_t}\left(\frac{R_E}{t_{fwhm}} \Upsilon^{fs}\right) \Upsilon^{fs\,2}\, du_0\, dD_S \quad ,
\end{aligned}
\tag{4.51}
$$

where we are using the following relations:

$$D_L(\Delta F, D_S) \approx D_S \left(1 + \frac{\Delta F^2}{C_{D_L} D_S}\right)^{-1} \quad ,$$

$$\left|\frac{dD_L(\Delta F, D_S)}{d\Delta F}\right| \approx 2 C_{D_L} D_S^2 \Delta F \left(C_{D_L} D_S + \Delta F^2\right)^{-2} \quad ,$$

$$C_{D_L} := \frac{16 F_0^2 G M}{c^2 R_*^2} \left[\text{flux}^2 \text{length}^{-1}\right] \quad .$$

Figure 4.5 shows contours of the event rate per t_{fwhm} time scale and flux excess, per year and square arcminute, with finite source effects taken into account. For the calculations we used the values for the source radius, luminosity and color-relations $R_*(\mathcal{M}, \mathcal{C})$ presented in chapter 3, Sects. 3.2 and 3.3. The event rates were derived for a position at $(x, y) = (1, 0)$ arcmin in the intrinsic M31 coordinate system, equivalent to a disk major axis distance of 1 arcmin. The upper panels show the distribution
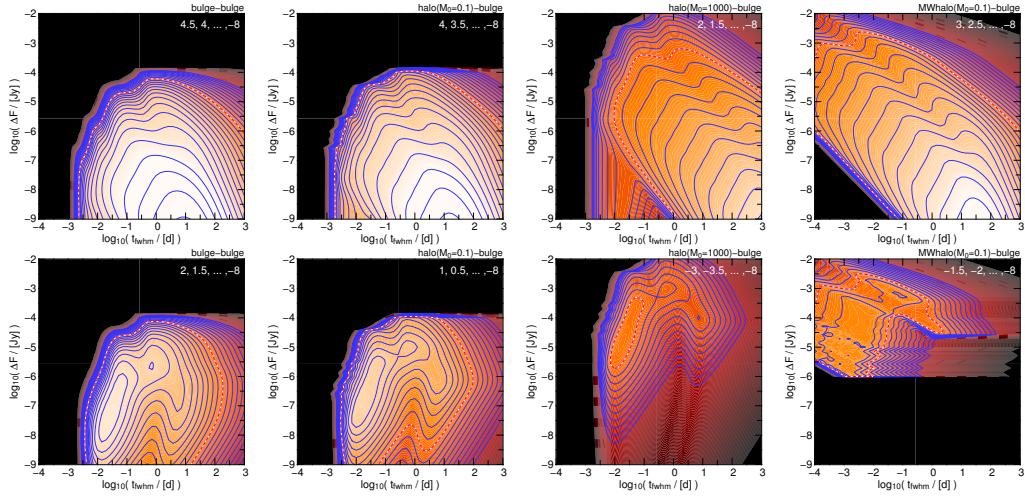
Figure 4.5: $\frac{d^2\Gamma}{d\log t_{\mathrm{fwhm}}\, d\log \Delta F}$ [$\mathrm{arcmin}^{-2}\,\mathrm{y}^{-1}$] at $(x,y) = (1,0)\,\mathrm{arcmin}$ in the $\log(\Delta F)$-$\log(t_{\mathrm{fwhm}})$ plane, for bulge-bulge (left), halo-bulge lensing with $0.1\mathrm{M}_\odot$-Machos (middle left), halo-bulge lensing with $1000\mathrm{M}_\odot$-Machos (middle right), and halo-bulge lensing with $0.1\mathrm{M}_\odot$-Machos residing in the MW halo (right). The upper panels shows the distribution for light curves not affected by the finite source sizes. The contours have been obtained from inserting Eq. 4.48 into Eq. 4.50 and carrying out the mass and source luminosity integral. The lower panels shows the distribution for light curves with finite source signatures (mass and source star luminosity integral of Eq. 4.51). The contour levels can be read off from the inserts in each diagram. The dashed line marks the $10^{-3}\,\mathrm{arcmin}^{-2}\,\mathrm{y}^{-1}$ level, areas with brighter colors correspond to higher contour values. Taking into account the finite source sizes implies an upper limit for ΔF and a lower limit for t_{fwhm} for all light curves, i.e. for light curves with and with out finite source signatures (see text). For the source-lens configurations shown here there are no lensing light curves with an excess fluxes $\Delta F > 5 \cdot 10^{-4}\,\mathrm{Jy}$.

for light curves showing no finite source effects (Eq. 4.48 with Eq. 4.50), whereas the lower panels show the distribution obtained from the mass and source luminosity integration of Eq. 4.51, i.e. for light curves affected by finite source effects.

The black areas indicate the event parameter space which is not available to source stars once their real sizes are taken into account: as finite source effects mainly occur at large amplifications, large ΔF and small t_{fwhm} values are suppressed. Events in the point source approximation, which fall into the black areas in the upper panels of Fig. 4.5 end up with longer time scales and lower excess fluxes if the sources sizes are taken into account.

The sharp cutoff at large flux excesses arises, since there is an upper limit in ΔF depending on source luminosity and size, and since the luminosity function of the stars has a steep cutoff at giant luminosities of $\mathcal{M}_R = -0.83\,\mathrm{mag}$ (bulge) and $\mathcal{M}_R = -2.23\,\mathrm{mag}$ (disk).

The maxima with vertical contours for finite source effects in the lower panels come from shifting events, for which the point source approximation 'just' fails, to longer times scales, see Eq. 4.18. Light curves with finite source effects have (depending on their flux excesses) most likely fwhm time scales of about 0.01 days, or 15 minutes. The sources lensed with that time scales are main sequence stars. The secondary maxima around 1 day and flux excesses of $5 \cdot 10^{-6} - 2 \cdot 10^{-5}\,\mathrm{Jy}$ for bulge-bulge and $0.1\mathrm{M}_\odot$ halo-bulge lensing, and of about $10^{-3}\,\mathrm{Jy}$ for $1000\mathrm{M}_\odot$ halo-bulge lensing, is due to lensing

of post main sequence stars.

As Fig. 4.5 shows, an increase in Macho mass dramatically reduces the event rate and increases the event time scales. This explains the shift in the contours towards longer time scales and the decrease in the contour levels. For larger Macho masses, Einstein radii do increase, and one expects finite source effects to become less important. The largest possible flux excess $\Delta F_{\max}$ for the lensing events indeed increases; the size of the shift is as expected, since the maximum flux excess is proportional to the square root of the Macho mass. The contours in the last row of Fig. 4.5 show MW-halo lensing with $0.1M_\odot$-Machos. Finite source effects are unimportant. According to Figure 4.5 lensing events above the maximum flux excess predicted for self lensing would be a clear hint for either massive Machos in M31 or Machos with unconstrained masses in the Milky Way.

4.7 Application to experiments: Total event rates

We now apply our results from Sects. 4.5 and 4.6 to difference imaging surveys. The goal of this section is to predict realistic event rates that take into account observational constraints like the time scales of events and the signal-to-noise ratios of the light curves, e.g. at maximum. These event rates can be taken for survey preparations or for a first order comparison of survey results with theoretical models. Exact survey predictions and quantitative comparisons with models can be obtained with numerical simulations of the survey efficiency.

4.7.1 Peak-threshold for event detection

In order to identify a variable object at position (x,y), its excess flux ΔF has to exceed the noise, i.e. rms-flux $\sigma_F(x,y)$ by a certain factor Q

$$\Delta F_{\min}(x,y) = Q \cdot \sigma_F(x,y) \quad . \tag{4.52}$$

The parameter Q characterizes the significance of the amplitude of a lensing event, but not of the event itself, since that also depends on the time-scale (and the sampling) of the event. Considering the maximum flux excess of an event only and neglecting its time scale will lead to an over-prediction of lensing events, as some events might be too fast to be detected.

The flux excess threshold that a source with intrinsic flux $F_0(\mathcal{M}, D_S, \text{ext}_s)$ must achieve in order to be identified as an event can be translated to thresholds in maximum magnification and relative impact parameter using Eqs. 4.1 and 4.7,

$$A_T(x,y,F_0(\mathcal{M},D_S,\text{ext}_s)) := \Delta F_{\min}(x,y) F_0^{-1} + 1 \approx \Delta F_{\min}(x,y) F_0^{-1} \quad , \tag{4.53}$$

$$u_T(x,y,F_0(\mathcal{M},D_S,\text{ext}_s)) \approx \frac{1}{A_T} \quad ; \tag{4.54}$$

in both cases we have also given the high magnification approximations in the last step. In contrast to the microlensing regime (where u_T is assumed to be constant), u_T depends on the local noise value via $\Delta F_{\min}(x,y)$ and the luminosity $\mathcal{M}$ of the source star being lensed. In Fig. 4.6 we show contours of the minimum magnification required to observe an event at a distance of $D_S = 770\,\text{kpc}$, assuming a source luminosity of $\mathcal{M}_R = 0\,\text{mag}$ and requiring a signal-to-noise threshold of $Q = 10$ for a survey like WeCAPP in the R-band. Since the M31 surface brightness and thus also the rms-photon-noise
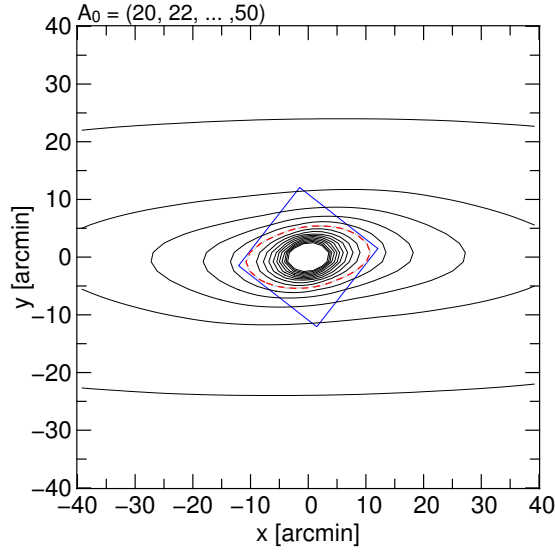
Figure 4.6: The contours in this figure show the minimum magnifications A_T needed for stars of a luminosity $\mathscr{M}_R = 0\,$mag at a distance of $D_S = 770\,$kpc to exceed the M31 rms-flux by a factor of $Q = \left(\frac{S}{N}\right) = 10$. We assumed an experimental setup as given in the WeCAPP survey (see Table 4.1). The contour levels are $A_T = 17, 18, ..., 32$. The dashed line marks the $A_T = 25$ level, the square shows the field observed by WeCAPP given in the intrinsic M31 coordinate system.

increases towards the center, magnifications of 50 or larger are needed in the central part. The M31 rms-photon noise and rms-flux within a PSF in the R-band had been estimated using Eqs. 4.56 and 4.57 below.

To obtain an upper limit for the event rate, we assume that all events with flux excesses above the peak-threshold can be identified, irrespective of their time scales. Ignoring the event time scales in analytical estimates, the event rate predictions are much more alike the upper limit we present here (Eq. 4.55). In this case one can simply use the transformation from minimum flux excess at maximum magnification to the threshold relative impact parameter u_T in Eqs. 4.53 and 4.54. We integrate Eq. 4.27 over lens mass, lens distance, relative velocities, multiply it with the relative impact parameter threshold $u_T(x, y, F_0(\mathscr{M}, D_S, \text{ext}_s))$ and the number density of sources with brightness $\mathscr{M}$ $(n_s(x, y, D_S) \, \Phi_s(\mathscr{M}))$, and finally integrate along the line of sight and over all source luminosities:

$$
\begin{aligned}
\frac{d^2\Gamma_{s,l}}{dx\,dy} &= \int\limits_0^\infty\int\limits_0^\infty n_s \, \Phi_s(\mathscr{M}) \int\limits_0^\infty\int\limits_0^{D_S}\int\limits_0^\infty \int\limits_0^{u_T(x,y,F_0(\mathscr{M},D_S,\text{ext}_s))R_E} \frac{d^4\Gamma}{dD_L\,d\mathrm{M}\,dv_t\,db}\, db\,dv_t\,d\mathrm{M}\,dD_L\,d\mathscr{M}\,dD_S \\
&= \int\limits_0^\infty\int\limits_0^\infty n_s(x,y,D_S)\,\Phi_s(\mathscr{M})\,u_T(x,y,F_0(\mathscr{M},D_S,\text{ext}_s))\,\Gamma_{1,l}(D_S)\,d\mathscr{M}\,dD_S \quad .
\end{aligned}
\tag{4.55}
$$

In this equation, the subscript 's' indicates the different stellar populations (bulge and disk). Their sum yields an upper limit for the total event rate, which can therefore also be obtained as a product of the single star event rate $\Gamma_{1,l}$ (Eq. 4.39, using $u_T(x, y, F_0(\mathscr{M}, D_S, \text{ext}_s))$) and the number density of sources with luminosity $\mathscr{M}$ on the line of sight. Equation 4.55 is similar to the equations given in

	WeCAPP
t_{exp} [sec]	500
l_{pixel} [″]	0.5
field of view [px]	2048 x 2048
field of view [']	17.2 x 17.2
filter	Johnson R
FWHM of the PSF [″]	1.5
Ω_{PSF} [□″]	5.1
AM	1.0
Δt [d]	200
$t_{\text{fwhm}}^{\text{min}}$ [d]	1
$t_{\text{fwhm}}^{\text{max}}$ [d]	200
inner saturation radius [″]	20
CCD orientation angle	45°

Table 4.1: Observational setup for the WeCAPP survey.

Han (1996) (Eq. 2.5) and Han & Gould (1996a) (Eq. 2.2.1)[8].

We have shown in Riffeser *et al.* (2001), that using our reduction pipeline (that propagates true errors through all reduction steps) errors in the light curves are dominated by the photon-noise contribution of the background light. Therefore the typical error can be estimated from the surface brightness profile $\text{SB}(x,y)$ of M31 and the typical, i.e. median, observing conditions of the survey. Using analytically predicted rms-values, one can study the impact of the observing conditions on event rates and optimize survey strategies. The variability of objects is measured by (psf-)photometry inside the angular area of the PSF $\Omega_{\text{PSF}} := \pi\,\text{FWHM}/\ln 4$, where FWHM is the full-width-half-maximum of the PSF. For a given experimental setup the rms photon noise $\sigma_{\text{photon}}(x,y)$ within an area Ω_{PSF} [arcsec^2] at a position (x,y) is given by

$$\sigma_{\text{photon}}(x,y) := \left[\left(10^{-0.4(\text{SB}(x,y)+\kappa\,\text{AM})} + 10^{-0.4\,m_{\text{sky}}}\right) 10^{-0.4(-\text{ZP})}\, t_{\text{exp}}\,\Omega_{\text{PSF}}\right]^{1/2} \quad , \qquad (4.56)$$

where m_{sky} [mag arcsec^{-2}] is the sky surface brightness, t_{exp} is the exposure time in [sec], AM is the airmass of the observation, ZP is the photometric zero-point of the telescope-camera configuration in [photons/sec] and κ is the atmospheric extinction for the observing site.[9]

The photon noise can be translated to physical units using the flux of Vega, $\mathscr{F}_{\text{Vega}}$, and its magnitude $m_{\text{Vega}} = 0$

$$\begin{aligned}
\sigma_F(x,y) &:= \frac{\mathscr{F}_{\text{Vega}}}{t_{\text{exp}}\, 10^{-0.4(m_{\text{Vega}}+\kappa\,\text{AM}-\text{ZP})}}\, \sigma_{\text{photon}} \\
&= \mathscr{F}_{\text{Vega}}\left[\left(10^{-0.4(\text{SB}(x,y)+\kappa\,\text{AM})} + 10^{-0.4\,m_{\text{sky}}}\right) 10^{0.8\,\kappa\,\text{AM}}\, 10^{-0.4\,\text{ZP}}\, \frac{\Omega_{\text{PSF}}}{t_{\text{exp}}}\right]^{1/2} .
\end{aligned} \qquad (4.57)$$

The last equation shows, that the rms-flux within an aperture is proportional to $1/\sqrt{t_{\text{exp}}}$, making

---

[8]With $\beta_{\max}(F_{0,i}) \equiv u_{\text{T}}$, $\Gamma_0 \equiv \Gamma_{1,l}(D_{\text{S}})$, $\frac{\Sigma}{\sum_i \phi(F_{0,i})F_{0,i}} \equiv \int_0^\infty n_{\text{s}}\, dD_{\text{S}}$.

[9]We have neglected readout-noise of the detector because it is negligible compared to the photon noise.

the signal-to-noise Q proportional to $\sqrt{t_{\mathrm{exp}}}$, as expected for background noise limited photometry of point-like objects.

The extincted surface brightness profile $\mathrm{SB}(x,y)$ in Eqs. 4.56 and 4.57 can be taken either from very high signal to noise measurements of M31 or from analytical models, that are constructed to match the observed SB-profile and the dynamics of M31 (see chapter 3). In the latter case, the extincted surface brightness $\mathrm{SB}(x,y)$-model combines the luminous matter density $\rho_\mathrm{s}(x,y,D_\mathrm{S})$ with the mass-to-light ratio for each source components ($s=$bulge,disk) and accounts for galactic and intrinsic extinction $\mathrm{ext}_\mathrm{s}(x,y,D_\mathrm{S})$ along the line of sight:

$$\mathrm{SB}(x,y) = -2.5\log\left(\mathscr{F}_{\mathrm{Vega}}{}^{-1}\sum_\mathrm{s}\int_0^\infty 10^{-0.4\,\mathrm{ext}_\mathrm{s}(x,y,D_\mathrm{S})}\frac{\rho_\mathrm{s}(x,y,D_\mathrm{S})}{\left(\frac{M}{L}\right)_\mathrm{s}\frac{\mathrm{M}_\odot}{\mathscr{F}_\odot}}\left(\frac{10\mathrm{pc}}{D_\mathrm{S}}\right)^2\left(\frac{2\pi}{360\cdot3600}\right)^2 D_\mathrm{S}{}^2\,dD_\mathrm{S}\right)\quad,$$
(4.58)

where the units are $\left[\mathrm{mag\,arcsec}^{-2}\right]$.

4.7.2   Total event rate with excess flux threshold $\Delta F_{\min}$ and time-scale $t_{\mathrm{fwhm}}^{\min}$-threshold

The upper limit derived in Sect. 4.7.1 still includes numerous events which can not be detected in finite time resolution experiments. At this point, where not only the flux-excess (maximum magnification or relative impact parameter) of the event have to be considered, but also the time scale of the event, the transformation of the event rate from the 'theoretical quantities' to the 'observational quantities' in Sect. 4.6 becomes most relevant. Using Eq. 4.48 we can simply integrate from the lower limits $\Delta F_{\min}$ and $t_{\mathrm{fwhm}}^{\min}$ to infinity (or any other value specified by the experiment):

$$\frac{d^2\Gamma_{l,s}}{dx\,dy} := \int_{t_{\mathrm{fwhm}}^{\min}(x,y)}^\infty\int_{\Delta F_{\min}(t_{\mathrm{fwhm}},x,y)}^\infty \frac{d^4\Gamma_{s,l}}{dx\,dy\,dt_{\mathrm{fwhm}}\,d\Delta F}\,d\Delta F\,dt_{\mathrm{fwhm}}\quad,$$
(4.59)

with

$$\frac{d^4\Gamma_{s,l}}{dx\,dy\,dt_{\mathrm{fwhm}}\,d\Delta F} := \int\int \frac{d^6\Gamma_{s,l}}{dx\,dy\,dt_{\mathrm{fwhm}}\,d\Delta F\,d\mathrm{M}\,d\mathscr{M}}\,d\mathrm{M}\,d\mathscr{M}\quad.$$
(4.60)

The thresholds $t_{\mathrm{fwhm}}^{\min}(x,y)$ and $\Delta F_{\min}(t_{\mathrm{fwhm}},x,y)$ (see Eq. 4.52) are set by the experiment and the detection process. Table 4.2 summarizes the event rate predictions for the WeCAPP experiment towards the bulge of M31, using different realistic thresholds for the signal-to-noise threshold necessary to derive 'secure' events, and for $t_{\mathrm{fwhm}}^{\min}$. These numbers do not take into account that events can not be observed when M31 is not visible (one third of the year), or that in the remaining time some – in particular short term events – escape detections because of observing gaps. Furthermore we do neglect that some of the area is not accessible for identification of lensing events due to intrinsically variable objects. We calculated the predictions for signal-to-noise thresholds of $Q = 10$ and $Q = 6$; these thresholds correspond to flux excess thresholds of $6.2\cdot10^{-6}\,\mathrm{Jy}$ (Q=10) and $3.7\cdot10^{-6}\,\mathrm{Jy}$ (Q=6) in the edges of the WeCAPP field. The corresponding values at a position $20''$ off center (i.e. just outside saturation of the reference image, see chapter 2) of the WeCAPP-field are $2.4\cdot10^{-5}\,\mathrm{Jy}$ (Q=10) and $1.5\cdot10^{-5}\,\mathrm{Jy}$ (Q=6). The $Q > 10$ events are events like those been published in the past (e.g., WeCAPP-GL1 and WeCAPP-GL2) with values of $Q \approx 85$ and $Q \approx 16$), whereas $Q = 6$ should be more similar to the medium bright event candidates as published by the MEGA survey. For the $Q = 10$ cases we have separated events that do not show finite source effects in the light curves ('without fs') from those
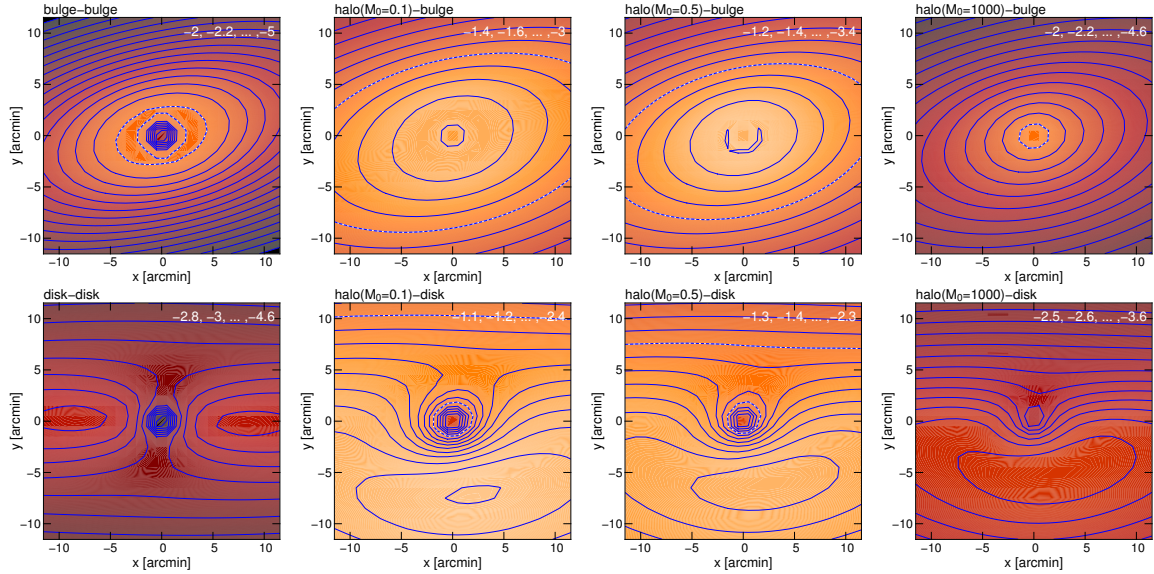
Figure 4.7: Event rate maps in logarithmic units (in units of events per year and square arcmin) for the WeCAPP survey for $Q = 10$ and $t_{\text{fwhm}}^{\min} = 1\,\text{d}$ (column I of Table 4.2). Coordinates are given in the intrinsic M31 coordinate system. The contour levels are shown in inserts in the upper right corners of each diagram. The dashed line marks the $0.01\,\text{event}\,\text{y}^{-1}\,\text{arcmin}^{-2}$ level in each diagram. The event rate decreases near the center of M31 due to higher noise combined with finite source effects. For the calculations we have taken into account the finite stellar source sizes; the numbers shown, however, include only those among all events which do not show finite source signatures in their light curves, i.e. those which are usually searched for in lensing experiments.

which show finite source effects ('with fs'). Finite source events are relatively more important for high signal to noise, short time scale self-lensing events.

For the $Q = 6$, $t_{\text{fwhm}} = 2\,\text{d}$ case we split the predictions into the near and far side of M31. Within our field, the predicted halo-bulge asymmetry is small, but the bulge-disk and halo-disk asymmetry are on a noticeable level. The disk-bulge lensing does show the reversed asymmetry. It has been pointed out in the past (An *et al.*, 2004) that dust lanes in the M31 disk are an additional source of asymmetry. This is obvious if one considers the spatial distributions of variables found in pixellensing experiments (see An *et al.* 2004, Ansari *et al.* 2004 and Fliri *et al.* 2006), which can, however, be used to quantitatively account for extinction, in addition to extinction maps. The values given in Table 4.2 do not account for the small spatial dependence of extinction, and thus place a lower limit to the observed far-near-asymmetry of the individual lens-source configuration. In the last line we add the analogous numbers for halo lensing resulting from Milky Way halo lenses of $0.1\,\text{M}_\odot$. The Macho events caused by the MW Machos should be roughly a third of that caused by M31 Machos.

Figure 4.7 shows the predictions for the spatial distribution of the lensing events for the WeCAPP survey, evaluated for the $Q = 10$ and $t_{\text{fwhm}} = 1\,\text{d}$ thresholds (column I in Table 4.2). One can see, that the event rate density becomes maximal close to the M31 center for bulge-bulge and halo-bulge lensing configurations. As it can also be seen in Table 4.2, a far to near side asymmetry (lower and upper part in the figure) is not present for bulge-bulge lensing, is modest for halo-bulge lensing, and stronger for the disk-bulge lensing. This is because, the disk effectively cuts the bulge in one part in

	I	II		III
Q	10	6		6
$t_{\text{fwhm}}^{\min}$ [d]	1	2		20
		near side	far side	
b-b	1.2 + 1.9	1.4 + 0.98	1.4 + 0.99	0.026 + 0.0062
h0.1-b	8.2 + 5.4	6.3 + 1.6	7.1 + 1.9	0.16 + 0.0094
h0.5-b	7.4 + 2.7	5.5 + 0.72	6.3 + 0.82	0.47 + 0.0074
h1000-b	0.7 + 0.0013	0.51 + 0.00051	0.59 + 0.00056	0.6 + $5 \cdot 10^{-5}$
d-b	0.57 + 0.34	0.89 + 0.16	0.087 + 0.026	0.0072 + 0.00031
h_{MW}0.1-b	3.9 + 0.0046	2.7 + 0.001	2.7 + 0.001	0.088 + $5 \cdot 10^{-6}$
h_{MW}0.5-b	2.4 + 0.0009	1.8 + 0.0001	1.8 + 0.0001	0.23 + $3 \cdot 10^{-7}$
b-d	2.3 + 1.6	0.43 + 0.22	3.8 + 1.3	0.082 + 0.0055
h0.1-d	11 + 4.3	4.9 + 0.72	12 + 2	0.5 + 0.014
h0.5-d	8.6 + 1.2	3.6 + 0.21	9.5 + 0.55	1 + 0.011
h1000-d	0.61 + 0.00015	0.26 + $5 \cdot 10^{-5}$	0.7 + $9 \cdot 10^{-5}$	0.55 + $2 \cdot 10^{-5}$
d-d	0.2 + 0.13	0.2 + 0.056	0.19 + 0.056	0.036 + 0.0055
h_{MW}0.1-d	3.1 + 0.0019	2.2 + 0.00025	2.2 + 0.00024	0.3 + $7 \cdot 10^{-7}$
h_{MW}0.5-d	1.9 + 0.00022	1.4 + $7 \cdot 10^{-5}$	1.4 + $7 \cdot 10^{-5}$	0.43 + $5 \cdot 10^{-7}$

Table 4.2: Total event rate $\Gamma_{s,l}$ [y^{-1}] for the WeCAPP experiment for self-lensing and halo-lensing: d - disk, b - bulge, h0.1 - halo consisting of 0.1 M$_\odot$ lenses, h0.5 - halo consisting of 0.5 M$_\odot$ lenses h1000 - halo consisting of 1000 M$_\odot$ lenses (h$_{\text{MW}}$ for MW-halo). The numbers give the event rate in events per year integrated over the observed field and applying the following peak-flux signal-to-noise thresholds: I) $Q = 10$ and $t_{\text{fwhm}}^{\min} = 1$ d, II) $Q = 6$ and $t_{\text{fwhm}}^{\min} = 2$ d for the near and far side, III) $Q = 6$ and $t_{\text{fwhm}}^{\min} = 20$ d. These $\left(\frac{S}{N}\right)$-limits (at the light curve peak) are more realistic than a flux threshold $\Delta F_{\min}$ which is constant over the observed field, since the central region shows a strong gradient in the surface brightness and photon noise values. We have also separated events that do not show finite source effects in the light curves from those with finite source effects by a plus sign. Note that light curves with finite source effect signatures might be missed when using event filters with a classical lensing event shape in a stringent way. For the ($Q = 6$, $t_{\text{fwhm}} = 2$)-case we split the predictions in those for the near and far side of the M31 (disk and bulge). Within our field, the predicted halo-bulge asymmetry is small, but the bulge-disk and halo-disk asymmetries are on a noticeable level. The comparison for different time scale thresholds shows that, with the exception of high mass halo-lensing, the majority of events has time scales smaller than 10 d. A peak of events with time scales of 20 d or larger can only be understood with super-massive Machos or miss-identifications of variable objects. In the last line we add the analogous numbers for halo lensing resulting from Milky Way halo lenses of 0.1 M$_\odot$. The Macho events caused by the MW Machos should be roughly a third of that caused by M31 Machos.

front and the other behind the disk, and only the stars in the second part can contribute to disk-bulge lensing. The bulge-disk self lensing shows the opposite far to near side asymmetry and attains its maximum event rate per area in the far side of the disk. The same is true for the halo-disk lensing, (main maximum on far side of disk), which shows a secondary maximum close to the M31-center caused by the increase of the disk-star density. The disk-disk lensing event rate per area is symmetric with respect to the near and far side of the disk. The fact that the maximum for bulge-bulge and disk-disk lensing is not located exactly at the M31 center is caused by the increased photon noise combined with finite-source effects. The total self-lensing (disk-bulge + bulge-disk + bulge-bulge+
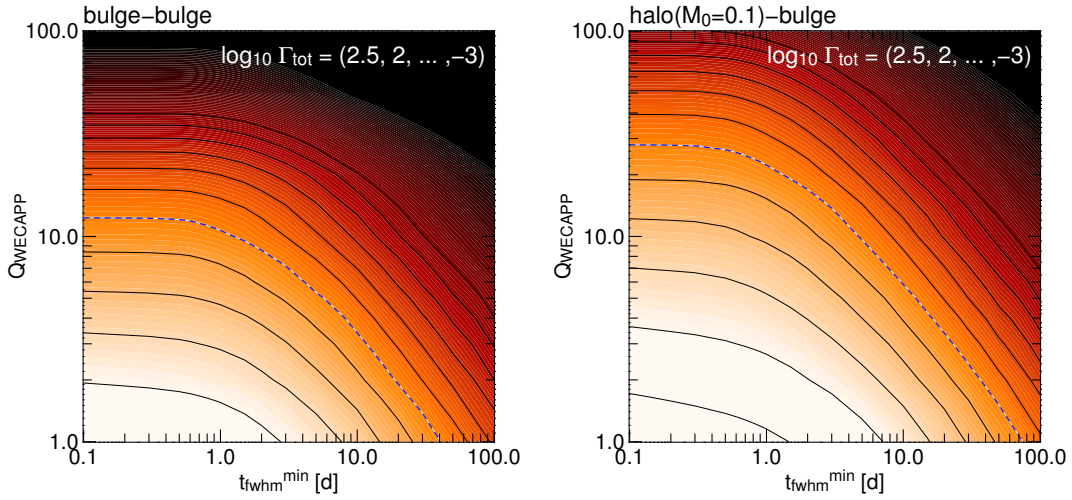
Figure 4.8: This figure shows contours of the logarithm of the lensing event rate per year within the $17.2' \times 17.2'$-WeCAPP field as a function of the signal-to-noise threshold Q for the peak-flux excess and as a function of the time scale threshold of the events. For these numbers, Eq. 4.59 was integrated over the WeCAPP field, and the noise was estimated for the WeCAPP survey (characterized by Table 4.1). We show results for two different lens-source configurations, bulge-bulge self-lensing and halo-disk lensing with $0.1 M_\odot$ lenses. The blue dashed line marks the 1 event per year level. For the calculations we have taken into account the finite stellar source sizes; the numbers shown, however, include only those among all events which do not show finite source signatures in their light curves, i.e. those which are usually searched for in lensing experiments. For signal-to-noise ratios of $Q > 10$, the rates for events with finite source effects can be of the same order as the rates for events with point-source light curves. For lower signal-to-noise ratios, events with finite source effects become much less important.

disk-disk) shows an asymmetry, arising from the different luminosity functions and mass functions of the bulge and disk population which leads to different event characteristics for disk-bulge and bulge-disk lensing. Therefore lens and source populations cannot easily be exchanged.

The last figure (Fig. 4.8) in this section shows how the total event rates $\Gamma_{l,s}(t_{\mathrm{fwhm}}^{\min}, Q) = \int \int \frac{d^2 \Gamma_{l,s}}{dx\,dy} dx\,dy$ in the WeCAPP field change with the peak-flux-threshold and the time scale threshold of the survey. We have taken into account the finite source sizes, but show only the rate for those events that do not show any finite source signature in their light curves. For very high signal-to-noise events (e.g., $Q = 20$), the two configurations show more or less flat contours in the t_{fwhm}-direction for t_{fwhm}-values between 0.1 and 1 days. This indicates that there are relatively few high signal-to-noise events with time scales around 0.1 days compared to events with time scales of about 1 day. That this is true is confirmed with Fig. 4.5, which shows that the highest signal-to-noise and thus highest flux excess events occur with time scales between 0.6 and a few days, and that events with time scales of about 0.1 days are significantly fainter. Only for smaller flux-excesses, the events with time scales of 0.1 days can be as common as events with time scales of a couple of days.

4.8   Conclusions and Outlook

Gravitational microlensing is a powerful method to detect compact luminous and dark matter objects in the foreground of stars in nearby galaxies. We used the distribution functions for the lens and source quantities (see Sects. 4.3 and 4.4) to re-derive well known relations like that for the optical depth, single star event rate or mean Einstein-time of the events. We accounted for the distance distribution of the sources and obtained the line of sight distance averaged quantities for the optical depth and Einstein time and show their values as a function of line of sight positions in Sect. 4.5. The shape of the total optical depth contours obtained in this way deviates from earlier results in Gyuk & Crotts (2000)(in a way that is understood by the simplifications made).

   We discussed the pixellensing or difference imaging regime, which is the situation where the majority of stars is hardly or not at all resolvable anymore. One then has to include the source luminosity function to account for the additional unknown variable, the intrinsic source flux. With that, we derived the distribution of the lensing events (at a fixed position in the central M31 field) as a function of the two main observables in the pixellensing regime, the excess flux and the full-width-half-maximum time scale. Due to the broad luminosity function there exists a variety of combinations of magnification and intrinsic source flux which yields the value for the flux excess. Events with high flux excess are dominated by evolved, i.e. post main sequence source stars.

   It had been noticed before (Gould, 1994; Auriere et al., 2001) that measuring or excluding finite source effects is useful to tighten constraints on the masses of lensing objects. But finite source effects also change the number and characteristics of events. In the presence of finite source effects, the event time scales are increased and the maximum magnification saturates below the maximum for the point-source approximation (see Fig. 4.1). This shifts events to longer time scales, but also suppresses the number of high magnification events, and therefore the number of observable events. Since events that are ultra-short (of order 0.001 d) in the point-source approximation are mostly high magnification events they all do show finite source effects (if the lenses are residing in M31), and thus have larger time scales than 0.001 d if the source sizes are taken into account. This explains the absence of ultra-short events for configurations with lenses in M31 in Fig. 4.5

   Using Eq. 4.47 and a flux-excess threshold one can predict the time scale distribution of the events in Fig. 4.5. The amplitudes of the contours will change for different locations within M31, and some details of the contours can be changed and moved in the flux-excess – full-width-half-maximum time scale plane. However, in any of the cases shown here one expects many more short term events with time scales of 1 to several days, than long term lensing events with 20 d or longer. Even super-massive Machos with $1000 M_\odot$ have about roughly the same number of events within 1 and 20 d as above 20 d.

   We used the event distributions as function of flux excess and full-width time scale, and the light distribution of M31 to derive the number of halo-lensing and self-lensing events within the WeCAPP field that exceed a given signal to noise ratio at the light curve maximum and have time scales of 1 day or larger in see Table 4.2. For minimum signal-to-noise ratios of $Q = 10$ and a minimum time scale of 1 d one expects about 4.3 (bulge-bulge, disk-bulge and bulge-disk) self-lensing events per year that have light curves as for point-like sources and about 4.0 with finite source signatures in their light curves. For time scales above 2 d these numbers decrease to about 2.4 for point-source and 1.6 finite source signature events per year. Since M31 cannot be observed more the 2/3's of a year, the total efficiency will be not larger than 50%, even for a survey with a good time coverage like WeCAPP. This means that there are not much more than a couple of self-lensing events with $Q = 10$ and time scales larger than 2 days in a WeCAPP field per year. A decrease of the 'acceptable'

$\left(\frac{S}{N}\right)$-ratio at maximum light to $Q = 6$ does increase the number of point-source events by roughly less than a factor of 5 and has little impact on the events with finite source signatures. In addition, at this variation level, a considerable fraction of the area is occupied by intrinsically variable objects, which makes the detection of lensing events even less effective. These values are much below than previous estimates. The identification of the WeCAPP-GL1 and WeCAPP-GL2 event with a signal-to-noise ratio of $Q \approx 85$ and $Q \approx 16$ at peak flux and a fwhm-time scale larger than 1 day in the WeCAPP 2000/2001 data therefore is in good agreement with our theoretical expectations.

Chapter 5

Macho candidates[1]

Abstract. We report the detection of the first 2 microlensing candidates from the Wendelstein Calar Alto Pixellensing Project (WeCAPP) in one years data (2000/2001). Both are detected with a high signal-to-noise-ratio and were filtered out from 4.5 million pixel light curves using a variety of selection criteria. Here we only consider well-sampled events with timescales of $1\,\mathrm{d} < t_{\mathrm{fwhm}} < 20\,\mathrm{d}$, high amplitude, and low reduced χ^2 of the microlensing fit. The two-color photometry (R,I) shows that the events are achromatic and that giant stars with colors of $(R-I) \approx 1.1\,\mathrm{mag}$ in the bulge of M31 have been lensed. The magnification factors are 64 and 10 which are obtained for typical giant stars with luminosities of $M_I = -2.5\,\mathrm{mag}$. Both lensing events lasted for only a few days ($t_{\mathrm{fwhm}}^{\mathrm{GL1}} = 1.7\,\mathrm{d}$ and $t_{\mathrm{fwhm}}^{\mathrm{GL2}} = 5.4\,\mathrm{d}$). The event GL1 is likely identical with PA-00-S3 reported by the POINT-AGAPE project. Assuming a 100% Macho halo, our calculations favor in both cases the possibility that Machos in the halo of M31 caused the lensing events. The most probable masses, $0.08\,M_\odot$ for GL1 and $0.02\,M_\odot$ for GL2, are in the range of the brown dwarf limit of hydrogen burning. Solar mass objects are a factor of two less likely. A detection on the whole data set yielded further 5 microlensing candidates with full-width timescales between 0.3 days and 4.7 days. We give the positions and the light curves of these new candidates.

---

[1]This chapter is an updated version of the article Riffeser, Fliri, Bender, Seitz, & Gössl (2003). Modified sections are highlighted by footnotes.

5.1   Introduction

Microlensing experiments are an ideal method to search for dark objects within and between galaxies. A large number of microlensing events have been detected towards the Galactic bulge constraining the number density of faint stars in this direction (Alard, 1999; Afonso et al., 1999; Alcock et al., 2000b; Udalski et al., 2000). Towards the LMC only 13-17 microlensing events have been reported so far (Alcock et al., 2000a). If all this events are attributed to $0.5 M_\odot$ Machos, the associated population of dark objects would contribute up to the 20% level to the dark matter content of the Milky Way (Alcock et al., 2000b). However, both the relatively large size of the LMC relative to its distance and the nature of the lenses has cast doubt on this interpretation. It is indeed likely that a large fraction of the microlensing events towards the LMC are due to self-lensing of stars within the LMC (Lasserre et al. 2000; Evans & Kerins 2000 and references therein).

Studying microlensing events towards M31 allows to separate self-lensing and halo-lensing in a statistical way, since the optical depth for halo lensing is larger on the far side of M31. In M31 individual stars can not be resolved and one therefore has to use the pixellensing technique (Crotts, 1992; Baillon et al., 1993a) to follow the variability of sources blended with thousands of other sources within the same pixel. First detections of possible microlensing events were reported by several pixellensing experiments (Crotts & Tomaney, 1996; Ansari et al., 1999; Auriere et al., 2001; Paulin-Henriksson et al., 2002, 2003; Calchi Novati et al., 2003). But since the candidate nature of only 5 of these events is convincing, no conclusions concerning the near-far asymmetry or the most likely dark matter lensing masses could be drawn yet.

The Wendelstein Calar Alto Pixellensing Project (WeCAPP, Riffeser et al. 2001) started in 1997 with test observations. Since 1999 the bulge of M31 was monitored continuously during the

time of visibility of M31. The analysis of our 4 years data will allow not only the identification of very short duration events, but also the separation of long duration ($\geq 20\,\mathrm{d}$) microlensing events from long periodic variables as Mira stars. For this letter we analyzed the short duration events ($t_{\mathrm{fwhm}} < 20\,\mathrm{d}$) within one season of Calar Alto data and restricted the detection to high-signal-to-noise, high-magnification events. We report our first 2 microlensing candidates of that type.

5.2   Observations and data reduction[2]

WeCAPP monitors the central region of M31 in a $17.2 \times 17.2\,\mathrm{arcmin}^2$ field with the 1.23 m telescope of the Calar Alto Observatory. In addition, a quarter of this field, pointing towards the far side of the M31 disk along the South-East minor axis, was observed with the 0.8 m telescope of the Wendelstein Observatory. The data analysis and candidate selection reported in this letter is based on the season from June, 23th 2000 to February, 25th 2001 and is restricted to the Calar Alto data only. During this period, M31 was observed during 43% percent of all nights. Observations were carried out in R and I filters close to the Kron-Cousins system.

We have developed a pipeline which performs the standard CCD reduction, position alignment, photometric alignment, stacking of frames, PSF matching using an implementation of the optimal image subtraction algorithm presented in Alard & Lupton (1998), and the generation of difference images (see chapter 2). The reduction package includes full error propagation for each pixel through all reduction steps. In this way, all data points are properly taken into account in the search for variables. For the data presented here all data within one night are co-added, yielding one difference image per night.

---

[2]Modified section.

selection criterion	number
analyzed light curves	4492250
light curves with > 10 data points	3835407
3 successive 3σ in R or I	517052
$\chi_R^2 < 1.3$ and $\chi_I^2 < 1.3$	186039
1 day $< t_{\mathrm{fwhm}} < 20$ days	9497
3σ light point inside t_{fwhm}	1829
sampling: $\mathrm{side}_1 > 20\%$, $\mathrm{side}_2 > 5\%$	256
$F_{\mathrm{eff}} > 10$ median$_{\mathrm{error}}$ in R and I	15
candidates	2

Table 5.1: Selection criteria for WeCAPP-GL1 and GL2.

5.3 Selection criteria

We investigate only pixels which have more than 10 data points in R and I, which applies for 85% of the 2K x 2K field. For each pixel we define a flux baseline by iterative 3σ-clipping of all outliers with higher flux. All pixels which have at least 3 successive positive 3σ deviations from this baseline are considered as variables.

We fit the microlensing light curve for high-amplification events (Gould, 1996) simultaneously to the R- and I-band pixel light curves for every variable. The fit has 6 free parameters: full-width-half-maximum t_{fwhm} and the time t_0 of maximum amplification (these 2 parameters are the same for both filters), amplitude $F_{\mathrm{eff},R}$, color $F_{\mathrm{eff},I}/F_{\mathrm{eff},R}$, and baseline levels c_R and c_I.

Variable light curves with a reduced $\chi_R^2 > 1.3$ or $\chi_I^2 > 1.3$ are discarded. In this way we exclude light curves that are not achromatic or not symmetric. We also exclude events with $t_{\mathrm{fwhm}} > 20$ days which can be confused with long periodic variables like Mira stars, as long as only one season of data is investigated. In addition, all candidates which do not have at least one significant data point (3σ deviation from the baseline) within t_{fwhm} of the time of maximum amplification are rejected. We further define the sampling quality for the falling and rising parts of each light curve within $(t_0 - 15\,\mathrm{d}, t_0)$ and $(t_0, t_0 + 15\,\mathrm{d})$: within these time intervals we require a sampling of the area under the light curve of at least 20%

on one side and of at least 5% on the other side (Table 5.1).

Here, we present only the two microlensing candidates which have amplitudes 10 times larger than the median error of the light curve (see Figure 5.1). Ruling out systematic offsets for the points and errors on the trailing side of GL2 (which is strongly proved by the 6 single images of that night in each filter) a non microlensing light curve of a variable source hardly fits the data points of GL2. Both microlensing candidates are detected in several pixels (11 for GL1 and 4 for GL2) inside the PSF of the position of the lensed object. This explains the reduction from 15 events to 2 events in the last line of Table 5.1. The amplification light curves were obtained by calculating the total flux within the PSF area of each microlensing event (see chapter 2). For both candidates, the selection criteria exclude variable stars like Miras, novae or dwarf novae. Extracting lensing events with less good time sampling, lower amplitude, or events located close to other variables requires refined selection criteria.

5.4 Microlensing candidates

The parameters of both lensing candidates are summarized in Table 5.2. Their light curves are shown in Figure 5.1. GL1, the highest S/N lensing event candidate in our sample, lies $4.^{\mathrm{m}}1$ to the SW of the nucleus of M31. GL2 is $4.^{\mathrm{m}}4$ to
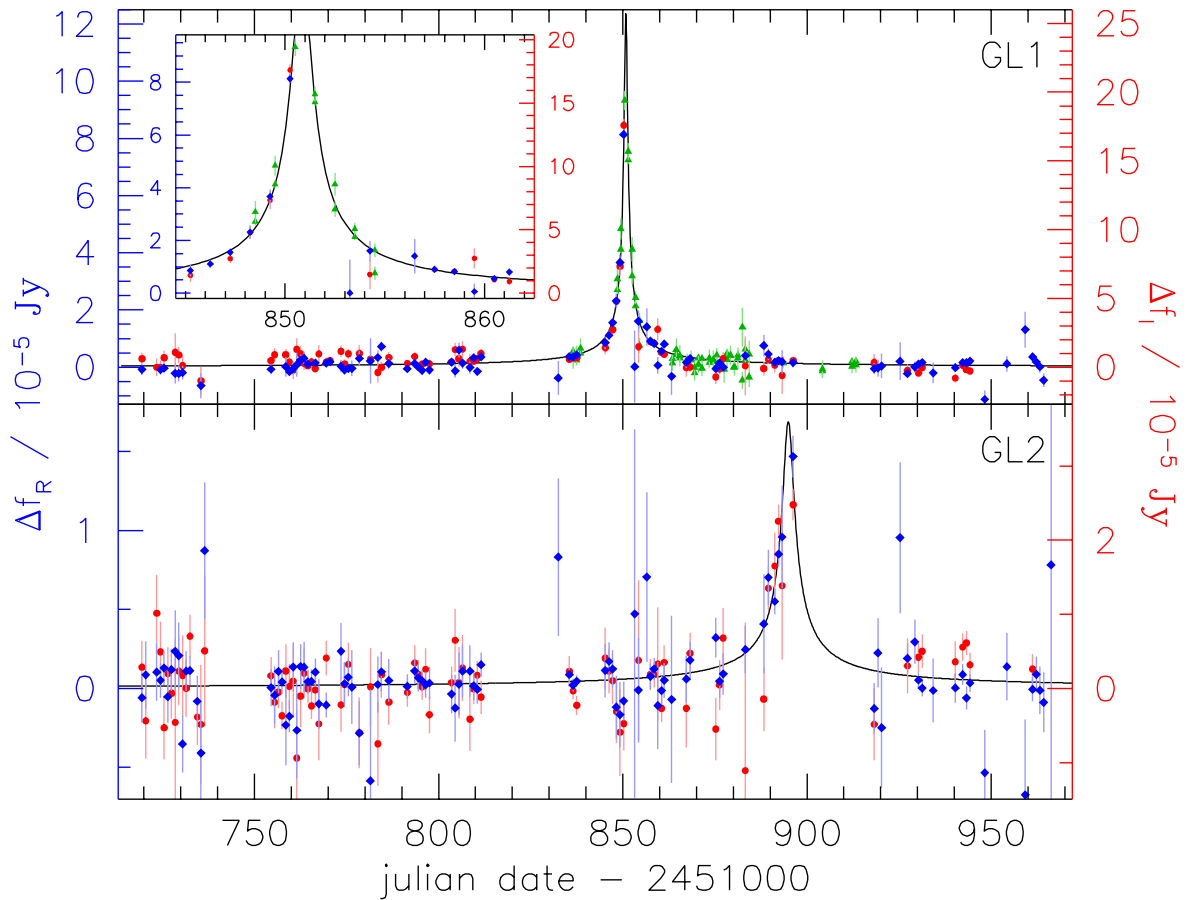
Figure 5.1: Light curves of WeCAPP-GL1 and WeCAPP-GL2. The *I*-band light curve (red symbols, right axis) has been scaled to the *R*-band light curve (blue symbols, left axis). The scaling factors were derived from the lensing fit (black curve) and correspond to a color $(R - I)$ of 1.05 for GL1 and 1.08 for GL2. In addition we show the r' and i' data from the POINT-AGAPE PA-00-S3 event (green symbols) scaled to our data.

the NW of the nucleus. Our data have been astrometrically calibrated using bright foreground stars observed with HST by Jablonka *et al.* (1999) and ground based observations by Magnier *et al.* (1992). Our two calibrations agree within 0.5″ in declination and 0.7″ in right ascension, well consistent with the astrometric accuracy of 0.8″ to 1.0″ of the Magnier et al. catalog. After we had detected GL1 and GL2, we cross-checked with events reported by the POINT-AGAPE survey for the same period of time and the same field in M31 (Paulin-Henriksson *et al.*, 2003). It appears that GL1 is likely identical with PA-00-S3 which occurred at the same time (Figure 5.1). Because POINT-AGAPE did not provide a flux calibration of their data, we had to assume a scaling factor for the amplitude. The zero point in time was not adjusted. The data points from WeCAPP and POINT-AGAPE complement each other nicely and make GL1 the best pixellensing event found so far in M31. GL2 also falls in the observing period covered by POINT-AGAPE but their time sampling around the event is poor. This may be the reason why GL2 was not detected.

	GL1	with PA-00-S3 [a]	GL2
R.A. (J2000)	00 42 30.3	00 42 30.3	00 42 32.8
Decl. (J2000)	+41 13 00.8	+41 13 00.8	+41 19 56.5
t_0 (JD-2451000)	850.80 ± 0.13	850.84 ± 0.02	894.77 ± 0.21
t_{fwhm} (days)	1.38 ± 0.53	1.65 ± 0.10	5.41 ± 2.49
$F_{\mathrm{eff,R}}$ (10^{-5} Jy)	13.4 ± 5.4	12.4 ± 0.6	1.7 ± 0.5
$F_{\mathrm{eff,I}}$ (10^{-5} Jy)	28.0 ± 11.2	25.7 ± 1.5	3.6 ± 1.1
$(R-I)$	1.05 ± 0.08	1.05 ± 0.08	1.08 ± 0.24
χ^2	1.23	1.22	1.02
$M_I = -1.9$ mag			
A_0	120	110	16
t_{E} (days)	47.4 ± 18.1	52.1 ± 3.2	23.9 ± 11.0
$M_I = -2.5$ mag			
A_0	69	64	10
t_{E} (days)	27.2 ± 10.4	30.0 ± 1.8	13.8 ± 6.3
$M_I = -3.7$ mag			
A_0	24	22	4
t_{E} (days)	9.0 ± 3.5	9.9 ± 0.6	4.6 ± 2.1
$M_I = 7.7$ mag			
A_0	$8.2 \cdot 10^5$	$7.6 \cdot 10^5$	$1.1 \cdot 10^5$
t_E (days/10^5)	3.3 ± 1.3	3.6 ± 0.2	1.7 ± 0.8

Table 5.2: Parameters of the microlensing candidates. *a*: Derived from a fit to the total set of data points (WeCAPP and POINT-AGAPE).

The parameters of the lensing fit are degenerate for high magnifications (Gould, 1996), i.e. for amplitudes $A_0 \gg 1$ which correspond to impact angles much smaller than the Einstein angle θ_{E}. In this case, we obtain for the light curve:

$$F_0 \left[A(t) - 1 \right] \longrightarrow F_{\mathrm{eff}} \left[\frac{12}{t_{\mathrm{fwhm}}^2} (t - t_0)^2 + 1 \right]^{-1/2}$$
(5.1)

with intrinsic flux of the source F_0 and $F_{\mathrm{eff}} = F_0/u_0 \approx F_0 A_0$, where u_0 is the impact angle in units of the Einstein angle.

In order to obtain A_0 we evidently need to know the source flux F_0. We can get rough constraints by considering the color of the light curves which due to our selection criteria are achromatic. We obtain $(R - I)_{\mathrm{GL1}} = 1.05$ and $(R - I)_{\mathrm{GL2}} = 1.08$. For main sequence stars this

converts[3] (Cassisi *et al.*, 1998) into absolute magnitudes of $M_I \approx 8$ mag. If the sources are giants, then the magnitudes are $M_I = -2.5$ mag with a minimum of -1.9 and maximum of -3.7 (Bessell, 1979; Grillmair *et al.*, 1996).

We now derive the lensing parameters as follows. The impact parameter is calculated from the fitted value of $F_{\mathrm{eff,I}}$ and the estimated value of $F_{0,I}$ as

$$u_0 = \frac{F_{0,I}}{F_{\mathrm{eff,I}}} \quad . \tag{5.2}$$

With this value we derive the the Einstein timescale t_{E}

$$t_{\mathrm{E}} = \frac{t_{\mathrm{fwhm}}}{u_0 \sqrt{12}} \quad , \tag{5.3}$$

---

[3]transformed on the observational plane by Maraston (1998)

M_I	A_0	t_E[d]
GL1		
-1.9	120	47.4 ± 18.1
-2.5	69	27.2 ± 10.4
-3.7	24	9.0 ± 3.5
7.7	$8.2 \cdot 10^5$	$(3.3 \pm 1.3) \cdot 10^5$
GL1	**& PA-00-S3**	
-1.9	110	52.1 ± 3.2
-2.5	64	30.0 ± 1.8
-3.7	22	9.9 ± 0.6
7.7	$7.6 \cdot 10^5$	$(3.6 \pm 0.2) \cdot 10^5$
GL2		
-1.9	16	23.9 ± 11.0
-2.5	10	13.8 ± 6.3
-3.7	4	4.6 ± 2.1
7.7	$1.1 \cdot 10^5$	$(1.7 \pm 0.8) \cdot 10^5$

Table 5.3: Amplifications for different source star luminosities

which then yields the lens mass

$$M_{\text{lens}} = \frac{(v_t t_E)^2 c^2 D_S}{4 G D_L (D_S - D_L)} \quad , \qquad (5.4)$$

where v_t is the transverse velocity between source and lens, and D_L and D_S are the angular distances to the lens and source.

To estimate plausible lens masses the Einstein timescales t_E are calculated for fixed luminosities of possible source stars (see Table 5.3). Note that the errors in t_E reflect the accuracy of the determination of t_{fwhm} in the degenerate Gould fit only, and do not account for the systematic uncertainties due to the unknown luminosities of the sources. If the source is a main sequence star, we need very high magnifications: typically $A_0 = 8 \cdot 10^5$ and $A_0 = 2 \cdot 10^5$ for GL1 and GL2, respectively. The corresponding lens masses (for $v_t = 210$ km/s, $D_L = 768$ kpc, $D_S = 770$ kpc) are $M \approx 10^8 M_\odot$, an implausibly large value. If the source is a giant, the required magnifications are reduced to $A_{0,\text{GL1}} = 64$ and $A_{0,\text{GL2}} = 10$ (see Table 5.3); the typical self-lensing masses become $M = 0.8 M_\odot$ and $M = 0.2 M_\odot$, i.e. they are typical for low mass stars.

Assuming the source to be a red giant with $M_I = -2.5$ mag we calculate the probability $p(M, t_E)$ that a microlensing event of observed timescale t_E can be produced by a lens of the mass M. Following the calculations of Jetzer & Massó (1994) Eq. 8 and Jetzer (1994) Eq. 11 we get

$$p(M, t_E) \sim \xi(M) \int \rho_S(D_S) \int \rho_L(D_L)$$
$$f\left(\frac{R_E}{t_E}\right) \frac{R_E^3}{t_E^3} dD_L dD_S \quad (5.5)$$

with the mass function (MF) $\xi(M)$, the sources density $\rho_S(D_S)$, the lenses density $\rho_L(D_L)$, the velocity distribution $f(v_t)$ and the Einstein radius $R_E(D_L, M, D_S)$.

The distribution of matter in the central part of M31 is based on the bulge model of Kent (1989b). The disk is modeled with a radial scale length of 6.4 kpc and an exponential shape, and with a vertical scale length of 0.3 kpc and a sech^2-shape. The halo is modeled as an isothermal sphere with a core radius of $r_c = 2$ kpc. The velocity distribution was calculated from a Maxwellian halo bulge and disk velocity distribution with an additional rotation for bulge and disk (Kerins et al., 2001).

For the bulge lenses we take the MF as derived for the galactic bulge $\xi \sim M^{-1.33}$ (Zoccali et al., 2000). For the disk population we adopt a Gould MF $\xi \sim M^{-2.21}$ with a flattening $\xi \sim M^{-0.56}$ below $0.59 M_\odot$ (Gould et al., 1997). Both are cut at the lower end at the hydrogen burning limit of $0.08 M_\odot$. At the upper end the bulge MF is cut at the main sequence turn-off $0.95 M_\odot$ (C. Maraston, priv. comm.) and the disk MF at $10 M_\odot$. The MF for the potential Macho population residing in the halo of M31 is of course unknown. We therefore calculate the probability distribution for halos consisting of one mass only, i.e. taking δ-function MFs centered on the lens mass $\xi = \delta(M - M_{\text{lens}})/M_{\text{lens}}$. Moreover we assume that the whole dark halo of M31 consists of Machos. Lensing by Galactic halo objects has an order of magnitude smaller optical depth and is therefore neglected in our considerations.

The results are shown in Figure 5.2. For M31
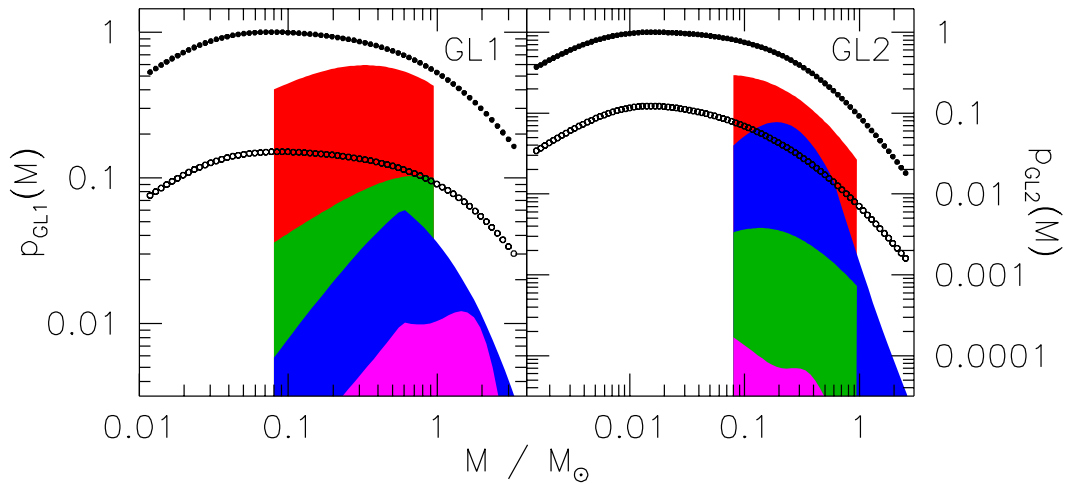
Figure 5.2: Mass probability function for GL1 (left panel) and GL2 (right panel) for lens-source configurations: halo-bulge (filled circles), halo-disk (open circles), bulge-bulge (red), bulge-disk (green), disk-bulge (blue), disk-disk (magenta). The maximum of each curve is scaled to reflect the total probability of a respective lens-source event relative to the case of a halo-bulge lensing event with the most probable Macho mass. For example in case of GL1 the probability for bulge-bulge lensing relative to halo-bulge lensing with $0.08 M_\odot$ lenses becomes 0.6 (maximum of red curve). A halo consisting of $0.014 M_\odot$ Machos would have the same probability as bulge-bulge lensing. Note that the shapes of the distributions for bulge and disk lenses are strongly affected by the used mass function $\xi(M)$.

halo lenses the most probable masses are $0.08 M_\odot$ for GL1 and $0.02 M_\odot$ for GL2. In the case of self-lensing the most probable masses are about a factor of 4 bigger. Taking the most likely halo lens masses, the ratio of the probabilities that the lenses are part of the dark halo or the stellar content $p_{\text{halo}}/(p_{\text{bulge}} + p_{\text{disk}})$ is 1.6 for GL1 and 3.3 for GL2. We conclude therefore that it is likely that lenses residing in the halo of M31 caused the events in both cases.

5.5 Degenerate parameters[4]

Due to the strong blending we were not able to derive the luminosity of the source well outside the event. Therefore we are also not able to derive the amplification of the events in an unambiguous way, as the amplification is strongly degenerate with the Einstein ring crossing time (see

chapter 4). However, the good time sampling of GL1/S3 allows us to constrain the parameters t_E and A_0 by means of a likelihood analysis from fits of the non-degenerate Paczynski form (Paczynski 1986, see also Eq. 4.2 in chapter 4) to the light curve. The fits have five free parameters: t_0, $F_{0,R}$, A_0, t_E, and a constant c. The I-band and POINT-AGAPE data are scaled to the R-band data using the color of the degenerate Gould fit (Eq.5.1). We are calculating the likelihood contours for t_E and A_0 while the other three parameters are minimized to yield the best χ^2-value for each (t_E, A_0) pair. In Fig. 5.3 we show the likelihood contours for the combined data set of GL1/S3. The amplifications are moderately high with a 1σ region between 58^{+52}_{-21}. The 1σ interval for t_E is 30^{+24}_{-9} days which agrees well with our estimates by deriving the source luminosity using the color of the event. Our estimated (t_E, A_0) value lies just outside the 1σ region well inside the 2σ contour level.

---

[4]Modified section.
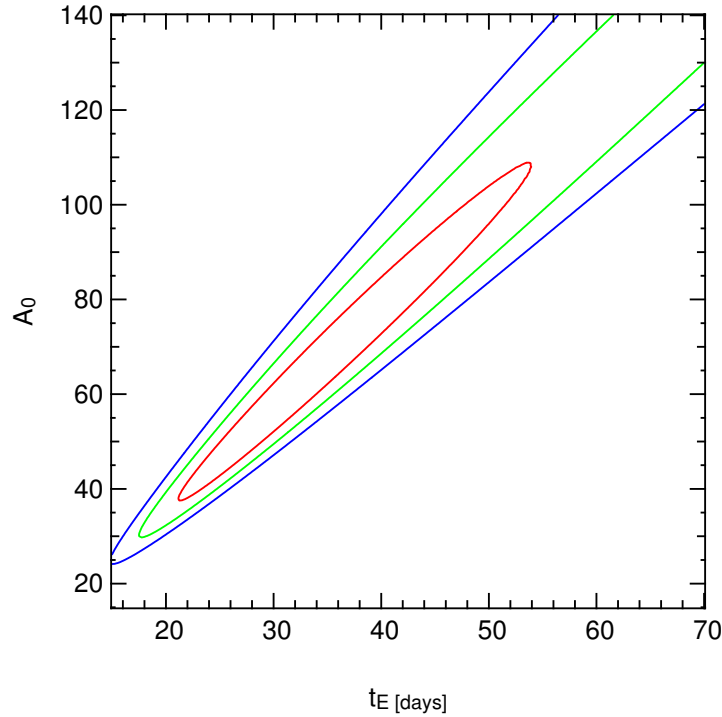
Figure 5.3: Likelihood contours of t_E and A_0 for GL1/S3 derived from the combined data set of WeCAPP and POINT-AGAPE. The red, green and blue lines mark the 1σ, 2σ and 3σ contour levels.

5.6   Further candidates[5]

The whole data set covering the years 1997-2005 allows a rather unbiased search for microlensing candidates. Due to the length of the survey and its adequate time sampling variable stars can be excluded efficiently by their large reduced χ^2 deviations of the theoretical microlensing fit to the light curves. We therefore were able to lower the thresholds for the detection of microlensing events, which yields a more unbiased sample of microlensing candidates.

The detection started in a similar way as described in Sec. 5.3. We performed Gould fits (see Eq. 5.1) to the pixel light curves containing local maxima and kept all light curves with a reduced $\chi^2 \leq 1.5$ (for all data points, as well as for the R- and I- band data separately). The t_{fwhm} threshold was weakened by only requiring $t_{fwhm} > 0.1$ days.

field	F1	F2	F3	F4
light curve cuts	1656	1721	1421	1482
position cuts	10	9	4	9
# candidates	3	2	1	2

Table 5.4: Number of microlensing candidates detected in the four fields (last row). In the second row we give the number of light curves after the cuts in the light curve fits. The third row gives the corresponding number after the the final cut. As one candidate was detected in two fields (GL6) and also adjacent pixels can pass the last cut the number of Macho candidates reduces to 7.

We kept a lower $\left(\frac{S}{N}\right)$ criterion by requiring that the ratio of the fitted values of the effective flux excess F_{eff} and the median error in the light curve should be at least 5 in both filters. To get well sampled light curves we kept the sampling criterion as in Sect. 5.3. This already strongly reduced

---

[5]Modified section.

WeCAPP	RA(2000)	DEC(2000)	t_0	t_{fwhm} [d]	$F_{\text{eff,R}}$ [10^{-5} Jy]	$(R-I)$	χ^2
GL1	00 42 30.3	+41 13 00.8	850.84 ± 0.02	1.65 ± 0.60	12.4 ± 0.60	1.05 ± 0.08	1.22
GL2	00 42 32.8	+41 19 56.5	894.77 ± 0.21	5.41 ± 2.49	1.70 ± 0.50	1.08 ± 0.24	1.02
GL3	00 42 57.3	+41 12 27.4	585.38 ± 0.15	2.47 ± 0.33	2.19 ± 0.08	1.48 ± 0.10	1.06
GL4	00 42 54.8	+41 14 36.7	1178.94 ± 0.03	2.23 ± 0.21	3.26 ± 0.16	0.70 ± 0.12	1.15
GL5	00 43 02.4	+41 18 28.7	1178.46 ± 0.24	4.74 ± 0.75	1.22 ± 0.10	0.96 ± 0.26	0.95
GL6	00 42 49.1	+41 14 54.9	1317.23 ± 0.03	0.46 ± 0.14	16.4 ± 4.78	0.98 ± 0.09	1.20
GL7	00 42 50.3	+41 18 40.4	1111.49 ± 0.12	0.27 ± 0.80	12.3 ± 34.6	0.90 ± 0.22	1.07

Table 5.5: Parameters of all microlensing candidates. We give the position in the WCS, the time of maximum magnification t_0 [julian date - 2451000], the full-width-half-maximum timescale t_{fwhm}, the effective R-band excess flux $F_{\text{eff,R}}$, the $(R-I)$ color, and the reduced χ^2 of the fit. For GL1 we give the values for the fits to the combined data set of WeCAPP and POINT-AGAPE.

the number of potential microlensing candidates. However, these cuts which are based on the microlensing fits alone, are not restrictive enough to yield a small and clean sample of microlensing candidates. They also yield a large sample of contaminants (see Table 5.4), from which the Macho candidates have to be extracted. Especially pixel light curves located at the wings of a variable star PSF can mimic microlensing light curves quite efficiently.

We therefore had to include a further criterion, requiring that the position of the event should coincide in the pixel light curves and when determined in the difference images at the time of maximum amplification. For this purpose we created 'event images' for all of the potential light curves which remained in the sample after the cuts based on the light curve fits. For the event frames we co-added the R- and I-band difference frames being closest to the fitted time t_0 of maximum amplification .

We applied the source detection software SExtractor (Bertin & Arnouts, 1996) to the event images, where we required 2σ detections in at least two contiguous pixels for a source to be detected. The rms-value σ of the noise in the difference images was determined by the SExtractor software. As final cut we extracted all candidates for which positions in the pixel light curves and in the SExtractor catalogues agreed within

$$r = \sqrt{(x_1 - x_2)^2 + (y_1 - y_2)^2} < 1.0 \quad \text{px} \quad, \tag{5.6}$$

where (x_1, y_1) and (x_2, y_2) are the positions of the candidates measured by the two methods.

This criterion selects the microlensing candidates and, at the same time, yields a minimal number of contaminants. As several pixel light curves belonging to the same Macho candidate survive the cuts based on the microlensing fits, and Eq. 5.6 is chosen weak enough that adjacent pixels can pass the last criterion, several of the detected light curves refer to the same microlensing candidate.

For the detection of the microlensing candidates we split the complete data set in four separate parts referring to the fields F1 to F4. The field borders are larger than the separating lines in Fig. 2.1, as the Wendelstein images of the fields differed slightly in the pointings. As consequence, the four analyzed fields overlapped in parts, which especially is evident in the Calar Alto data set, for which we also cut the images to the new field boundaries.

In Table 5.4 we show the numbers of light curves passing the cuts based on the light curve fitting, split into the four fields. The third row gives the corresponding number after the last cut, whereas the last line we give the numbers of the detected microlensing candidates. Table 5.5 shows the parameters of all 7 microlensing candidates detected by this procedure. The reduced χ^2 of the microlensing fits to the light curves generally is compatible with unity. This underlines that the candidates fit perfectly to a sym-

metric microlensing light curve. Due to the short timescale of GL7 the fitted parameters show large error bars, with especially $F_{\mathrm{eff,R}}$ being relatively uncertain. The $(R - I)$ colors of the events lie in the range between 0.7 mag and 1.5 mag. These value again favor giant stars as sources for the lensing events (see above).

In Figs. 5.4 to 5.8 we show the light curves of the Macho candidates GL3 to GL7 along with the detection frames of the candidates. We also present time series of the R-band difference images around the time of maximum amplification.

5.7 Discussion and outlook[6]

In this chapter we presented 7 candidates for microlensing events as detected in the WeCAPP data. A first search in one years data (200/2001) was restricted to high $\left(\frac{S}{N}\right)$ and short timescale events and yielded two candidates, WeCAPP-GL1 and WeCAPP-GL2. GL1 is likely identical to PA-00-S3 found by the POINT-AGAPE collaboration. Combining the data from POINT-AGAPE with ours shows that the error bar of the derived Einstein time scale becomes smaller by a factor of 5 compared to the individual error bar. This demonstrates the importance of a good time sampling of the events which is also underlined by the detection of GL2 which fell in an observational gap in the POINT-AGAPE data.

We derived the colors of the lensed stars, the amplification factors and likely lens masses for both bulge and disk self-lensing and Macho lensing. We showed that the most likely source stars are red giants, while main sequence stars are highly implausible.

For GL1 and GL2 we calculated the mass probability functions. The bulge self-lensing hypothesis yields lensing stars at or below the the main sequence turn-off of the M31 bulge. On the other hand, if the lensing events are caused by Machos, their masses are typically very low, most probable below $0.1\,M_\odot$. Masses in the range

---

[6]Modified section.
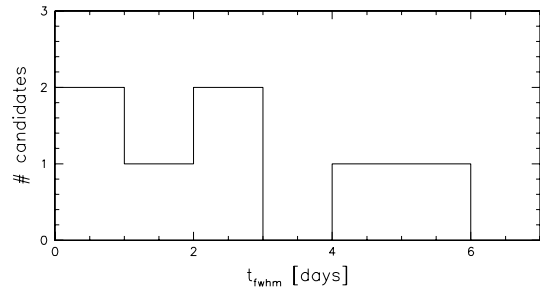
Figure 5.9: Distribution of the full-width time scales of the 7 WeCAPP event candidates.

of $0.5\,M_\odot$ to $1\,M_\odot$ are more unlikely.

The analysis of the whole data set allowed us to lift the restriction of the lensing search to short timescale and high amplification events, as it was possible to identify the positions and the periods of all intrinsic variable sources (see chapter 6). Furthermore, the good temporal coverage and the length of the observations lead to a large χ^2 deviation of the microlensing fits to light curves of variable stars. As it turned out, however, pixel light curves at positions in the wings of the PSFs of bright variables tend to mimic lensing light curves. We therefore had to modify the detection algorithms that only used the information from the the light curve fits, and had to use a further cut based on the agreement of the positions derived from the light curve fit and from photometry in the difference images. This criterion enabled us to weaken the criteria regarding the light curve fits and to search rather unbiased for microlensing candidates. This yielded a clean and robust sample of further 5 candidate microlensing events, for which we showed the light curves and the time series of the R-band difference images around the time of maximum amplification of the source. The full-width times scales of these events range from below 1 day to about 5 days. In Fig. 5.9 we show a histogram of the distribution of the time scales. The time scales appear to be rather uniformly distributed, although this statement is restricted by the low number statistics.

Two of the events (GL6 and GL7) have full-width time scales below 0.5 days and do not have
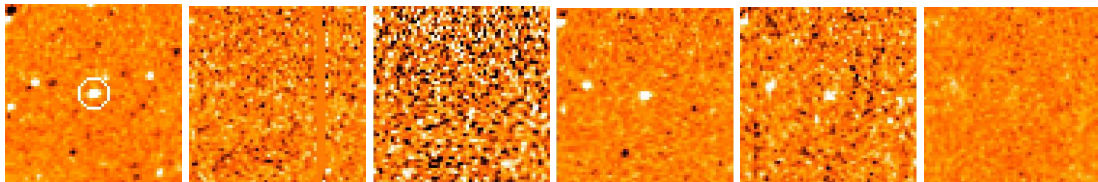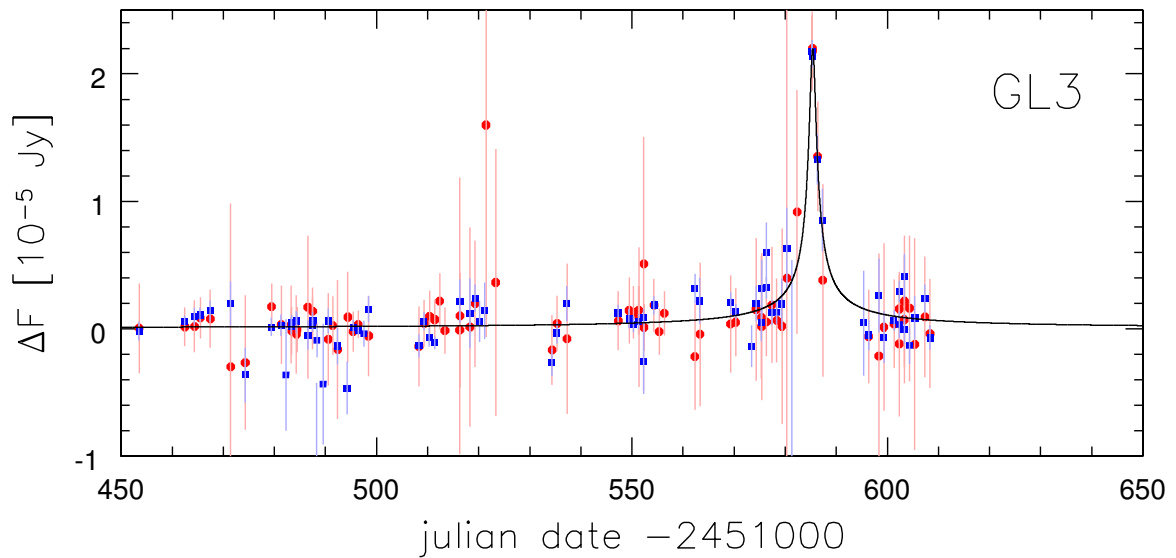
Figure 5.4: *Top:* Light curve of WeCAPP-GL3. The *R*-band data are shown by blue symbols, the *I*-band data by red symbols. The *I*-band data were scaled to the *R*-band data using the $(R - I)$ color of the event as derived from the degenerate fits to the light curves. *Bottom:* This figure shows on the left the 'event image' of WeCAPP-GL3. This image is the co-added *R*- and *I*-band frame at the time of maximum amplification, and was used to detect the microlensing events. The white ellipse around the object shows the SExtractor detection. On the right we show the *R*-band time series at the position of GL3 around the time of maximum amplification.
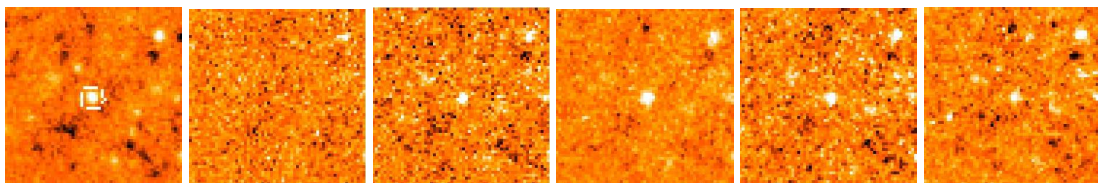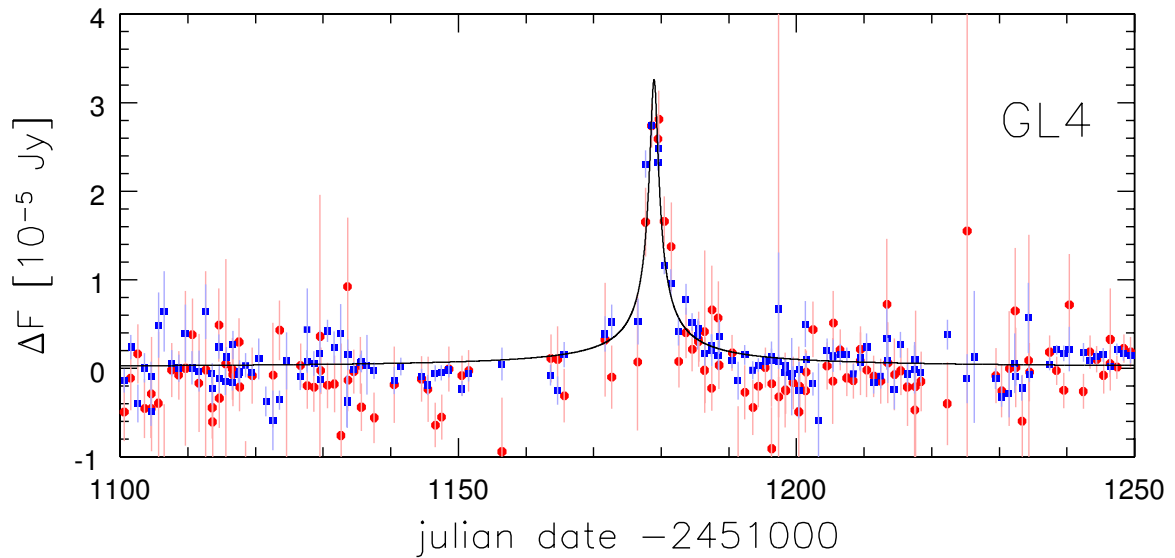
Figure 5.5: *Top:* Light curve of WeCAPP-GL4. The *R*-band data are shown by blue symbols, the *I*-band data by red symbols. The *I*-band data were scaled to the *R*-band data using the $(R-I)$ color of the event as derived from the degenerate fits to the light curves. *Bottom:* This figure shows on the left the 'event image' of WeCAPP-GL4. On the right we show the *R*-band time series at the position of GL4 around the time of maximum amplification.
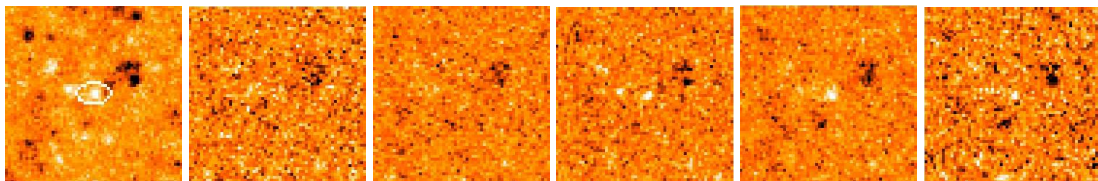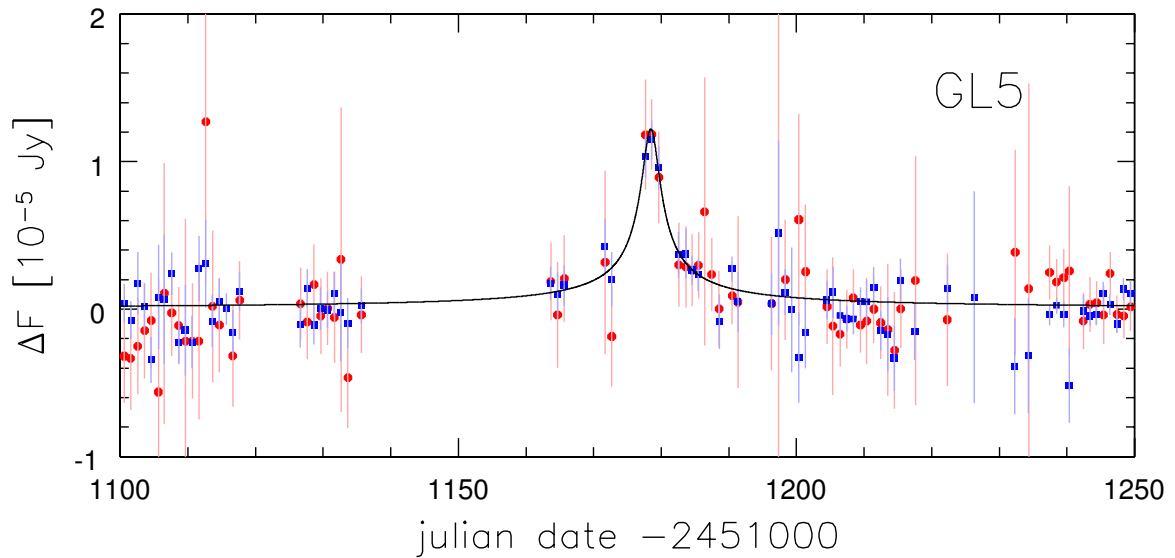
Figure 5.6: *Top:* Light curve of WeCAPP-GL5. The *R*-band data are shown by blue symbols, the *I*-band data by red symbols. The *I*-band data were scaled to the *R*-band data using the $(R - I)$ color of the event as derived from the degenerate fits to the light curves. *Bottom:* This figure shows on the left the 'event image' of WeCAPP-GL5. On the right we show the *R*-band time series at the position of GL5 around the time of maximum amplification.
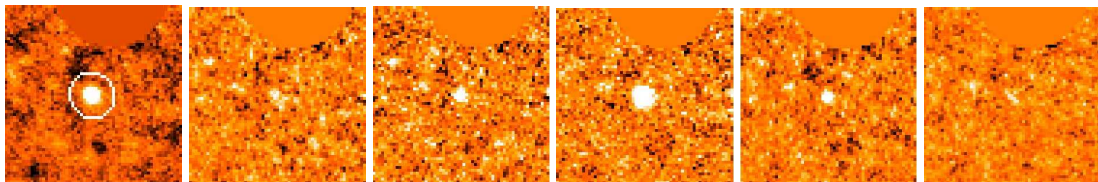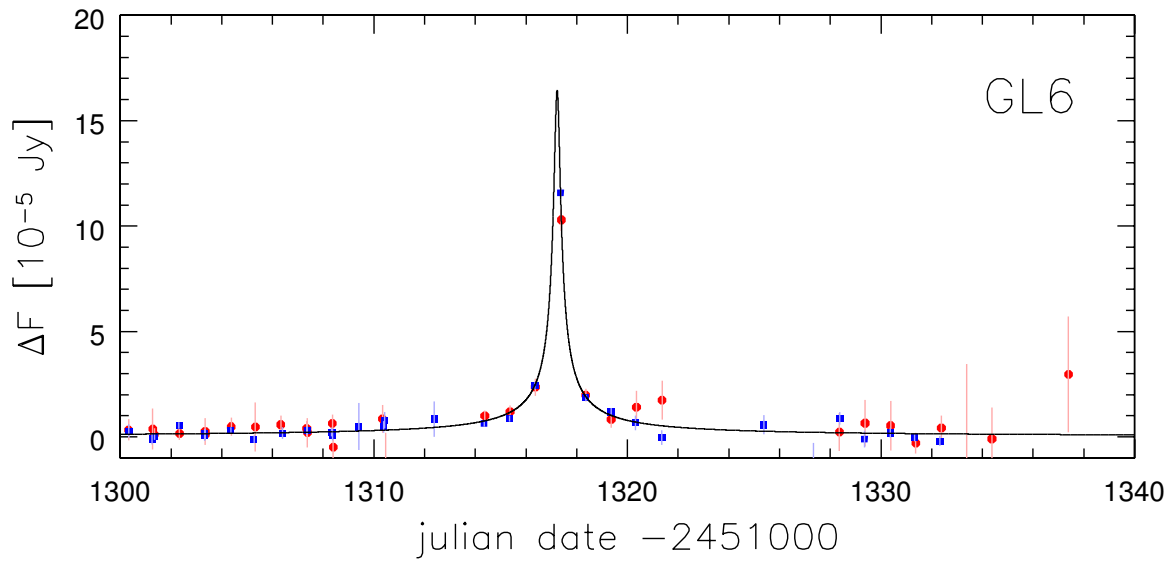
Figure 5.7: *Top:* Light curve of WeCAPP-GL6. The *R*-band data are shown by blue symbols, the *I*-band data by red symbols. The *I*-band data were scaled to the *R*-band data using the $(R-I)$ color of the event as derived from the degenerate fits to the light curves. This event has a full-width timescale below 0.5 days. *Bottom:* This figure shows on the left the 'event image' of WeCAPP-GL6. On the right we show the *R*-band time series at the position of GL6 around the time of maximum amplification.
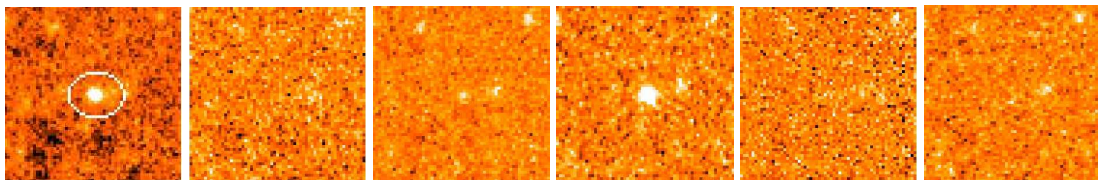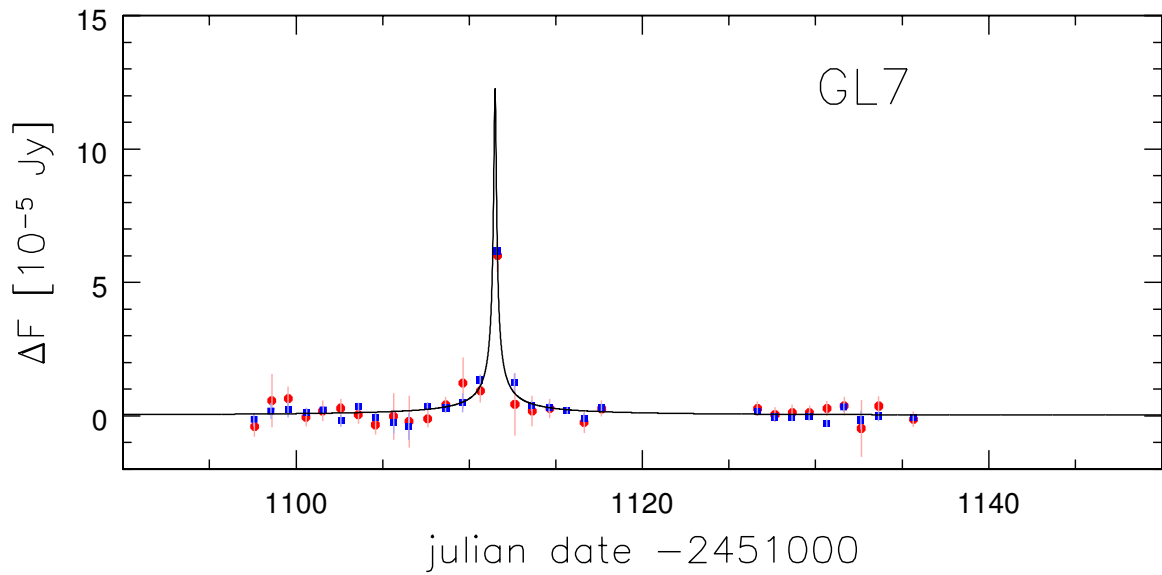
Figure 5.8: *Top*: Light curve of WeCAPP-GL7. The *R*-band data are shown by blue symbols, the *I*-band data by red symbols. The *I*-band data were scaled to the *R*-band data using the $(R - I)$ color of the event as derived from the degenerate fits to the light curves. This event has a full-width timescale below 0.5 days. *Bottom:* This figure shows on the left the 'event image' of WeCAPP-GL7. On the right we show the *R*-band time series at the position of GL7 around the time of maximum amplification.
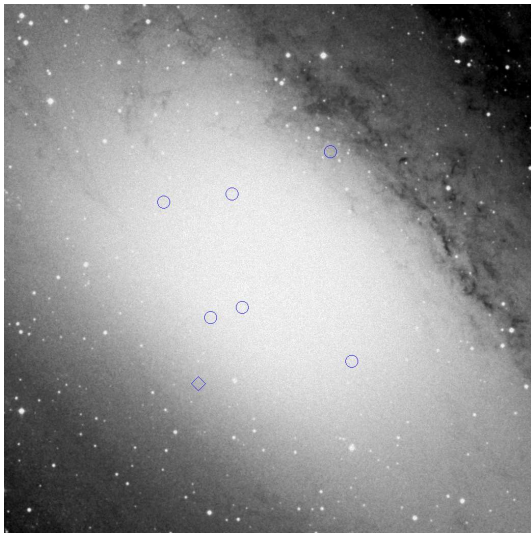
Figure 5.10: Spatial distribution of the microlensing events. With blue circles we mark events which were detected with approximately the same survey efficiency. With a blue diamond we mark GL3, which had its maximum amplification at a time where the survey was restricted to field F1.

a confirmation in the Wendelstein data as bad weather prevented observations during the time of the event. However, both events are well detected in *R*- and in the *I*-band data taken at Calar Alto. This again proves the importance of a good time sampling of the observations. For GL6 and GL7 we have constructed difference images of each image taken during the nights of maximum amplification of the sources. Both events are visible in each of these non-stacked difference images, and show well behaved PSFs in these frames. We can therefore exclude non-detected cosmic rays as possible sources of the events. The light curves of GL6 and GL7 are well covered for more than 4 years and show these singular brightenings only. Optical novae show asymmetric light curves with fast rises and longer decline timescales (see chapter 7). The symmetry of the light curves and their short timescales makes novae and other erupting variables unlikely as being the cause of the events. We therefore conclude that microlensing is the most probable interpretation for GL6 and GL7.

As can be seen in Table 4.2 in chapter 4, self-lensing shows a small asymmetry of the expected events rates towards the near and far side of the M31 disk. This can be ascribed to the different luminosity and mass functions of the bulge and disk population which leads to different event characteristics for disk-bulge and bulge-disk lensing. Halo-disk lensing by a 100% Macho halo, on the other hand, shows a more pronounced asymmetry. The spatial distribution of the 7 microlensing events is given in Fig. 5.10. The candidate event GL3 is marked with a blue diamond, as at the time of its detection the survey was restricted to the lower left part of the field (field F1, see chapter 2). The distribution does not show an evident asymmetry (as far as one can say from the small number of events), which points to self-lensing as being the dominant source for the lensing events. Moreover, also the detected number of events seems to be consistent with the expectations for self-lensing. According to Table 4.2 in chapter 4 we expect self-lensing to contribute 4.3 events per year without finite-source effects affecting the light curves. This number was derived for a minimal signal-to-noise ratio of 10 and a minimal full-width timescale of 1 day, which are comparable thresholds as used in our detection procedure. All of our 7 candidates show signal-to-noise ratios in the *R*-band above 7 (6 of them have values above 10), but they have been detected using a lower threshold for the full-width-timescale. However, as can be seen from Fig. 4.8 in chapter 4, the number of events stays rather constant for high $\left(\frac{S}{N}\right)$ thresholds and rises only moderately for smaller thresholds, when reducing the lower threshold for the full-width timescale. Therefore we do not expect the event rate to increase much for lower $t_{\text{fwhm}}^{\min}$ thresholds. For the search for microlensing events we basically are restricted to the three campaigns 1999-2002 where the simultaneous observations at Wendelstein and Calar Alto resulted in a dense time sampling of the observations. Furthermore, the campaign 1999/2000 which yielded one microlensing candidate (GL3) was restricted to one quadrant of the whole observed area. The

subsequent campaigns at Wendelstein from 2002-
2005 have a time sampling to sparse to search effi-
ciently for microlensing candidates. Moreover, as
a part of the observed field is covered by intrinsic
variable sources (see chapter 6), the effective area
which can be used for the search for microlensing
events is reduced. Assuming that the efficiency
of the survey has not exceeded 50% also during
the years 1999-2002, where the non-observability
of M31 during one third of the year is already
included, the number of the detected 7 events is
in agreement with the theoretical predictions for
self-lensing. To strengthen this result we have,
however, to take into account the effects of the
time sampling and noise properties of our sample
on the detectability of lensing events. Results of
the modeling of these effects for events of differ-
ent durations and amplitudes using Monte-Carlo
simulations is part of the future work on the data
set.

By combining the number and the distribu-
tions of the flux excesses and timescales of the
detected candidates with the efficiency simula-
tions and the theoretical predictions we expect to
constrain the halo fraction of the Macho popu-
lation in M31 further. These upcoming calcula-
tions will add an independent result to the con-
flicting interpretations of the M31 Macho popu-
lation published by the POINT-AGAPE (Calchi
Novati *et al.*, 2005) and MEGA (de Jong *et al.*,
2005) collaborations.

Chapter 6

The M31 variable star catalogue[1]

Abstract. In this chapter we present the WeCAPP catalogue of variable stars found in the bulge of M31. Observations in the WeCAPP microlensing survey (optical R and I bands) for a period of three years (2000-2003) resulted in a database with unprecedented time coverage for an extragalactic variable star study. We detected 23781 variable sources in a $16.1' \times 16.6'$ field centered on the nucleus of M31. The catalogue of variable stars contains the positions, the periods, and the variation amplitudes in the R and I bands. We classified the variables according to their position in the R-band period-amplitude plane. Three groups can be distinguished; while the first two groups can be mainly associated with Cepheid-like variables (population I Cepheids in group I; type II Cepheids and RV Tauri stars in group II), the third one consists of Long Period Variables (LPVs). We detected 37 RV Tauri stars and 11 RV Tauri candidates, which makes this catalogue one of the largest collections of this class of stars so far. The classification scheme is supported by Fourier decomposition of the light curves. Our data shows a correlation of the low-order Fourier coefficients Φ_{21} with Φ_{31} for classical Cepheids, as well as for type II Cepheids and RV Tauri stars. Correlating our sample of variable stars with X-ray based catalogues of Kaaret (2002) and Kong *et al.* (2002) results in 23 and 31 coincidences, 8 and 12 of which are M31 globular clusters. The number density of detected variables is clearly not symmetric, which has to be included in the calculations of the expected microlensing event rate towards M31. This asymmetry is due to the enhanced extinction in the spiral arms superimposed on the bulge of M31, which reduces the number of sources to about 60%, if compared to areas of equivalent bulge brightness without enhanced extinction.

---

[1]This chapter has been published in Fliri, Riffeser, Seitz, & Bender (2006).

6.1   Introduction

In the past decade the microlensing surveys of the galactic bulge and the Magellanic Clouds (LMC and SMC) have greatly extended our knowledge of variable stars. As the observations of these experiments usually cover a long time span with good time sampling, the resulting data sets are perfectly suited for the study of many different types of variable sources. Hence, lots of the progress in this field has resulted from the work of collaborations like MACHO (e.g., Alcock *et al.* 1995b, 1998), EROS (e.g., Beaulieu *et al.* 1995; Derue *et al.* 2002), OGLE (e.g., Cieslinski *et al.* 2003; Wray *et al.* 2004) or MOA (e.g., Noda *et al.* 2002, 2004). The list of identified variable stars in the Galaxy and the Magellanic Clouds was enlarged in numerous publications, which not only improved on the number statistics, but has also helped to understand the physical processes dominating these stars better.

M31 has been surveyed for variable sources since the 1920s, starting with the pioneering work of Edwin Hubble. With plates taken at the newly available Mount Wilson telescope, Hubble succeeded in resolving Cepheid variables in the outer parts of M31. Using the already established period-luminosity relation, Hubble (1922) was able to determine the distance to M31 to 300 kpc (the difference to the actual value of 770 kpc (Freedman & Madore, 1990) is mainly due to an erroneous calibration of the zero-point of the PL-relation and a missing reddening correction) and in this way to reveal the extragalactic nature of the 'Andromeda Nebula'. Baade & Swope (1963, 1965) continued the work on variable stars in M31 and detected over 400 variables, among them Cepheids and novae. Looking at the relations between period, luminosity, amplitude, and frequency, they found that these Cepheids resemble the ones in the Milky Way, but seem to be different from those in the Small Magellanic Cloud.

More recently, the DIRECT project (Kaluzny *et al.*, 1998) performed a comprehensive variable star study in M31 with the main goal being to re-duce the uncertainties in its distance determination. The DIRECT collaboration identified and examined Cepheids and Detached Eclipsing Binaries in five fields of the M31 disk, which was published in a series of papers. Unfortunately, the data of a 6th field of the bulge of M31, which in part overlaps with our surveyed area, remained unpublished.

In the last years Andromeda was a preferred target for a new kind of microlensing experiment. M31 has the advantage of offering the possibility to distinguish between lensing by dark halo objects (Machos) and lensing by stars in M31 (a contribution called 'self-lensing') in a statistical way, using the near-far asymmetry of the microlensing event rate. As the disk of M31 is highly inclined ($77°$, Stanek & Garnavich 1998) one expects more Macho events towards the far side of the M31 disk than towards the near side. Detecting an asymmetry in the event rates would thus help to distinguish between both kinds of events.

Several 'pixellensing' surveys - AGAPE (Ansari *et al.*, 1997), POINT-AGAPE (Auriere *et al.*, 2001), WeCAPP (Riffeser *et al.*, 2001), MEGA (de Jong *et al.*, 2004), SLOTT/AGAPE (Calchi Novati *et al.*, 2002) - therefore observed the bulge and parts of the disk of M31 fairly continuously, and also generated catalogues of variable sources. The work presented in this chapter thus overlaps with the work resulting from the AGAPE (Ansari *et al.*, 2004) and POINT-AGAPE (An *et al.*, 2004) data sets.

In contrast to classical microlensing surveys, pixellensing experiments monitor the variation in the surface brightness of a nearby galaxy rather than the variation in the luminosities of resolved stars. Two methods were developed and implemented to overcome the problem of crowding: the super-pixel method (Baillon *et al.* 1993b, used by the AGAPE and POINT-AGAPE collaborations) and difference imaging (Tomaney & Crotts, 1996; Alard & Lupton, 1998), which we used to extract and measure the variable sources.

The principle of difference imaging is
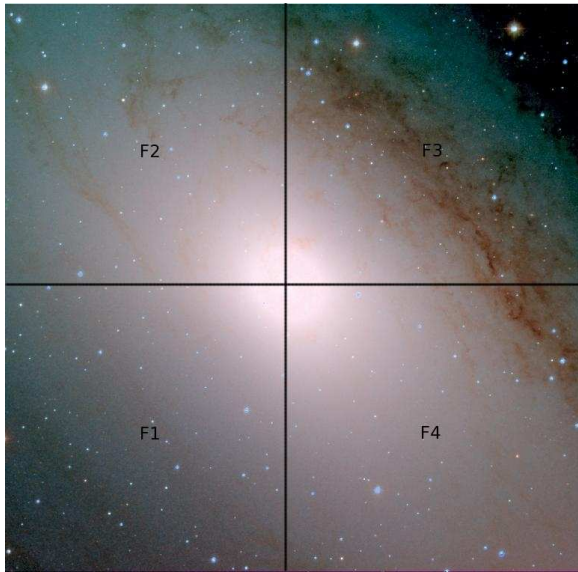
Figure 6.1: *V*-, *R*-, and *I*-band composite image of the observed fields F1 to F4, taken at Calar Alto Observatory during the campaign 2000/2001. The black lines mark the positions of fields F1 to F4. The identified variable sources lie within RA(2000): [00h43m25.0s, 00h41m59.9s] and DEC(2000): [41d08′00.1″, 41d24′18.0″].

straightforward: positionally and photometrically aligned images of two different epochs are subtracted from one another, and if a source changes its luminosity between the two epochs, it shows up as a point source in the difference image. All blended flux cancels out and contributes only to the noise level in the difference image. The success of difference imaging strongly depends on the quality of the matching of the point spread functions (PSFs) between the two images. In our implementation, the residuals in the difference images reach the theoretical Poisson noise limit (see chapter 2). As the Poisson noise of the M31 surface brightness is the limiting factor for the detection of the variable sources, we stacked all images of one night and generate difference images from these co-added images.

Due to this daily stacking scheme, we were not sensitive to variations and to periods smaller than 1.3 days, and focus therefore on longer pe-

riod variables, namely Cepheids, RV Tauri stars, and Long Period Variables (LPVs), i.e. Miras and semi-regular variables. The catalogue is completed by eclipsing binaries and by variables showing eruptive or irregular variations. The δ Scuti and RR Lyrae stars show variation amplitudes below our detection limit and will therefore be missed in this study.

This chapter is organized as follows. In Sect. 6.2 we give an overview of the survey, the observations, and data reduction. Section 6.3 deals with source detection and the derivation of periods of the variables. In Sects. 6.4 and 6.5, we show the different groups of variable sources detected in the survey. The catalogue of variable stars is presented in Sect. 6.6 and is correlated with *X*-ray selected catalogues in Sect. 6.7. While Sect. 6.8 summarizes the chapter, the appendix deals with the accuracy of the derived periods.

6.2 Data and data reduction

The results presented in this chapter are based on three years of observations of the central part of M31 by the WeCAPP project. We analyzed the data covering the years 2000 to 2003 for variable sources. The field of views (FOVs) and the cameras and filters used are given in chapter 2. The epochs with data taken for the four fields F1 to F4 (see Fig. 6.1) are shown in Fig. 6.2. The data were reduced using the reduction pipeline mupipe (see chapter 2). In the last step, mupipe returns roughly $4 \cdot 10^6$ pixel light curves together with appropriate errors, with each of the light curves representing the time variability of the flux present inside the PSF centered on the particular pixel. The extraction of intrinsic variable sources from these pixel light curves is presented in the next section.

The astrometric solution for our fields was created using the IRAF[2] tasks ccmap and cctran

---

[2]IRAF is distributed by the National Optical Astronomy Observatories, which are operated by the Association of Universities for Research in Astronomy, Inc., under cooperative
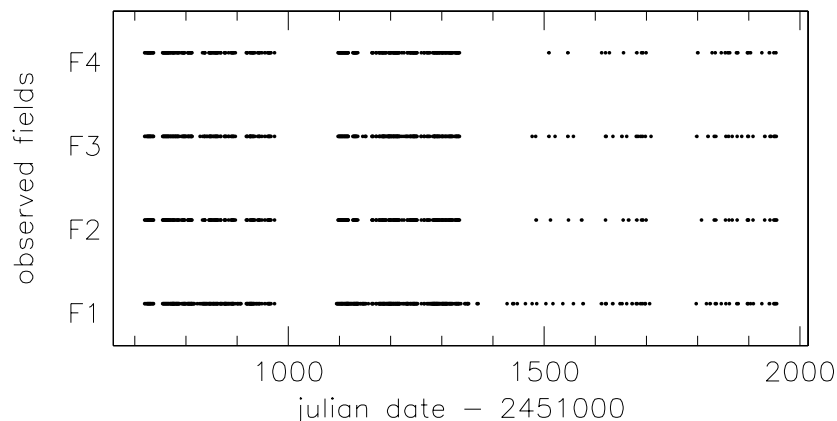
Figure 6.2: Distribution of the observations for the four fields. During the first two campaigns, we reached a very dense time sampling of the observations. Note that the third and fourth campaigns were restricted to Wendelstein Observatory only.

for 92 stars whose positions were taken from the Local Group Survey (LGS, Massey *et al.* 2001). The rms of the solution is $0.10''$ in declination and $0.12''$ in right ascension. The coordinates derived here agree perfectly with the ones derived in Riffeser *et al.* (2001) and Riffeser *et al.* (2003).

6.3 Detection of variable sources

6.3.1 Source selection

For the selection of the intrinsic variable sources, we used the *R*-band data from the Calar Alto campaigns 2000/2001 and 2001/2002 to create a χ^2_ν variation frame. To get rid of systematic effects induced by the different seeing conditions of each frame we used the following approach. We selected a stacked image with roughly the median seeing of the 2000/2001 campaign (about $1.5''$) as the master frame and matched the PSF of each stacked frame with a smaller PSF to the one of the master frame. In this way we ended up with difference images for 113 epochs (i.e. 48 % of the epochs with *R*-band data obtained at Calar Alto), which were then used to detect the variable sources. For each of the light curves extracted from the PSF$_{1.5}$ difference images, we calculated

the reduced χ^2_ν deviation from a constant (i.e. zero) baseline fit. The errors entering these calculations were the errors propagated by mupipe. The results were written into a χ^2_ν-frame of the field. The mode of the χ^2_ν-frame is 1.02, which shows the accuracy of the propagated errors. To avoid contamination of the M31 sample with foreground objects, we set all pixels in a radius of 5 pixels around the positions of bright foreground stars to zero before detecting the variable sources in the χ^2_ν-frame. We determined the positions of the variable sources using the SExtractor software (Bertin & Arnouts, 1996) for source detection applied on the χ^2_ν-frame. In this way we detected 25571 variable sources in our observed field. Figure 6.3 shows an extract of the χ^2_ν-frame with the positions of the detected sources marked.

6.3.2 Period determination

We used an algorithm developed by Lomb (1976) and Scargle (1982) to determine the significance and the value of the period of the variables sources. The method of Lomb is perfectly suited for this problem as it is able to deal with unevenly sampled data.

The algorithm extracts the power in the first sine and cosine terms for a set of equally spaced

---
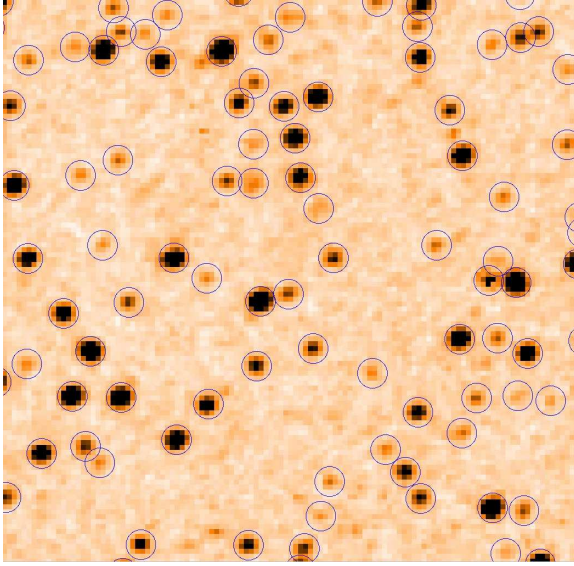
Figure 6.3: Extract $(1' \times 1')$ of the χ_ν^2-frame of over 25000 variable sources detected by the We-CAPP microlensing survey of M31. The circles give the positions of the sources detected by SEx-tractor. Most of the sources are first identifica-tions, the majority of them being Long Period Variables (LPVs), i.e. Miras and semi-regular variables (see Sect. 6.4).

Figure 6.4: Two examples of power spectra $P_N(\omega)$ of WeCAPP variables. In the upper panel, we show the periodogram for a Cepheid (see also Fig. 6.20) derived from the R-band data; in the lower panel, we show the periodogram for a LPV (see also Fig. 6.24) derived from the I-band data.

frequencies and also yields the significance of the detected peaks in the power spectrum. The Lomb normalized periodogram for N measured data points $h_j = h(t_j)$, $j = 1, ..., N$, taken at epochs t_j, is defined by

$$P_N(\omega) = \frac{1}{2\sigma^2} \frac{\left[\sum_j (h_j - \bar{h}) \cos \omega (t_j - \tau)\right]^2}{\sum_j \cos^2 \omega (t_j - \tau)}$$
$$+ \frac{1}{2\sigma^2} \frac{\left[\sum_j (h_j - \bar{h}) \sin \omega (t_j - \tau)\right]^2}{\sum_j \sin^2 \omega (t_j - \tau)} \quad , \quad (6.1)$$

where $\omega = 2\pi\nu = \frac{2\pi}{P}$ is the angular frequency for period P. The mean $\bar{h}$, variance σ^2, and constant τ are defined as follows

$$\bar{h} \equiv \frac{1}{N} \sum_{j=1}^{N} h_j \ , \qquad (6.2)$$

$$\sigma^2 \equiv \frac{1}{N-1} \sum_{j=1}^{N} (h_j - \bar{h})^2 \ , \qquad (6.3)$$

$$\tan(2\omega\tau) \equiv \frac{\sum_j \sin 2\omega t_j}{\sum_j \cos 2\omega t_j} \ . \qquad (6.4)$$

The last definition ensures that the power spec-trum is independent on a shift of each t_j by Δt, as τ transforms in that case into $(\tau + \Delta t)$. Lomb (1976) has shown that the evaluation of the pe-riodogram according to Eq. 6.1 is identical to a linear least-squares fit of the first harmonics

$$F(t) = A \sin \omega t + B \cos \omega t \qquad (6.5)$$

to the data points. In Fig. 6.4 we show two ex-amples for $P_N(\omega)$, the first one derived from a Cepheid light curve and the second from the light curve of a LPV.

The significance level $P(> z)$ of a peak with amplitude z in the power spectrum is given by

$$P(> z) \equiv 1 - (1 - e^{-z})^M \quad , \qquad (6.6)$$

with $(1 - e^{-z})^M$ being the probability that none of the M tested frequencies shows a greater ampli-

tude than z in case of pure Gaussian noise. Horne & Baliunas (1986) showed, with extensive Monte Carlo simulations, that the value of M, i.e. the number of independent frequencies, does not differ much from the number of data points N, if the data points are not closely clumped.

We used the algorithm from the Numerical Recipes (Press, 1988). Small modifications in the code allowed us to search for the different maxima in the power spectrum. The positions and values of the peaks are returned and can be used for further study of the light curves. In this implementation, the significance $P(>z)$ is approximated for small values of $P(>z)$ by

$$P(>z) \approx Me^{-z} \quad , \qquad (6.7)$$

where M is a product of the number of data points N and a user supplied value, which determines the high end cut-off of the tested frequencies relative to the Nyquist frequency.

6.4 The variable sources

6.4.1 Creating the catalogue

We detected 25571 variable point sources in a $16.1' \times 16.6'$ field centered on the nucleus of M31. As this sample still can contain spurious detections or sources with only a few data points measured in the light curve, we applied a couple of cuts which marked different levels of accuracy of the derived periods and showed the need for a visual inspection.

As first cut we demanded that the light curve comprises at least 40 data points in both filters. All sources which did not pass this criterion were removed from the sample. This reduced the number of variables to 25316 and defined the **level A sample**. In Fig. 6.5 we show the histogram of the number of epochs for these sources in the R-band (black curve) and I-band (red curve). The lowest number peaks represent the time sampling present in fields F2 and F4, followed by the peak corresponding to field F3. As F2 and F4 were observed with comparable frequency, both fields
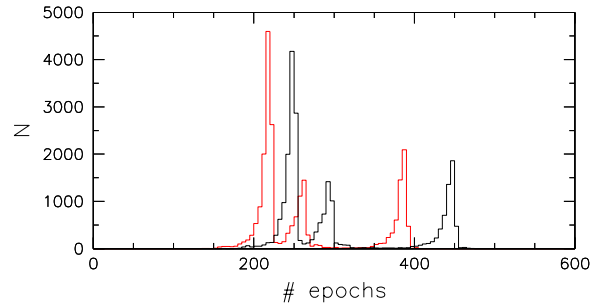
Figure 6.5: Histogram of the number of epochs of the level A sources in the R- band (*black curve*) and I-band (*red curve*). For sources located in field F1, we usually got data points in the R-band on more than 400 epochs.

contributed to the lowest number peak. The last peak, with usually more than 400 epochs in the R-band, is related to field F1.

As the Lomb algorithm assumes that all data points have the same error (see Eqs. 6.1 and 6.3), data points with big error bars or outliers can spoil the period-finding process and yield spurious periods. To avoid this, we first eliminated in each light curve ten data points with the biggest errors and, in a second step, five data points with the highest as well as five data points with the lowest values. In doing so, we ensure that we have at least 20 data points in both filters to look for a periodic signal.

We then checked the R-band and I-band light curves separately for periodicities. As the color of variable stars usually changes during a cycle, combing the two data sets would not result in accurate determinations of the period of the sources. Finally we obtained 25316 variables with determined periods (of any significance level) in both bands.

We regard those periods as real that are the same in both bands inside tight boundaries reflecting the error of the period determination. For periods $P_R < 215$ days, we took the theoretical error (see Eq. 6.17) resulting from ν_{FWHM} as limit, while from 215 days onwards we chose a more conservative constant limit of 30 days, which was

increased to 60 days for $P_R > 400$ days. This criterion defined the **level B sample** (20311 objects).

As the final cut we selected all those variables from level B which showed a significance level of the period determination of $P(> z) < 10^{-10}$ in R or I and which had a determined R-band period $P_R \leq 450$ days. This final cut reduced the number of sources to 19551 and defined the **level C sample** with well-determined periods. The remaining sources in level B were inspected visually and assigned to the group of regular, irregular, long-variation (period could not be determined because of an incomplete cycle) or miscellaneous variables in the **final catalogue**, or were rejected from the sample as spurious detections. Finally, all sources of the level C sample were added automatically to the final catalogue.

For the variables which showed deviant periods in R and I, we proceeded as follows. If the significance level of one of the deviant periods was better than 10^{-15} and at the same time better than the significance in the other band by a factor of 10^{10}, we chose the period in the first band and add the variable to the final catalogue. If this was not the case, we inspected the light curve visually and decided if one of the periods was the real one, or if the variation was of an irregular nature. In this step we also rejected the last spurious detections from the sample and the true variables were added to the final catalogue.

Search for eclipsing binaries

By visual inspection of the folded light curves of the Lomb sample, we detected 28 eclipsing binary (EB) candidates, amongst them one (semi-) detached system. However, the Lomb algorithm can fail in detecting periods for potential EB systems in M31. As EB light curves, especially the ones of detached systems, show strong power in the higher harmonics, they are not recovered well by Fourier techniques using only the first harmonic. Since some EB candidates could therefore be missed by using the Lomb algorithm alone, we added another step to the search for EBs. We once

Figure 6.6: Histogram of the periods of the 31 eclipsing binary candidates. The 4 (semi-) detached systems populate the low period area up to a period of 7 days, whereas the contact system candidates generally have longer periods.
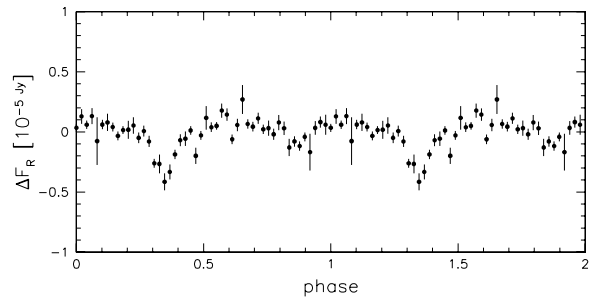
Figure 6.7: Binned R-band light curve of a semi-detached system in the phase representation. The system has a R-band period of 7.0791 days.

more investigated all light curves that had been removed in the previous steps; however this time we used the dedicated transit finding algorithm 'boxfitting' (Kovács *et al.*, 2002) for the period determination. As Tingley (2003) has shown, the boxfitting algorithm is a powerful tool for detection of eclipsing systems. We implemented the original Fortran code[3] into our detection pipeline and ran the algorithm over the mostly noisy light curves that had been removed from the sample as spurious detections in the previous steps. In this way we made certain to have proper periods for all potential EB candidates present in our variable sources.

Selecting all light curves with a reasonable

---

[3]http://www.konkoly.hu/staff/kovacs.html

signal detection efficiency (SDE, Kovács *et al.* 2002) SDE > 6, periods $P > 1.30$ days and rejecting periods between 1.95 days and 2.05 days (to avoid to pick up aliasing periods) together resulted in an additional sample of 155 light curves. Visual inspection of the folded light curves finally yielded 3 additional candidates for (semi-) detached eclipsing binary systems.

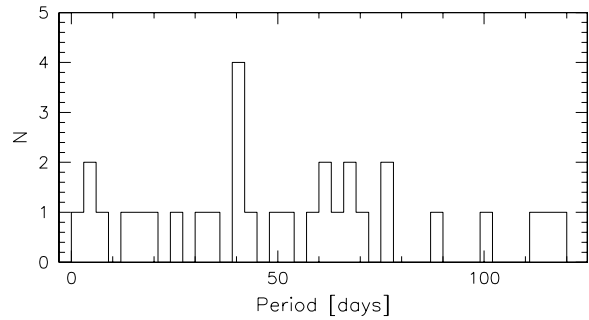In Fig. 6.6 we show the distribution of periods of the 31 EB candidates. The 4 (semi-) detached systems populate the low period area up to a period of 7 days, whereas the contact system candidates generally have longer periods. Figure 6.7 presents the binned *R*-band light curve of a semi-detached system in the phase representation. The system was detected using the Lomb algorithm and has a *R*-band period of 7.0791 days.

6.4.2   Number counts and asymmetry

The positions of the variables from the final catalogue suggest a connection of the enhanced extinction in M31's spiral arms and the depletion of sources in certain regions in the northern part of the bulge (field F3). This depletion is also evident from number counts of the sources in the northern and southern hemispheres of M31 (see Fig.6.8).

By summing up all variables in 100×100 pixel $[50'' \times 50'']$ bins, we calculated the number density of variable sources. In the resulting density map (Fig. 6.9), the spiral arms are clearly visible. A comparison of the number densities at equivalent positions in the M31 bulge - one in the dust lane of the spiral arms, the other in the opposite hemisphere - shows a reduction to about 60% compared to the part with no strong extinction.

To examine this subject further, we compared the number density map (see Fig. 6.9) with an extinction map of our field. In Fig. 6.10 we plot the positions of the sources on top of the *R*-band extinction map, which we derived from the *V*- and *R*-band frames taken by the Local Group Survey (LGS, Massey *et al.* 2001) in the following way:

We started from the relation between the color excess $E(V - R)$ and the extinction A_R in the *R*-
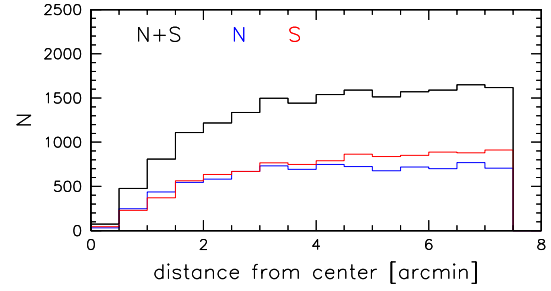
Figure 6.8: Number counts of sources of the catalogue as function of the distance to the center of M31. *Black:* all sources. *Blue:* sources in the northern hemisphere of M31. *Red:* sources in the southern hemisphere of M31. The asymmetry of the detected sources is clearly visible and is due to the enhanced disk-extinction in the northern part. The low number of sources near the center is due to incompleteness induced by crowding and saturated parts in the frames.

band ($a \approx 3$, see Binney & Merrifield 1998)

$$A_R = a \, E(V - R) \quad . \tag{6.8}$$

With the non-reddened magnitudes $M_{R,0}$, $M_{V,0}$ and reddened counterparts $M_{R,r}$, $M_{V,r}$, this writes as

$$M_{R,r} - M_{R,0} = a \left[(M_{V,r} - M_{R,r}) - (M_{V,0} - M_{R,0}) \right] . \tag{6.9}$$

The transformation to fluxes $F_{i,j}$ ($i = R, V; j = 0, r$) yields

$$F_{R,0} = F_{R,r} \left(\frac{F_{R,r}}{F_{V,r}} \right)^a \left(\frac{F_{V,0}}{F_{R,0}} \right)^a \quad . \tag{6.10}$$

If we now suppose that the intrinsic stellar population gradients are negligible over the field (which is not exactly true but a valid approximation for our purposes), we can set $\left(\frac{F_{V,0}}{F_{R,0}} \right) \approx constant$.

Using this assumption, we finally obtain a relation for $F_{R,0}$

$$F_{R,0} = \frac{F_{R,r}^{1+a}}{F_{V,r}^a} \left(\frac{F_{V,0}}{F_{R,0}} \right)^a , \tag{6.11}$$
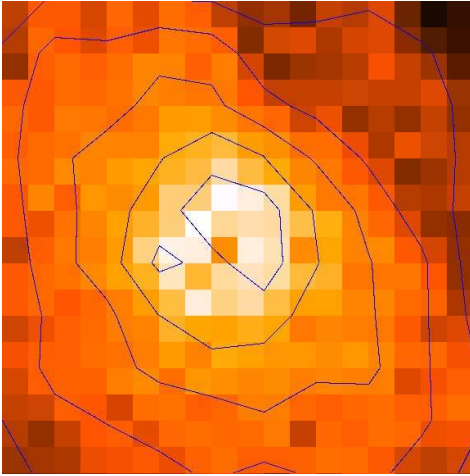
Figure 6.9: Number density of variable sources by summing up all variables in 100×100 pixel [$50'' \times 50''$] bins. To avoid effects induced by the border of the frame, we only use pixels in the region [200:2000,200:2000]. The contour levels are 1, 2, 3, 4, and 5 $\times 10^{-2}$ [arcsec^{-2}], respectively. The spiral arm is clearly visible. The regions with underdensities near the center are due to saturated parts in the frame with no variable sources detected.
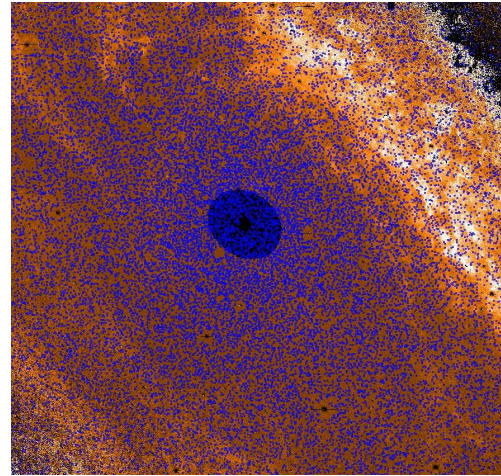
Figure 6.10: R-band extinction map of the M31 field. White areas correspond to high extinction values. The extinction in the R-band was derived using the V- and R-band images taken from the LGS survey (Massey *et al.*, 2001). Overplotted are the positions of the catalogue variables (*blue dots*). In the central regions, the extinction map could not be calculated due to saturation in the original LGS frames.

which can be used to calculate the extinction ext_R in the R-band

$$ext_R = -2.5 \log \left(\frac{F_{R,r}}{F_{R,0}} \right) \ . \qquad (6.12)$$

For the intrinsic color $(V - R)_0$ required in the calculation we use the theoretical value $(V - R)_0 = 0.63$, assuming the bulge to be a 12 Gyr old SSP of $2Z_\odot$ metalicity (C. Maraston, priv. comm., based on Maraston 1998). Figure 6.10 shows the resulting extinction map, indeed, under-dense variable source regions coincide with high extinction regions.

Finally we compared the number densities of sources present in our catalogue with theoretical predictions, using the fuel consumption theorem (Renzini & Buzzoni, 1986), which derives the

number of stars $\mathcal{N}_i$

$$\mathcal{N}_i = b_t \, t_{\mathrm{ev},i} \qquad (6.13)$$

in any evolved phase, given the size, metalicity, and age of a population. The evolutionary flux b_t is the number of stars which leave the main sequence at a certain time t, and the evolutionary timescale $t_{\mathrm{ev},i}$ is the time a star spends in a certain evolutionary phase. The evolutionary flux b_t is related to the specific evolutionary flux B(t), i.e. the number of stars which leave the main sequence per year and per bolometric solar luminosity of the population by

$$b_t = B(t) L_T \quad , \qquad (6.14)$$

where L_T is the total bolometric luminosity of the population. b_t is very close to the rate at which stars enter or leave any subsequent evolutionary stage.
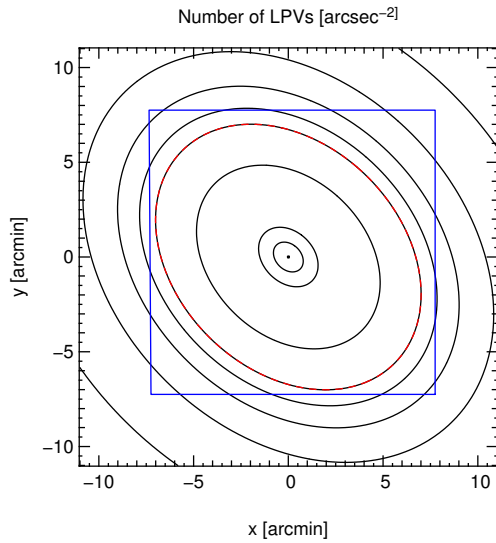
Figure 6.11: Theoretically expected number densities of LPVs according to Renzini (1998) calculated with the small bulge decomposition of Kent (1989b). The field is centered on the nucleus of M31; North is on top, and East is on the left of the diagram. The WeCAPP field for which we calculated the number density in Fig. 6.9 is shown by the blue rectangle. Contour levels are 1, 2, 3, 4 and 5 $\times 10^{-2}$, 0.1, 0.5, 1, 5 and 10 sources [arcsec^{-2}]. The red dashed line marks the 5×10^{-2} contour level.

According to Renzini (1998), the number of LPVs per integrated 10^5 bolometric luminosities is equal to 0.5. Renzini (1998) uses a slightly older (15 Gyrs) and less metal-rich (1 $Z_\odot$) bulge when compared to the model used for calculating the extinction frame. With the small bulge decomposition of Kent (1989b) and under the assumption that the LPVs are present in the bulge only, we derived the expected number densities of LPVs and show it in Fig. 6.11. There is a reasonable agreement between the theoretical predictions and the measured number densities in the outer parts of the field. Towards the center, we suffer from incompleteness due to enhanced noise, on the one hand, and crowding of the variable sources, on the other.

6.4.3 Classification scheme

As practically all of the detected sources are unresolved in the original frames, we cannot derive luminosities for the variable sources. Therefore, we are neither able to put the sources in the color-magnitude plane and to construct a color-magnitude diagram nor to derive period-luminosity relations for the different classes. The parameters available for establishing a classification scheme are therefore reduced, leaving the period, its significance, the amplitude of the variation, its (flux excess)-color, and finally the light curve shape as classification parameters. The light curve shape is of particular interest as it can be described mathematically and parameterized in terms of the parameters resulting from low order Fourier fits to the data. For classical Cepheids, the Fourier parameters show a progression with the period of the variation, echoing the well-known 'Hertzsprung progression' (Hertzsprung, 1926) of the light curve shape with period. For type II Cepheids similar correlations have already been found; analysis of the RV Tauri stars in our sample reveals a correlation between different phase parameters. Fourier decomposition of the light curves is, therefore, a powerful method to support the classification of Cepheid-like variables and distinguish them from other types of variables. Our classification scheme is based on the position of the stars in the R-band period-amplitude plane. For certain groups of stars, we refined and checked our classification by using the Fourier parameters of the fits to the light curves.

Period-amplitude-relations

Amplitudes ΔF_R and ΔF_I of the variation in the R-band and I-band are determined as half the difference of the maximum to the minimum of the light curves. As we calculated the amplitudes after having eliminated data points with the largest error bars and biggest flux differences, these amplitudes act only as a lower limit, but can be regarded as a robust measurement of the variation ampli-

tude. The amplitudes were transformed in magnitudes using the R- and I-band fluxes of Vega. Note that these magnitudes reflect the flux difference on the frame only, and are not the real variation magnitudes of a single star.

Figure 6.12 shows the relation between the logarithm of the period and the logarithm of the amplitude ΔF_R (i.e. the variation magnitude as measured in the frame) for the sources of the final catalogue. Three different groups can be distinguished in this diagram:

Group I has periods between 1.7 and 21.5 days, and there seems to be a correlation of the period and the amplitude of the variation as larger periods show larger amplitudes. We required $-2.5\log(\Delta F_R/F_{\mathrm{Vega}}) \le 23.1 - 2.76(\log P_R - 0.55)$ for sources belonging to this group. This relation as well as the dividing relation for group II sources is shown as a black line in Fig. 6.12. The stars in group I are most likely connected to the disk, as their light curves and the periods are connected to Cepheids of type I which belong to a young population.

Group II has periods in the range 12 and about 140 days. Also in this group, the period and the variation amplitude are correlated, whereas the sequence for the group II stars lies at fainter magnitudes than the one for the group I stars. The defining relations for this group are given by $-2.5\log(\Delta F_R/F_{\mathrm{Vega}}) > 23.1 - 2.76(\log P_R - 0.55)$ and $-2.5\log(\Delta F_R/F_{\mathrm{Vega}}) \le 23.0 - 3.5(\log P_R - 1.35)$. Group II stars most likely belong to the old spheroid population; RV Tauri stars, type II Cepheids, and the low period tail of the semi-regular (SR) stars are found in this group.

Group III finally contains the bulk of the detected variables and has periods longer than about 50 days. For this group no clear correlation between the amplitude and the period can be seen. All sources with $-2.5\log(\Delta F_R/F_{\mathrm{Vega}}) > 23.0 - 3.5(\log P_R - 1.35)$ belong here.

Fourier fits

We fitted truncated Fourier series of the form

$$\Delta F(t) = C + A_0 \Sigma_{i=1}^{N} A_i \cos(i\omega(t - t_0) + \Phi_i) \tag{6.15}$$

to the R-band light curves of groups I and II. Here C defines the baseline of the fit, A_0 reflects the overall amplitude of the light curve, and A_i and Φ_i define the amplitudes and phases of the different harmonics. The periods entering the fit are those returned by the Lomb algorithm. A fitting order of $N = 5$ leads to acceptable fits to the data.

Simon & Lee (1981) were the first to calculate amplitude ratios of the form $R_{ij} = A_i/A_j$ and phase differences $\Phi_{ij} = \Phi_i - i\Phi_j$ of the parameters of the different harmonics. Since for classical Cepheids both definitions show a progression with the period, as well as a correlation among one another, Fourier analysis proved to be an excellent diagnostic for examining the pulsation properties of these stars. Fourier analysis therefore was widely used in the past to examine Cepheids (e.g., Simon & Moffett 1985; Alcock *et al.* 1999), particularly to distinguish between fundamental and first overtone pulsators (e.g., Antonello & Poretti 1986; Beaulieu *et al.* 1995).

6.5 Classes of variables

6.5.1 Group I and II – Cepheid-like variables

Groups I and II are populated by Cepheid-like variables (population I Cepheids in group I, type II Cepheids and RV Tauri stars in group II) and by the small period tail of semi-regular variable stars, which start to contribute at periods from about 16 days onwards.

Population I Cepheids

Classical Cepheids are relatively young, intermediate mass population I stars. They pulsate in
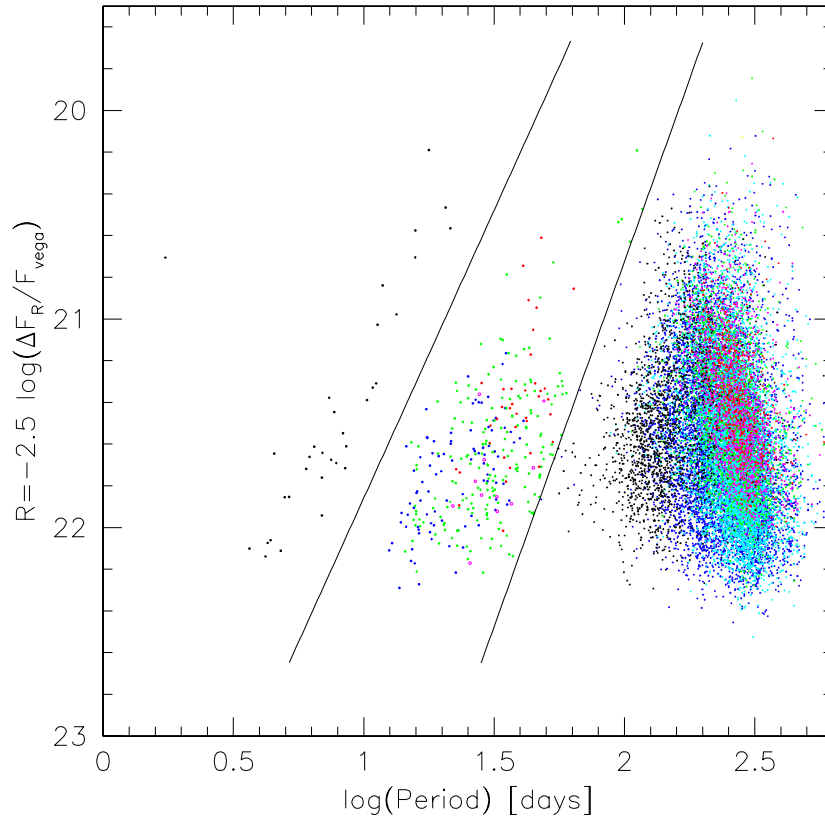
Figure 6.12: Period-amplitude relation in the *R*-band for the catalogue sources (eclipsing binaries, irregular, long-variation, and miscellaneous variables excluded). The amplitudes were transformed into magnitudes using the *R*-band fluxes of Vega. Note that these magnitudes only reflect the flux difference and are not the real variation magnitude of a single star. Three populations are visible in this diagram. The black lines show the defining relations (from left to right) for group I (population I Cepheids: *black dots*), group II (type II Cepheids: *blue dots*; RV Tauri stars: *red dots*; RV Tauri candidates: *open magenta circles*; SR variables: *green dots*), and group III (LPVs). For the RV Tauri stars and candidates, we use the single or fundamental period (minimum to minimum). The sources in group III are color-coded according to the significance of the *I*-band period as returned by the Lomb algorithm (low significance: black → blue → red: high significance).

the fundamental mode, which discriminates them from s-Cepheids, that are believed to pulsate in the first overtone. Both groups of population I stars have distinctive light curves, with the classical showing skewed and the s-type showing smooth sinusoidal variations.

We detected 33 population I Cepheids in our sample. To check whether our classification is correct and if there are first overtone pulsators (s-Cepheids) amongst the detected Cepheids, we fitted truncated Fourier series (see Sec. 6.4.3) to the light curves of group I. Figure 6.13 shows the characteristic progression of the Fourier parameters with the period of the light curve for the classical Cepheids: as the amplitude ratio R_{21} between the first and second harmonic drops the corresponding phase difference shows a mild rise. The amplitude ratio R_{21} declines until a period of about 10 days is reached, and then starts to rise again. Due to suppression of the second har-

monic, the Cepheid light curves in the vicinity of this period look quite sinusoidal. Figure 6.13 shows that the minimum of R_{21} is connected to a dramatic change of Φ_{21}. It is generally believed that this change is connected to the resonance between the fundamental mode and the second overtone $P_2/P_0 \approx 0.5$ (e.g., Simon & Moffett 1985).

First overtone pulsators can be detected using the amplitude ratio R_{21}, as s-Cepheids show lower values than their fundamental mode counterparts. Following Beaulieu *et al.* (1995) we demanded $R_{21} < 0.3$ for $P < 3$ days and $R_{21} < 0.2$ for $3 \le P < 5.5$ days for the Cepheids to be classified as first overtone pulsators. Using this criterion we identified 2 first overtone pulsators in our sample. One source with a R_{21} value close to the border with the s-Cepheids fell off the fundamental mode sequence in the phase difference diagram. Following Beaulieu *et al.* (1995), we classify this source as an intermediate Cepheid.

One source is clearly separated from the Cepheid relation in the period-amplitude plane (see Fig. 6.12). This variable shows Cepheid-like variations that are modulated by a period of 208 days in R. The modulation is most likely due to another variable source inside the PSF. Fourier decomposition of the R-band data shows that the source has two excited periods, 1.7330 days and 2.3515 days, besides the subdominant modulation of the light curve. In Fig. 6.14 we show the power spectrum of this source. The two periods would classify the source as a beat Cepheid, the first one detected in M31. Beat Cepheids are a rare sub-class of Cepheids in which two pulsation modes are excited simultaneously. The ratio of the two periods $P_{short}/P_{long} \approx 0.737$ makes it likely that we see a fundamental mode / first overtone (F/1H) pulsator, if the Cepheid hypothesis for this source is confirmed. For F/1H beat Cepheids, the first overtone should be the dominant mode, which is fulfilled for our candidate. Interestingly, the position in the (P_1/P_0) - $\log(P_0)$ diagram would place this beat Cepheid on a sequence defined by the SMC beat Cepheids of Beaulieu *et al.* (1997), well above the relations for
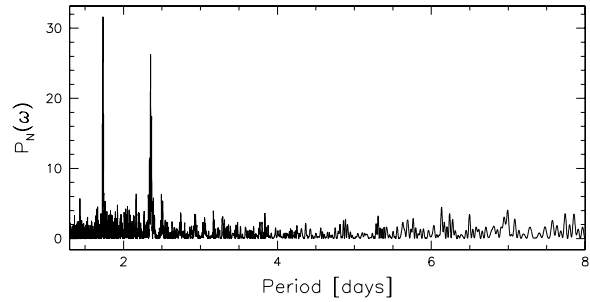
Figure 6.14: Power spectrum of the beat Cepheid candidate in the R-band. The two peaks in the spectrum correspond to periods of 1.7330 days and 2.3515 days.

the LMC and the Galaxy. This would point to a Cepheid in M31 of approximately the same metal content by mass as the SMC beat Cepheids. The position of this object coincides with a resolved source in our reference image, one which is classified as a star (Id 261262) in the Haiman *et al.* (1994) catalogue and which also correlates with an X-ray source in the Kong *et al.* (2002) catalogue. As the X-ray hardness ratio of this source points to a soft spectrum consistent with stellar X-ray emission, it is classified as a possible foreground star in the Kong *et al.* (2002) catalogue (J004301.8+411726, see also Table 6.3). Future investigations will show if these correlations are real or coincidental.

In addition to the beat Cepheid, there is another peculiar source in group I. It shows two periods of 6.9489 and 20.4960 days and remains unclassified at this stage.

Type II Cepheids and RV Tauri stars

Type II Cepheids are low-mass population II variables that follow a period luminosity relation about 1.5 mag below the classical Cepheid relation. They are found in old populations like globular clusters, the halo, the thick disk, or the bulge. Type II Cepheids with periods less than 5 days are also called BL Her or CVB stars, whereas type II Cepheids with periods between 10 and 20 days are often referred to as W Virgini stars. At
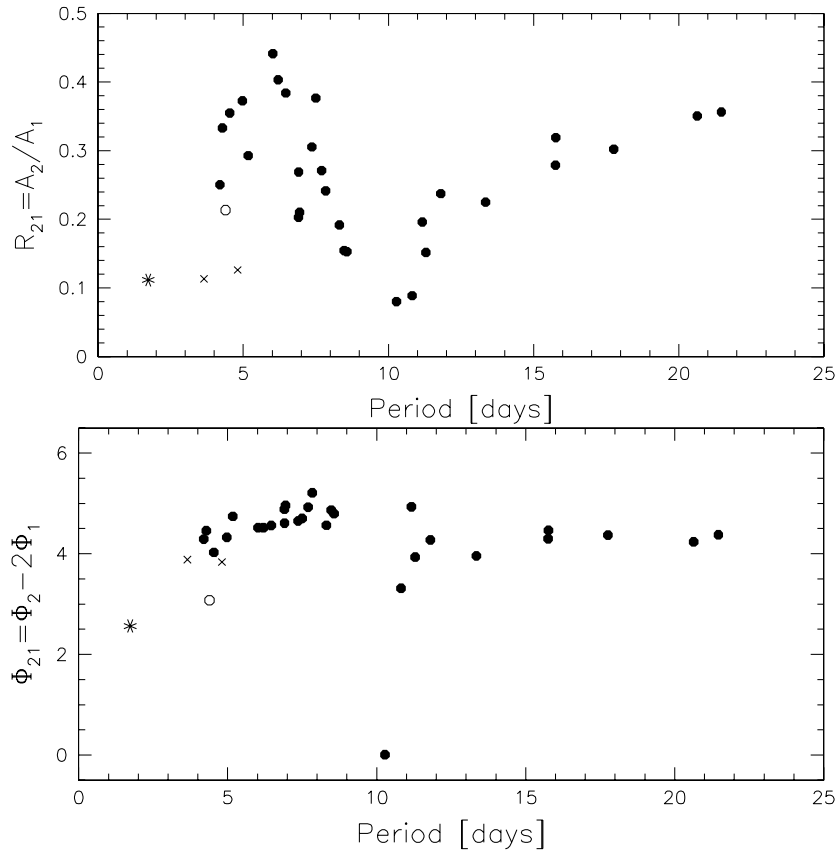
Figure 6.13: Amplitude ratio $R_{21} = A_2/A_1$ (upper panel) and phase difference $\Phi_{21} = \Phi_2 - 2\Phi_1$ (bottom panel) determined from the R-band data for the population I Cepheids (group I) plotted against the period. The ratio and phase difference drop as the periods approach the resonance $P_2/P_0 \approx 0.5$ at about 10 days and rise again afterwards. The R_{21} value classifies 29 of the detected Cepheids as fundamental mode pulsators (*closed circles*), whereas 2 are overtone pulsators (*crosses*). One of the Cepheids falls off the fundamental mode sequence in the phase difference diagram. Following Beaulieu *et al.* (1995), we classify this source as intermediate type Cepheid (*open circle*). The beat Cepheid candidate for which we used the dominant period (presumably the first overtone) in the analysis is marked with an *asterisk*.

the upper period limit, a period doubling can often be observed in the light curves. An approximate period limit of about 20 days (Alcock *et al.*, 1998) separates type II Cepheids from RV Tauri stars that share the same light curve and often also the same chemical and dynamical characteristics (Fokin, 2001). RV Tauri stars can be recognized by a typical double-wave light curve with alternating deep and shallow minima, their semi-periods (minimum to minimum) ranging from 20 to over 50 days. The current understanding places RV Tauri stars at the end of stellar evolution. After leaving the Asymptotic Giant Branch (AGB, Iben & Renzini 1983), they move left in the HR-diagram to enter the instability strip at high luminosities. For a recent review of population II Cepheids and related stars see Wallerstein (2002). A comprehensive collection of type II Cepheids and RV Tauri stars detected in the LMC by the MACHO collaboration can be found in Alcock
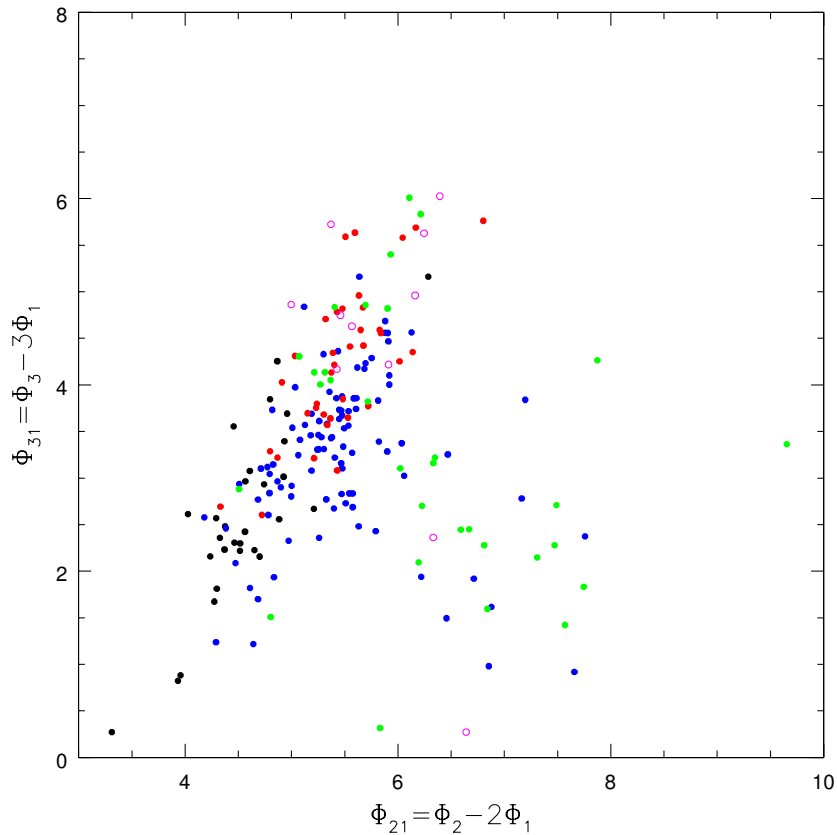
Figure 6.15: Phase differences $\Phi_{ij} = \Phi_i - i\,\Phi_j$ as determined from the *R*-band data plotted against each other. *Black dots:* population I Cepheids (group I); *blue dots:* type II Cepheids (group II); *red dots:* RV Tauri stars (group II); *open magenta circles:* RV Tauri candidates (group II). As *green dots*, we show the LMC type II Cepheids and RV Tauri stars from Alcock *et al.* (1998), which fall on the sequences of the WeCAPP sources. For the RV Tauri stars, we use the formal period in the analysis. The classical Cepheids show a clear correlation for the two parameters, but also for the type II Cepheids and the RV Tauri stars both phase differences are correlated. The sequences of RV Tauri stars and type II Cepheids overlap, making the RV Tauri sequence into an extension of the Cepheid II sequence. This favors the close connection between these two types of stars.

et al. (1998).

We detected 37 RV Tauri stars and 11 RV Tauri candidates, which makes this catalogue one of the largest collections of RV Tauris to date. The light curves show the typical alternation of deep and shallow minima, the second maximum being fainter than the first one, although for a few sources this latter difference is rather marginal. The light curve shape can be divided into two groups, one resembling the *'flat-topped'* Cepheid II shape (see Fig. 6.22), the other showing sinu-

soidal variations. To avoid misclassification of the sinusoidal light curves of RV Tauri stars with the not-too-different light curves of β-Lyrae eclipsing binaries, we extracted the phase difference between the second and the fourth harmonic from Fourier fits to the light curves. According to Szymanski *et al.* (2001) these two phases should be strongly coupled for sinusoidal contact systems, yielding $\Delta\Phi = \Phi_4 - 2\Phi_2 = 0$ (M. Szymanski, priv. comm.). For pulsating stars, the correlation is much weaker. Five of our RV Tauri candidates
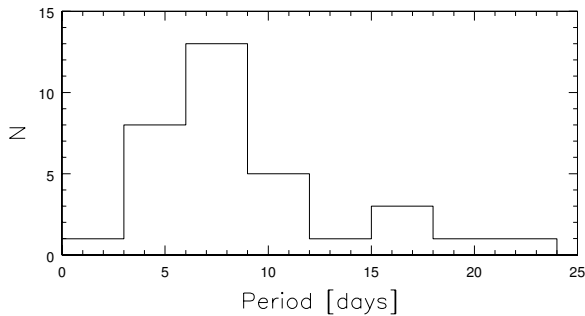
Figure 6.16: Histogram of the periods of the Cepheid variables in group I.

with sinusoidal light curves have a $\Delta\Phi$ within 1σ compatible with 0 (or equivalently 2π) and another 6 lie within 3σ. We classified all 11 RV Tauris whose $\Delta\Phi$ values are within 3σ compatible with 0 as RV Tauri candidates, and the remaining 37 sources as RV Tauri stars.

Using the fundamental period (minimum to minimum) for the Fourier extension of the RV Tauri sources yields relatively bad fits and subsequently more uncertain Fourier parameters. We therefore used the formal period in the analysis, which yields a more appropriate description of the data, better fits, and more reliable Fourier parameters. In Fig. 6.15 we show a 'phase-phase' diagram as a further result of the Fourier analysis of the RV Tauri and candidate RV Tauri light curves. The phase differences Φ_{31} and Φ_{21} correlate for the RV Tauri light curves (red dots), showing that these sources form a homogeneous group of stars. The RV Tauri candidates (magenta open circles) also follow the relation that supports the RV Tauri nature of these stars. Furthermore we show the detected type II Cepheids as blue dots in this figure. The sequences of RV Tauri stars and type II Cepheids overlap, making the RV Tauri sequence an extension of the Cepheid sequence at higher periods. This supports the close connection between RV Tauri stars and type II Cepheids. In fact, Alcock *et al.* (1998) show that a single period-luminosity-color relationship describes both the type II Cepheids and RV Tauri stars in the LMC. We show the phase

parameters for the stars presented in this study as green dots in Fig. 6.15. For this purpose we reanalyzed the light curves taken from the MACHO project database[4] and used the formal period to derive the Fourier parameters. Two stars with an uncertain classification were rejected from the analysis. The LMC variables lie on the sequence of the WeCAPP RV Tauri and Cepheid II stars, supporting our classification of the variables in group II. However, as we are not able to resolve the RV Tauri stars due to the high surface brightness of the central parts of M31 in the analyzed data set, we cannot finally prove the assignment of these stars as RV Tauri by placing the sources on a color-magnitude diagram.

The period range of the 93 type II Cepheids extends to periods longer than the approximate limit of about 20 days, as proposed by Alcock *et al.* (1998). There is still the possibility that some of these long-period Cepheids are in reality RV Tauri stars, since noise in the light curves can prevent the detection of the alternation of deep and shallow maxima as required for assigning of the variable as a RV Tauri candidate or star. The majority of the light curves of this type of variable have a '*flat-topped*' shape (Kwee, 1967) with relatively long and flat maxima. As already mentioned, the light curves of type II Cepheids show a progression of the phase differences and occupy distinct regions in Fourier space. The sample of type II Cepheids outnumbers the sample of population I Cepheids by about a factor of three. As the type II Cepheids trace the old bulge population, this is not unexpected, even when taking their smaller brightness compared to population I Cepheids (at the same period) into account. The population I Cepheids, more massive and younger than the type II Cepheids, are typical members of the M31 disk population, which is superimposed on the M31 bulge.

The third constituent of the group II sources are small-period semi-regular variables that contribute from periods of about 16 days onwards.

---

[4]http://wwwmacho.mcmaster.ca/Data/MachoData.html
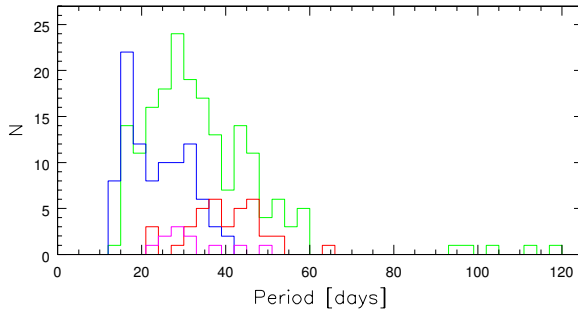
Figure 6.17: Histogram of the periods of variables belonging to group II. We show the distributions for type II Cepheids (*blue line*), RV Tauri stars (*red line*), RV Tauri candidates (*magenta line*), and the semi-regular stars (*green line*). For the RV Tauri stars and candidates, we use the single or fundamental period (minimum to minimum).

The Fourier analysis of the light curves shows no correlations of the amplitude ratios or phase differences with period. Phase-phase diagrams also do not reveal a correlation of the phase parameters. In Fig. 6.16 we give the period distribution of the population I Cepheids, whereas Fig. 6.17 shows the distribution of periods for variables belonging to group II. In red, magenta, blue, and green we present the distribution for the RV Tauri stars, RV Tauri candidates, type II Cepheids, and semi-regular variables.

6.5.2   Group III - LPVs

Group III consists of LPVs, i.e. Mira and semi-regular variable stars. LPVs are members of the AGB that marks the final stage of the stellar evolution for intermediate mass stars with masses between 0.5 and 8 $M_{\odot}$. Stars with masses up to $\approx 2.3 M_{\odot}$ evolve from the main sequence and populate the red giant branch up to a maximum luminosity at the TRGB (tip of the red giant branch). After ignition of helium burning in an electron degenerate core, they drop in luminosity and form the horizontal branch. At the end of this stadium, the luminosity rises again as the stars evolve upwards the AGB. For higher mass stars

helium ignition occurs under non-degenerate conditions. With a helium burning core they leave the RGB and perform blue loops in the Hertzsprung-Russell diagram (HRD, see chapter 1). Finally they also climb the AGB. The evolution sequence on the AGB is characterized by pulsation and extensive mass loss.

LPVs are a very promising tool for many astrophysical questions. They follow tight period-luminosity relations in the near-IR (especially the K-band) (Feast *et al.*, 1989; Wood, 2000; Feast *et al.*, 2002), which makes them excellent galactic and extragalactic distance estimators. They are furthermore good indicators of the parent population to which they belong, as there exists a dependence of the luminosity (hence, period) of Miras on the age. Longer period Miras should have higher mass progenitors and therefore belong to a younger population (e.g., Habing 1996). LPVs are historically separated into two main groups: i) Miras with regular variations, periods between 80 and 1000 days, and an amplitude of the variation in the *V*-band of more than 2.5 mag; ii) semi-regulars (SR) with less regular variations, smaller periods, and a *V*-band variation smaller than 2.5 mag. Semi-regulars are divided in two sub-groups, SRas with more regular variations and SRbs with less regular variations. Finally, there is the class of irregular variables, with show no evidence of periodicity. Stars with not well-studied light curves are often assigned to this class. As some semi-regular variables show phases of irregular variations, it is not clear if the irregular variables represent a fundamental different type of variability or are belonging to the semi-regular variable stars (Sterken & Jaschek, 1996; Lebzelter *et al.*, 2002).

Recently Lebzelter *et al.* (2002) proposed a new classification scheme that is less dependent on the artificial division in variation amplitudes, and used it for the AGAPEROS survey of variable red stars towards the Magellanic Clouds. Their classification is only based on the regularity of the variation, thereby providing three classes of stars: i) LPVs with regular variation ii) LPVs
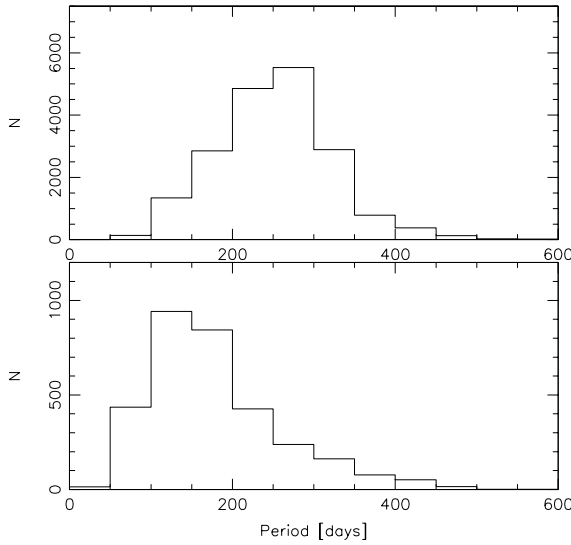
Figure 6.18: Distribution of the periods of LPVs in the bulge of M31. Top: class i - regular and semi-regular variables (significance level $P(> z) < 10^{-20}$ in R or I). Bottom: class ii - irregular variables (significance level $P(> z) \geq 10^{-20}$ in R and I). Only irregulars selected by the significance cut are shown. Note that the distribution for the sources classified as irregular variables is of a qualitative nature only, as the periods for these sources are not well-determined. In general irregular variables show smaller 'periods' than the group of regular and semi-regular variables.

with semi-regular variation iii) LPVs with irregular variation. No cuts in amplitude were applied, therefore class i contains members of the classical Mira group, as well as members of the SRa type of objects.

We modified this classification scheme for our purposes and defined a significance cut of $P(> z) = 10^{-20}$ according to the period-finding algorithm in R or I for the division of our sample of LPVs in classes i (regular and semi-regular) and ii (irregular). Class ii coincides with the class of irregular stars introduced in Sect. 6.4. Because of the non-linear dependence of the significance on the $\left(\frac{S}{N}\right)$ of the light curve (see discussion below), we do not rely on an automatic cut for the division into semi-regular and regular variations. The

cut at 10^{-20} is somewhat subjective, as stars with semi-regular variations, but low $\left(\frac{S}{N}\right)$ light curves are classified as irregular, since the low $\left(\frac{S}{N}\right)$ prevents the period being determined with better significance. On the other hand, this cut ensures that most of the irregular light curves are classified in the right way. The histograms of the periods for the irregular and the regular/semi-regular sample of LPVs are shown in Fig. 6.18. The irregular variables show on average smaller 'periods' than the group of regular or semi-regular variables. Note, that this statement is of qualitative nature only, as the periods for these sources are not well-determined.

We color-coded the LPVs in Fig. 6.12 according to the significance $P(> z)$ of the I-band period. The slope of the variation magnitude-period relation changes from slightly positive for the low significance tail (black dots) to negative for the sources with intermediate and high significant periods (green and red dots). The same trend can be seen in the left panel of Fig. 6.19, which shows the variation color $R - I$ as a function of the R-band variation magnitude. The significance of the I-band period rises for brighter R variation magnitudes and redder variation colors. The differences in the significance of the LPV I-band periods, therefore, is a result of the different $\left(\frac{S}{N}\right)$ of the I-band light curves (rising $\left(\frac{S}{N}\right)$ in I due to higher $R - I$ values), but can in part also be attributed to different stages of regularity in the light curves. The right panel of Fig. 6.19 finally shows the variation color $R - I$ as function of the period of the variable sources. The variation of the LPVs gets redder with increasing period, and at the same time shows more significant periods.

6.6   The catalogue

The final catalogue comprises 23781 variable objects with group I containing one beat Cepheid candidate, 2 s-Cepheids, one Cepheid of intermediate type, and 29 classical Cepheids pulsating in the fundamental mode. One further group I
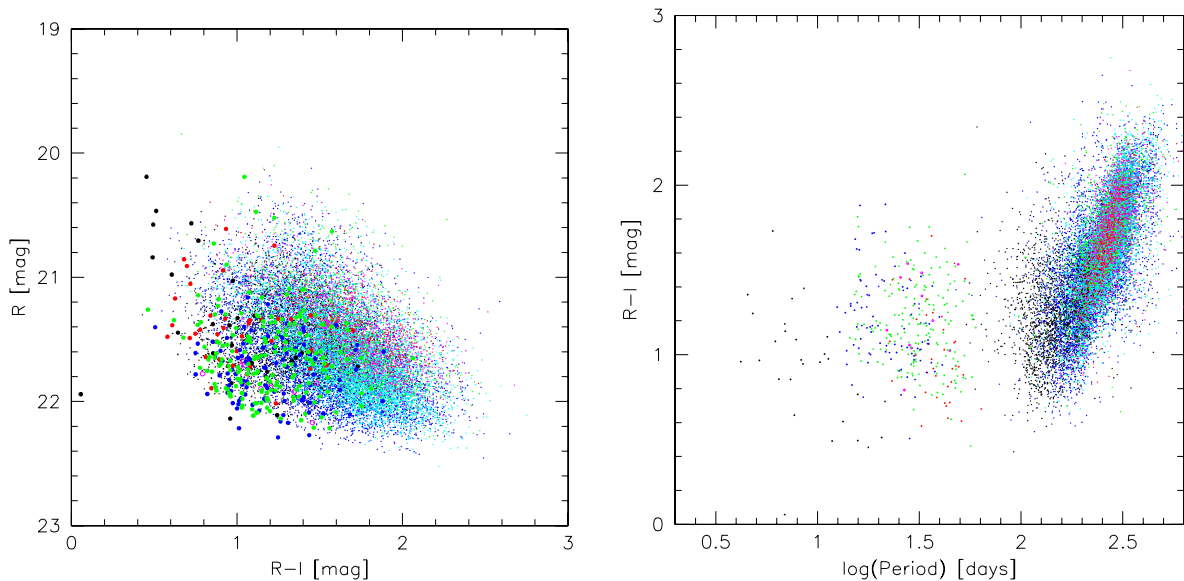
Figure 6.19: *Left panel:* Variation color $R - I$ shown as a function of the R-band variation magnitude. The sources of groups I and II are shown as big closed circles, the sources of group III as small closed circles. The color coding is the same as in Fig. 6.12, i.e. the LPVs are again color-coded according to the significance of the I-band period. The sources in groups I and II as a whole show bluer variations than the LPVs in group III. The significance of the I-band period rises for brighter R variation magnitudes and redder variation colors. This is a result of the higher $\left(\frac{S}{N}\right)$ of the I-band light curves, but can in part also be attributed to the enhanced regularity of the light curves. *Right panel:* This figure shows the variation color $R - I$ as function of the period of the variable sources. Note that due to the normalization to the fluxes of Vega in the particular systems, this $R - I$ color should not be mistaken with the color of the variation amplitudes of the sources. Nevertheless, some trends are visible in this diagram: As the variation of the LPVs gets redder with increasing period, the I-band periods become more significant, reflecting the rising $\left(\frac{S}{N}\right)$ in I due to higher $R - I$ values and a rising regularity of the light curves.

source, which remains unclassified in this catalogue, shows two periods.

Group II comprises 93 type II Cepheids, 37 RV Tauri stars, 11 RV Tauri candidates, and 193 low period semi-regular variables. Group III consists of 4287 irregular and 18974 regular/semi-regular variables. The 82 presumably group III members show variations on longer timescales than the survey length. The positions on the R-band period-amplitude plane of the 31 eclipsing binary candidates coincide with the positions of groups I and II. Finally we detected 39 miscellaneous variables, among them 16 novae and 15 R Coronae Borealis candidates.

The full catalog is available in electronic form at the CDS. We give the name, the position in the WCS, the periods (if available) derived from the R- and I-band data, the amplitudes of the variation ΔF_R and ΔF_I, and provide classification according to Sects. 6.4 and 6.5: DC (classical or δ-Cepheids), SC (s-Cepheids), BC (beat Cepheids), IC (intermediate Cepheids), W (type II Cepheids), RV (RV Tauri stars), rv (RV Tauri candidates), S (regular and semi-regular variations), and I (irregular variables). We also mark the identified Novae (N), eclipsing binary candidates (E), RCB candidates (RCB), and other miscellaneous variables (M). As an illustration of its

contents, in Table 6.1 we list the entries 100 − 120 in the catalogue. In Figs. 6.20 to 6.28 we show typical light curves for each of the groups.

6.7 Correlation with other catalogues

We cross-correlated our *R*-band selected catalogue with the General Catalogue of Variable Stars (GCVS, Durlevich *et al.* 1996) and catalogues selected in the *X*-ray (Kaaret, 2002; Kong *et al.*, 2002).

We found 23 coincidences with the Kaaret (2002) catalogue when using a search radius of $1''$. To estimate how many coincidences we expected by chance, we followed the approach proposed by Hornschemeier *et al.* (2001). We shifted one of the catalogues to be compared (in our case we shifted the catalogues taken from the literature) by $20''$ in north-east, south-east, south-west, and north-west directions, and checked for coincidences between these mock catalogues and our catalogue. By averaging these numbers, we got the expected number of coincidences by chance.

By applying a search radius of $1''$, the number of false coincidences with the Kaaret (2002) catalogue becomes 12. This high level of false coincidences (about 50%) results from the high number density of the variable star catalogue. Nevertheless, the false detections rate suggests that about 11 of the coincidences should be real. This is supported by the fact that 6 of the coincident sources are detected in the infrared and have an entry in the 2 MASS catalogue (Cutri, 2000), and 8 of the Kaaret-WeCAPP sources are identified as globular clusters (4 of them with a 2MASS entry, Kaaret 2002). Furthermore, we found that 13 of the sources have coincident counterparts in the Kong *et al.* (2002) catalogue as well (see below). In Table 6.2 we give the positions of all 23 coincidences, and we give the 2MASS name also for sources with entries in the 2MASS catalogue. Two of the Kaaret-WeCAPP sources with 2MASS fluxes (WeCAPP_V8946 and We-

CAPP_V10578) have no globular cluster (gc) counterpart (Kaaret, 2002). While V8946 coincides with a gc-candidate identified by Wirth *et al.* (1985), a gc-counterpart for WeCAPP_V10578 is completely unknown. Another two of the WeCAPP-Kaaret sources (V16322 and V10431) have been identified as optical novae showing supersoft *X*-ray emission (Pietsch *et al.*, 2005).

The Kong *et al.* (2002) catalogue contains 31 coincidences with our variable star catalogue when applying a $1''$ search radius. As we expect 17 coincidences by chance, about 14 of the coincidences should be real. As mentioned above, 13 of the sources are also coincident with the Kaaret (2002) catalogue. According to Kong *et al.* (2002), 12 of the sources have a globular cluster counterpart ($3''$ search radius), and 22 of the coincidences are variable in the X-rays at the 3σ level. We show the positions and identifiers of all 31 coincidences in Table 6.3.

The GCVS (Durlevich *et al.*, 1996) comprises 250 entries within our field of view, most of them of nova type. Of there 161 (6) were classified as novae, along with 53 as novae of fast type (NA), 9 (2) of slow type (NB), and (2) of very slow type (NC). Furthermore the GCVS reports 1 SNIa remnant in our field, 1 (1) LC type (irregular variable supergiant), 3 (1) semi-regular variables (SR), 3 δ-Cepheids, (1) SDOR variable, 2 (1+2) irregular variables, and 1 unstudied (S: classification) variable. The numbers in brackets give additional candidates for the particular variable star group with questionable classifications according to the GCVS.

The crowding of the WeCAPP sources demands that we keep the search radius at $1''$, even when comparing with the GCVS, whose accuracy is well below this value. We found 27 coincidences; the number of false detections (21) suggests, however, that most of the coincidences are not real. As 23 of them are classified as novae in the GCVS, we only show the 4 coincidences that we regard as real in Table 6.4. Note, that we do not match the positions of all three δ-Cepheids found in the GCVS inside our field.
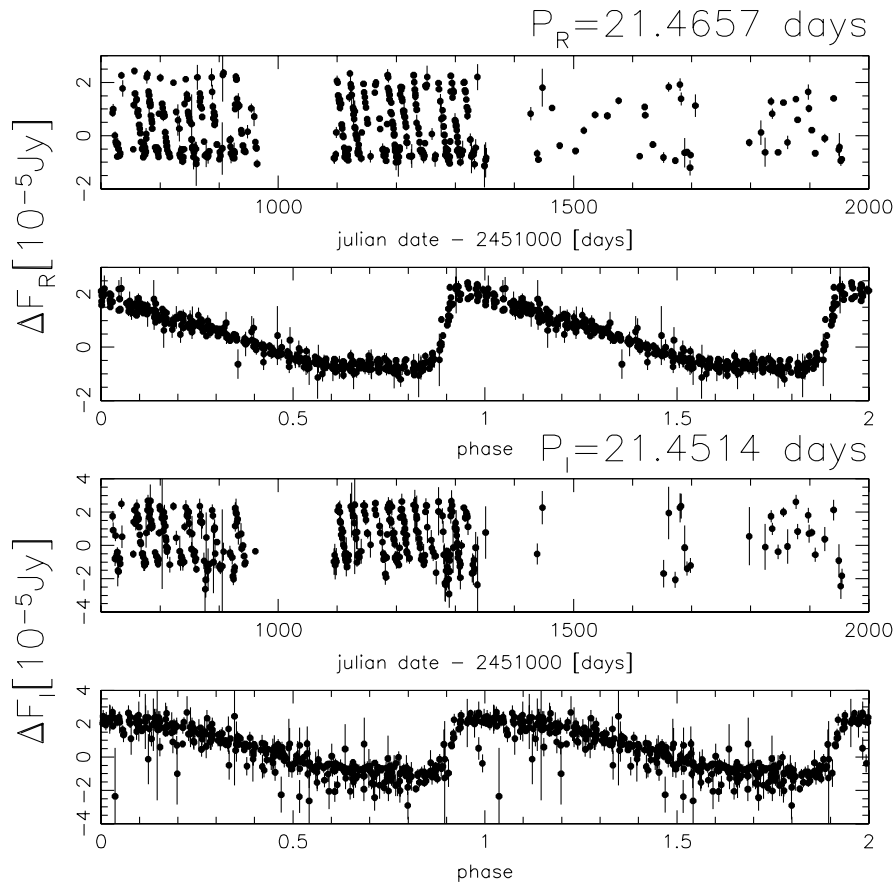
Figure 6.20: Light curve of a δ-Cepheid (group I) in the R-band (top panels) and the I-band (bottom panels). In both bands the light curves are presented in the time domain (top for each band) and in the phase domain, i.e. convolved with the derived periods (bottom for each band). We also show the periods P_R and P_I derived in the R- and I-band, respectively.

The GCVS Cepheid V0934 has a position difference of $2.1''$ when compared to our position, and GCVS Cepheid V0811 is off by $10.2''$. Because of these in part large uncertainties in the positions of the GCVS, we are not trying to match the two remaining semi-regulars, given their smaller variation amplitude.

6.8 Conclusions and outlook

The WeCAPP observations in the optical R and I bands towards the bulge of M31 covering the years 2000-2003 with very good time sampling resulted in a database of over 23000 variable sources. In this paper we have presented the catalogue of variable stars identified in the central parts of M31.

The distribution of the detected variable sources shows an asymmetry due to the enhanced extinction in the spiral arms projected on the M31 bulge. Assuming that the non-variable stars in the bulge behave the same way as the variable counterparts, this asymmetry increases the expected asymmetry in the microlensing signal resulting from the high inclination of M31. Theoretical calculations, therefore, have to take a modified dis-
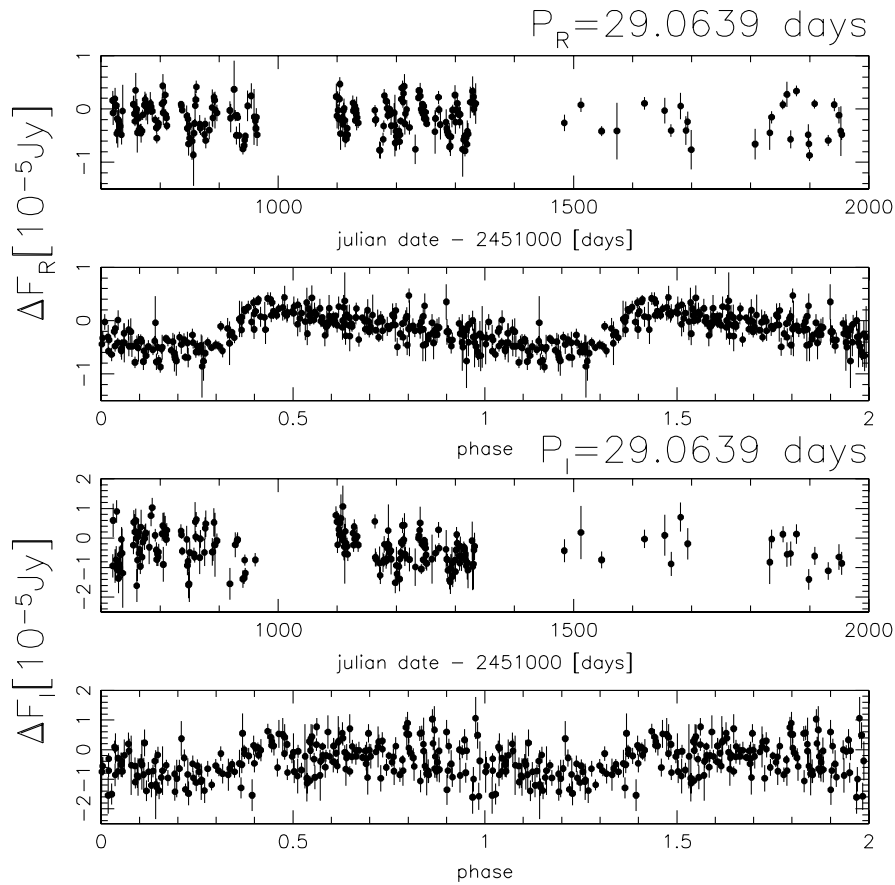
Figure 6.21: Light curve of a long period type II Cepheid (group II) in the *R*-band (top panels) and the *I*-band (bottom panels).

tribution of sources (or the distribution of the extinction in a given band) into account.

The catalogue containing regular, semi-regular and irregular LPVs, Cepheids, RV Tauri stars, eclipsing binary, and R Coronae Borealis candidates enlightens the rich population of variable sources in M31, which can then be exploited for various astrophysical questions. A fraction of the WeCAPP nova catalogue has already been correlated with supersoft *X*-ray sources (SSSs) in M31, showing that classical novae constitute the major class of SSSs in M31 (Pietsch *et al.*, 2005).

Wood *et al.* (1999) found five distinct period-luminosity sequences in the MACHO data towards the LMC bar, of which three could be at-

tributed to different evolutionary phases and pulsation modes. For two of them, sequences D and E, it was suggested that they are populated by contact binaries and by semi-detached binaries with an invisible companion. Recently it was proposed that sequence E is populated by ellipsoidal red giants (Soszynski *et al.*, 2004). Analyzing the data of the LMC ellipsoidal candidates from the OGLE web archive[5] and accounting for the distance modulus of M31 proves that these sources are below the detection limit of our survey. Therefore, we cannot put any constraints on a possible population of ellipsoidal red giants in M31.

Until now we have measured the dominant

---

[5]http://ogle.astrouw.edu.pl/
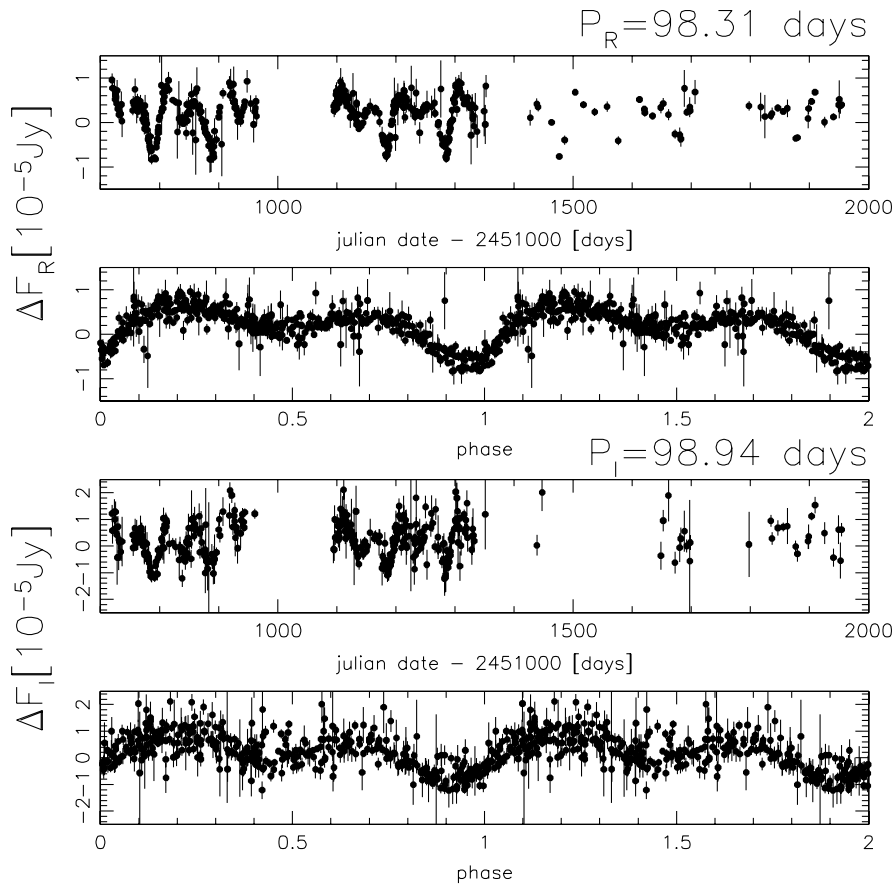
Figure 6.22: Light curve of a RV Tauri star (group II) in the *R*-band (top panels) and the *I*-band (bottom panels). We show the light curves convolved with the formal periods (deep minimum to deep minimum). The double wave light curve with alternating deep and shallow minima is nicely uncovered.

period in these stars that are known to show multiperiodic phenomena. Future work will include extraction of the sub-dominant periods and distribution of the ratio of the different periods. Furthermore, the distribution and possible correlations of the Fourier parameters for these stars is an interesting and, so far, unexamined problem which we can address with this data set.
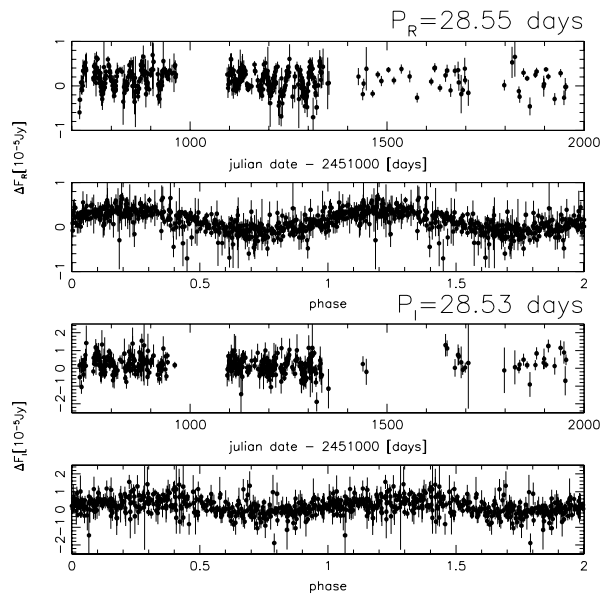
Figure 6.23: Light curve of a low period semi-regular variable (group II) in the *R*-band (top panels) and the *I*-band (bottom panels).
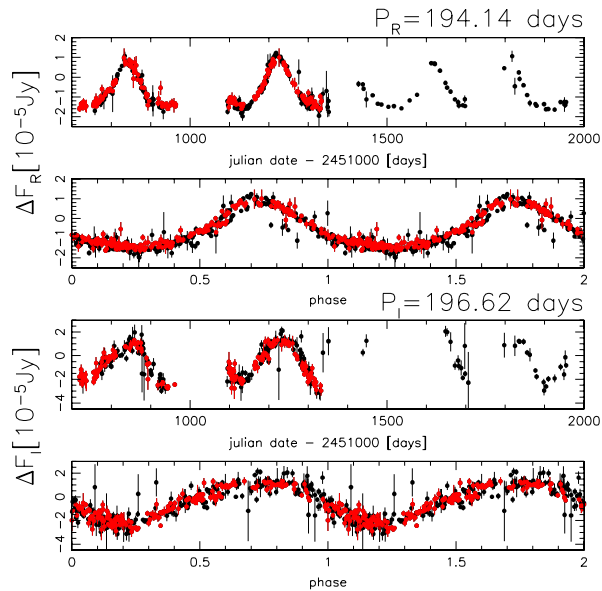
Figure 6.24: Light curve of an LPV with regular variation (group III) in the *R*-band (top panels) and the *I*-band (bottom panels). As illustration of the agreement of the data taken with different telescopes, we show the data collected at Calar Alto as grey dots (red dots in the online version) and data taken at Wendelstein as black dots.
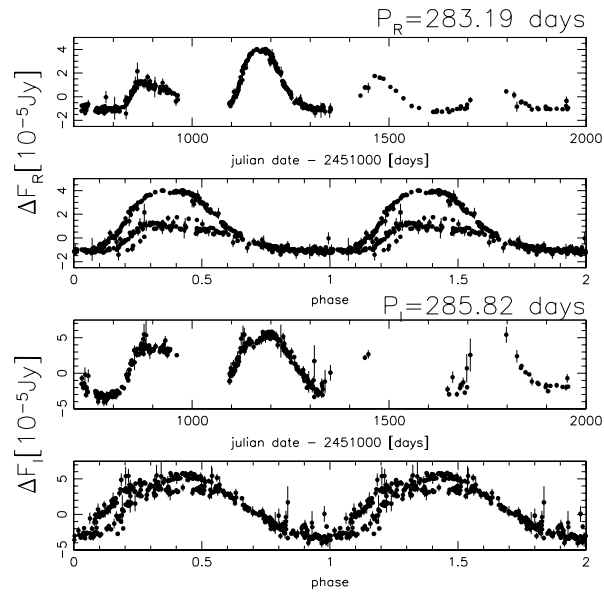
Figure 6.25: Light curve of a LPV (group III) with changing variation amplitudes from cycle to cycle. Top panels: *R*-band. Bottom panels: *I*-band.
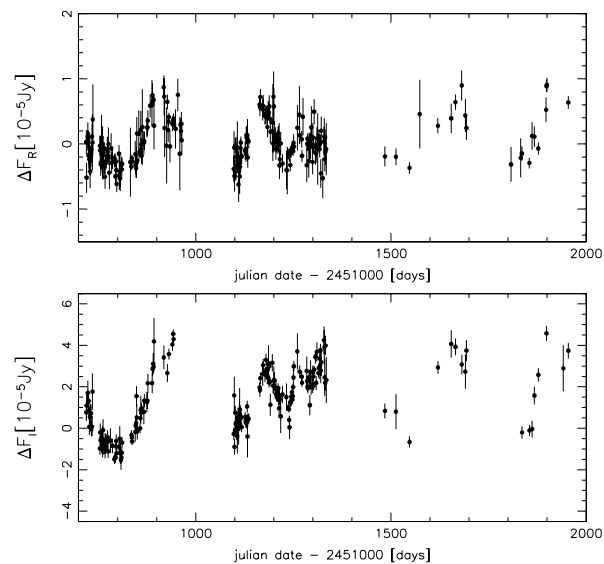
Figure 6.26: Light curve of an irregular LPV (group III). Top panel: *R*-band. Bottom panel: *I*-band.
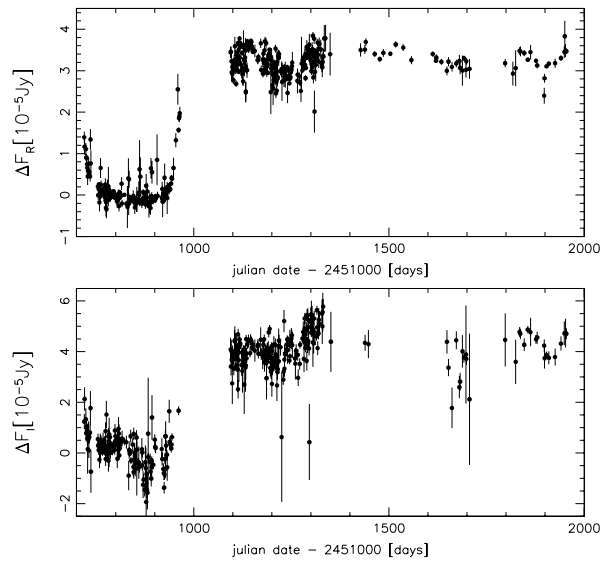
Figure 6.27: Light curve of a R Coronae Borealis candidate (miscellaneous variables). Top panel: *R*-band. Bottom panel: *I*-band. These rare carbon-rich stars show unpredictable and frequent fading of light in optical wavebands, most probably due to dust grains ejected from the stellar photosphere. For a review of these RCB stars see Clayton (1996).
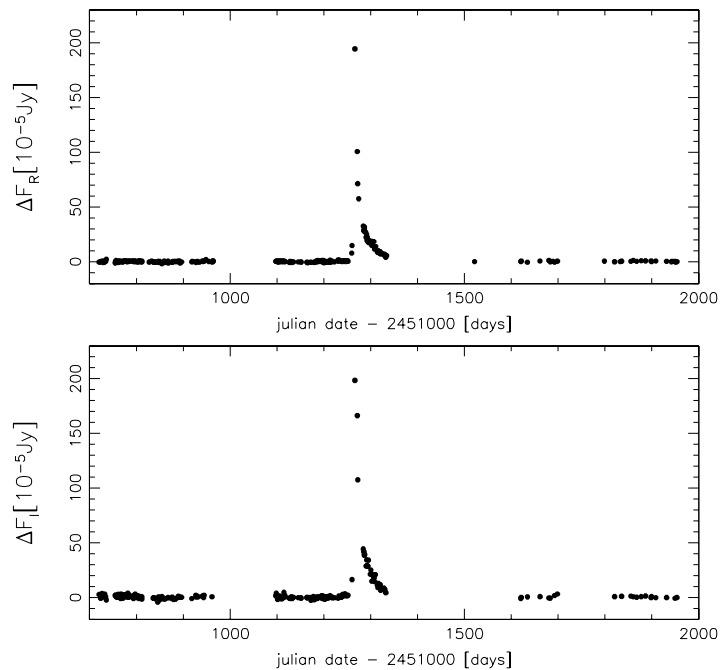
Figure 6.28: Light curve of a nova (miscellaneous variables). Top panel: *R*-band. Bottom panel: *I*-band.

Id	$\alpha(2000.0)$	$\delta(2000.0)$	P_R[days]	$-\log(s_R)$	P_I[days]	$-\log(s_I)$	ΔF_R	ΔF_I	Type
WeCAPP_V00100	0h42m18.46s	41d08′09.0″	119.70	13.18	122.10	8.52	0.37	1.06	I
WeCAPP_V00101	0h42m09.65s	41d08′08.1″	274.99	21.65	277.50	26.10	0.78	2.86	S
WeCAPP_V00102	0h42m31.76s	41d08′11.5″	500.40	9.60	478.70	22.69	0.47	3.48	S
WeCAPP_V00103	0h42m20.06s	41d08′04.4″	180.79	29.32	180.21	26.71	0.76	1.70	S
WeCAPP_V00104	0h42m31.53s	41d08′08.1″	289.96	18.52	293.51	23.71	0.74	3.18	S
WeCAPP_V00105	0h42m52.12s	41d08′11.0″	299.24	33.60	302.18	41.93	0.63	2.59	S
WeCAPP_V00106	0h43m17.73s	41d08′12.8″	136.3	8.920	140.74	4.86	0.49	1.05	I
WeCAPP_V00107	0h42m19.93s	41d08′09.7″	284.59	10.99	273.54	29.43	0.43	2.03	S
WeCAPP_V00108	0h42m45.51s	41d08′10.7″	268.01	19.64	267.94	38.87	0.57	2.56	S
WeCAPP_V00109	0h42m18.84s	41d08′08.8″	240.35	21.15	247.07	27.50	0.51	1.74	S
WeCAPP_V00110	0h42m17.75s	41d08′08.8″	423.96	5.730	423.96	24.32	0.48	1.36	S
WeCAPP_V00111	0h42m17.43s	41d08′08.6″	280.04	16.27	278.51	27.95	0.48	1.69	S
WeCAPP_V00112	0h42m30.69s	41d08′07.9″	216.48	17.07	218.03	21.92	0.81	2.21	S
WeCAPP_V00113	0h42m17.04s	41d08′06.8″	229.50	25.36	229.51	28.31	0.79	2.58	S
WeCAPP_V00114	0h43m02.66s	41d08′13.0″	226.44	29.33	230.99	35.27	0.53	1.96	S
WeCAPP_V00115	0h42m35.32s	41d08′12.0″	-	-	-	-	-	-	L
WeCAPP_V00116	0h42m23.24s	41d08′11.1″	314.68	24.78	319.13	31.99	0.53	2.60	S
WeCAPP_V00117	0h42m14.70s	41d08′10.1″	214.96	26.14	209.84	27.26	0.59	1.77	S
WeCAPP_V00118	0h42m24.75s	41d08′12.4″	277.49	10.20	280.04	23.22	0.42	1.53	S
WeCAPP_V00119	0h42m47.43s	41d08′11.0″	497.12	24.86	505.28	28.47	0.80	6.19	S
WeCAPP_V00120	0h42m24.29s	41d08′11.5″	198.21	21.46	198.61	23.74	0.46	2.82	S

Table 6.1: Extract from the WeCAPP catalogue of variable stars. We give the identification, the right ascension and declination, the assigned period and its significance s ($0.1 \stackrel{\wedge}{=}$ un-significant, $70 \stackrel{\wedge}{=}$ highly significant) in R and I, the amplitude of variation in both bands, and finally a classification according to the scheme presented in Sects. 6.4 and 6.5. The variation amplitudes ΔF_R and ΔF_I are given in units of $[10^{-5}$ Jy].

WeCAPP	α(2000)	δ(2000)	Kaaret	2MASS	Δr (arcsec)
10578	0h42m10.30s	41d15′10.4″	J004210.2+411510	0042102+411510	0.5
16262	0h42m12.14s	41d17′58.8″	J004212.1+411758	0042121+411758	0.4
8624	0h42m18.68s	41d14′01.8″	J004218.6+411402	0042186+411402	0.5
8946	0h42m21.58s	41d14′19.8″	J004221.5+411419	0042215+411419	0.4
7582	0h42m25.11s	41d13′40.7″	J004225.1+411340		0.6
19068	0h42m31.26s	41d19′38.7″	J004231.2+411938	0042312+411938	0.2
7979	0h42m36.59s	41d13′49.9″	J004236.6+411350		0.7
9082	0h42m39.60s	41d14′28.6″	J004239.5+411428		0.9
11406	0h42m41.45s	41d15′23.9″	J004241.4+411524		0.3
16322	0h42m43.97s	41d17′55.5″	J004243.9+411755		0.4
15344	0h42m44.88s	41d17′39.5″	J004244.8+411740		0.4
12503	0h42m46.99s	41d16′15.3″	J004246.9+411615		0.7
8501	0h42m47.13s	41d14′13.9″	J004247.1+411413		0.8
10431	0h42m47.45s	41d15′07.6″	J004247.4+411507		0.2
11736	0h42m47.90s	41d15′50.6″	J004247.8+411550		0.6
12891	0h42m48.65s	41d16′25.0″	J004248.6+411624		0.7
20170	0h42m55.27s	41d20′45.1″	J004255.3+412045		0.7
18374	0h42m59.66s	41d19′19.3″	J004259.6+411919		0.3
12404	0h42m59.88s	41d16′06.0″	J004259.8+411606		0.1
21059	0h43m03.31s	41d21′21.8″	J004303.2+412121		0.5
6049	0h43m08.42s	41d12′46.9″	J004308.4+411247		0.7
17815	0h43m09.88s	41d19′00.8″	J004309.8+411900		0.7
9991	0h43m10.62s	41d14′51.3″	J004310.5+411451	0043106+411451	0.5

Table 6.2: Coincidences between the WeCAPP catalogue of variable stars and the X-ray selected catalogue of point sources by Kaaret (2002). A search radius of 1″ was used. We give the identifier and WCS coordinates for the WeCAPP sources, and the identifier for the Kaaret (2002) sources. For sources coincident with the 2MASS catalogue (Cutri, 2000), we give the 2MASS identifier also. We also show the difference Δr of the matching of both catalogues for each of the correlated sources.

WeCAPP	α(2000)	δ(2000)	id (Kong et al.)	IAU name (CXOM31)	Δr (arcsec)	Notes
14906	0h42m07.08s	41d17′20.2″	r3-79	J004207.0+411719	0.9	
15982	0h42m09.49s	41d17′45.6″	r3-59	J004209.4+411745	0.7	g,v
16262	0h42m12.14s	41d17′58.8″	r3-54	J004212.1+411758	0.8	g,v
5801	0h42m15.09s	41d12′34.8″	r3-50	J004215.0+411234	0.6	v
14846	0h42m15.65s	41d17′21.9″	r3-47	J004215.6+411721	0.7	v
12198	0h42m16.06s	41d15′53.3″	r3-76	J004216.0+411552	0.4	v
7582	0h42m25.11s	41d13′40.7″	r2-45	J004225.1+411340	0.3	
20282	0h42m27.61s	41d20′49.0″	r3-37	J004227.6+412048	0.3	
13905	0h42m30.23s	41d16′54.3″	r2-44	J004230.2+411653	0.9	
19068	0h42m31.26s	41d19′38.7″	r2-33	J004231.2+411939	0.7	g,v
11863	0h42m32.51s	41d15′45.7″	r2-55	J004232.5+411545	0.2	
10895	0h42m34.76s	41d15′22.9″	r2-28	J004234.7+411523	0.3	v,t
7979	0h42m36.59s	41d13′49.9″	r2-42	J004236.5+411350	0.3	
11406	0h42m41.45s	41d15′23.9″	r1-32	J004241.4+411523	0.3	g,v
10626	0h42m43.74s	41d15′14.4″	r1-28	J004243.7+411514	0.8	v
15344	0h42m44.88s	41d17′39.5″	r2-18	J004244.8+411739	0.3	
15318	0h42m46.12s	41d17′36.3″	r2-15	J004246.0+411736	0.8	g,v
12503	0h42m46.99s	41d16′15.3″	r1-3	J004246.9+411615	0.6	v
11736	0h42m47.90s	41d15′50.6″	r1-25	J004247.8+411549	0.8	
22406	0h42m48.94s	41d24′06.1″	r3-84	J004248.9+412406	1.0	v
17309	0h42m56.93s	41d18′44.4″	r2-8	J004256.9+411844	0.2	v,t
18374	0h42m59.66s	41d19′19.3″	r2-6	J004259.6+411919	0.4	g,v
12404	0h42m59.88s	41d16′06.0″	r2-5	J004259.8+411606	0.2	g,v
15035	0h43m01.80s	41d17′26.5″	r2-46	J004301.8+411726	0.5	
10871	0h43m02.99s	41d15′22.3″	r2-4	J004302.9+411522	0.6	g,v
21059	0h43m03.31s	41d21′21.8″	r3-19	J004303.3+412122	0.6	g,v
16325	0h43m03.90s	41d18′04.7″	r2-2	J004303.8+411805	0.5	g,v
19890	0h43m07.55s	41d20′20.0″	r3-18	J004307.5+412020	0.1	g,v
17815	0h43m09.88s	41d19′00.8″	r3-16	J004309.8+411901	0.4	v,t
9991	0h43m10.62s	41d14′51.3″	r3-15	J004310.6+411451	0.8	g,v
17140	0h43m16.14s	41d18′41.5″	r3-9	J004316.1+411841	0.6	v

Table 6.3: Coincidences between the WeCAPP catalogue of variable stars and the X-ray selected catalogue of point sources by Kong *et al.* (2002). A search radius of 1″ was used. We give the identifier and WCS coordinates for the WeCAPP sources, and the identifier and IAU name for the Kong *et al.* (2002) sources. We also show the difference Δr of the matching of both catalogues for each of the correlated sources. Symbols in the last row are taken from Kong *et al.* (2002), and they mark globular cluster counterparts (g, search radius 3″), X-ray variable sources (v), and X-ray transients (t).

WeCAPP	α(2000)	δ(2000)	GCVS	Δr (arcsec)	GCVS class	WeCAPP class
906	0h43m22.50s	41d07′28.6″	V0871	0.7	I:	I
2375	0h43m15.73s	41d07′54.7″	V0727	0.1	IA:	I
559	0h43m24.16s	41d07′12.7″	V0743	0.2	DCEP	DC
742	0h43m17.27s	44d15′58.0″	V0726	1.0	SR	I

Table 6.4: Coincidences between the WeCAPP catalogue of variable stars and the General Catalogue of Variable Stars (GCVS, Durlevich *et al.* (1996)). A search radius of 1″ was used. We give the identifier, WCS coordinates and a classification for the WeCAPP sources, and the identifier and a classification according to the GCVS. We also the difference Δr of the matching of both catalogues for each of the correlated sources.

6.9   Appendix to chapter 6

6.9.1   Survey window function and leakage function

Effects induced by the discrete time sampling of astronomical surveys can yield strong power in frequencies not caused by a periodic or quasi-periodic signal. The affected frequencies are often connected to the daily separation of observations or to observing blocks that are interrupted by the non-observability of the object. In the case of M31, the observation gap usually lasts from the middle of March to the beginning of June.

A quantitative way to describe the effects of the time sampling of observations on the power spectrum is given by the window function $W(v)$. $W(v)$ is defined as the Fourier transform of the sampling function $s(t)$, where $s(t_i)$ is of constant value in case of observations taking place at times t_i, and $s(t_i)$ is zero otherwise:

$$W(v) = \int s(t)\, e^{-2\pi i v t}\, dt \ . \tag{6.16}$$

In Figs. 6.29 and 6.30 we show the window function $W(v)$ (in the frequency and period representation, respectively) calculated with the Lomb algorithm for the sampling given in Field F1. For this purpose, we created a high (order of 10^{14}) $\left(\frac{S}{N}\right)$ light curve with $s(t_i) = 1 + \sigma(t_i)$ and a minimal noise contribution $\sigma(t_i)$ to allow for the calculation of the variance of the data (see Eqs. 6.1 and 6.3).

The strong power in periods around 450 days (at $v = 2.2 \times 10^{-3}$ days^{-1}) is clearly visible, whereas no 'aliasing' problem is expected at small periods (high frequencies). The full width half maximum v_{FWHM} of the main peak of the window function $W(v)$ determines the theoretical error in the period calculation

$$\Delta P \approx \frac{\Delta v}{2} P^2 \tag{6.17}$$

with $\Delta v = v_{\text{FWHM}}$. According to Roberts *et al.* (1987) Δv can be approximated by $\Delta v \approx 1/T$ with T the total time span of the observations, if the sampling is not to non-uniform.
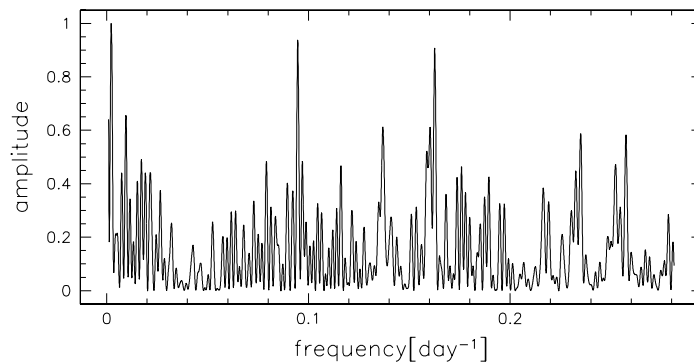
Figure 6.29: The window function $W(v)$ present in the survey. The amplitude is normalized to 1. $W(v)$ is defined as the Fourier transform of the sampling function s(t), $W(v) = \int s(t)\, e^{-2\pi i v t}\, dt$. The main peak of the window function has a full width half maximum $v_{FWHM} = 0.0013$ day^{-1}, which is 1.60 times larger than what one would expect from the total duration of the observations (Roberts *et al.*, 1987).
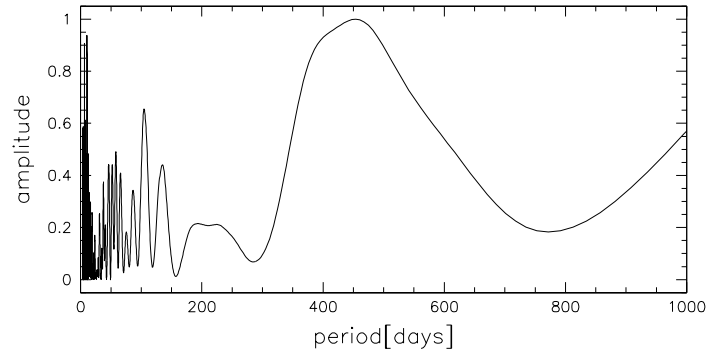
Figure 6.30: Window function $W(\nu)$ shown in the period representation. Clearly visible is the sampling induced strong power in periods around 450 days, which give rise to the aliasing problems (see also Fig. 6.31).

The measured $\nu_{\mathrm{FWHM}} = 0.0013$ day^{-1} is 1.60 times larger than this theoretical value, which can be explained by the non-uniform sampling of the observations (see Fig. 6.2). With this value, Eq. 6.17 becomes

$$\Delta P \approx 6.5 \times \left(\frac{P}{100\,\mathrm{d}} \right)^2 . \tag{6.18}$$

An alternative way to illustrate the sampling effect is given by the 'leakage function' for different periodic signals. This function describes how a signal that is located at zero offset 'leaks' into neighboring frequencies. Figure 6.31 (left panel) shows the leakage function for a periodic signal of the form

$$h_j = 10^{\sin(2\pi(t_i - t_0)/P)} \tag{6.19}$$

calculated with the Lomb algorithm for the sampling $s(t_i)$ of field F1 and different periods P. The problem of high amplitudes in the power spectrum for frequencies corresponding to periods in the range of 350 and 550 days is also apparent in this figure.

In the right panel of Fig. 6.31 we show the leakage function in the period representation. For periods between about 350 and 550 days the power in the second peak in the Fourier spectrum can exceed the power in the first peak, which means that the derived period is offset from the real one by the position of the second peak.

6.9.2   Monte Carlo simulation

We also tested the accuracy of the period determination with Monte Carlo simulations of the survey. We analyzed the accuracy for different mean magnitudes and amplitudes at a fixed position, thus fixed noise contributions of the galaxy and the sky. We chose the mean magnitude M_R of the variable to be $M_R = -1, 0, 1, 2$ mag and shift them to a distance of M31. For each of these mean magnitudes, we changed the amplitude A_R of the variation from 0.5 mag to 2 mag. The background (surface brightness of the galaxy + sky contribution) was set to $M_{bg,R} = 19$ mag per area of the PSF. In each run we simulated 10^5 light curves according to

$$F_R(t_i) = 10^{-0.4(M_R + (m_R - M_R) + A_R \sin(2\pi(t_i - t_0)/P_{in}))} . \tag{6.20}$$
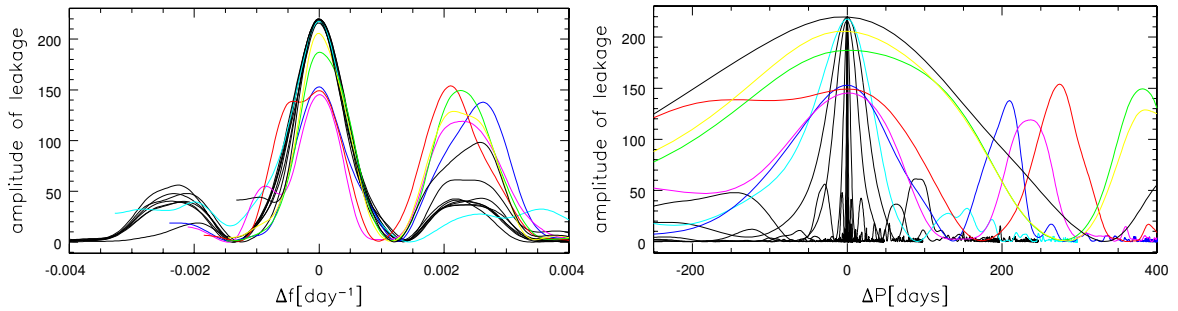
Figure 6.31: *Left panel:* Leakage function for the sampling given in the survey for different periodic signals. The function shows how a signal which is located at zero offset leaks into neighboring frequencies. We calculated this function for a signal according to Eq. 6.19 and periods of 5, 10, 20, 50, 100, 200, 250, 300 (cyan curve), 400, 450, 500, 550, 600, and 700 days (black curves, if not mentioned otherwise). The power in the second peak is high for periods of 400 (blue curve), 450 (magenta curve), and 500 days (red curve). In this period regime, the power in the second peak can exceed the power in the first peak (at zero frequency difference) resulting in an aliasing of periods. The aliasing decreases for periods of 550 (green curve) and 600 days (yellow curve), and vanishes for even longer periods. The aliasing is also evident in the Monte-Carlo simulation of the survey. *Right panel:* Leakage function in the period representation for the sampling given in the survey for different periodic signals. For periods between 350 and about 550 days, the power in the second peak can exceed the power in the first peak (at zero period difference) resulting in a possible aliasing of periods. The resulting displacement of the true period can be read from the x-axis.

The epochs t_i were given by the sampling of field F1 (see Fig. 6.2); periods P_{in} were chosen randomly between 3 and 700 days; and t_0, the epoch of mean luminosity, was randomly distributed between the beginning and the end of the survey. Note that this also ensured that the phase is randomly chosen. For each simulated light curve, the period was derived according to Eq. 6.1. Figure 6.32 then shows the derived periods P_{out} as a function of the input period. It is clear that the accuracy of the period determination decreases at around 500 days, independent of the $\left(\frac{S}{N}\right)$ of the light curves. This can partly be explained by the sparse time sampling in the last two campaigns. On the other hand, aliasing effects due to the yearly observing window also seem to play a role for periods between 350 days and 550 days (see Figs. 6.31 and 6.32). This holds for $\left(\frac{S}{N}\right)$-ratios above a certain threshold. Noise present in the light curves tends to level out the different peaks in the power spectrum, which results in a generally bad performance of the period determination for light curves with low $\left(\frac{S}{N}\right)$. For higher $\left(\frac{S}{N}\right)$ light curves, the accuracy of the period determination is good, apart from the problem that periods around 400 and 500 days tend to be shifted to much smaller (i.e. around half of the true) values.
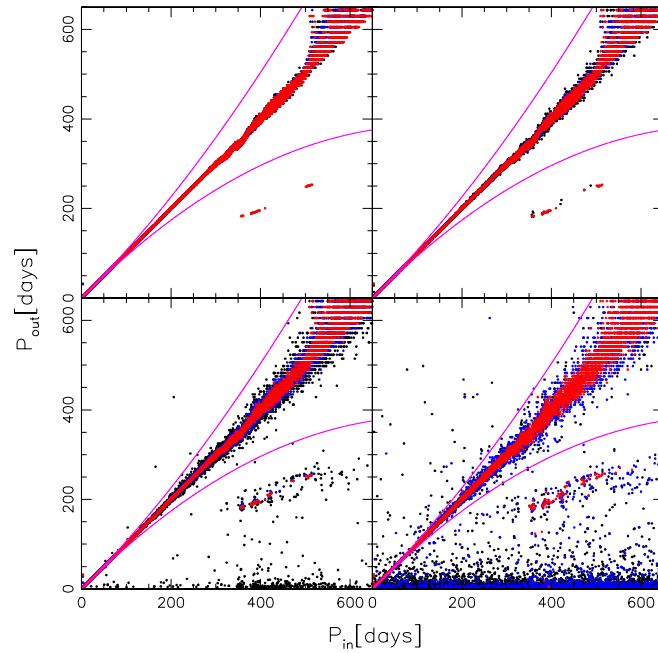
Figure 6.32: Result of simulations for decreasing $\left(\frac{S}{N}\right)$ of the light curves from the upper left to the lower right corner. The mean magnitude of the source changes in steps of one magnitude from $M_R = -1$ mag in the upper left corner to $M_R = 2$ mag in the lower right corner. Red dots show the accuracy of the period determination for light curves with an amplitude $A_R = 2.0$ mag; blue dots correspond to $A_R = 1.0$ mag; and black dots have $A_R = 0.5$ mag. The apparent horizontal lines at large periods result from the finite frequency resolution of the period-finding algorithm. Above a threshold in $\left(\frac{S}{N}\right)$, the accuracy of the period determination seems independent of the particular $\left(\frac{S}{N}\right)$ of the light curves. In this regime only periods longer than 500 days have a large false detection probability. Below the threshold the accuracy breaks down very rapidly, independent of the period. In magenta we show the theoretical expected errors of the period determination according to Eq. 6.18.

Chapter 7

The nova catalogue of M31

7.1 Introduction

Classical novae are a subclass of cataclysmic variable stars, i.e. close contact binary systems of a compact white dwarf (WD) and a late main sequence star. The main sequence star transfers mass to the WD via Roche lobe overflow, where it forms a rotationally supported accretion disk. The inner part of this disk settles slowly on the WD surface and mixes partly with the WD material. Although the process of mixing is still a matter of debate, it plays a very important role for the initial conditions and the evolution of novae, as the heavy WD nuclei are catalytic converters in the CNO chain of hydrogen burning. Further evidence for the mixing process stems from the detection of super-solar enhancements in novae ejecta which has to be due to mixing of the WD material and the solar composition material of the donator main sequence star (e.g., Prialnik *et al.* 1978; Bode & Evans 1989; Hernanz 2005).

The explosion of novae is best described by a thermonuclear runaway in the lower parts of the accreted hydrogen rich envelope (e.g., Gallagher & Starrfield 1978; Prialnik & Kovetz 1995; Starrfield *et al.* 1998). For not too high accretion rates (e.g., $10^{-10} M_\odot \, \mathrm{yr}^{-1} < dM/dt < 10^{-8} M_\odot \, \mathrm{yr}^{-1}$) and white dwarfs massive enough, hydrogen ignition conditions are reached in the degenerate envelope of the white dwarf. At temperatures high enough hydrogen burning starts in the lower envelope via the p-p chain whose energy production shows only a moderate temperature dependence (rate $\varepsilon_{nuc} \approx T^4$). Due to the degeneracy of the hydrogen burning material pressure and temperature are decoupled preventing the envelope to expand. At temperatures above $\sim 10^7$ K the CNO cycle becomes the dominant energy production chain. Its steep temperature dependence ($\varepsilon_{nuc} \approx T^{16-18}$) leads to a fast temperature rise in the inner envelope and to high temperatures before the degeneracy is lifted in larger parts of the envelope (as $T_{env} > T_F = E_F/k$ with E_F being the Fermi energy of the gas). The hydrogen burning creates many short living β^+ unstable products (e.g., ^{13}N, ^{14}O, ^{15}O, ^{17}F) with life times of the order of minutes. Convection, which shortly after ignition covers the whole envelope, transports these elements to the outer envelope, where they lead to a huge, but somewhat delayed energy release. Moreover, the convection zone transports unburned material from the outer parts of the envelope to the burning shell, fueling the burning with fresh material. The delayed energy release from the β^+-unstable isotopes in the outer envelope finally leads to the expansion and to an increase in luminosity of up more than 10 magnitudes (factor 10^4 in energy release) in optical bands, which in some cases stops for a short time (hours to several days for fast and slow novae, respectively) about 2 magnitudes below maximum.

The time after visual maximum is characterized by a constant bolometric (i.e. total) luminosity.

Author(s)	Epoch	Filter(s)	Detector	Novae	Rate	References
Hubble	1907-1927	B	Plates	85	~ 30	Hubble (1929)
Arp	1953-1954	B	Plates	30	26 ± 4	Arp (1956)
Rosino et al.	1955-1986	B	Plates	142		Rosino *et al.* (1989)
Ciardullo et al.	1982-1986	B,H$_\alpha$	CCD	40		Ciardullo *et al.* (1987)
Sharov & Alksnis	1969-1989	B	Plates	21		Sharov & Alksnis (1992)
Tomaney & Shafter	1987-1989	H$_\alpha$	CCD	9		Tomaney & Shafter (1992)
Shafter & Irby	1990-1997	H$_\alpha$	CCD	72	37^{+12}_{-8}	Shafter & Irby (2001)
Rector et al.	1995-1999	H$_\alpha$	CCD	44		Rector *et al.* (1999)
Agape	1994-1996	*R,I*	CCD	12		Ansari *et al.* (2004)
POINT-AGAPE	1999-2002	*r',i',g'*	CCD	20		Darnley *et al.* (2004)
NMS	2001/2002	*R,I*	CCD	2		Joshi *et al.* (2004)
WeCAPP	1997-2005	*R,I*	CCD	68		this work

Table 7.1: Compilation of the major nova surveys towards M31. Updated table adapted from Shafter & Irby (2001).

This stadium of a constant high (i.e. often close to Eddington) luminosity can be ascribed to a hydrostatic hydrogen burning of the remaining envelope. During this stage the spectral energy distribution (SED) shifts its maximum to shorter wavelengths, which leads to a decline of the luminosity in optical wavelengths and a hardening of the SED. The UV luminosity rises as deeper and hotter regions of the photosphere can be observed. At the end of the UV emission phase novae can show an enhanced infrared (IR) emission as the UV photons are re-emitted by dust grains which have formed in the ejecta. During all this time the nova continuously loses mass (probably) through an optically thick wind (e.g., Kato 1997).

Novae are classified according to the time $t2$ ($t3$) they need to decline 2 mag (3 mag) from their maximum brightness (McLaughlin, 1939). Payne-Gaposchkin (1957) proposed a separation of the *V*-band light curves in four speed classes: very fast ($t2 < 10$ days), fast ($t2 \approx 11 - 25$ days), moderately fast ($t2 \approx 26 - 80$ days), slow ($t2 \approx 81 - 150$ days), and very slow ($t2 \approx 151 - 250$ days). We will adopt this scheme also for our *R*-band data. The timescale of the decline is tightly correlated with the maximum brightness of novae, leading to a maximum magnitude–rate of decline relationship (MMRD, e.g. Zwicky 1936; McLaughlin 1942, 1945; Schmidt 1957).

The M31 nova population was target of several surveys (see Table 7.1), starting in the 1920s with the work of Hubble (1929), already noticing that bright novae in M31 fade faster than faint novae. As in the Andromeda galaxy all novae are at approximately the same distance and the line of sight suffers only from a moderate Galactic extinction, the interpretation of the nova properties is easier than in the Milky Way, which nova population shows a large spread in distances and reddenings. Arp (1956) continued the work on novae in M31 and presented the first MMRD for M31, based on a sample of 30 novae. Rosino (1964, 1973) and Rosino *et al.* (1989) gave an update of the MMRD, and also showed further light curves of novae detected at the Asiago Observatory since 1955. Finally, Capaccioli *et al.* (1989) performed a systematic study of the novae population of M31, based on a combined sample of novae detected in M31 until then. The authors of this paper determined the incompleteness corrected M31 nova rate to 29 ± 4 per year, which is consistent with the revised rate given in Arp (1956).

As novae develop a strong and long-lasting H$_\alpha$ emission, surveys at this wavelength are very efficient in their detection. Shafter & Irby (2001) presented the results of the largest H$_\alpha$ survey for novae to date, finding a higher global novae rate of 37^{+12}_{-8} yr^{-1} if compared to previous studies. Moreover, they determined the bulge fraction of the novae to be as high as 70%. In the course of the pixellens-

ing surveys towards M31, novae detections in red optical bands (R and I) got more numerous (e.g., POINT-AGAPE – Darnley *et al.* 2004, NMS – Joshi *et al.* 2004). Especially the R-band luminosity is very interesting, as it inhibits the H_α emission line at $\lambda = 6563\mathring{A}$ in its bandpass. A varying H_α emission in the declining part of the optical light curve therefore has effects on the evolution and shape of the R-band light curve.

7.2 Detection

We developed a detection algorithm which works nearly automatically without a great amount of human interaction. To get an unbiased novae sample we introduced a number of automatic cuts which strongly reduced the number of nova candidates, before the classical novae finally were selected by visual inspection of the light curves. We only use the R band data in the detection process, as it offers a better time sampling and therefore a better efficiency for detecting the novae in the data set. Moreover, although novae are quite red during maximum (and get bluer afterwards), and therefore have smaller flux excesses in the R than in the I band, the R band offers a better $\left(\frac{S}{N}\right)$ for the nova light curves on the varying background of M31. Most of the variable sources in M31 are quite red and show higher variation amplitudes in I (see chapter 6), which reduces the $\left(\frac{S}{N}\right)$ for the nova detection.

Novae are amongst the brightest sources in our survey. As a first step in the detection procedure we therefore apply a cut in the R-band flux excess ΔF_R. At each epoch we calculate the flux excess f_i ($i = 1,...,N$) relative to the baseline of the light curve. We extract all pixel light curves which variation amplitude f_i exceeds a flux level of $\Delta F_R = 5 \cdot 10^{-5}$ Jy in at least one epoch. For all pixel light curves which fulfill this cut we calculate the χ^2 deviation from a constant line fit and save the value in a deviation image. For all local maxima in this detection image we apply further cuts to extract the nova candidates. This first and rather loose criterion selects very efficiently bright amplitudes in the difference images. Most variable stars have amplitudes below the threshold and therefore are not the main source of contamination.

In a second step we make use of the eruptive nature of classical novae. Because of this, the difference light curves vary around a baseline close to zero for most of the time. During eruption the light curves then move to large difference fluxes. In order to use this behavior we define two parameters, one of them reflecting the integral height m of the outburst, the other reflecting the asymmetry s between positive and negative outliers:

$$m = \frac{\sum\limits_{nf_{i,max}} nf_i e_i^{-2}}{\sum\limits_{nf_{i,max}} e_i^{-2}} \quad , \tag{7.1}$$

and

$$s = \frac{\sum\limits_{nf_i > thresh_i} nf_i}{\sum\limits_{nf_i < (-thresh_i)} nf_i} \quad , \tag{7.2}$$

with $nf_i = f_i - median(f_i)$, $thresh_i = 4 \times e_i$ and e_i are the errors of the individual flux measurements. We define the parameter m as the weighted mean of the three data points with maximum difference flux, and s as the flux weighted ratio of positive and negative 4σ outliers relative to the median of the light curve. The mean brightness of the highest data points should be large for novae and therefore
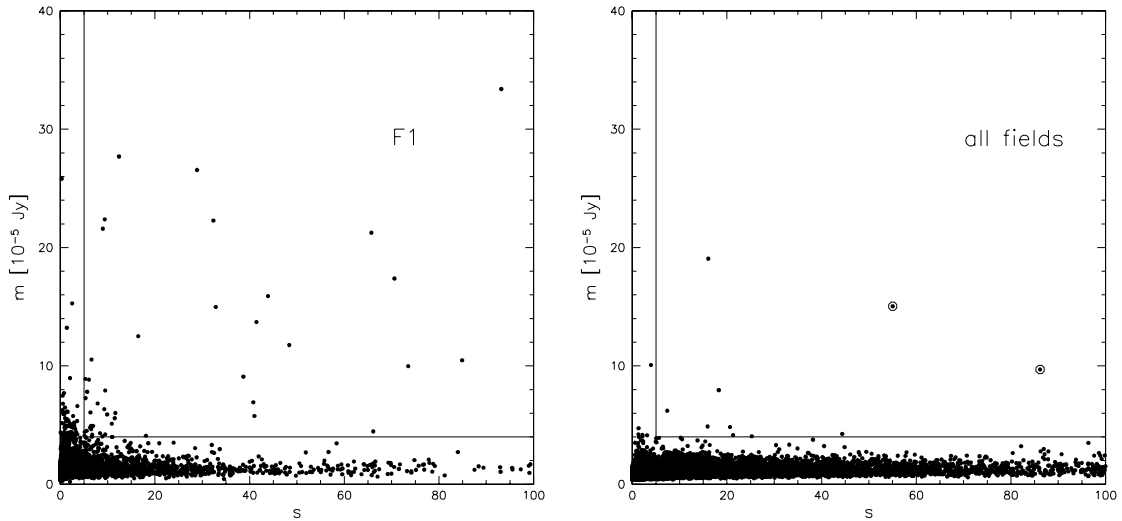
Figure 7.1: *Left panel:* Positions of the light curves with at least one data point above $\Delta F_R = 5 \cdot 10^{-5}$ Jy (corresponding to a magnitude limit of $m_R \approx 19.5$ mag, see below) in the detection (*m-s*) plane, shown for field F1. The thresholds used for the detection of the novae candidates are shown by black lines. This figure only shows a fraction of the novae, as they reach asymmetry values up to 800 in this field. *Right panel:* Positions of the over 20000 variable star light curves (see chapter 6) in the detection plane. The variables generally show smaller amplitudes as the novae. Two of the novae being already published in Fliri *et al.* (2006) are marked by open circles.

field	F1	F2	F3	F4
$m_{min}[10^{-5}$ Jy]	4	4	4	4
s_{min}	5	5	5	5
# candidates	49	39	29	32
# novae	33	24	19	20

Table 7.2: Number of novae detected in the four fields. In the second and third row we give the thresholds m_{min} and s_{min} used for detecting the novae.

separate them from spurious outliers, which often show just one bright data point. Already the cut in *m* strongly reduces the number of candidates. After the asymmetry criterion we are basically left with the nova light curves (see Fig. 7.1). Residual light curves with a small number of spurious positive outliers are removed by requiring the light curve to have at least two data points above a low threshold ($\Delta F_R = 2 \cdot 10^{-5}$ Jy). The remaining light curves are finally inspected visually to confirm the nova light curves.

Similarly to the detection of the microlensing events we detect the novae in each of our four fields separately. In Table 7.2 we give the number of novae detected along with the detection thresholds used for the four fields. Due to the split of the Calar Alto data novae can be detected multiple times, which reduces the total number of novae to 68. In Table 7.3 we give the WCS positions, the time of observed maximum t_{max}, and the brightness at observed maximum $m_{R,max}$.

No.	RA(2000)	DEC(2000)	t_{max}	$m_{R,max}$	No.	RA(2000)	DEC(2000)	t_{max}	$m_{R,max}$
01	0h43m18.62s	41d09′49.1″	1094.6	18.7	35	0h42m46.75s	41d12′51.9″	726.6	18.7
02	0h43m10.62s	41d17′58.0″	1163.7	18.5	36	0h42m46.63s	41d14′49.2″	125.4	19.2
03	0h43m08.65s	41d15′35.4″	2039.3	17.8	37	0h42m46.45s	41d15′55.6″	1925.4	18.9
04	0h43m07.45s	41d18′04.6″	2319.5	17.5	38	0h42m45.46s	41d16′33.2″	2346.2	18.7
05	0h43m05.26s	41d19′08.2″	948.3	17.4	39	0h42m45.12s	41d17′54.0″	1820.5	17.0
06	0h43m05.38s	41d14′59.3″	-254.5	17.5	40	0h42m44.65s	41d20′40.6″	755.7	18.1
07	0h43m04.73s	41d12′21.9″	1992.3	17.2	41	0h42m44.49s	41d15′53.0″	1940.5	17.5
08	0h43m03.31s	41d12′11.5″	1190.5	17.0	42	0h42m43.97s	41d17′55.5″	754.6	16.8
09	0h43m01.85s	41d15′38.4″	372.6	16.8	43	0h42m42.81s	41d18′27.8″	2319.6	17.2
10	0h43m01.08s	41d16′19.9″	1476.5	18.4	44	0h42m42.82s	41d15′55.2″	940.3	16.6
11	0h43m00.76s	41d11′26.9″	1979.3	17.4	45	0h42m42.77s	41d15′44.7″	2254.4	18.7
12	0h42m58.38s	41d16′08.3″	1797.5	17.9	46	0h42m42.13s	41d15′10.5″	-246.5	18.0
13	0h42m57.75s	41d08′12.4″	1095.5	18.1	47	0h42m41.44s	41d16′24.5″	1266.3	15.5
14	0h42m54.95s	41d16′09.2″	948.34	17.2	48	0h42m41.14s	41d18′32.4″	1832.6	17.6
15	0h42m54.14s	41d15′12.2″	1994.3	16.9	49	0h42m41.20s	41d16′16.0″	1925.5	17.4
16	0h42m53.78s	41d18′46.2″	1949.5	17.3	50	0h42m41.19s	41d15′45.0″	2006.2	18.4
17	0h42m53.24s	41d22′35.9″	1997.5	17.4	51	0h42m40.60s	41d07′59.9″	1164.7	18.7
18	0h42m52.89s	41d15′10.4″	1283.3	17.1	52	0h42m40.27s	41d14′42.5″	2254.4	17.8
19	0h42m52.79s	41d14′28.9″	2427.3	18.0	53	0h42m39.74s	41d17′03.2″	1521.6	18.8
20	0h42m52.48s	41d18′00.2″	2319.5	19.0	54	0h42m39.59s	41d09′03.0″	1299.3	18.7
21	0h42m52.35s	41d16′13.2″	-249.6	18.1	55	0h42m38.76s	41d14′44.4″	1097.6	18.2
22	0h42m52.24s	41d13′54.5″	1797.5	18.2	56	0h42m37.70s	41d17′37.8″	766.6	17.5
23	0h42m51.84s	41d16′18.2″	2293.4	18.3	57	0h42m36.37s	41d18′41.8″	2427.4	19.1
24	0h42m49.64s	41d18′02.0″	1867.5	18.2	58	0h42m34.62s	41d18′13.1″	1151.6	16.7
25	0h42m49.64s	41d16′06.5″	251.3	18.5	59	0h42m33.89s	41d18′23.9″	1282.3	16.8
26	0h42m49.69s	41d15′05.6″	359.5	17.8	60	0h42m32.29s	41d19′25.7″	2346.4	19.4
27	0h42m48.90s	41d16′05.3″	1661.2	17.0	61	0h42m30.74s	41d19′05.9″	1327.3	17.4
28	0h42m48.68s	41d16′26.4″	1573.6	18.8	62	0h42m30.79s	41d14′36.1″	1130.6	18.7
29	0h42m47.45s	41d15′07.7″	763.7	18.6	63	0h42m30.11s	41d15′27.3″	719.6	18.1
30	0h42m47.27s	41d16′21.4″	2039.3	16.6	64	0h42m28.39s	41d16′36.2″	2382.4	15.1
31	0h42m47.24s	41d15′54.5″	2291.5	18.7	65	0h42m28.09s	41d09′54.8″	2381.4	18.1
32	0h42m47.21s	41d16′18.7″	1197.3	17.4	66	0h42m21.77s	41d12′16.3″	-245.4	19.3
33	0h42m47.15s	41d16′19.8″	2319.5	17.9	67	0h42m18.52s	41d12′39.3″	1164.7	19.1
34	0h42m46.74s	41d19′47.4″	1931.3	18.3	68	0h42m15.84s	41d12′00.0″	1834.4	16.7

Table 7.3: Coordinates of the 68 detected novae in the data covering the time span September 1997 to March 2005. We give the identification, the right ascension and declination in the WCS in the first three columns. The time of the observed maximum in the R-band t_{max} is shown as (julian date - 2451000). The observed maximal R-band brightness $m_{R,max}$ is given in magnitudes (see below).

7.3 Spatial Distribution

We show the spatial distribution of the detected novae in Fig. 7.2. The apparent overdensity of novae in field F1 can be ascribed to the longer time coverage and denser time sampling compared to the other fields (see also chapter 2). To draw conclusions on the spatial distribution of the novae we therefore adjusted the survey efficiencies in all four fields to approximately the same value. This has been done by deleting the Wendelstein observations prior to 2002 and the Calar Alto observations 1999/2000 from the data set. Re-running the detection procedures on this reduced data set yields 59 novae, which are marked as red diamonds in Fig. 7.2. As the Calar Alto data covers all four fields simultaneously and the post 2002 Wendelstein observations have a comparable time coverage for all

four fields the resulting novae sample now has approximately the same survey efficiency.

The distribution of novae is strongly concentrated which agrees with recent results and disproves the early claims in Arp (1956) that the central part of M31 is depleted from novae. Most likely, the apparent lack of novae in the central arcminute in Arp (1956) can be attributed to a saturation of the photographic plates due to the high surface brightness in the central part, as already noted in Ciardullo *et al.* (1987).

We derive the cumulative fraction of the WeCAPP novae as function of the isophotal radius and compare the results with the cumulative bulge light, disk light and total light in the Gunn *r*-band. Note, that we are not correcting for a patchy absorption in our field. Indeed, it seems that the regions with dust lanes in the spiral arms in the north-west part of the field are depleted from novae. However, comparing the detections in the outer parts of the south-east and north-west fields shows that in these regions also small number statistics can be responsible for this apparent underdensity of novae.

For the distribution of the M31 bulge and disk light we use the model of M31 presented in chapter 3, which is based on the small bulge decomposition of Kent (1989b) in the Gunn *r*-band. The total *r*-band light was taken from Kent (1987). As the run of ellipticities is approximately the same as for the bulge isophotes in Kent (1989b) we could use the same parameterization of the ellipticities (see chapter 3). The cumulative distributions are calculated by summing up the light contributions in elliptic areas. The novae distribution was derived in the same way, i.e. counted in ellipses with a flattening given by the bulge model and the inclination of the disk, respectively. Due to saturation we had to exclude the innermost 20 arcsec of the observed field, which was accounted for in the calculations of the light distributions.

The comparison of the novae distributions with the ones of the M31 light in Fig. 7.3 shows that the disk light hardly agrees. The agreement with bulge light and total light is much better, with the bulge light yielding the best results. To compare the cumulative distributions in a quantitative way, we apply a Kolmogorov-Smirnov (K-S) test (e.g., Press 1988). The K-S test calculates the probability that two cumulative distributions are drawn from the same parent distribution. For two cumulative distributions $S_{N_1}(x)$ and $S_{N_2}(x)$ the K-S statistic is given by their maximal absolute deviation D, i.e.

$$D = \max|S_{N_1}(x) - S_{N_2}(x)| \quad , \tag{7.3}$$

where N_1 and N_2 are the number of data points in both distributions. With

$$Q_{KS}(\lambda) = 2 \sum_{j=1}^{\infty} (-1)^{j-1} e^{-2j^2\lambda^2} \quad , \tag{7.4}$$

the probability $P(D > \text{observed})$ is approximately given by

$$P = Q_{KS} \left(\left[\sqrt{N} + 0.12 + 0.11/\sqrt{N} \right] D \right) \quad , \tag{7.5}$$

where

$$N = \frac{N_1 N_2}{N_1 + N_2} \quad . \tag{7.6}$$

Comparing the distributions of the nova sample with the disk light, total light, and bulge light yields K-S probabilities that both are drawn from the same distribution of 0.52, 0.93, and 0.99, respectively. This underlines the good agreement between the distributions of the *r*-band bulge light and the nova sample, and supports the results from Ciardullo *et al.* (1987) and Shafter & Irby (2001). However, as we are not tracing regions with a less strong contribution of the bulge to the total light, we cannot finally conclude that the M31 novae originate from the old bulge population.
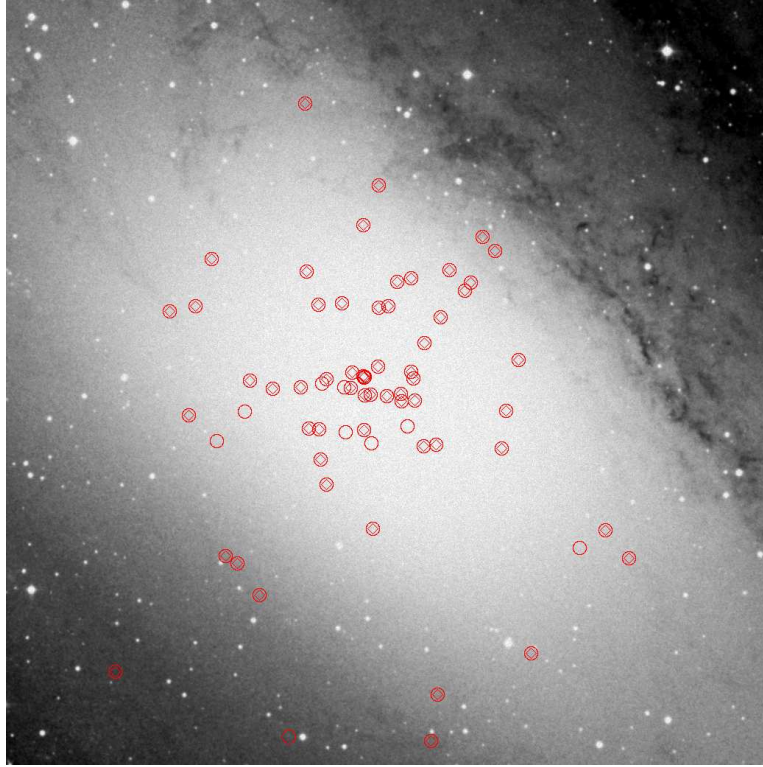
Figure 7.2: This figure shows the spatial distribution of the identified novae. Novae detected on the full data set are shown by red circles, whereas the novae detected on the reduced data set with approximately the same survey efficiency are marked by red diamonds. North is to the top and East is to the left of this figure.

7.4 Smoothing of the light curves

A subsample of 40 novae which erupted between 2000 and 2003 is further investigated. We smoothed the R-band light curves using a free parameter fit according to the method of Vondrák (1969, 1977). This technique is a variant of the Whittaker fitting method (Whittaker & Robinson, 1946), but can be used for unevenly sampled data. The method is based on minimizing the value of

$$Q = F + \lambda^2 S \quad , \tag{7.7}$$

where F is the weighted χ^2 deviation of the data points $\tilde{y}_i$ (observed at epochs x_i with $r \leq x_i \leq s$) from the smoothed values y_i, i.e.

$$F = \sum_i w_i (y_i - \tilde{y}_i (x_i))^2 \quad , \tag{7.8}$$

where w_i are the weight factors for the individual data points. The smoothness S of the graduated curve ϕ is given by the third derivatives according to

$$S = \int_r^s [\phi'''(x)]^2 dx \quad , \tag{7.9}$$

Figure 7.3: Cumulative fraction of the WeCAPP novae as function of the isophotal radius of the bulge and total *r*-band light (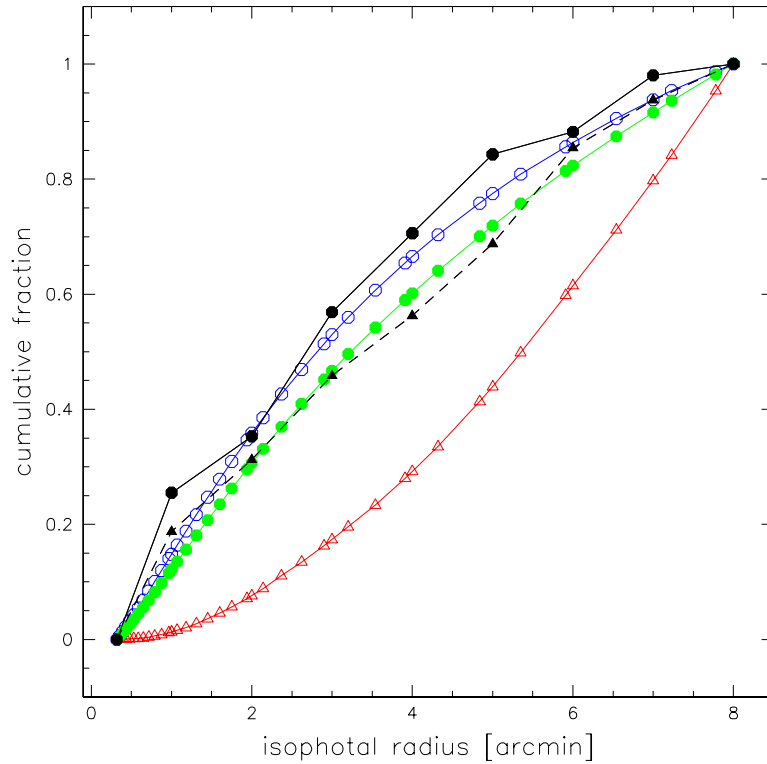black dots, black line), and for the disk light (black triangles, black dashed line). For comparison we show the cumulative r-band light for the bulge (open blue dots, blue line) and the disk (open red triangles, red dashed line). In green we show the distribution for the total light.

and is controlled by the parameter λ, which defines the degree of graduation. The data were smoothed using the program hec13, written by Dr. Harmanec based on Vondrák's method. Input parameters are the width ΔT, inside which the data will be binned, and ε (corresponding to λ^{-2}). We found that $\Delta T = 2$ d and $\varepsilon = 10^{-3}$ yielded the best results. With this parameter set we smoothed the light curves but retained the large fluctuations. In Fig. 7.4 we show two examples of the the smoothed light curves (red points) along with the original data points (black points) and a linear interpolation between the smoothed data.

7.5   Calculating the magnitudes

Before we derive magnitudes from the difference light curves we investigate the systematic error induced by an unknown source luminosity. Let $F_b \equiv F(t_0)$ and $F_t \equiv F(t)$ the luminosity of a source at epochs t_0 and t respectively, where F_b describes the constant (baseline) luminosity of the source. The measurement of the difference flux at epoch t relative to F_b yields $\Delta F_t(t) = F_t - F_b$. The magnitude of the source at each epoch t is given by

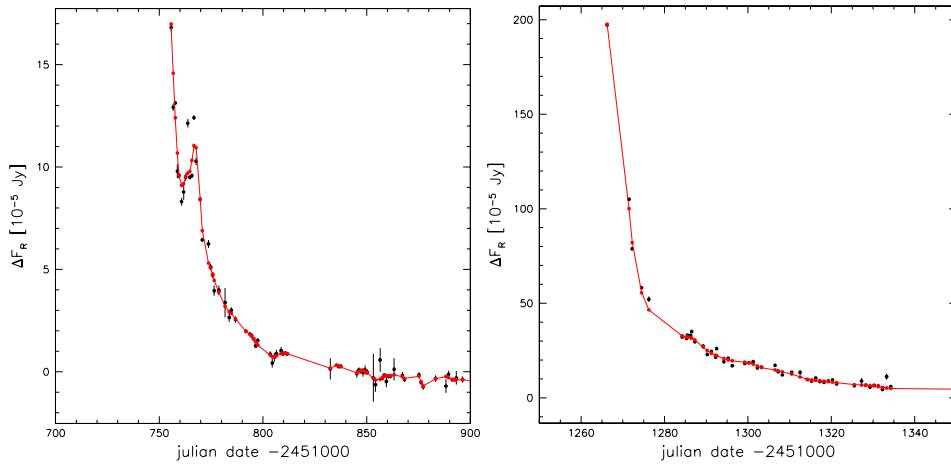$$m(F_t) = -2.5 \cdot \log(F_t/F_0) \tag{7.10}$$

Figure 7.4: Two examples of smoothed nova light curves in the *R*-band. The left panel shows nova N40 , the right panel nova N47. In black we show the original data, whereas in red we show the data smoothed using the implementation hec13 of the method of Vondrák (1969, 1977), which was kindly provided by Dr. Harmanec.

where F_0 is the flux of Vega in the particular waveband. With f describing the fraction of the flux F_t being due to the difference flux ΔF_t, i.e.

$$f = \frac{\Delta F_t}{F_t} \quad , \tag{7.11}$$

we can write

$$F_t = \Delta F_t + F_b = f F_t + (1 - f) F_t \tag{7.12}$$

During eruption, novae reach amplitudes of more than 10 mag in optical bands, thus f gets close to unity in this case. The baseline flux therefore can be neglected and the magnitudes derived from the difference fluxes, without an a priori knowledge of the source luminosity at the reference epoch, can be regarded as the real magnitude of the source:

$$m(F_t) = -2.5 \log \left(\frac{F_t}{F_0} \right) = -2.5 \log \left(\frac{f F_t + (1-f) F_t)}{F_0} \right) \approx -2.5 \log \left(\frac{f F_t}{F_0} \right) = m(\Delta F_t) \tag{7.13}$$

Our analysis covers novae down to approximately 1% of their maximal luminosity, corresponding to f-values larger than 0.99. As can be seen from Fig. 7.5, the systematic error in the magnitude determination can be neglected in the whole analyzed luminosity region.

We further correct the magnitudes for extinction using the extinction frame presented in chapter 6. To reduce the noise in the extinction estimation, we smooth the frame by applying a median filter with a box size of 5×5 pixels. For the central part of the field the extinction values are unknown due to saturation of the frames used to calculate the extinction map (see chapter 6). As in the center no heavily extincted regions are visible in the optical data and the extinction frame shows rather constant values in the regions surrounding the central part, we extrapolate our extinction frame to the regions where no extinction values are available. For these parts we assume a constant extinction of
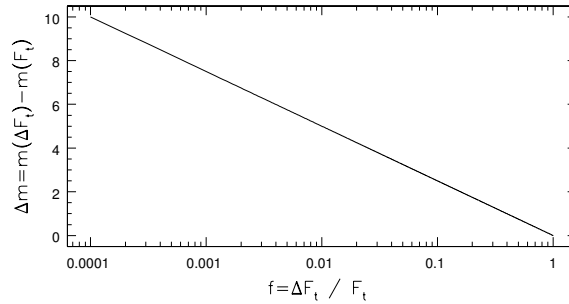
Figure 7.5: Difference of magnitudes derived from difference fluxes and real magnitudes as function of the fraction $f = \Delta F_t/F_t$. For novae at maximum $f \approx 1$, thus the magnitudes derived from the difference fluxes without any knowledge of the luminosity at the reference epoch are reliable (see text for details).

$ext_R = 0.28$. The corrected magnitudes $m(\Delta F_{t,0})$ are finally derived according to

$$m(\Delta F_{t,0}) = m(\Delta F_t) - ext \quad . \tag{7.14}$$

7.6 The M_{15} relation

From the examination of V-band light curves of Galactic novae Buscombe & de Vaucouleurs (1955) derived that all novae should have the same V-band luminosity

$$M_V(15) = -5.2\text{mag} \pm 0.1 \quad , \tag{7.15}$$

15 days past maximum light (epoch t_0). Around this time the dispersion of the light curves of different speed classes gets minimal, making it possible to derive a mean luminosity of novae around this epoch. Pfau (1976) re-calibrated this relation and derived

$$M_B(15) = -5.7\text{mag} \pm 0.6 \quad , \tag{7.16}$$

using a sample of 46 well-observed novae in the Galaxy, M31, M33, the LMC, and the SMC. For simple assumptions on the rate of decline Shara (1981) deduced the constancy of $M_B(15)$ theoretically from the existence of a maximum magnitude–rate of decline relationship. The light curves should intercept at a certain timescale past maximum as the brighter novae decline faster. For the R-band the results are inconclusive. Darnley *et al.* (2005) could not confirm the existence of the relation for the Sloan $r'-$band using novae from the POINT-AGAPE catalogue (Darnley *et al.*, 2004). This negative result could, however, be due to an underestimation of the maximal errors in the time estimation of maximum light for the novae used to calibrate this relation.

   Using light curves from our sample, for which the maximum was known better than 6 days, we examined if the dispersion of the data points shows a minimum at some point after maximum. Furthermore, we investigated if a delay of 15 days past maximum is correct. For this purpose we calculated the dispersion of the R-band light curves of 8 novae from 2000 to 2003, for which we could constrain the epoch of the outburst with an accuracy of better than 6 days. This was possible using our data alone, and by a comparison with the outburst dates and the photometry of published novae, which correlated with novae from our sample (see below).
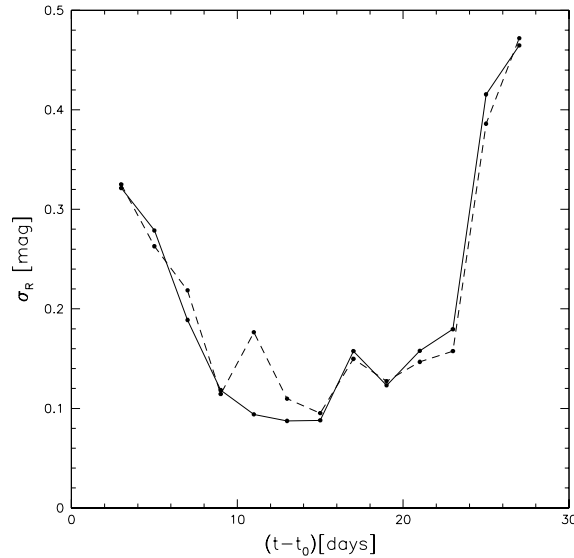
Figure 7.6: Dispersion of the binned light curves with well defined maximum as function of the time passed since maximum light. The solid line was derived using 8 novae. Although the dispersion shows fluctuations there is a clear sign of a minimum at $(t - t_0) \approx 15$ days. The inclusion of nova N7 enhances the dispersion in the region between 10 and 12 days past maximum (dashed line). This can be ascribed to a flare-like feature, appearing at an early stage of the decline.

We transformed the smoothed light curves to magnitudes and corrected the brightness for extinction as described above. Then we binned the data in time intervals of two days starting at the epoch of maximum light t_0, which was obtained as the midpoint of the uncertainty interval of the outburst time. In each bin we calculated the weighted mean of the data points and their weighted standard deviation σ. The weight of each data point was chosen as the inverse of the accuracy of the time of maximum light. The solid line in Fig. 7.6 shows the resulting σ_R as function of the time passed since the outburst of the novae. The dispersion of the novae light curves shows a smooth decline until it reaches a minimum around 15 days past maximum. The mean brightness of the novae is derived to

$$m_R(15) = 18.05 \pm 0.1 \text{mag} \quad , \tag{7.17}$$

where the error corresponds to the dispersion of the light curves. The result implies that the $m_R(15)$ relation seems to hold for fast and moderately fast novae. However, as the 3 light curves with the largest weights are quite similar, the result could be biased against moderately fast novae. With the distance modulus of M31 $(m - M) = 24.43$ the derived $m_R(15)$ translates to an absolute magnitude $M_R(15) = -6.38 \pm 0.1$ mag. This is in agreement with the aforementioned values found for the V and B bands (see Eqs. 7.15 and 7.16). The relation seems to break down for very fast novae with $t2$ times smaller than about 10 days, with the novae being too faint for the time passed since maximum light. This deviation was already found by van den Bergh & Younger (1987) using a large sample of Galactic nova light curves in the U, B, and V bands.

The dashed line in Fig. 7.6 shows the dispersion after including nova N7, which had a well observed maximum too. The now enhanced dispersion at 10 to 12 days past maximum can be ascribed to a flare-like feature in the light curve of nova N7, which appeared at an early stage of the decline.

The region around 15 days past maximum remained unaffected as the nova returned already to its pre-flare decline at this stage. Recently, Liller & Shida (2005) re-examined the M_{15} relation in the V-band using two samples of Galactic and LMC novae. They found that the V-band dispersion of the LMC sample showed a minimum 13 days past maximum, whereas the sample of Galactic novae showed on average the same brightness 15 days after maximum V-band luminosity. As in our case the dispersion shows a rather broad valley (narrowed by the inclusion of N7), we cannot rule out a delay of 13 days for the M31 R-band nova light curves from our data.

The flare-like feature in nova N7 could also be observed in some other nova light curves, although it appeared later (> 20 days past maximum) and showed lower luminosities. This behavior was already observed by Šimon et al. (2005) in their sample of R-band nova light curves. The mean brightness of this flare-type feature was derived to approximately −6.5 mag in the R-band. In our sample N18, N32, N40, N44, N55, and N56 show this brightening after more than 20 days past maximum light. The maximal luminosity seems rather constant and can be estimated as $m_{20,flare} \approx$ −6.6 mag, very similar with the value given in Šimon et al. (2005). Among other possibilities like a rapid change of the continuum luminosity, Šimon et al. (2005) proposed a rapid change of the H_α emission as source of this brightening. However, as our data showed the brightening in the I-band data too, the H_α emission could not be the source of these variations in the light curves.

7.7   Light curve fitting

We used the brightness of novae 15 days past maximum $m_R(15)$ to determine the date of the outburst t_0 for the novae with unsampled maxima more precisely. If the value of $m_R(15)$ was bracketed by observations, we interpolated linearly between adjacent points in the smoothed and extinction corrected light curves $\Delta F_R^c(t)$. If the maximum brightness of the novae was fainter than $m_R(15)$, we extrapolated the smoothed light curves linearly to the value of the difference flux corresponding to $m_R(15)$. For the upper and lower 1σ limits $m_R(15^+)$ and $m_R(15_-)$ we proceeded the same way. The epoch of maximum light t_0 and its error interval were determined from the epochs $t15$, $t15^+$, and $t15_-$, at which the light curves reached $m_R(15) \pm 1\sigma$. With t_0 and its error range we then could fit the light curves in order to determine the maximum brightness and the decay timescale of the novae. We used an assumed exponential fitting function

$$\log(m(F_t)) = a_1(t - t_0) + b_1 \qquad t \leq t_c \quad , \tag{7.18}$$

$$\log(m(F_t)) = a_2(t - t_c) + b_2 \qquad t > t_c \quad , \tag{7.19}$$

where we allowed for the slope to change from a_1 to a_2 at any point of the light curve. The time t_c of the change of slope (if present) was determined by visual inspection of the light curves. For the fit at the bright end (Eq. 7.18) the temporal zero-point was kept fixed at the estimated t_0 from the $m_R(15)$ relation (or its upper and lower error limits, respectively).

The theoretical function of Eqs. 7.18 and 7.19 fitted the data well, reflecting the exponential evolution of the light curves. Overlayed on this decline in luminosity smooth fluctuations often modulate the exponential change of the magnitudes. In Fig. 7.7 we give an example of the fits to the light curves, where we show the fits using $t15$, $t15^+$, and $t15_-$ as the epochs 15 days past maximum light, respectively.
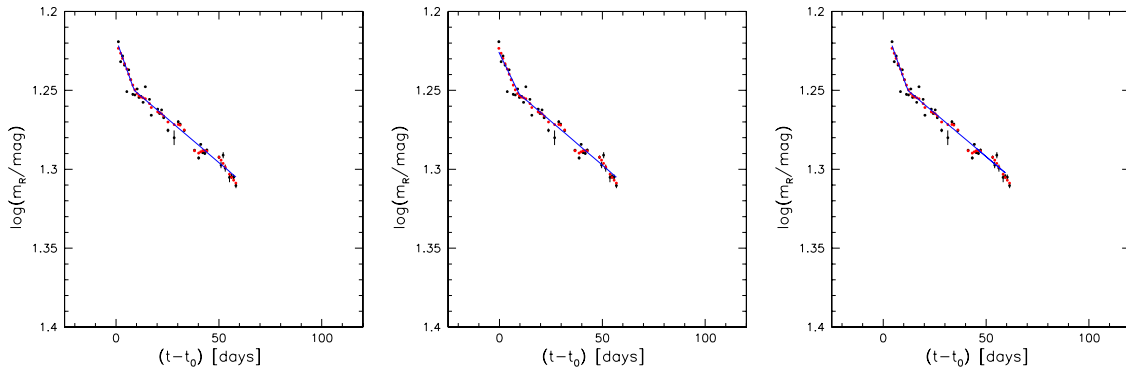
Figure 7.7: This figure shows as an example the light curve of nova N42 (black points), its smoothed light curve (red points), and the fit to the un-smoothed data points (blue line). From left to right we show the fits using $t15$, $t15^+$, and $t15_-$ as the epochs 15 days past maximum light, respectively.

We could determine the maximum magnitude $m(R)_0$ and the $t2$ timescale for 21 of the 40 novae erupting between 2000 and 2003. We excluded light curves which were sparsely sampled during the decline and light curves which did not allow to estimate t_c. For the novae with well sampled outbursts we obtained the time of the outburst directly from the light curve and then proceeded with the fits. The errors of $m(R)_0$ and $t2$ where determined from the range of the solutions for the time of the outburst t_0 using the mean value of $m_R(15)$ and its 1σ values $m_R(15^+)$ and $m_R(15_-)$. We add or subtract the formal fit errors to the values obtained using $m_R(15^+)$ and $m_R(15_-)$ as absolute values, since the latter error is of systematic nature. In the appendix to this chapter we show the fits to all 21 novae where we have used the mean value of $m_R(15)$ for the estimation of the outburst date. In Fig. 7.8 we show the resulting MMRD for the R-band light curves. The MMRD is fairly well recovered and well populated for $t2$ timescales from 12 days to 50 days. In this regime the MMRD shows the expected linear decline, as already found for bluer bands (see e.g., Capaccioli *et al.* 1989 and Sharov & Alksnis 1992). At longer timescales the MMRD seems to flatten and to develop an 's-shape', which was also observed by Capaccioli *et al.* 1989. The same trend should be present at short timescales, i.e. very fast novae should fall of the relation to fainter maximal magnitudes. Due to the lack of well sampled novae and the uncertainty of the M_{15} relation in this regime we can not confirm this result with our data.

Figure 7.9 finally shows the R-band luminosity function of the 21 novae from the MMRD. For this diagram we used the maximum brightness as derived from fits using $m_R(15) = 18.05$ mag. The luminosity function shows a bimodal distribution which can be ascribed to the 's-shape' of the MMRD according to Capaccioli *et al.* (1989).

7.8 Correlations with published novae

To search for coincidences with already published novae and for candidates of recurrent novae, we correlated the positions of our sample with the positions of novae taken from the literature.

For historical novae prior to 1995, we correlated our sample with novae taken from the General Catalogue of Variable Stars (GCVS, Durlevich *et al.* 1996), which compiles novae towards M31 published until then. For later novae we correlated the sample with novae from
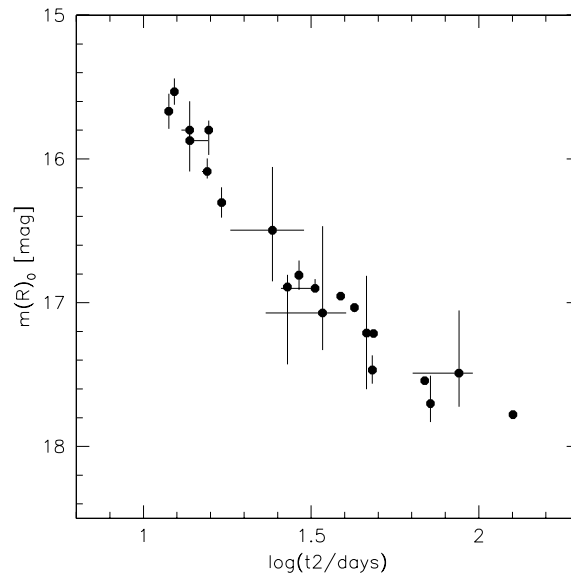
Figure 7.8: Diagram showing the maximum magnitude–rate of decline relationship (MMRD) for the *R*-band data. The MMRD is well recovered by our data. Between 12 days and 50 days the MMRD shows a linear behavior, whereas it seems to flatten at longer timescales, leading to an 's-shaped' relation. For the novae with very small error bars we could derive the time of the outburst directly from the light curves.
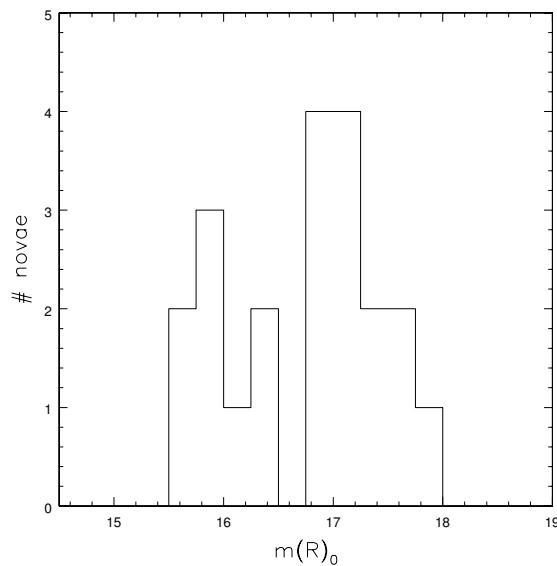
Figure 7.9: This figure shows the *R*-band luminosity function of the novae with fitted maximal luminosities. The bimodal distribution can be ascribed to the 's-shape' of the MMRD according to Capaccioli *et al.* (1989).

the IAU Circulars and with unpublished novae from the web-based archive of David Bishop at www.supernovae.net/snyyyy/novae.html[1], where most of the extensive results of Dr. Hornoch are presented. We also used novae published on the web-archive 'The apparent novae page' at http://cfa-www.harvard.edu/iau/CBAT_M31.html[2]. Furthermore, we used novae published by Rector *et al.* (1999); Sharov *et al.* (2000); Shafter & Irby (2001); Darnley *et al.* (2004); Ansari *et al.* (2004); An *et al.* (2004); Joshi *et al.* (2004); Šimon *et al.* (2005), and from 'The Astronomer's Telegram (ATEL)'.

7.8.1 Coincidences with novae since 1995

By using a search radius of 4 arcsec we found 50 novae in our sample coincident with novae published since 1995. Tables 7.4 and 7.5 contain all correlations along with the coordinates, the time of observed maximum, and the references for the published novae. Our nova sample therefore contains 18 first detections. The correlations show that during the campaigns 2000-2002 we detected the novae usually relatively early, as expected for the simultaneous campaigns at Wendelstein and Calar Alto. With the sparser sampled observations from 2002 on we still detect novae, but miss the time of the outburst more likely.

7.8.2 Recurrent novae

For the correlation with historical novae, i.e. novae which appeared before our observational campaigns we used a search radius of 7 arcsec. We chose this somewhat larger search radius as the positions of very early novae could show larger uncertainties than novae detected nowadays.

   We found 7 coincidences, whereas one historical nova correlates with three novae in our sample. These novae we regard as candidates for recurrent novae and show them in Table 7.6.

Nova 41   Nova 41 correlates with Nova N27 in Ciardullo *et al.* (1987). N27 was observed on 1985, October 15th at a maximum brightness of 15.59 mag in the *B*-band, corresponding to a recurrence time of ≈ 6600 days. The fits to WeCAPP N41 yield a maximal brightness of $m(R)_0 = 16.3 \pm 0.1$ mag and classify the nova as fast ($t2 = 17.1 \pm 0.1$ days).

Novae 30, 32, and 33   All three novae correlate with with Nova N137 in Rosino *et al.* (1989). N137 was observed on 1984, July 31st at a maximum brightness of 17.6 mag in the *B*-band.

   Of all three coincidences WeCAPP N33 is the most likely candidate for a recurrent nova as it shows the smallest difference in the positions. This does not mean, however, that the other two correlations are ruled out as possible recurrent counterparts to N137. Our novae N32 and N33 appear at slightly different positions, so that both have to be regarded as separate novae.

   The fits to WeCAPP N30 yield a maximal brightness $m(R)_0 = 16.1 \pm 0.1$ mag and classify the nova as fast ($t2 = 18.2 \pm 0.2$ days). The recurrence time can be estimated to ≈ 7100 days.

   WeCAPP N32 had a well observed maximum. The fits yield a maximal brightness of $m(R)_0 = 17.5$ mag and classify the nova as moderately fast ($t2 = 69$ days). Due to the known time of the outburst the fit yields errors below 0.1 mag. The recurrence time can be estimated to ≈ 6300 days.

---

[1]yyyy refers to the year of the outburst. These novae are marked with '(a)' behind the identifications in Tables 7.4 and 7.5

[2]These novae are marked with '(b)' behind the identifications in Tables 7.4 and 7.5

WeCAPP	t_{max}	RA(2000)	DEC(2000)	t_{max}	$\Delta r[^{\prime\prime}]$	Reference
01	1094.6	0h43m18.6s	41d09′50 ″	1133	0.9	PAV-74935, An *et al.* (2004)
02	1163.7	0h43m10.6s	41d17′57.6″	1148.7	0.5	PACN-01-03, Darnley *et al.* (2004)
03	2039.3	0h43m08.63s	41d15′36.4″	2027.2	1.0	*N*2004_1 (a)
	2039.3	0h43m08.6s	41d15′36″	2035	0.8	*N*9, Šimon *et al.* (2005)
04	2319.5	0h43m07.43s	41d18′04.4″	2315.3	0.3	2004 − 11*b* (b)
06	-254.5	0h43m05.4s	41d14′59″	-245.5	0.4	*N*1997 − 14 , Shafter & Irby (2001)
07	1992.3	0h43m04.77s	41d12′20.8″	1994.2	1.2	*IAUC* 8262
	1992.3	0h43m04.8s	41d12′23″	1997	1.4	*N*8, Šimon *et al.* (2005)
08	1190.5	0h43m03.3s	41d12′11.3″	1188.9	0.2	*IAUC* 7729
	1190.5	0h43m03.2s	41d12′10.5″	1194.6	1.6	PACN-01-06, Darnley *et al.* (2004)
	1190.5	0h43m03.3s	41d12′10.8″	1202	0.7	*NMS*2, Joshi *et al.* (2004)
09	372.6	0h43m01.82s	41d15′38.5″	379.5	0.4	Rector *et al.* (1999)
10	1476.5	0h43m01.07s	41d16′20.1″	1478.0	0.2	*IAUC* 7937
	1476.5	0h43m01.00s	41d16′20.3″	1461.5	1.0	*IAUC* 7938
11	1979.3	0h43m00.75s	41d11′26.7″	1979.3	0.2	*IAUC* 8253
12	1797.5	0h42m58.34s	41d16′07.8″	1809.5	0.7	*IAUC* 8155
15	1994.3	0h42m54.08s	41d15′12.1″	1998.3	0.7	*IAUC* 8262
16	1949.5	0h42m53.64s	41d18′45.9″	1952.6	1.6	*IAUC* 8248
17	1997.5	0h42m53.22s	41d22′35.5″	1997.2	0.5	*IAUC* 8266
18	1283.3	0h42m52.83s	41d15′10.6″	1288.3	0.7	*IAUC* 7794
	1283.3	0h42m52.9s	41d15′11″	1296	0.6	PAV-79136, An *et al.* (2004)
19	2427.3	0h42m52.76s	41d14′29.0″	2420.3	0.4	2005 − 02*a* (b)
	2427.3	0h42m52.76s	41d14′29″	2420.3	0.4	ATEL 421
21	-249.6	0h42m52.4s	41d16′13″	-245.5	0.6	1997 − 10, Shafter & Irby (2001)
22	1797.5	0h42m52.22s	41d13′54.2″	1809.5	0.4	*IAUC* 8155
23	2293.4	0h42m51.84s	41d16′18.2″	2287.8	0	2004 − 10*a* (b)
	2293.4	0h42m51.84s	41d16′18.2″	2287.8	0	*N*2004_15 (a)
24	1867.5	0h42m49.61s	41d18′01.8″	1883.3	0.4	*IAUC* 8210
26	359.5	0h42m49.7s	41d15′08″	426	2.4	PAV-78668, An *et al.* (2004)
	359.5	0h42m49.5s	41d15′06″	360.9	2.2	*IAUC* 7218
29	763.7	0h42m47.47s	41d15′07.5″	762.7	0.3	2000 − 08*a* (b)
31	2291.5	0h42m47.24s	41d15′54.6″	2287.8	0.1	2004 − 10*b* (b)
	2291.5	0h42m47.24s	41d15′54.6″	2287.8	0.1	*N*2004_16 (a)
33	2319.5	0h42m47.20s	41d16′19.7″	2335.4	0.6	2004 − 11*f* (b)
34	1931.3	0h42m46.72s	41d19′46.7″	1913.3	0.7	*IAUC* 8222
	1931.3	0h42m46.7s	41d19′47″	1913	0.6	*N*5, Šimon *et al.* (2005)

Table 7.4: Correlations of the WeCAPP novae with published novae. We give the identification and the time of the observed maximum t_{max} for the WeCAPP novae in the first two columns. For the published novae we give the reference and the identification, the coordinates in the WCS, the published time of the observed maximum t_{max}, and the distance in arcsec between the detections. The time of the observed maximum is shown as (julian date − 2451000).

WeCAPP	t_{max}	RA (2000)	DEC (2000)	t_{max}	$\Delta r[{}'']$	Reference
35	726.6	0h42m46.76s	41d12′51.8″	762.7	0.2	$2000-08b$ (b)
36	125.4	0h42m46.6s	41d14′50″	71.8	0.9	*IAUC* 7015
	125.4	0h42m46.64s	41d14′47.8″	70.4	1.4	Sharov *et al.* (2000)
38	2346.2	0h42m45.63s	41d16′32.8″	2334.2	2.0	$2004-11d$ (b)
39	1820.5	0h42m45.10s	41d17′53.7″	1840.5	0.4	*IAUC* 8165
40	755.7	0h42m44.6s	41d20′42.1″	766.6	1.6	PACN-00-03, Darnley *et al.* (2004)
41	1940.5	0h42m44.43s	41d15′52.3″	1938.5	1.0	*IAUC* 8238
42	754.6	0h42m44.0s	41d17′56.5″	760.5	1.1	PACN-00-01, Darnley *et al.* (2004)
43	2319.6	0h42m42.82s	41d18′26.8″	2317.0	1.0	$2004-11a$ (b)
	2319.6	0h42m42.76s	41d18′28.0″	2315.3	0.6	*N*2004_18 (a)
45	2254.4	0h42m42.77s	41d15′44.4″	2239.5	0.3	ATEL 330
46	-246.5	0h42m42.14s	41d15′10.8″	-245.5	0.3	$1997-07$, Shafter & Irby (2001)
47	1266.3	0h42m41.38s	41d16′24.6″	1288.3	0.7	*IAUC* 7794
48	1832.6	0h42m41.10s	41d18′32.0″	1840.5	0.6	*IAUC* 8165
49	1925.5	0h42m41.11s	41d16′16.1″	1929.5	1.0	*IAUC* 8226
51	1164.7	0h42m40.6s	41d07′59.9″	1148.7	0	PACN-01-04, Darnley *et al.* (2004)
52	2254.4	0h42m40.25s	41d14′42.9″	2251.5	0.5	*IAUC* 8404
	2254.4	0h42m40.25s	41d14′42.9″	2251.5	0.5	$2004-09a$ (b)
56	766.6	0h42m37.6s	41d17′38.6″	766.7	1.4	PACN-00-04, Darnley *et al.* (2004)
58	1151.6	0h42m34.55s	41d18′13.8″	1156.4	1.1	*IAUC* 7709
	1151.6	0h42m34.6s	41d18′13″	1165	0.2	PAV-26277, An *et al.* (2004)
59	1282.3	0h42m33.79s	41d18′23.7″	1288.3	1.1	*IAUC* 7794
	1282.3	0h42m33.9s	41d18′24″	1290	0.2	PAV-26285, An *et al.* (2004)
60	2346.4	0h42m32.27s	41d19′25.2″	2326.3	0.5	$2004-11c$ (b)
	2346.4	0h42m32.3s	41d19′25″	2318.4	0.7	*N*2004_17 (a)
62	1130.6	0h42m30.72s	41d14′36.8″	1121	1.1	*IAUC* 7674
	1130.6	0h42m30.6s	41d14′36.8″	1135.6	2.3	PACN-01-01, Darnley *et al.* (2004)
64	2382.4	0h42m28.38s	41d16′36.2″	2378.4	0.1	$2005-01a$ (b)
	2382.4	0h42m28.40s	41d16′36.8″	2377.3	0.6	*N*2005_01 (a)
65	2381.4	0h42m28.05s	41d09′55.6″	2370.2	0.9	$2004-12a$ (b)
66	-245.4	0h42m21.8s	41d12′17″	-276.5	0.8	$1997-02$, Shafter & Irby (2001)
67	1164.7	0h42m18.47s	41d12′38.9″	1138	0.7	*IAUC* 7684
	1164.7	0h42m18.4s	41d12′40.3″	1142.7	1.7	PACN-01-02, Darnley *et al.* (2004)
68	1834.4	0h42m15.81s	41d12′00.5″	1835.5	0.6	*IAUC* 8165
	1834.4	0h42m15.8s	41d12′0″	1835	0.5	*N*3, Šimon *et al.* (2005)

Table 7.5: Correlations of the WeCAPP novae with published novae. This table continues Table 7.4.

WeCAPP	t_{max}	GCVS	RA (2000)	DEC (2000)	$\Delta r[{}'']$	Reference
41	1940.5	V0905	0h42m44.64s	41d15′53.8″	1.9	N27, Ciardullo *et al.* (1987)
30	2039.3	V0922	0h42m47.24s	41d16′19.8″	1.6	N137, Rosino *et al.* (1989)
32	1197.3	V0922	0h42m47.24s	41d16′19.8″	1.2	N137, Rosino *et al.* (1989)
33	2319.5	V0922	0h42m47.24s	41d16′19.8″	1.0	N137, Rosino *et al.* (1989)
43	2319.6	V0893	0h42m42.95s	41d18′33.8″	6.2	N65, Rosino (1973)
62	1130.6	V0820	0h42m31.07s	41d14′37.9″	3.6	N111, Stratton (1936)
13	1095.5	V0979	0h42m57.71s	41d08′11.9″	0.7	N48=N79, Rosino (1973)

Table 7.6: Correlations of the WeCAPP novae with historical novae. The coincidences can be regarded as candidates for recurrent novae. We give the identification and the time of the observed maximum t_{max} for the novae in our catalogue in the first two columns. For the historical novae we give the identification in the GCVS as well as in the original publication, the coordinates in the WCS, and the distance in arcsec between the detections. The time of the observed maximum is shown as (julian date -2451000).

The fits to WeCAPP N33 yield a maximal brightness of $m(R)_0 = 17.6 \pm 0.2$ mag and classify the nova as moderately fast ($t2 = 60.5 \pm 1.5$ days). The recurrence time can be estimated to ≈ 7400 days.

Nova 43   Nova 43 is at relatively large distance of approximately 6 arcsec to Nova N65 in Rosino (1973). N65 was observed on 1967, January 1st at a maximum brightness of 17.3 photographic magnitudes, corresponding to a recurrence time of ≈ 14200 days. The fits to WeCAPP N43 yield a maximal brightness of $m(R)_0 = 17.2 \pm 0.1$ mag and classify the nova as moderately fast ($t2 = 39.2 \pm 1$ days).

Nova 62   Nova 62 is at a distance of 3.6 arcsec to the historical nova Nova N111 in Stratton (1936). Unfortunately, we do not have access to this publication. According to the GCVS the nova erupted 1932, corresponding to a recurrence time of ≈ 69 years. Its maximal brightness is not known. WeCAPP N62 was observed at an uncorrected maximum brightness $m_{R,max} = 18.7$ mag and appears to be a slow nova. As the nova was caught late in the decline, the light curve did not allow a robust fit to the data.

Nova 13   Nova 13 is already known as a recurrent nova. As the agreement between the positions is very good, it appears that WeCAPP N13 corresponds to novae N48 and N79 in Rosino (1973). The first outburst (N48) was observed on 1963, September 15th, where it reached a maximal amplitude of 17.8 photographic magnitudes. The second outburst (N79) appeared on 1968, September 24th with an estimated maximal luminosity of 17.1 photographic magnitudes. We observed the outburst on 2001, July 4th approximately at its maximum where it showed an uncorrected maximal brightness $m_{R,max} = 18.1$ mag. The recurrence times can be estimated to ≈ 1800 days (N48 to N79) and ≈ 12000 days (N79 to Nova 13), respectively. The nova can be classified as very fast as it declined 2 mag in the first three days after detection. In Fig. 7.8.2 we show the light curves of N48 and N79 along with the light curve of WeCAPP N13.

   Due to its small recurrence time the GCVS classifies N48≡N79 in Rosino (1973) as dwarf nova. This subclass of cataclysmic variables shows repeated outbursts with maximum luminosities below that of classical novae. In contrast to classical novae the brightening is caused by a change of the accretion properties in the system. Note, that the dwarf nova classification is not part of the original publication. However, as we detected the outburst close to its maximum brightness, being to small for its decay time, the dwarf nova classification gains further support. We therefore did not include N13 in the calibration of the M_{15} relation, despite the very good time coverage of the outburst.

7.9   Summary

In this chapter we presented the WeCAPP novae catalogue, comprising over 60 novae which erupted between autumn 1997 and spring 2005. We developed detection algorithms which select the novae candidates rather automatically from the pixel light curves and yield only a small number of contaminants. The selection criteria are based on the eruptive nature of novae light curves with large excess fluxes and asymmetric light curves (with respect to positive and negative difference fluxes). We detected 68 novae which makes this sample to one of the largest and most homogeneous samples of optical novae. We examined the spatial distribution of the novae and compared it with the distribution of the M31 r-band bulge, disk, and total light. We find that the novae distribution agrees best with the
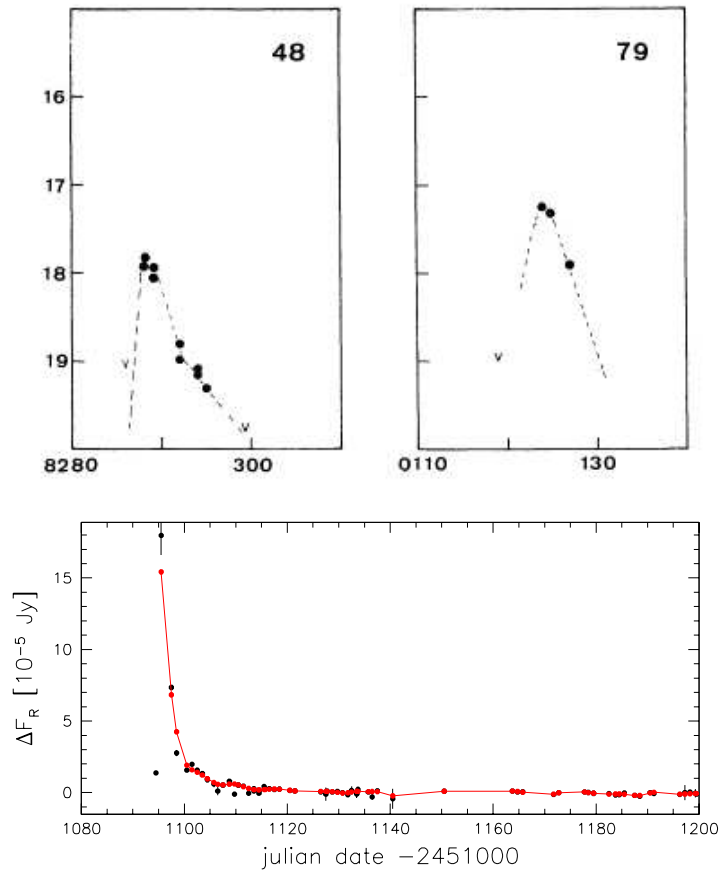
Figure 7.10: Candidate for a recurrent nova. In the upper two panels we show the historic light curves of N48≡N79 taken from Rosino (1973). In the lower panel we show the light curve of the WeCAPP N13 which was detected in July 2001.

r-band bulge light. The good time coverage of the WeCAPP data enabled us to determine the time of the outburst quite accurately for a subsample of the novae. Using these light curves, we investigated the M_{15} relation for the *R*-band, i.e. the constancy of the brightness of novae 15 days past maximum. This relation seems to hold for fast and moderately fast novae, but probably breaks down for very fast novae. With the time of the outburst given by the M_{15} relation we derived the maximum magnitude - rate of decline relationship (MMRD) from exponential fits to the *R*-band light curves, using a sub-sample of well sampled light curves with outburst dates between 2000 and 2003. The MMRD shows a linear behavior over most of the range of decline rates. At small rates the relation flattens leading to an 's-shaped' MMRD as already found by Capaccioli *et al.* (1989). We correlated our nova sample with published novae and with the positions of historical novae. The coincidences showed that 18 of the novae are first detections which underlines the efficiency of the difference imaging method in crowded fields. Furthermore, we found 5 candidates for recurrent novae. One of the candidates was already known as candidate for a recurrent nova with two observed outbursts in 1963 and 1968. For the other candidates only two outbursts, one historic and one in the WeCAPP data are known. Pietsch *et al.* (2005) correlated a subsample of the WeCAPP novae with super-soft *X*-ray sources in M31. As the envelope of a nova gets transparent to *X*-rays after a timespan of months, super-soft emission can

escape the shell. The detection of super-soft emission in novae strongly supports the existence of a steady-state hydrogen burning in the not-expelled envelope of the white dwarf. Moreover, the large number of coincidences between novae and super-soft sources found in this study favors the idea that novae are the major source for super-soft emission in M31. For some of the novae the X-ray emission started with a long delay of several years, which makes it likely that the emission stems from recurrent novae, whose X-ray emitting outburst was missed in optical bands.
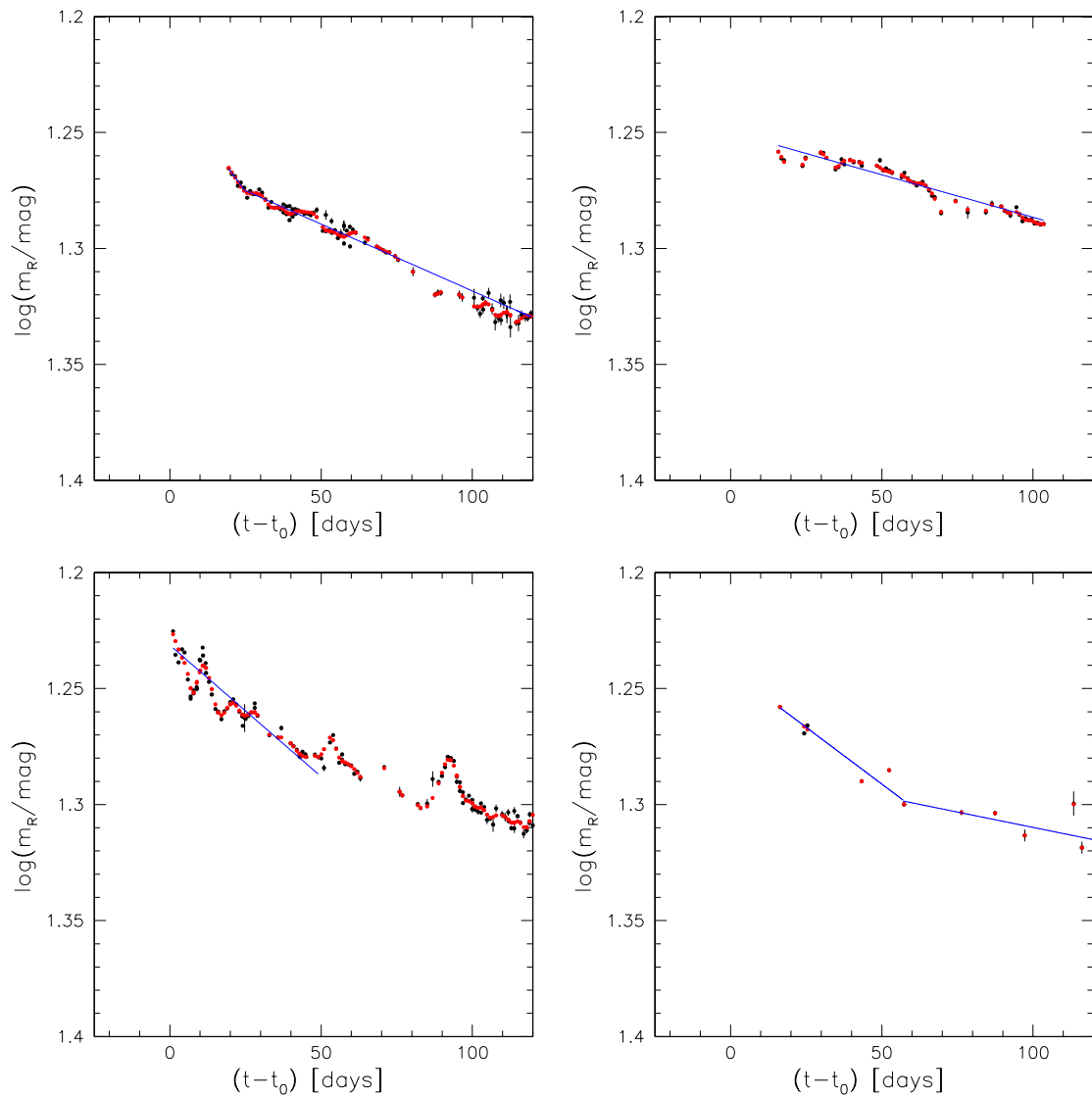
7.10   Appendix to chapter 7

Figure 7.11: Fits to the R-band light curves using the mean value of $m_R(15)$. In black we show the original data, whereas the red points give the smoothed values. The blue lines show the fits to the original data points, necessary to derive $m(R)_0$ and $t2$. Note that, for a better comparison, we have used the same range for all plots.
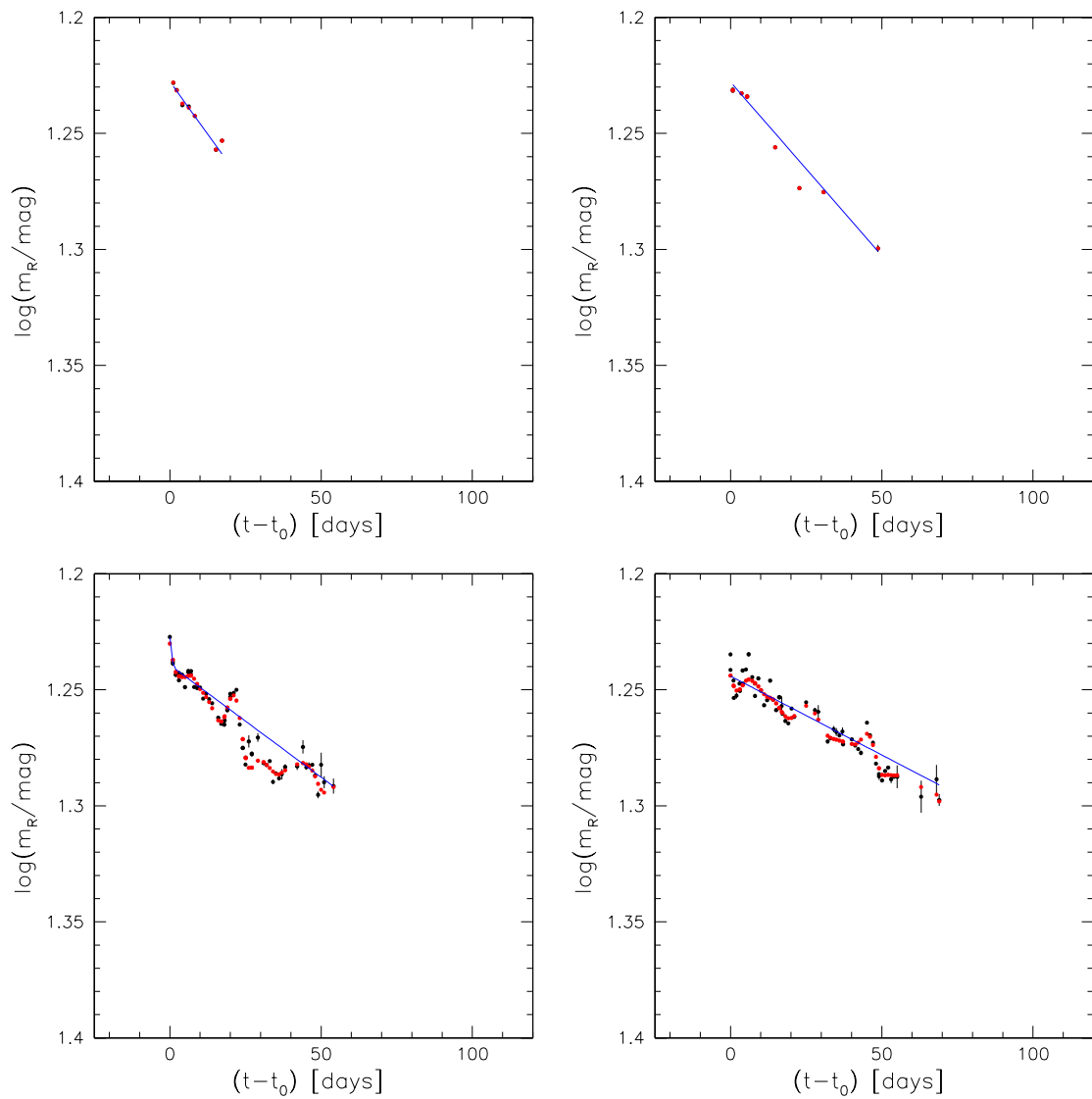
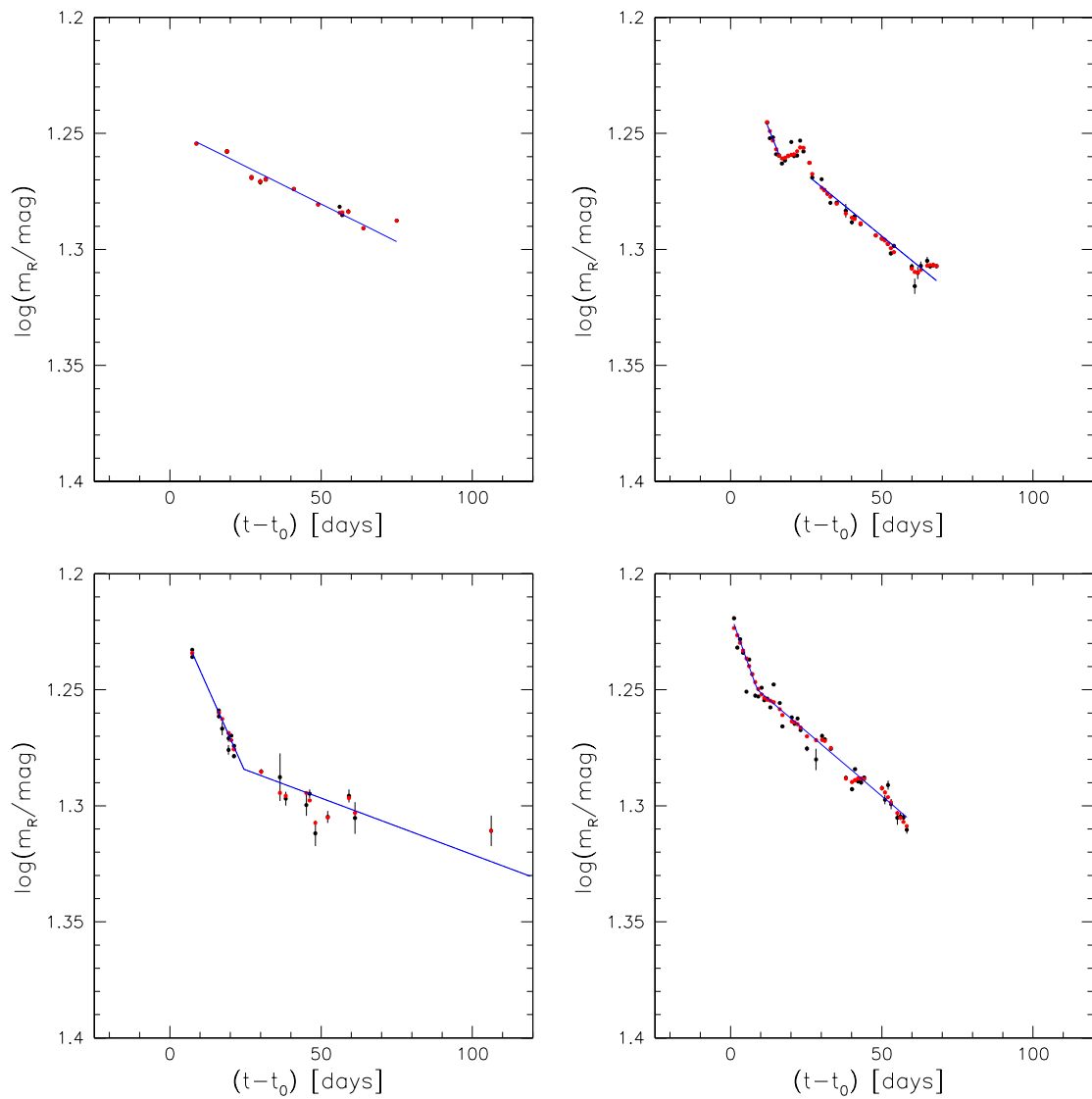Figure 7.12: Fits to the R-band light curves using the mean value of $m_R(15)$. This figure continues Fig. 7.11.

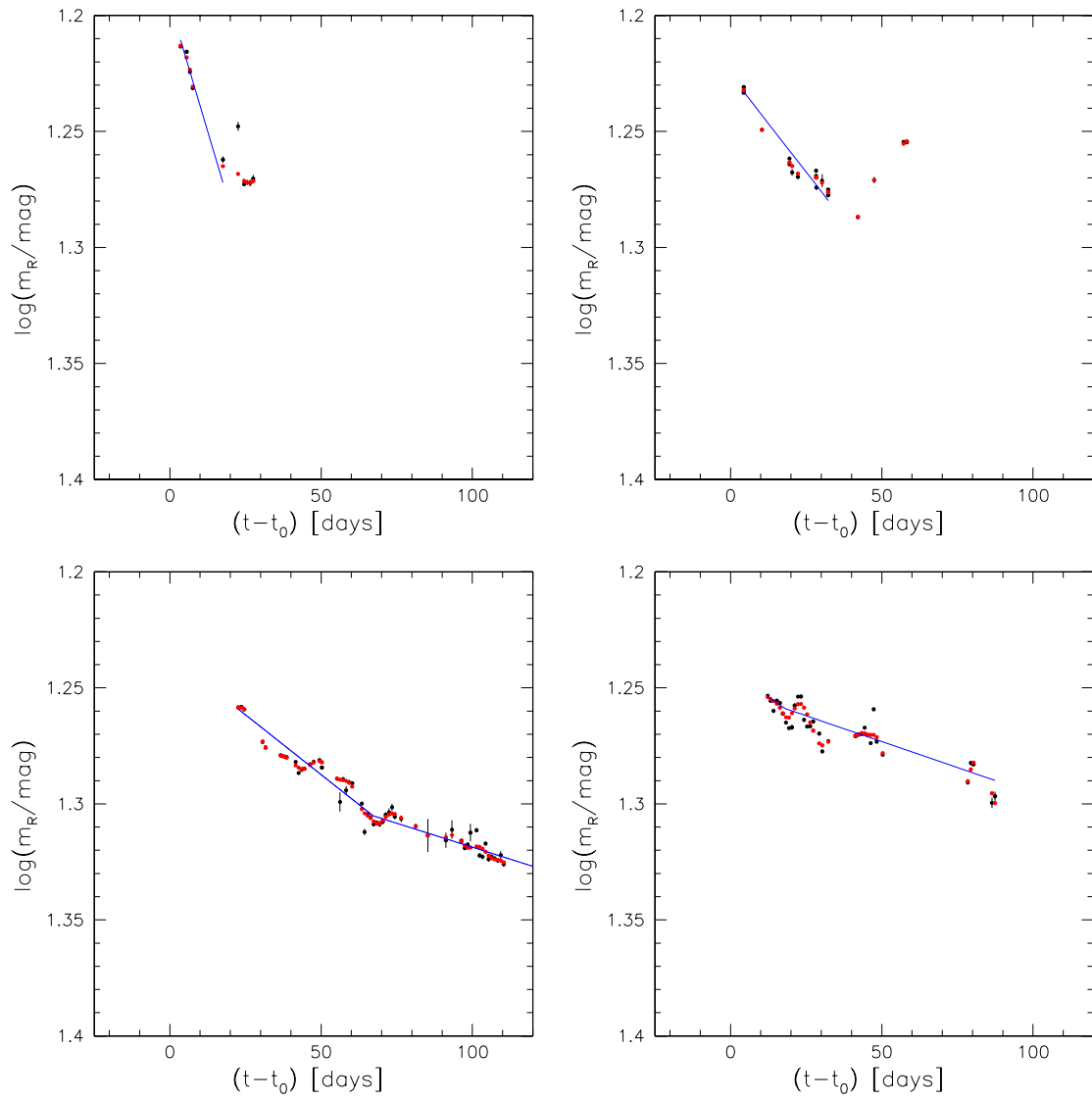Figure 7.13: Fits to the *R*-band light curves using the mean value of $m_R(15)$. This figure continues Fig. 7.11.

Figure 7.14: Fits to the R-band light curves using the mean value of $m_R(15)$. This figure continues Fig. 7.11.

Figure 7.15: Fits to the *R*-band light curves using the mean value of $m_R(15)$. This figure continues Fig. 7.11.

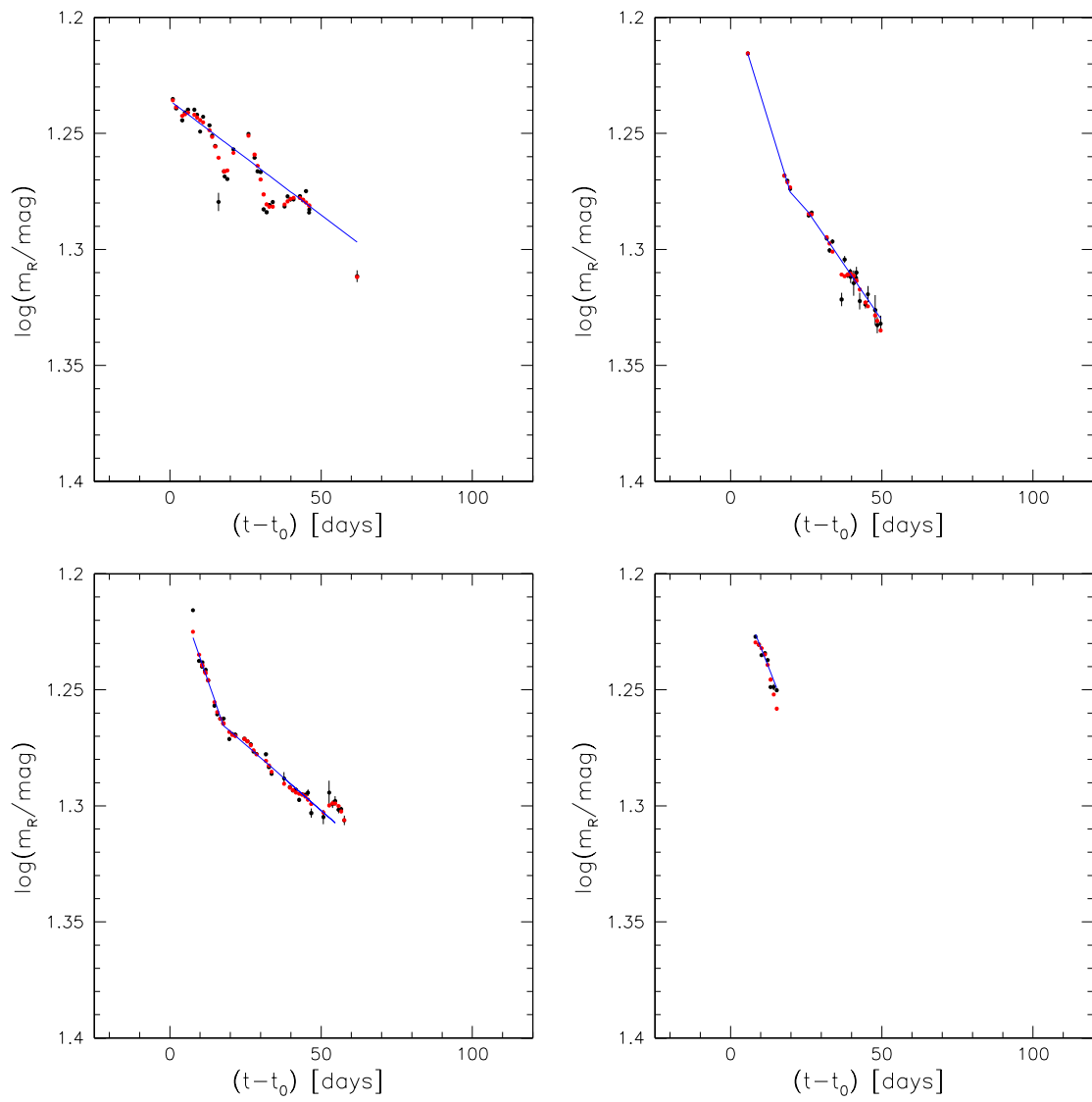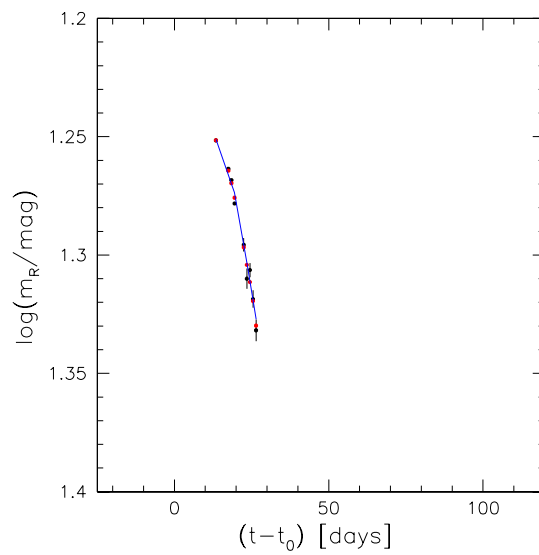Figure 7.16: Fits to the *R*-band light curves using the mean value of $m_R(15)$. This figure continues Fig. 7.11.

Chapter 8

Summary

This thesis is based on the results of the Wendelstein Calar Alto Pixellensing Project (WeCAPP) which was designed as a survey for microlensing events towards the Andromeda galaxy (M31). We detected seven candidate events which can be caused by Massive Compact Halo Objects (Machos, halo-lensing) or by the stars in M31 themselves (self-lensing). As second main result we identified and classified thousands of variable sources in the central part of M31.

Chapter 2 gives an overview of the project, as well as of the data collected during the survey, and introduces the techniques and algorithms used to reduce the data and to obtain the pixel light curves. We used data taken on two telescopes to build up (in terms of time sampling) a perfect data set for the study of variable sources. By observing simultaneously in two red wavebands (R and I) we improved the analysis of the light curves considerably. The quality of the data proved to be appropriate for both the detection of microlensing events and the proper identification of the intrinsic variable sources. In the central part of the Andromeda galaxy the sources cannot be resolved in single stars anymore. To overcome this severe crowding in the surveyed field we implemented a difference imaging technique which yielded residuals at the photon noise limit for the WeCAPP data. By the inclusion of Gaussian error propagation through all reduction steps in the reduction pipeline we were able to use all data collected over the years to search for variable sources.

Chapter 3 presents our model of the Andromeda galaxy. For the event rate calculations towards the center of M31 it was essential to precisely describe the distributions of the luminous and dark matter. We derived a bulge model which matches the observed surface brightness values of M31 better than previously published analytical models, and introduced the mass and luminosity functions for the different components (bulge, disk and halo) of M31. We showed that bulge and disk masses as given in the literature yield mass-to-light ratios in agreement with stellar population synthesis models. Our bulge and disk models yield the same contribution to the rotation curve as the model of Kerins *et al.* (2001), which allowed us to to assume the same density distribution for the dark halo as they did.

Chapter 4 uses the updated model of M31 (chapter 3) to calculate the expected event rates for the WeCAPP experiment as a function of position, field-of-view and $\left(\frac{S}{N}\right)$ threshold at maximum magnification. The calculations assume the Macho fraction in the halo to be 100% and neglect the detection efficiency of the survey.

We first introduced the basics of micro- and pixellensing. In the microlensing regime, where the sources of possible events are resolved, the observables are the maximum magnification of the source and the Einstein time scale of the event. For this regime, we re-derived the characteristic quantities for microlensing, and calculated the distribution of these quantities for our observed field. We then went on to the pixellensing regime, where crowding prevents the resolution of individual sources and the precise measurement of the source luminosity outside of the event. In this case, only the maximum excess flux of the source above a background and the full-width-half-maximum time of the event can be measured. We derived the distribution of the event rate as function of these two parameters. We included the finite size of the source in the calculations and showed, that these so-called 'finite-source effects' strongly affect the distributions, moving events to smaller excess fluxes and larger full-width timescales. We finally used the M31-photon-noise profile, deduced from the M31 surface-brightness-profile and the setup of the experiment to calculate the number and spatial distribution of events in our field.

Chapter 5   presents the seven Macho candidates detected in the survey. We first focused on high $\left(\frac{S}{N}\right)$ and short timescale events in data of the 2000/2001 campaign, as such events could not be confused with variable stars in a one years campaign. We applied different stringent cuts on the results of fits of theoretical microlensing curves to over 4.5 million pixel light curves, and identified two Macho candidates, WeCAPP-GL1 and GL2.

For GL2 and GL2 we calculated the mass probability distribution for self-lensing and halo-lensing. Under the assumption of a 100% Macho halo the distributions favor the lensing events to be caused by Machos in the halo of M31. The distributions yield most probable masses of $0.08M_\odot$ for GL1 and $0.02M_\odot$ for GL2, whereas solar-like objects are a factor of two less likely. This means that, for the full Macho halo hypothesis, the most likely masses lie in the range of the brown dwarf limit of hydrogen burning rather than in the range of white dwarfs as favored by the Galactic microlensing results. For a full Macho halo, self-lensing of stars in M31 is a factor of 2-3 less likely than lensing by halo objects. In this case the most probable masses are a factor of 4 larger than in the halo lensing case, yielding low mass stars as possible lenses.

The whole data set (covering the years 1997-2005) allowed to weaken the detection criteria and an unbiased search for microlensing events. This was possible, as due to the good time sampling and the length of the observations the theoretical microlensing fit to variable stars light curves showed large χ^2 deviations. However, light curves from pixels located at the wings of variable stars PSFs could efficiently mimic microlensing light curves, which required a further criterion to automatically select microlensing candidates. This identified further 5 Macho candidates with full-width time scales between about 0.3 days and 4.7 days. Although restricted by low number statistics, the – efficiency uncorrected – distribution of the event timescales seems to be uniform. The spatial distribution of the events does not show an evident near-far asymmetry as expected for halo-lensing, which points to self-lensing as the dominant source for the identified lensing events. This result is also supported by the number of the 7 detected events, which is in agreement with the expectations for self-lensing.

Chapter 6   presents over 20000 variable sources detected in the central parts of M31, most of which have been identified for the first time. We classified the variables according to their position in the *R*-band period amplitude plane where we could identify three regions: region I is occupied by population I Cepheids, whereas in region II we find predominantly type II Cepheids and RV Tauri stars. The sample of RV Tauri stars and RV Tauri candidates makes this catalogue to one of the largest collections

of this class of stars so far. Whereas small period semi-regular stars complete the stars in group II, group III consists of Long Period Variables.

Since the light curves of Cepheids show a progression with period which can be mathematically well described using Fourier analysis techniques, we applied it to all variables in groups I and II. With the extracted parameters we could reproduce the 'Hertzsprung' progression of the amplitude ratios and phase differences for the population I Cepheids, which confirmed the classification based on the period-amplitude plane. Furthermore, the Fourier parameters could be used to distinguish between fundamental mode pulsators and sources pulsating in higher modes among the stars in group I. In this way we identified two first overtone pulsators among the population I Cepheids. One of the group I sources seems to pulsate in the fundamental mode and the first overtone simultaneously. For such 'beat'-Cepheids the period ratio of the first overtone to the fundamental mode allows to constrain the metalicity of the star. Interestingly, the period ratio places this source on a sequence defined by Cepheids in the Small Magellanic Cloud and therefore on a much lower metalicity than expected for the bulge of M31. We further investigated the Fourier parameters of the light curves of the population I Cepheids, type II Cepheids and RV Tauri stars to search for parameter correlations. This analysis revealed a correlation of the low order phase differences for all three classes of stars. We found, that the relation of the RV Tauri stars is an extension of the relation for the type II Cepheids at longer period. This supports a close connection between these two classes of stars.

To study the effects of a spatially varying extinction in the field we calculated the spatial distribution of the variables and derived the number density of variables across the field. We found a strong depletion of sources in regions connected to the spiral arms of M31. By comparing the depletion areas with the calculated extinction map of our field we could show that the depletion areas correspond to highly extincted regions covered by dust lanes. Finally, we compared the number densities of variable sources with theoretical predictions, which depend on the age and metalicity of the stellar population of the M31 bulge. The comparison showed a reasonable agreement in the outer part of the observed field. This supports the picture that the M31 bulge is predominately metal rich and has an age around 12 Gyr, which was also used in our modeling of M31. The agreement between measured number density and theoretical prediction got worse in the more central parts of the observed field due to a lower detection efficiency of the variable sources. This can be attributed to a lower $\left(\frac{S}{N}\right)$ of the light curves and more severe crowding of the variable sources towards the center of M31.

Chapter 7 presents the WeCAPP nova catalogue, comprising over 60 novae which erupted between autumn 1997 and spring 2005. We developed detection algorithms that select the novae candidates rather automatically from the pixel light curves and yield only a small number of contaminants. The selection criteria were based on the eruptive nature of novae light curves which show large excess fluxes and asymmetric light curves (with respect to positive and negative difference fluxes). We detected 68 novae which makes the sample to one of the largest and most homogeneous samples of optical novae to date. To investigate if the novae emerge predominantly from the disk or the bulge populations we examined the spatial distribution of the novae and compared it with the distribution of the M31 bulge, disk, and total light in the Gunn r-band. The Kolmogorov-Smirnov statistics showed that the nova distribution agrees best with the r-band bulge light which supports their bulge origin.

The good time coverage of the WeCAPP data enabled us to determine the time of the outburst quite accurately for a subsample of novae. Using these light curves, we investigated the M_{15} relation for the R band, i.e. the constancy of the brightness of novae 15 days past maximum. This relation seems to hold for fast and moderately fast novae, but probably breaks down for very fast novae. With

the time of the outburst given by the M_{15} relation we derived the maximum magnitude $-$ rate of decline relationship (MMRD). Therefore, we performed exponential fits to all well sampled R-band light curves with outburst times between 2000 and 2003. The MMRD shows a linear behavior over most of the range of decline rates. At small decline rates the relation flattens leading to an 's-shaped' MMRD as already found by Capaccioli *et al.* (1989).

We correlated our nova sample with published novae and with the positions of historical novae. The coincidences showed that 18 of the novae are first identifications, which underlined the efficiency of the difference imaging method in crowded fields. Furthermore, we found 5 candidates for recurrent novae, i.e. novae with more than one known outburst. One of the candidates was already known as a candidate for a recurrent nova with two observed outbursts in 1963 and 1968. For the other candidates only two outbursts, one historic and one in the WeCAPP data are known.

Bibliography

Abazajian, K., Adelman-McCarthy, J. K., Agüeros, M. A., Allam, S. S., Anderson, S. F., Annis, J., Bahcall, N. A., Baldry, I. K., Bastian, S., Berlind, A., Bernardi, M., et al. 2003: *The First Data Release of the Sloan Digital Sky Survey*, AJ, 126, 2081

Afonso, C., Alard, C., Albert, J., Amadon, A., Andersen, J., Ansari, R., Aubourg, É., Bareyre, P., Bauer, F., Beaulieu, J., Bouquet, A., et al. 1999: *Observation of microlensing towards the galactic spiral arms. EROS II. 2 year survey*, A&A, 351, 87

Afonso, C., Albert, J. N., Andersen, J., Ansari, R., Aubourg, É., Bareyre, P., Beaulieu, J. P., Blanc, G., Charlot, X., Couchot, F., Coutures, C., et al. 2003: *Limits on Galactic dark matter with 5 years of EROS SMC data*, A&A, 400, 951

Afshordi, N., McDonald, P., & Spergel, D. N. 2003: *Primordial Black Holes as Dark Matter: The Power Spectrum and Evaporation of Early Structures*, ApJ, 594, L71

Ahlen, S. P., Avignone, F. T., Brodzinski, R. L., Drukier, A. K., Gelmini, G., & Spergel, D. N. 1987: *Limits On Cold Dark Matter Candidates From An Ultralow Background Germanium Spectrometer*, Phys. Lett. B, 195, 603

Ahmad, Q. R., Allen, R. C., Andersen, T. C., Anglin, J. D., Barton, J. C., Beier, E. W., Bercovitch, M., Bigu, J., Biller, S. D., Black, R. A., Blevis, I., et al. 2002: *Direct Evidence for Neutrino Flavor Transformation from Neutral-Current Interactions in the Sudbury Neutrino Observatory*, Physical Review Letters, 89, 011301

Akerib, D. S., Alvaro-Dean, J., Armel, M. S., Attisha, M. J., Baudis, L., Bauer, D. A., Bolozdynya, A. I., Brink, P. L., Bunker, R., Cabrera, B., Caldwell, D. O., et al. 2003: *New results from the Cryogenic Dark Matter Search experiment*, Phys. Rev. D, 68, 082002

Alard, C. 1997: *Lensing of unresolved stars towards the Galactic Bulge.*, A&A, 321, 424

Alard, C. 1999: *Analysis of the OGLE microlensing candidates using the image subtraction method*, A&A, 343, 10

Alard, C. 2000: *Image subtraction using a space-varying kernel*, A&AS, 144, 363

Alard, C. 2001: *Unbiased reconstruction of the mass function using microlensing survey data*, MN-RAS, 320, 341

Alard, C. & Guibert, J. 1997: *The DUO single lens candidates. I. The 1994 campaign.*, A&A, 326, 1

Alard, C., Guibert, J., Bienayme, O., Valls-Gabaud, D., Robin, A. C., Terzan, A., & Bertin, E. 1995: *The DUO programme : first results of a microlensing investigation of the Galactic Disk and Bulge conducted with the ESO Schmidt telescope.*, The Messenger, 80, 31

Alard, C. & Lupton, R. H. 1998: *A Method for Optimal Image Subtraction*, ApJ, 503, 325

Alcock, C., Akerloff, C. W., Allsman, R. A., Axelrod, T. S., Bennett, D. P., Chan, S., Cook, C. H., Freeman, K. C., Griest, K., Marshall, S. L., Park, H. S., et al. 1993: *Possible Gravitational Microlensing of a Star in the Large Magellanic Cloud*, Nature, 365, 621

Alcock, C., Allsman, R. A., Alves, D., Axelrod, T. S., Becker, A. C., Bennett, D. P., Cook, K. H., Freeman, K. C., Griest, K., Guern, J., Lehner, M. J., et al. 1997: *The MACHO Project Large Magellanic Cloud Microlensing Results from the First Two Years and the Nature of the Galactic Dark Halo*, ApJ, 486, 697

Alcock, C., Allsman, R. A., Alves, D., Axelrod, T. S., Becker, A. C., Bennett, D. P., Cook, K. H., Freeman, K. C., Griest, K., Lehner, M. J., Marshall, S. L., et al. 1999: *The MACHO Project LMC Variable Star Inventory. VI. The Second Overtone Mode of Cepheid Pulsation from First/Second Overtone Beat Cepheids*, ApJ, 511, 185

Alcock, C., Allsman, R. A., Alves, D. R., Axelrod, T. S., Becker, A., Bennett, D. P., Cook, K. H., Freeman, K. C., Griest, K., Lawson, W. A., Lehner, M. J., et al. 1998: *The MACHO Project LMC Variable Star Inventory. VII. The Discovery of RV Tauri Stars and New Type II Cepheids in the Large Magellanic Cloud*, AJ, 115, 1921

Alcock, C., Allsman, R. A., Alves, D. R., Axelrod, T. S., Becker, A. C., Bennett, D. P., Cook, K. H., Dalal, N., Drake, A. J., Freeman, K. C., Geha, M., et al. 2000a: *The MACHO Project: Microlensing Results from 5.7 Years of Large Magellanic Cloud Observations*, ApJ, 542, 281

Alcock, C., Allsman, R. A., Alves, D. R., Axelrod, T. S., Becker, A. C., Bennett, D. P., Cook, K. H., Dalal, N., Drake, A. J., Freeman, K. C., Geha, M., et al. 2001: *The MACHO Project Hubble Space Telescope Follow-Up: Preliminary Results on the Location of the Large Magellanic Cloud Microlensing Source Stars*, ApJ, 552, 582

Alcock, C., Allsman, R. A., Alves, D. R., Axelrod, T. S., Becker, A. C., Bennett, D. P., Cook, K. H., Drake, A. J., Freeman, K. C., Geha, M., Griest, K., et al. 2000b: *The MACHO Project: Microlensing Optical Depth toward the Galactic Bulge from Difference Image Analysis*, ApJ, 541, 734

Alcock, C., Allsman, R. A., Axelrod, T. S., Bennett, D. P., Cook, K. H., Evans, N. W., Freeman, K. C., Griest, K., Jijina, J., Lehner, M., Marshall, S. L., et al. 1995a: *Theory of Exploring the Dark Halo with Microlensing. I. Power-Law Models*, ApJ, 449, 28

Alcock, C., Allsman, R. A., Axelrod, T. S., Bennett, D. P., Cook, K. H., Freeman, K. C., Griest, K., Marshall, S. L., Peterson, B. A., Pratt, M. R., Quinn, P. J., et al. 1995b: *The MACHO project LMC variable star inventory. 1: Beat Cepheids-conclusive evidence for the excitation of the second overtone in classical Cepheids*, AJ, 109, 1653

An, J. H., Evans, N. W., Hewett, P., Baillon, P., Calchi Novati, S., Carr, B. J., Crézé, M., Giraud-Héraud, Y., Gould, A., Jetzer, P., Kaplan, J., et al. 2004: *The POINT-AGAPE Survey - I. The variable stars in M31*, MNRAS, 351, 1071

Ansari, R., Aurière, M., Baillon, P., Bouquet, A., Coupinot, G., Coutures, C., Ghesquière, C., Giraud-Héraud, Y., Gillieron, D., Gondolo, P., Hecquet, J., et al. 2004: *Variable stars towards the bulge of M 31: The AGAPE catalogue*, A&A, 421, 509

Ansari, R., Aurière, M., Baillon, P., Bouquet, A., Coupinot, G., Coutures, C., Ghesquière, C., Giraud-Héraud, Y., Gondolo, P., Hecquet, J., Kaplan, J., et al. 1999: *AgapeZ1: a large amplification microlensing event or an odd variable star towards the inner bulge of M31*, A&A, 344, L49

Ansari, R., Auriere, M., Baillon, P., Bouquet, A., Coupinot, G., Coutures, C., Ghesquiere, C., Giraud-Heraud, Y., Gondolo, P., Hecquet, J., Kaplan, J., et al. 1997: *AGAPE: a search for dark matter towards M 31 by microlensing effects on unresolved stars*, A&A, 324, 843

Ansari, R., Cavalier, F., Moniez, M., Aubourg, E., Bareyre, P., Brehin, S., Gros, M., Lachieze-Rey, M., Laurent, B., Lesquoy, E., Magneville, C., et al. 1996: *Observational limits on the contribution of sub-stellar and stellar objects to the galactic halo*, A&A, 314, 94

Antonello, E. & Poretti, E. 1986: *Structural properties of the light curves of s-Cepheids*, A&A, 169, 149

Arp, H. C. 1956: *Novae in the Andromeda nebula.*, AJ, 61, 15

Aubourg, E., Bareyre, P., Brehin, S., Gros, M., Lachieze-Rey, M., Laurent, B., Lesquoy, E., Magneville, C., Milsztajn, A., Moscoso, L., Queinnec, F., et al. 1993: *Evidence for Gravitational Microlensing by Dark Objects in the Galactic Halo*, Nature, 365, 623

Auriere, M., Baillon, P., Bouquet, A., Carr, B. J., Crézé, M., Evans, N. W., Giraud-Héraud, Y., Gould, A., Hewett, P. C., Kaplan, J., Kerins, E., et al. 2001: *A Short-Timescale Candidate Microlensing Event in the POINT-AGAPE Pixel Lensing Survey of M31*, ApJ, 553, L137

Baade, W. & Swope, H. H. 1963: *Variable star field 96' south preceeding the nucleous of the Andromeda galaxy*, AJ, 68, 435

Baade, W. & Swope, H. H. 1965: *Variables in the Andromeda galaxy - Fields I and III*, AJ, 70, 212

Bahcall, J. N. 1984: *Self-consistent determinations of the total amount of matter near the sun*, ApJ, 276, 169

Bahcall, J. N., Flynn, C., & Gould, A. 1992: *Local dark matter from a carefully selected sample*, ApJ, 389, 234

Bahcall, J. N., Soneira, R. M., & Schmidt, M. 1983: *The galactic spheroid*, ApJ, 265, 730

Baillon, P., Bouquet, A., Giraud-Héraud, Y., & Kaplan, J. 1993a: *Detection of Brown Dwarfs by the Microlensing of Unresolved Stars*, A&A, 277, 1

Baillon, P., Bouquet, A., Giraud-Héraud, Y., & Kaplan, J. 1993b: *Searching brown dwarfs by the micro-lensing of unresolved stars*, in: Particle Astrophysics, IVth Rencontres de Blois, eds. G. Fontaine, J. Tran Thanh Van, June 1992 (Editions Frontiŕes 1993)

Baillon, P., Bouquet, A., Kaplan, J., & Giraud-Héraud, Y. 1992: *Search for dark matter as brown dwarfs by looking at Andromeda (M31)*, in: Towards a major atmospheric Cerenkov detector for TeV astroparticle physics, eds. P. Fleury and G. Vacanti, Palaiseau, June 1992 (Editions Frontiéres 1992), 51

Baker, N. & Kippenhahn, R. 1962: *The Pulsations of Models of δ Cephei Stars*, Zeitschrift für Astrophysik, 54, 114

Baltz, E. A. & Gondolo, P. 2001: *Implications of Muon Anomalous Magnetic Moment for Supersymmetric Dark Matter*, Physical Review Letters, 86, 5004

Baltz, E. A. & Gondolo, P. 2003: *Improved constraints on supersymmetric dark matter from muon g-2*, Phys. Rev. D, 67, 063503

Baltz, E. A., Lauer, T. R., Zurek, D. R., Gondolo, P., Shara, M. M., Silk, J., & Zepf, S. E. 2004: *Microlensing Candidates in M87 and the Virgo Cluster with the Hubble Space Telescope*, ApJ, 610, 691

Baltz, E. A. & Silk, J. 2000: *Event Rate and Einstein Time Evaluation in Pixel Microlensing*, ApJ, 530, 578

Baraffe, I., Alibert, Y., M'era, D., Chabrier, G., & Beaulieu, J.-P. 1998: *Cepheid Models Based on Self-Consistent Stellar Evolution and Pulsation Calculations: The Right Answer?*, ApJ, 499, L205

Beaulieu, J. P., Grison, P., Tobin, W., Pritchard, J. D., Ferlet, R., Lepeintre, F., Vidal-Madjar, A., Maurice, E., Prevot, L., Gry, C., Guibert, J., et al. 1995: *EROS variable stars: fundamental-mode and first-overtone Cepheids in the bar of the Large Magellanic Cloud.*, A&A, 303, 137

Beaulieu, J. P., Krockenberger, M., Sasselov, D. D., Renault, C., Ferlet, R., Vidal-Majar, A., Maurice, E., Prevot, L., Aubourg, E., Bareyre, P., Brehin, S., et al. 1997: *EROS VARIABLE STARS: Discovery of Beat Cepheids in the Small Magellanic Cloud and the effect of metallicity on pulsation.*, A&A, 321, L5

Belokurov, V., Evans, N. W., & Le Du, Y. 2004: *Light-curve classification in massive variability surveys - II. Transients towards the Large Magellanic Cloud*, MNRAS, 352, 233

Bennett, C. L., Halpern, M., Hinshaw, G., Jarosik, N., Kogut, A., Limon, M., Meyer, S. S., Page, L., Spergel, D. N., Tucker, G. S., Wollack, E., et al. 2003: *First-Year Wilkinson Microwave Anisotropy Probe (WMAP) Observations: Preliminary Maps and Basic Results*, ApJS, 148, 1

Bergstroem, L. 2000: *Non-baryonic dark matter: observational evidence and detection methods.*, Reports of Progress in Physics, 63, 793

Bernabei, R., Amato, M., Belli, P., Cappella, F., Cerulli, R., Dai, C. J., He, H. L., Ignesti, G., Incicchitti, A., Kuang, H. H., Ma, J. M., et al. 2003: *DAMA results and status report*, in Identification of Dark Matter, 278–283

Bertin, E. & Arnouts, S. 1996: *SExtractor: Software for source extraction.*, A&AS, 117, 393

Bessell, M. S. 1979: *UBVRI photometry. II - The Cousins VRI system, its temperature and absolute flux calibration, and relevance for two-dimensional photometry*, PASP, 91, 589

Binney, J. & Merrifield, M. 1998, Galactic astronomy (Princeton University Press)

Binney, J. & Tremaine, S. 1987, Galactic dynamics (Princeton University Press, 1987)

Blanton, M. R., Hogg, D. W., Bahcall, N. A., Brinkmann, J., Britton, M., Connolly, A. J., Csabai, I., Fukugita, M., Loveday, J., Meiksin, A., Munn, J. A., et al. 2003: *The Galaxy Luminosity Function and Luminosity Density at Redshift z = 0.1*, ApJ, 592, 819

Bode, M. F. & Evans, A. 1989, Classical novae (Chichester: Wiley, edited by Bode, M.F.; Evans, A.)

Bosma, A. 1981a: *21-cm line studies of spiral galaxies. I - Observations of the galaxies NGC 5033, 3198, 5055, 2841, and 7331. II - The distribution and kinematics of neutral hydrogen in spiral galaxies of various morphological types*, AJ, 86, 1791

Bosma, A. 1981b: *21-cm line studies of spiral galaxies. II. The distribution and kinematics of neutral hydrogen in spiral galaxies of various morphological types.*, AJ, 86, 1825

Bosma, A. 1998: *The Dark Matter Problem*, Celestial Mechanics and Dynamical Astronomy, 72, 69

Bozza, V., Calchi Novati, S., Capaccioli, M., Capozziello, S., Cardone, V., Covone, G., de Paolis, F., de Ritis, R., Ingrosso, G., Iovane, G., Lambiase, G., et al. 2000: *SLOTT-AGAPE project.*, Memorie della Societa Astronomica Italiana, 71, 1113

Braun, R. 1991: *The distribution and kinematics of neutral gas in M31*, ApJ, 372, 54

Brinks, E. & Burton, W. B. 1984: *A high resolution hydrogen line survey of Messier 31. II - The warped flaring hydrogen layer*, A&A, 141, 195

Broadhurst, T., Benítez, N., Coe, D., Sharon, K., Zekser, K., White, R., Ford, H., Bouwens, R., Blakeslee, J., Clampin, M., Cross, N., et al. 2005: *Strong-Lensing Analysis of A1689 from Deep Advanced Camera Images*, ApJ, 621, 53

Buscombe, W. & de Vaucouleurs, G. 1955: *Novae in the Magellanic Clouds and in the Galaxy*, The Observatory, 75, 170

Calchi Novati, S., Iovane, G., Marino, A. A., Aurière, M., Baillon, P., Bouquet, A., Bozza, V., Capaccioli, M., Capozziello, S., Cardone, V., Covone, G., et al. 2002: *Microlensing search towards M 31*, A&A, 381, 848

Calchi Novati, S., Jetzer, P., Scarpetta, G., Giraud-Héraud, Y., Kaplan, J., Paulin-Henriksson, S., & Gould, A. 2003: *Microlensing towards M 31 with MDM data*, A&A, 405, 851

Calchi Novati, S., Paulin-Henriksson, S., An, J., Baillon, P., Belokurov, V., Carr, B. J., Crézé, M., Evans, N. W., Giraud-Héraud, Y., Gould, A., Hewett, P., et al. 2005: *POINT-AGAPE pixel lensing survey of M 31. Evidence for a MACHO contribution to galactic halos*, A&A, 443, 911

Capaccioli, M., della Valle, M., Rosino, L., & D'Onofrio, M. 1989: *Properties of the nova population in M31*, AJ, 97, 1622

Carr, B. J. 2001: *Baryonic Dark Matter in Galaxies*, in ASP Conf. Ser. 239: Microlensing 2000: A New Era of Microlensing Astrophysics, 37

Carr, B. J. & Lidsey, J. E. 1993: *Primordial black holes and generalized constraints on chaotic inflation*, Phys. Rev. D, 48, 543

Carr, B. J. & Sakellariadou, M. 1999: *Dynamical Constraints on Dark Matter in Compact Objects*, ApJ, 516, 195

Cassisi, S., Castellani, V., degl'Innocenti, S., & Weiss, A. 1998: *An updated theoretical scenario for globular cluster stars*, A&AS, 129, 267

Castillo-Morales, A. & Schindler, S. 2003: *Distribution of dark and baryonic matter in clusters of galaxies*, A&A, 403, 433

Chabrier, G. 2003: *Galactic Stellar and Substellar Initial Mass Function*, PASP, 115, 763

Chadwick, P. 2005: *HESS High-energy astrophysics: Mapping the gamma-ray sky*, Astronomy and Geophysics, 46, 12

Chang, K. & Refsdal, S. 1979: *Flux variations of QSO 0957+561 A, B and image splitting by stars near the light path*, Nature, 282, 561

Christy, R. F. 1966: *Pulsation Theory*, ARA&A, 4, 353

Chung, D. J. H., Kolb, E. W., & Riotto, A. 1998: *Nonthermal Supermassive Dark Matter*, Physical Review Letters, 81, 4048

Ciardullo, R., Ford, H. C., Neill, J. D., Jacoby, G. H., & Shafter, A. W. 1987: *The spatial distribution and population of novae in M31*, ApJ, 318, 520

Ciardullo, R., Tamblyn, P., & Phillips, A. C. 1990: *A search for novae in M 31 globular clusters*, PASP, 102, 1113

Cieslinski, D., Diaz, M. P., Mennickent, R. E., & Pietrzyński, G. 2003: *Identification of New Eruptive Cataclysmic Variables toward the Galactic Bulge and Magellanic Clouds Using the OGLE-II Database*, PASP, 115, 193

Clayton, G. C. 1996: *The R Coronae Borealis Stars*, PASP, 108, 225

Cole, S., Norberg, P., Baugh, C. M., Frenk, C. S., Bland-Hawthorn, J., Bridges, T., Cannon, R., Colless, M., Collins, C., Couch, W., Cross, N., et al. 2001: *The 2dF galaxy redshift survey: near-infrared galaxy luminosity functions*, MNRAS, 326, 255

Cox, J. P., Cox, A. N., Olsen, K. H., King, D. S., & Eilers, D. D. 1966: *Self-Excited Radial Oscillations in Thin Stellar Envelopes. I*, ApJ, 144, 1038

Cozzini, C., Altmann, M., Angloher, G., Bruckmayer, M., Bucci, C., Cooper, S., di Stefano, P., von Feilitzsch, F., Frank, T., Hauff, D., Jagemann, T., et al. 2002: *Results of CRESST phase I*, AIP Conf. Proc. 605: Low Temperature Detectors, 605, 481

Creze, M., Chereul, E., Bienayme, O., & Pichon, C. 1998: *The distribution of nearby stars in phase space mapped by Hipparcos. I. The potential well and local dynamical mass*, A&A, 329, 920

Crotts, A. P. S. 1992: *M31 - A unique laboratory for gravitational microlensing*, ApJ, 399, L43

Crotts, A. P. S. & Tomaney, A. B. 1996: *Results from a Survey of Gravitational Microlensing toward M31*, ApJ, 473, L87

Crotts, A. P. S., Uglesich, R., Gyuk, G., & Tomaney, A. B. 1999: *MEGA: Mapping Halo and Bulge Microlensing in M31*, in: ASP Conf. Ser. 182, 409

Cusumano, G., Agnetta, G., Biondo, B., Catalano, S., Giarrusso, S., Gugliotta, G., La Barbera, A., La Fata, L., Maccarone, M. C., Mangano, A., Mineo, T., et al. 2002: *GAW (Gamma Air Watch): a novel imaging Cherenkov telescope.*, Memorie della Societa Astronomica Italiana, 73, 1211

Cutri, C. e. a. 2000: *Explanatory Supplement to the 2MASS Second Incremental Data Release*, in , 1

Cyburt, R. H. 2004: *Primordial nucleosynthesis for the new cosmology: Determining uncertainties and examining concordance*, Phys. Rev. D, 70, 023505

Darnley, M. J., Bode, M. F., Kerins, E., Newsam, A. M., An, J., Baillon, P., Belokurov, V., Novati, S. C., Carr, B. J., Creze, M., Evans, N. W., et al. 2005: *Classical novae from the POINT-AGAPE microlensing survey of M31 – II. Rate and statistical characteristics of the nova population,* astro-ph/0509493

Darnley, M. J., Bode, M. F., Kerins, E., Newsam, A. M., An, J., Baillon, P., Novati, S. C., Carr, B. J., Crézé, M., Evans, N. W., Giraud-Héraud, Y., et al. 2004: *Classical novae from the POINT-AGAPE microlensing survey of M31 - I. The nova catalogue*, MNRAS, 353, 571

de Jong, J. T. A., Kuijken, K., Crotts, A. P. S., Sackett, P. D., Sutherland, W. J., Uglesich, R. R., Baltz, E. A., Cseresnjes, P., Gyuk, G., Widrow, L. M., & The MEGA collaboration. 2004: *First microlensing candidates from the MEGA survey of M 31*, A&A, 417, 461

de Jong, J. T. A., Widrow, L. M., Cseresnjes, P., Kuijken, K., Crotts, A. P. S., Bergier, A., Baltz, E. A., Gyuk, G., Sackett, P. D., Uglesich, R. R., Sutherland, W. J., et al. 2005: *MACHOs in M31? Absence of evidence but not evidence of absence,* astro-ph/0507286

de Rujula, A., Jetzer, P., & Masso, E. 1991: *Dark mass moments*, MNRAS, 250, 348

Derue, F., Marquette, J.-B., Lupone, S., Afonso, C., Alard, C., Albert, J.-N., Amadon, A., Andersen, J., Ansari, R., Aubourg, É., Bareyre, P., et al. 2002: *Observation of periodic variable stars towards the Galactic spiral arms by EROS II*, A&A, 389, 149

Diemand, J., Moore, B., & Stadel, J. 2005: *Earth-mass dark-matter haloes as the first structures in the early Universe*, Nature, 433, 389

Dominik, M. 1998: *Estimating physical quantities for an observed galactic microlensing event*, A&A, 330, 963

Durlevich, O. V., Kazarovets, E. V., Kholopov, P. N., Kireeva, N. N., Samus, N. N., & Tsvetkova, T. M. 1996: *General Catalogue of Variable Stars V1.1, Vol. IV. (Durlevich+ 1996)*, VizieR Online Data Catalog, 2172, 0

Eddington, A. S. 1919: *The total eclipse of 1919 May 29 and the influence of gravitation on light*, The Observatory, 42, 119

Eddington, A. S. 1926, The Internal Constitution of the Stars (Cambridge University Press)

Efstathiou, G., Bond, J. R., & White, S. D. M. 1992: *COBE background radiation anisotropies and large-scale structure in the universe*, MNRAS, 258, 1P

Ellis, J., Falk, T., Olive, K. A., & Srednicki, M. 2000: *Calculations of neutralino-stau coannihilation channels and the cosmologically relevant region of MSSM parameter space*, Astroparticle Physics, 13, 181

Evans, N. W. & Belokurov, V. 2005: *Is There a Microlensing Puzzle?,* astro-ph/0505167

Evans, N. W. & Kerins, E. 2000: *Is the Large Magellanic Cloud a Large Microlensing Cloud?*, ApJ, 529, 917

Feast, M., Whitelock, P., & Menzies, J. 2002: *Globular clusters and the Mira period-luminosity relation*, MNRAS, 329, L7

Feast, M. W., Glass, I. S., Whitelock, P. A., & Catchpole, R. M. 1989: *A period-luminosity-colour relation for Mira variables*, MNRAS, 241, 375

Fields, B. D., Freese, K., & Graff, D. S. 2000: *Chemical Abundance Constraints on White Dwarfs as Halo Dark Matter*, ApJ, 534, 265

Fliri, J., Riffeser, A., Seitz, S., & Bender, R. 2006: *The Wendelstein Calar Alto Pixellensing Project (WeCAPP): the M 31 variable star catalogue*, A&A, 445, 423

Fokin, A. B. 2001, *RV Tauri stars,* in: Stellar pulsation - Nonlinear Studies, ed. M. Takeuti & D. D. Sasselov, (Kluwer Academic Publishers), 103

Freedman, W. L. & Madore, B. F. 1990: *An empirical test for the metallicity sensitivity of the Cepheid period-luminosity relation*, ApJ, 365, 186

Freeman, K. C. 1970: *On the Disks of Spiral and so Galaxies*, ApJ, 160, 811

Fukuda, Y., Hayakawa, T., Ichihara, E., Inoue, K., Ishihara, K., Ishino, H., Itow, Y., Kajita, T., Kameda, J., Kasuga, S., Kobayashi, K., et al. 1998: *Evidence for Oscillation of Atmospheric Neutrinos*, Physical Review Letters, 81, 1562

Fukugita, M. 2003: *Cosmic Matter Distribution: Cosmic Baryon Budget Revisited,* astro-ph/0312517

Fukugita, M. & Peebles, P. J. E. 2004: *The Cosmic Energy Inventory*, ApJ, 616, 643

Gössl, C. A. & Riffeser, A. 2002: *Image reduction pipeline for the detection of variable sources in highly crowded fields*, A&A, 381, 1095

Gabasch, A., Bender, R., Seitz, S., Hopp, U., Saglia, R. P., Feulner, G., Snigula, J., Drory, N., Appenzeller, I., Heidt, J., Mehlert, D., et al. 2004: *The evolution of the luminosity functions in the FORS Deep Field from low to high redshift. I. The blue bands*, A&A, 421, 41

Gallagher, J. S. & Starrfield, S. 1978: *Theory and observations of classical novae*, ARA&A, 16, 171

García-Bellido, J. & Linde, A. 1998: *Preheating in hybrid inflation*, Phys. Rev. D, 57, 6075

Gautschy, A. & Saio, H. 1995: *Stellar Pulsations Across The HR Diagram: Part 1*, ARA&A, 33, 75

Girardi, L., Bertelli, G., Bressan, A., Chiosi, C., Groenewegen, M. A. T., Marigo, P., Salasnich, B., & Weiss, A. 2002: *Theoretical isochrones in several photometric systems. I. Johnson-Cousins-Glass, HST/WFPC2, HST/NICMOS, Washington, and ESO Imaging Survey filter sets*, A&A, 391, 195

Goldberg, D. M. 1998: *Using Astrometry to Deblend Microlensing Events*, ApJ, 498, 156

Gondolo, P. 1999: *Optical Depth Evaluation in Pixel Microlensing*, ApJ, 510, L29

Gondolo, P. 2004: *Introduction to Non-Baryonic Dark Matter,* astro-ph/0403064

Gould, A. 1994: *Proper motions of MACHOs*, ApJ, 421, L71

Gould, A. 1995: *Search for Intracluster MACHOs by Pixel Lensing of M87*, ApJ, 455, 44

Gould, A. 1996: *Theory of Pixel Lensing*, ApJ, 470, 201

Gould, A., Bahcall, J. N., & Flynn, C. 1997: *M Dwarfs from Hubble Space Telescope Star Counts. III. The Groth Strip*, ApJ, 482, 913

Gould, A. & Welch, D. L. 1996: *MACHO Proper Motions from Optical/Infrared Photometry*, ApJ, 464, 212

Griest, K. 1991: *Galactic microlensing as a method of detecting massive compact halo objects*, ApJ, 366, 412

Griest, K. & Thomas, C. L. 2005: *Contamination in the MACHO data set and the puzzle of Large Magellanic Cloud microlensing*, MNRAS, 359, 464

Grillmair, C. J., Lauer, T. R., Worthey, G., Faber, S. M., Freedman, W. L., Madore, B. F., Ajhar, E. A., Baum, W. A., Holtzman, J. A., Lynds, C. R., O'Neil, E. J., et al. 1996: *Hubble Space Telescope Observations of M32: The Color-Magnitude Diagram*, AJ, 112, 1975

Gyuk, G. & Crotts, A. 2000: *Optical Depth from Realistic Microlensing Models of M31*, ApJ, 535, 621

Habing, H. J. 1996: *Circumstellar envelopes and Asymptotic Giant Branch stars*, 7, 97

Haiman, Z., Magnier, E., Lewin, W. H. G., Lester, R. R., van Paradijs, J., Hasinger, G., Pietsch, W., Supper, R., & Truemper, J. 1994: *Extension of the Magnier et al. catalogue of objects in the field of M31*, A&A, 286, 725

Han, C. 1996: *Pixel Lensing Experiment toward the M31 Bulge*, ApJ, 472, 108

Han, C. 1997: *The Effects of Amplification Bias in Gravitational Microlensing Experiments*, ApJ, 484, 555

Han, C. & Gould, A. 1996a: *Galactic versus Extragalactic Pixel Lensing Events toward M31*, ApJ, 473, 230

Han, C. & Gould, A. 1996b: *Statistical Determination of the MACHO Mass Spectrum*, ApJ, 467, 540

Han, C. & Park, S. 2001: *Colour change measurements of gravitational microlensing events by using the difference image analysis method*, MNRAS, 320, 41

Han, C., Park, S., & Jeong, J. 2000: *Chromaticity of gravitational microlensing events*, MNRAS, 316, 97

Hanany, S., Ade, P., Balbi, A., Bock, J., Borrill, J., Boscaleri, A., de Bernardis, P., Ferreira, P. G., Hristov, V. V., Jaffe, A. H., Lange, A. E., et al. 2000: *MAXIMA-1: A Measurement of the Cosmic Microwave Background Anisotropy on Angular Scales of $10' - 5$ deg*, ApJ, 545, L5

Heidt, J., Appenzeller, I., Gabasch, A., Jäger, K., Seitz, S., Bender, R., Böhm, A., Snigula, J., Fricke, K. J., Hopp, U., Kümmel, M., et al. 2003: *The FORS Deep Field: Field selection, photometric observations and photometric catalog*, A&A, 398, 49

Hernanz, M. 2005: *Classical nova explosions*, in ASP Conf. Ser. 330: The Astrophysics of Cataclysmic Variables and Related Objects, ed. J.-M. Hameury & J.-P. Lasota, 265–+

Hertzsprung, E. 1926: *On the relation between period and form of the light-curve of variable stars of the δ Cephei type*, 3, 115

Holmberg, J. & Flynn, C. 2000: *The local density of matter mapped by Hipparcos*, MNRAS, 313, 209

Horne, J. H. & Baliunas, S. L. 1986: *A prescription for period analysis of unevenly sampled time series*, ApJ, 302, 757

Hornschemeier, A. E., Brandt, W. N., Garmire, G. P., Schneider, D. P., Barger, A. J., Broos, P. S., Cowie, L. L., Townsley, L. K., Bautz, M. W., Burrows, D. N., Chartas, G., et al. 2001: *The Chandra Deep Survey of the Hubble Deep Field-North Area. II. Results from the Caltech Faint Field Galaxy Redshift Survey Area*, ApJ, 554, 742

Hubble, E. P. 1922: *A general study of diffuse galactic nebulae*, ApJ, 56, 162

Hubble, E. P. 1929: *A spiral nebula as a stellar system, Messier 31.*, ApJ, 69, 103

Iben, I. & Renzini, A. 1983: *Asymptotic giant branch evolution and beyond*, ARA&A, 21, 271

Jablonka, P., Bridges, T. J., Sarajedini, A., Meylan, G., Maeder, A., & Meynet, G. 1999: *No Increase of the Red Giant Branch Tip Luminosity toward the Center of M31*, ApJ, 518, 627

Jetzer, P. 1994: *On the mass of the dark compact objects in the Galactic disk*, ApJ, 432, L43

Jetzer, P. & Massó, E. 1994: *On the mass of the dark compact halo objects*, Physics Letters B, 323, 347

Joshi, Y. C., Pandey, A. K., Narasimha, D., Giraud-Héraud, Y., Sagar, R., & Kaplan, J. 2004: *Photometric study of two novae in M 31*, A&A, 415, 471

Joshi, Y. C., Pandey, A. K., Narasimha, D., & Sagar, R. 2001: *Search for Microlensing Events Towards M31 Galaxy*, Bulletin of the Astronomical Society of India, 29, 531

Joshi, Y. C., Pandey, A. K., Narasimha, D., & Sagar, R. 2005: *First microlensing candidate towards M 31 from the Nainital Microlensing Survey*, A&A, 433, 787

Kaaret, P. 2002: *A Chandra High Resolution Camera Observation of X-Ray Point Sources in M31*, ApJ, 578, 114

Kaluzny, J., Stanek, K. Z., Krockenberger, M., Sasselov, D. D., Tonry, J. L., & Mateo, M. 1998: *DIRECT Distances to Nearby Galaxies Using Detached Eclipsing Binaries and Cepheids. I. Variables in the Field M31B*, AJ, 115, 1016

Kato, M. 1997: *Optically Thick Winds from Degenerate Dwarfs. I. Classical Novae of Populations I and II*, ApJS, 113, 121

Kauffmann, G., Heckman, T. M., White, S. D. M., Charlot, S., Tremonti, C., Brinchmann, J., Bruzual, G., Peng, E. W., Seibert, M., Bernardi, M., Blanton, M., et al. 2003: *Stellar masses and star formation histories for 105 galaxies from the Sloan Digital Sky Survey*, MNRAS, 341, 33

Kent, S. M. 1987: *Surface photometry of six local group galaxies*, AJ, 94, 306

Kent, S. M. 1989a: *A comparison of optical and H I rotation curves in M 31*, PASP, 101, 489

Kent, S. M. 1989b: *An improved bulge model for M31*, AJ, 97, 1614

Keres, D., Yun, M. S., & Young, J. S. 2003: *CO Luminosity Functions for Far-Infrared- and B-Band-selected Galaxies and the First Estimate for Ω_{HI+H_2}*, ApJ, 582, 659

Kerins, E., Carr, B. J., Evans, N. W., Hewett, P., Lastennet, E., Le Du, Y., Melchior, A.-L., Smartt, S. J., & Valls-Gabaud, D. 2001: *Theory of pixel lensing towards M31 - I. The density contribution and mass of MACHOs*, MNRAS, 323, 13

Kerins, E., Darnley, M. J., Duke, J., Gould, A., Han, C., Jeon, Y. B., Newsam, A., & Park, B. G. 2005: *The Angstrom Project: a microlensing survey of the structure and composition of the bulge of the Andromeda galaxy,* astro-ph/0502545

Kerins, E. & the Point-Agape Collaboration. 2000: *Pixel lensing towards M31 in principle and in practice*, astro-ph/0004254

Khlopov, M. Y., Rubin, S. G., & Sakharov, A. S. 2000: *Possible origin of antimatter regions in the baryon dominated universe*, Phys. Rev. D, 62, 083505

Kong, A. K. H., Garcia, M. R., Primini, F. A., Murray, S. S., Di Stefano, R., & McClintock, J. E. 2002: *X-Ray Point Sources in the Central Region of M31 as Seen by Chandra*, ApJ, 577, 738

Kovács, G., Zucker, S., & Mazeh, T. 2002: *A box-fitting algorithm in the search for periodic transits*, A&A, 391, 369

Kuijken, K. & Gilmore, G. 1991: *The galactic disk surface mass density and the Galactic force K(z) at Z = 1.1 kiloparsecs*, ApJ, 367, L9

Kwee, K. K. 1967: *Investigations on Population II Cepheids. III. Light-curves and two-colour diagrams*, 19, 260

Landolt, A. U. 1992: *UBVRI photometric standard stars in the magnitude range 11.5-16.0 around the celestial equator*, AJ, 104, 340

Lasserre, T., Afonso, C., Albert, J. N., Andersen, J., Ansari, R., Aubourg, E., Bareyre, P., Bauer, F., Beaulieu, J. P., Blanc, G., Bouquet, A., et al. 2000: *Not enough stellar mass Machos in the Galactic halo*, A&A, 355, L39

Lawrie, D. G. 1983: *Velocity dispersion of planetary nebulae in the nuclear bulge of M31*, ApJ, 273, 562

Leavitt, H. S. & Pickering, E. C. 1912: *Periods of 25 Variable Stars in the Small Magellanic Cloud.*, Harvard College Observatory Circular, 173, 1

Lebzelter, T., Schultheis, M., & Melchior, A. L. 2002: *AGAPEROS: Searching for variable stars in the LMC Bar. II. Temporal and near-IR analysis of Long-Period Variables*, A&A, 393, 573

Lejeune, T., Cuisinier, F., & Buser, R. 1998: *A standard stellar library for evolutionary synthesis. II. The M dwarf extension*, A&AS, 130, 65

Liller, W. & Shida, R. Y. 2005: *Large Magellanic Cloud Novae 13 Days After Peak Brightness*, Journal of the American Association of Variable Star Observers (JAAVSO), 33, 207

Loinard, L., Allen, R. J., & Lequeux, J. 1995: *An unbiased survey for CO emission in the inner disk of the Andromeda galaxy.*, A&A, 301, 68

Lomb, N. R. 1976: *Least-squares frequency analysis of unequally spaced data*, Ap&SS, 39, 447

Lorenz, E. & Martinez, M. 2005: *High energy astrophysics: The MAGIC telescope*, Astronomy and Geophysics, 46, 21

Magnier, E. A., Lewin, W. H. G., van Paradijs, J., Hasinger, G., Jain, A., Pietsch, W., & Truemper, J. 1992: *BV RI CCD photometry of 361,281 objects in the field of M 31*, A&AS, 96, 379

Maraston, C. 1998: *Evolutionary synthesis of stellar populations: a modular tool*, MNRAS, 300, 872

Marigo, P. & Girardi, L. 2001: *Coupling emitted light and chemical yields from stars: A basic constraint to population synthesis models of galaxies*, A&A, 377, 132

Massey, P., Hodge, P. W., Holmes, S., Jacoby, G., King, N. L., Olsen, K., Saha, A., & Smith, C. 2001: *A Survey of Local Group Galaxies*, Bulletin of the American Astronomical Society, 33, 1496

McLaughlin, D. B. 1939: *The Light Curves of Novae*, Popular Astronomy, 47, 410

McLaughlin, D. B. 1942: *The Luminosities of Novae*, Popular Astronomy, 50, 233

McLaughlin, D. B. 1945: *The Relation between Light-Curves and Luminosities of Novae*, PASP, 57, 69

Melchiorri, A., Ade, P. A. R., de Bernardis, P., Bock, J. J., Borrill, J., Boscaleri, A., Crill, B. P., De Troia, G., Farese, P., Ferreira, P. G., Ganga, K., et al. 2000: *A Measurement of Omega from the North American Test Flight of Boomerang*, ApJ, 536, L63

Metcalf, R. B. & Silk, J. 1996: *Gravitational Microlensing by Clustered MACHOs*, ApJ, 464, 218

Moore, B., Diemand, J., Stadel, J., & Quinn, T. 2005: *On the survival and disruption of Earth mass CDM micro-haloes,* astro-ph/0502213

Moro, D. & Munari, U. 2000: *The Asiago Database on Photometric Systems (ADPS). I. Census parameters for 167 photometric systems*, A&AS, 147, 361

Noda, S., Takeuti, M., Abe, F., Bond, I. A., Dodd, R. J., Hearnshaw, J. B., Honda, M., Honma, M., Jugaku, J., Kabe, S., Kan-ya, Y., et al. 2002: *Study of variable stars in the MOA data base: long-period red variables in the Large Magellanic Cloud*, MNRAS, 330, 137

Noda, S., Takeuti, M., Abe, F., Bond, I. A., Dodd, R. J., Hearnshaw, J. B., Honda, M., Honma, M., Jugaku, J., Kan-ya, Y., Kato, Y., et al. 2004: *Study of variable stars in the MOA data base: long-period red variables in the Large Magellanic Cloud - II. Multiplicity of the period-luminosity relation*, MNRAS, 348, 1120

Nollez, G. & The EDELWEISS Collaboration. 2002: *New Exclusion Limits from the EDELWEISS WIMP Search*, in SF2A-2002: Semaine de l'Astrophysique Francaise, 65-+

Ostriker, J. P., Nagamine, K., Cen, R., & Fukugita, M. 2003: *The Probability Distribution Function of Light in the Universe: Results from Hydrodynamic Simulations*, ApJ, 597, 1

Overduin, J. M. & Wesson, P. S. 2003, Dark sky, dark matter (Series in astronomy and astrophysics)

Paczynski, B. 1986: *Gravitational microlensing by the galactic halo*, ApJ, 304, 1

Paczynski, B., Stanek, K. Z., Udalski, A., Szymanski, M., Kaluzny, J., Kubiak, M., Mateo, M., & Krzeminski, W. 1994: *Are the OGLE microlenses in the galactic bar?*, ApJ, 435, L113

Padmanabhan, J. 1995: *Structure formation in the universe*, Cambridge Universtity press, 73, 436

Page, L., Nolta, M. R., Barnes, C., Bennett, C. L., Halpern, M., Hinshaw, G., Jarosik, N., Kogut, A., Limon, M., Meyer, S. S., Peiris, H. V., et al. 2003: *First-Year Wilkinson Microwave Anisotropy Probe (WMAP) Observations: Interpretation of the TT and TE Angular Power Spectrum Peaks*, ApJS, 148, 233

Palanque-Delabrouille, N., Afonso, C., Albert, J. N., Andersen, J., Ansari, R., Aubourg, E., Bareyre, P., Bauer, F., Beaulieu, J. P., Bouquet, A., Char, S., et al. 1998: *Microlensing towards the Small Magellanic Cloud EROS 2 first year survey*, A&A, 332, 1

Paulin-Henriksson, S., Baillon, P., Bouquet, A., Carr, B. J., Crézé, M., Evans, N. W., Giraud-Héraud, Y., Gould, A., Hewett, P., Kaplan, J., Kerins, E., et al. 2002: *A Candidate M31/M32 Intergalactic Microlensing Event*, ApJ, 576, L121

Paulin-Henriksson, S., Baillon, P., Bouquet, A., Carr, B. J., Crézé, M., Evans, N. W., Giraud-Héraud, Y., Gould, A., Hewett, P., Kaplan, J., Kerins, E., et al. 2003: *The POINT-AGAPE survey: 4 high signal-to-noise microlensing candidates detected towards M 31*, A&A, 405, 15

Payne-Gaposchkin, C. 1957: *The Galactic Novae*, Science, 126, 1350

Percival, W. J., Baugh, C. M., Bland-Hawthorn, J., Bridges, T., Cannon, R., Cole, S., Colless, M., Collins, C., Couch, W., Dalton, G., De Propris, R., et al. 2001: *The 2dF Galaxy Redshift Survey: the power spectrum and the matter content of the Universe*, MNRAS, 327, 1297

Pfau, W. 1976: *Recalibration of the absolute magnitudes of novae and application Nova CYG 1975.*, A&A, 50, 113

Pfenniger, D., Combes, F., & Martinet, L. 1994: *Is dark matter in spiral galaxies cold gas? I. Observational constraints and dynamical clues about galaxy evolution*, A&A, 285, 79

Pietsch, W., Fliri, J., Freyberg, M. J., Greiner, J., Haberl, F., Riffeser, A., & Sala, G. 2005: *Optical novae: the major class of supersoft X-ray sources in M 31*, A&A, 442, 879

Prada, F., Klypin, A., Flix, J., Martínez, M., & Simonneau, E. 2004: *Dark Matter Annihilation in the Milky Way Galaxy: Effects of Baryonic Compression*, Physical Review Letters, 93, 241301

Prada, F., Vitvitska, M., Klypin, A., Holtzman, J. A., Schlegel, D. J., Grebel, E. K., Rix, H.-W., Brinkmann, J., McKay, T. A., & Csabai, I. 2003: *Observing the Dark Matter Density Profile of Isolated Galaxies*, ApJ, 598, 260

Press, W. H. 1988, Numerical recipes C (Cambridge University Press)

Prialnik, D. & Kovetz, A. 1995: *An extended grid of multicycle nova evolution models*, ApJ, 445, 789

Prialnik, D., Shara, M. M., & Shaviv, G. 1978: *The evolution of a slow nova model with a Z = 0.03 envelope from pre-explosion to extinction*, A&A, 62, 339

Rector, T. A., Jacoby, G. H., Corbett, D. L., Denham, M., & RBSE Nova Search Team. 1999: *A Search for Novae in the Bulge of M31*, Bulletin of the American Astronomical Society, 31, 1420

Reiprich, T. H. & Böhringer, H. 2002: *The Mass Function of an X-Ray Flux-limited Sample of Galaxy Clusters*, ApJ, 567, 716

Renzini, A. 1998: *The Stellar Populations of Pixels and Frames*, AJ, 115, 2459

Renzini, A. & Buzzoni, A. 1986: *Global properties of stellar populations and the spectral evolution of galaxies*, in ASSL Vol. 122: Spectral Evolution of Galaxies, 195–231

Riess, A. G., Nugent, P. E., Gilliland, R. L., Schmidt, B. P., Tonry, J., Dickinson, M., Thompson, R. I., Budavári, T., Casertano, S., Evans, A. S., Filippenko, A. V., et al. 2001: *The Farthest Known Supernova: Support for an Accelerating Universe and a Glimpse of the Epoch of Deceleration*, ApJ, 560, 49

Riffeser, A., Fliri, J., Bender, R., Seitz, S., & Gössl, C. A. 2003: *The Wendelstein Calar Alto Pixel-lensing Project (WeCAPP): First MACHO Candidates*, ApJ, 599, L17

Riffeser, A., Fliri, J., Gössl, C. A., Bender, R., Hopp, U., Bärnbantner, O., Ries, C., Barwig, H., Seitz, S., & Mitsch, W. 2001: *WeCAPP - Wendelstein Calar Alto pixellensing project I. Tracing dark and bright matter in M31*, A&A, 379, 362

Riffeser, A., Fliri, J., Seitz, S., & Bender, R. 2005: *Microlensing towards crowded fields: Theory and applications to M31,* ApJS, in print, astro-ph/0510723

Roberts, D. H., Lehar, J., & Dreher, J. W. 1987: *Time Series Analysis with Clean - Part One - Derivation of a Spectrum*, AJ, 93, 968

Rosino, L. 1964: *Novae in Messier 31 discovered and observed at Asiago from 1955 to 1963.*, Annales d'Astrophysique, 27, 498

Rosino, L. 1973: *Novae in M 31 discovered and observed at Asiago from 1963 to 1970*, A&AS, 9, 347

Rosino, L., Capaccioli, M., D'Onofrio, M., & della Valle, M. 1989: *Fifty-two novae in M31 discovered and observed at Asiago from 1971 to 1986*, AJ, 97, 83

Roulet, E. & Mollerach, S. 1997: *Microlensing*, Physics Reports, 279, 67

Rubin, V. C., Ford, W. K., Thonnard, N., & Burstein, D. 1982: *Rotational properties of 23 SB galaxies*, ApJ, 261, 439

Rubin, V. C., Thonnard, N., & Ford, W. K. 1978: *Extended rotation curves of high-luminosity spiral galaxies. IV - Systematic dynamical properties, SA through SC*, ApJ, 225, L107

Rubin, V. C., Thonnard, N., & Ford, W. K. 1980: *Rotational properties of 21 SC galaxies with a large range of luminosities and radii, from NGC 4605 to UGC 2885*, ApJ, 238, 471

Sachs, R. K. & Wolfe, A. M. 1967: *Perturbations of a Cosmological Model and Angular Variations of the Microwave Background*, ApJ, 147, 73

Sahu, K. C. 1994: *Microlensing events of the LMC are better explained by stars within the LMC than by MACHOs*, PASP, 106, 942

Sahu, K. C. 2003: *Microlensing towards the Magellanic Clouds: nature of the lenses and implications on dark matter*, in The Dark Universe: Matter, Energy and Gravity, 14–23

Scargle, J. D. 1982: *Studies in astronomical time series analysis. II - Statistical aspects of spectral analysis of unevenly spaced data*, ApJ, 263, 835

Schlegel, D. J., Finkbeiner, D. P., & Davis, M. 1998: *Maps of Dust Infrared Emission for Use in Estimation of Reddening and Cosmic Microwave Background Radiation Foregrounds*, ApJ, 500, 525

Schmidt, T. 1957: *Die Lichtkurven-Leuchtkraft-Beziehung Neuer Sterne*, Zeitschrift für Astrophysik, 41, 182

Shafter, A. W. & Irby, B. K. 2001: *On the Spatial Distribution, Stellar Population, and Rate of Novae in M31*, ApJ, 563, 749

Shara, M. M. 1981: *On the constancy of the absolute magnitude $M_B(15)$ of a classical nova 15 days after maximum light*, ApJ, 243, 268

Sharov, A. S. & Alksnis, A. 1992: *Novae in M31 discovered with wide-field telescopes in Crimea and Latvia - The maximum magnitude versus rate of decline relation for Novae in M31*, Ap&SS, 190, 119

Sharov, A. S., Alksnis, A., Zharova, A. V., & Shokin, Y. A. 2000: *Novae in M31 in 1998*, Astronomy Letters, 26, 433

Sheldon, E. S., Annis, J., Böhringer, H., Fischer, P., Frieman, J. A., Joffre, M., Johnston, D., McKay, T. A., Miller, C., Nichol, R. C., Stebbins, A., et al. 2001: *Weak-Lensing Measurements of 42 SDSS/RASS Galaxy Clusters*, ApJ, 554, 881

Silk, J. 1968: *Cosmic Black-Body Radiation and Galaxy Formation*, ApJ, 151, 459

Simon, N. R. & Lee, A. S. 1981: *The structural properties of Cepheid light curves*, ApJ, 248, 291

Simon, N. R. & Moffett, T. J. 1985: *Classical Cepheid light curves revisited*, PASP, 97, 1078

Slott-Agape Collaboration. 1999: *Slott-Agape Project*, astro-ph/9907162

Smail, I., Ellis, R. S., Dressler, A., Couch, W. J., Oemler, A. J., Sharples, R. M., & Butcher, H. 1997: *A Comparison of Direct and Indirect Mass Estimates for Distant Clusters of Galaxies*, ApJ, 479, 70

Soszynski, I., Udalski, A., Kubiak, M., Szymanski, M. K., Pietrzynski, G., Zebrun, K., Wyrzykowski, O. S. L., & Dziembowski, W. A. 2004: *The Optical Gravitational Lensing Experiment. Ellipsoidal Variability of Red Giants in the Large Magellanic Cloud*, Acta Astronomica, 54, 347

Spergel, D. N., Verde, L., Peiris, H. V., Komatsu, E., Nolta, M. R., Bennett, C. L., Halpern, M., Hinshaw, G., Jarosik, N., Kogut, A., Limon, M., et al. 2003: *First-Year Wilkinson Microwave Anisotropy Probe (WMAP) Observations: Determination of Cosmological Parameters*, ApJS, 148, 175

Stanek, K. Z. & Garnavich, P. M. 1998: *Distance to M31 with the Hubble Space Telescope and HIPPARCOS Red Clump Stars*, ApJ, 503, L131

Starrfield, S., Truran, J. W., Wiescher, M. C., & Sparks, W. M. 1998: *Evolutionary sequences for Nova V1974 Cygni using new nuclear reaction rates and opacities*, MNRAS, 296, 502

Stephens, A. W., Frogel, J. A., DePoy, D. L., Freedman, W., Gallart, C., Jablonka, P., Renzini, A., Rich, R. M., & Davies, R. 2003: *The Stellar Content of the Bulge of M31*, AJ, 125, 2473

Sterken, C. & Jaschek, C. 1996, Light Curves of Variable Stars, A Pictorial Atlas (Cambridge University Press)

Stratton, F. J. M. 1936: *Novae*, Handbuch der Astrophysik, 7, 671

Szymanski, M., Kubiak, M., & Udalski, A. 2001: *Contact Binaries in OGLE-I Database*, Acta Astronomica, 51, 259

Tingley, B. 2003: *Improvements to existing transit detection algorithms and their comparison*, A&A, 408, L5

Tomaney, A. B. & Crotts, A. P. S. 1996: *Expanding the Realm of Microlensing Surveys with Difference Image Photometry*, AJ, 112, 2872

Tomaney, A. B. & Shafter, A. W. 1992: *The spectroscopic and photometric evolution of novae in the bulge of M31*, ApJS, 81, 683

Tripp, T. M., Savage, B. D., & Jenkins, E. B. 2000: *Intervening O VI Quasar Absorption Systems at Low Redshift: A Significant Baryon Reservoir*, ApJ, 534, L1

Udalski, A., Szymanski, M., Kaluzny, J., Kubiak, M., Krzeminski, W., Mateo, M., Preston, G. W., & Paczynski, B. 1993: *The optical gravitational lensing experiment. Discovery of the first candidate microlensing event in the direction of the Galactic Bulge*, Acta Astronomica, 43, 289

Udalski, A., Zebrun, K., Szymanski, M., Kubiak, M., Pietrzynski, G., Soszynski, I., & Wozniak, P. 2000: *The Optical Gravitational Lensing Experiment. Catalog of Microlensing Events in the Galactic Bulge*, Acta Astronomica, 50, 1

Uglesich, R. R., Crotts, A. P. S., Baltz, E. A., de Jong, J., Boyle, R. P., & Corbally, C. J. 2004: *Evidence of Halo Microlensing in M31*, ApJ, 612, 877

Šimon, V., Hornoch, K., Kušnirák, P., Šarounová, L., & Wolf, M. 2005: *Discovery and Photometry of 8 Novae in the M31 Galaxy in 2002 - 2004*, in ASP Conf. Ser. 330: The Astrophysics of Cataclysmic Variables and Related Objects, 449–+

Valls-Gabaud, D. 1994: *Chromatic, spectroscopic and polarisation effects in microlensing events from stellar sources*, in: Large scale structure in the universe, 326

van Albada, T. S., Bahcall, J. N., Begeman, K., & Sancisi, R. 1985: *Distribution of dark matter in the spiral galaxy NGC 3198*, ApJ, 295, 305

van den Bergh, S. & Younger, P. F. 1987: *UBV photometry of novae*, A&AS, 70, 125

van der Kruit, P. C. & Bosma, A. 1978: *The rotation curves and orientation parameters of the spiral galaxiesNGC 2715, 5033 and 5055.*, A&AS, 34, 259

Verde, L., Heavens, A. F., Percival, W. J., Matarrese, S., Baugh, C. M., Bland-Hawthorn, J., Bridges, T., Cannon, R., Cole, S., Colless, M., Collins, C., et al. 2002: *The 2dF Galaxy Redshift Survey: the bias of galaxies and the density of the Universe*, MNRAS, 335, 432

Vondrák, J. 1969: *A contribution to the problem of smoothing observational data*, Bulletin of the Astronomical Institutes of Czechoslovakia, 20, 349

Vondrák, J. 1977: *Problem of Smoothing Observational Data II*, Bulletin of the Astronomical Institutes of Czechoslovakia, 28, 84

Wagoner, R. V., Fowler, W. A., & Hoyle, F. 1967: *On the Synthesis of Elements at Very High Temperatures*, ApJ, 148, 3

Wallerstein, G. 2002: *The Cepheids of Population II and Related Stars*, PASP, 114, 689

Walterbos, R. A. M. & Kennicutt, R. C. 1987: *Multi-color photographic surface photometry of the Andromeda galaxy*, A&AS, 69, 311

Whittaker, E. & Robinson, G. 1946, The Calculus of Observations (Blackie & Son Ltd, London)

Widrow, L. M., Perrett, K. M., & Suyu, S. H. 2003: *Disk-Bulge-Halo Models for the Andromeda Galaxy*, ApJ, 588, 311

Williams, B. F. 2002: *Clues about the star formation history of the M31 disc from WFPC2 photometry*, MNRAS, 331, 293

Wirth, A., Smarr, L. L., & Bruno, T. L. 1985: *The missing bulge globular clusters in M31 - New optical candidates*, ApJ, 290, 140

Witt, H. J. 1995: *The Effect of the Stellar Size on Microlensing at the Baade Window*, ApJ, 449, 42

Wood, P. R. 2000: *Variable red giants in the LMC: Pulsating stars and binaries?*, Publications of the Astronomical Society of Australia, 17, 18

Wood, P. R., Alcock, C., Allsman, R. A., Alves, D., Axelrod, T. S., Becker, A. C., Bennett, D. P., Cook, K. H., Drake, A. J., Freeman, K. C., Griest, K., et al. 1999: *MACHO observations of LMC red giants: Mira and semi-regular pulsators, and contact and semi-detached binaries*, in IAU Symp. 191: Asymptotic Giant Branch Stars, 151

Wozniak, P. & Paczynski, B. 1997: *Microlensing of Blended Stellar Images*, ApJ, 487, 55

Wray, J. J., Eyer, L., & Paczyński, B. 2004: *OGLE small-amplitude variables in the Galactic bar*, MNRAS, 349, 1059

Xiong, D. R., Deng, L., & Cheng, Q. L. 1998: *Turbulent Convection and Pulsational Stability of Variable Stars. I. Oscillations of Long-Period Variables*, ApJ, 499, 355

Zhao, H., Taylor, J. E., Silk, J., & Hooper, D. 2005: *Earth-mass dark halos are torn into dark mini-streams by stars,* astro-ph/0502049

Ziaeepour, H. 2001: *Searching the footprint of WIMPZILLAs*, Astroparticle Physics, 16, 101

Zoccali, M., Cassisi, S., Frogel, J. A., Gould, A., Ortolani, S., Renzini, A., Rich, R. M., & Stephens, A. W. 2000: *The Initial Mass Function of the Galactic Bulge down to $\sim 0.15\,M_{solar}$*, ApJ, 530, 418

Zwaan, M. A., Staveley-Smith, L., Koribalski, B. S., Henning, P. A., Kilborn, V. A., Ryder, S. D., Barnes, D. G., Bhathal, R., Boyce, P. J., de Blok, W. J. G., Disney, M. J., et al. 2003: *The 1000 Brightest HIPASS Galaxies: The H I Mass Function and $\Omega_H I$*, AJ, 125, 2842

Zwicky, F. 1933: *Die Rotverschiebung von extragalaktischen Nebeln*, Helvetica Physica Acta, 6, 110

Zwicky, F. 1936: *Life-Luminosity Relation for Novae*, PASP, 48, 191

Acknowledgments

CURRICULUM VITAE

Name:	Jürgen Fliri
Born:	April the 24th, 1972, Schlanders, Italy
Marital Status:	Single
Citizenship:	Italian
Home:	Waldspielplatz 1, 82319 Starnberg, Germany

Education		
	1978 – 1981	Elementary School Student in Taufers. i.M.
	1981 – 1982	Elementary School Student in Söcking
	1982 – 1991	High-School Student, Gymnasium, Starnberg
	1991	Abitur, Gymnasium, Starnberg
	1991 – 2000	Diploma Student, Physics, LMU Munich
	1999 – 2000	Diploma Thesis, Physics, LMU Munich
	2000	Physics Diploma, LMU Munich
	2000 – 2006	Ph.D. Student, Astronomy & Astrophysics, LMU Munich